University of Alberta

Wetting Performance of Worn Superhydrophobic Surfaces

by

Maninderjit Singh

A thesis submitted to the Faculty of Graduate Studies and Research
in partial fulfillment of the requirements for the degree of

MASTER of SCIENCE

DEPARTMENT OF MECHANICAL ENGINEERING

Spring 2013

Edmonton, Alberta

This is not dedicated to my parents, who did not give me up for adoption to a rich family.

TO

Doris Vollmer, a great mentor.

Alidad Amirfazli, scholar and a gentleman.

Karamdeep Bhullar, for all time.

Abstract

This thesis is concerned with the effect of mechanical wear on superhydrophobic surfaces (SHS). This work, for the first time, systematically details the simultaneous surface topography and wetting behavior changes upon abrasion of SHS. The process of physical abrasion was also simulated on the artificial terrains. An intrinsically hydrophobic polymer (PTFE) was plasma etched to fabricate SHS, as wear would solely change surface topography and avoid chemical complications. Wetting behavior was monitored using advancing and receding contact angles (CA). Confocal scanning microscopy (CSM) was used to monitor topography quantitatively using surface topographical descriptors.

In initial stages of wear receding and advancing CA, remained largely unchanged. Excessive wear resulted in a large increase in CA hysteresis and lowering of the advancing CA. Wetting behavior was correlated with topographical descriptors. Trends in RMS roughness, Skewness and Kurtosis can act as guiding factors towards predicting CA hysteresis on the surface. Main finding was that the physical abrasion can be simulated computationally on analogous artificial terrains.

Acknowledgements

Thank you, Alidad Amirfazli, for giving me an important role and the atmosphere to pursue it. He is one of the smartest people and the funniest advisor that I know of. I hope to someday command an audience as well as he can and be as patient, lively, enthusiastic and energetic as him.

Thank you, Doris Vollmer, for the encouragement, freedom, and the creative avenue you gave at Max Planck Institute for Polymer Research (MPIP) and letting me think for myself. Your advice has always been valuable and helped me stay on the right path.

Thank you, Michael Bockstaller, my mentor in undergraduate years. You are the reason I decided to continue doing research. Your penchant for being curious and inquisitive is addictive.

Thank you, Justin Ng and Matthew Dickau, research students in surface engineering and instrumentation laboratory, University of Alberta. They played an important role in the work done in this thesis by setting the foundation for this research. Justin assembled the experimental setup and did initial abrasion experiments, and calibrated the abrasion speed to be used for further experiments. Figure 2-2, 2-5 and 2-7 are also inspired by him. Matthew abraded, collected wetting and confocal imaging data for all the samples analyzed in this thesis.

Thank you, scientists at Leibniz Institute of Polymer Research (IPF), for preparing superhydrophobic surfaces used in this study.

Thank you, Andrew Milne, for your help with SEM imaging and MATLAB coding, and, David Barona, for helping analyze various data. Thank you both for providing valuable inputs continually during this thesis. Andrew Milne also supplied major graphical work for Figure 2-9.

Thank you, Lena Mammen, for providing Silicon masks used to fabricate various PDMS/PTFE regular geometry surfaces during the course of thesis.

Thank you, Nanofab staff at University of Alberta, Bernie Faulkner, and Scott Munro for their invaluable advice and expertise with the instruments used in this thesis.

Thank you, Natural Science and Engineering Research Council of Canada (NSERC), Consortium for Research and Innovation in Aerospace in Quebec (CRIAQ), Bombardier and Pratt & Whitney Canada for financial support.

Thank you, to all Office and IT staff for helping with all the chores with big smiles.

Thank you, Aishvarya Agarwal, Shailesh Chauhan, Shekhar Singh Dalal, and Ajmer Purewal for playing an important role in my life.

Thank you, Huanchen Chen, for being a good sport.

Special thanks to my parents for their love and encouragement.

Thank you, Satinder Cheema, for picking up calls at all odd hours and for the help extended in all the fields called “not science”.

Thank you, those that are no longer with me, but never forgotten, for being exceptionally warm during their life with me.

Thank you, to all those I missed, I am indebted to you.

Table of Contents

List of Tables

List of Figures

List of Symbols, Nomenclature and Abbreviations

γ_{sl}, γ_{lv} and γ_{sv}	Surface tension between the solid (*s*) and the liquid (*l*), the liquid (*l*) and the vapor (*v*), and the solid (*s*) and the vapor (*v*), respectively
θ	Intrinsic contact angle on the smooth surface
θ_c	Cassie contact angle
θ_{cl}	Cassie contact angle on a *linear* density basis
θ_w	Wenzel contact angle
θ_x	Contact angle on smooth surface of material *x* (*x* in this thesis is generally material 1 and 2, denoting solid and air, respectively)
θ_{xl}	Contact angle on smooth surface of material *x* on a *linear* density basis (*x* in this thesis is generally material 1 and 2, denoting solid and air, respectively)
Δh	Height matrix containing values to be abraded at each wear iteration of abrasion algorithm
λ	Real number (used in abrasion algorithm)
c	Wear iteration number of the abrasion algorithm
f	Solid fraction of the surface
f_x	Total area of material *x* under the drop per unit projected area under the drop
f_{xl}	Total area of material *x* under the drop per unit projected area under the drop on a *linear* density basis
r	Roughness parameter
$R_t(c)$	Difference between highest peak and valley depth on a surface (used in abrasion algorithm)
S_a	Average roughness
S_{al}	Autocorrelation length

S_{cl20}	Correlation length at 20%
S_{cl37}	Correlation length at 37%
S_{dq}	Root mean square surface slope
S_{dq6}	Area root mean square surface slope
S_{dr}	Surface area ratio
S_{ds}	Summit density
S_{fd}	Fractal dimension
S_{hw}	Mean half wavelength
S_k	Core roughness depth
S_{ku}	Kurtosis
S_{mr1}	Peak material portion
S_{mr2}	Peak valley portion
S_p	Maximum peak height
S_{pk}	Reduced peak height
S_q	Root mean square roughness
S_{rw}	Dominant radial wavelength
S_{rwi}	Radial wave index
S_{sc}	Mean summit curvature
S_{sk}	Skewness
S_{td}	Texture direction
S_{tdi}	Texture direction index
S_{tr}	Texture aspect ratio
S_{tr20}	Texture aspect ratio at 20%
S_{tr37}	Texture aspect ratio at 37%
S_v	Maximum valley depth

S_{vk}	Reduced valley depth
S_z	Maximum height of surface
$W_{\lambda}(x,c)$	Probability of erosion of pixel located at position x, at wear cycle c.
AAATC	American Association of Textile Chemists and Colorists
ADSA	Axisymmetric Drop Shape Analysis
ASTM	American Society for Testing and Materials
CA	Contact Angle(s)
CAH	Contact Angle Hysteresis
CL	Contact Line
CSM	Confocal Scanning Microscopy
CVD	Chemical Vapor Deposition
DI	De-ionized
GNU	GNU's Not Unix
GUI	Graphical User Interface
LDPE	Low density polyethylene
MMC	Metal Matrix Composite
PDMS	Polydimethylsiloxane
PTFE	poly(tetrafluoroethylene)
RF	Radio Frequency
RMS	Root Mean Square
SHS	Superhydrophobic surface(s)
SEM	Scanning Electron Microscopy
TFA	Textile Friction Analyzer
THF	Tetrahydrofuran
TPCL	Three phase contact line

Chapter 1 - Introduction

In this thesis, superhydrophobic surfaces (SHS) were studied. A superhydrophobic surface (surfaces with contact angle greater than 150° and low contact angle hysteresis) repels water with extreme efficiency, making the water drop bead up on the surface and the drop rolls with (sometimes without) the application of a slight force/tilt. As also discussed later in Section 1.2, superhydrophobicity results from a combination of low surface energy and microtextured irregular topography. A significant body of research has been devoted to various aspects of superhydrophobicity ranging from their fabrication and application to its fundamental investigation. Some of the applications that stem from SHS include self-cleaning [1-5], preventing frost from adhering to the surfaces [6-10], stain-resistant garments [11-13], and reducing frictional drag in water [14-15]. This brief list of applications should explain the intensified interest in superhydrophobicity and impetus the research in this field has achieved over last few years.

Superhydrophobic surfaces are presently an untapped resource; despite various widely reported applications they have not been able to make significant commercial inroads and widespread usage has remained elusive. Durability of SHS is limited by the fragility of microtextured topography present on them. Mild mechanical wear on SHS results in loss of superhydrophobicity. Abrasive mechanical wear “planarizes” the roughness features on SHS resulting in rise of CAH. Figure 1-1 (on page 2) depicts this loss of superhydrophobicity. Poor robustness of SHS potentially marginalizes them to be used only in closed atmosphere applications where degree of prevalent wear is considerably less, like microfluidics [16-18].

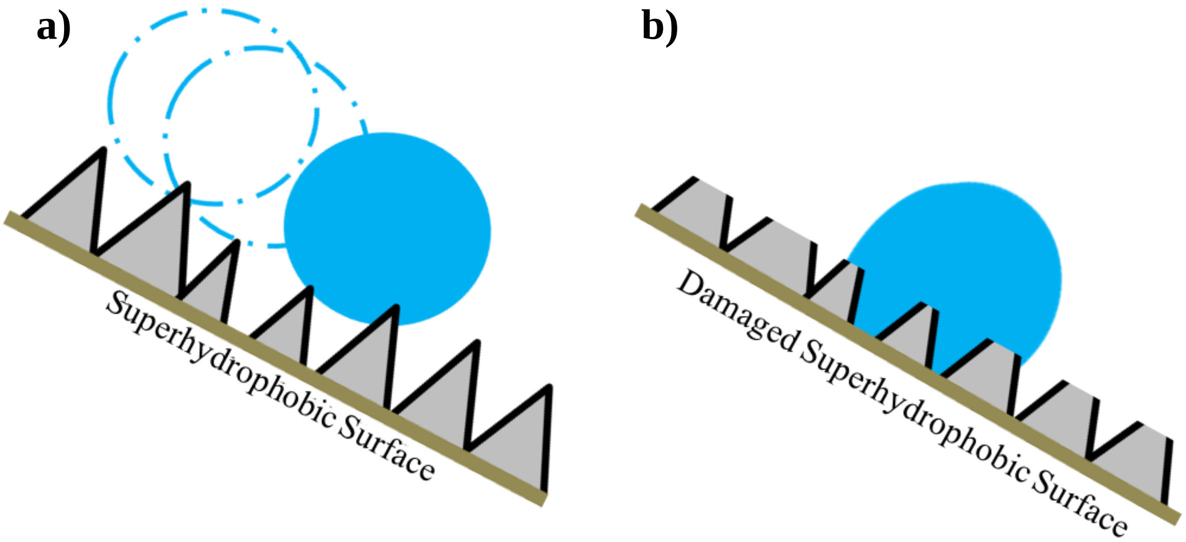

Figure 1-1 : Schematic of a) Water drop rolling on a superhydrophobic surface, b) Water drop stuck on a damaged superhydrophobic surface, due to increased contact angle hysteresis. Light part of the topography signifies the bulk polymer, while dark line on the asperities signifies the hydrophobic coating that imparts superhydrophobicity. Inspired by [41].

The response of researchers until now has been to seek ever more diverse ways of making SHS in hope of achieving robustness. A systematic look into how wetting of a SHS changes as it wears, has not been investigated until now, although many durability studies have been conducted on SHS. This aspect is detailed later in Section 1.4. For SHS to be used for various potential applications, an in-depth study on mechanical wear of SHS is needed, and this was the aim of this research.

The focus of this thesis was to understand the changes in surface topography as SHS undergo wear, while simultaneously also monitoring the wetting characteristics (CAH). This would help in understanding the effect of topography on wetting, and help analyze topographical features needed to provide robustness to SHS topography. Topography can be evaluated using a set of surface topography descriptors, which quantify surface relief through mathematical approach. For the first time, surface topography was abraded, quantified using various surface topography descriptors, and an attempt was made to relate them to wetting. The rest of this chapter details the theories explaining superhydrophobicity, followed by literature review on durability of SHS. Finally, the scope and outline for the remainder of thesis chapters is given.

1.1 Wetting on solids

A sessile liquid drop at rest on a solid surface assumes a shape similar to a spherical cap. The angle between the solid/liquid and liquid/vapor interface at the three phase contact line is quantified as equilibrium contact angle. When the drop volume is increasing, the contact angle (CA) exhibited just before the three phase contact line (CL) moves across the solid surface is termed as advancing contact angle. While vice-versa holds true for receding contact angle, i.e. the angle exhibited just before the three phase CL (TPCL) starts receding across the surface as the drop volume decreases.

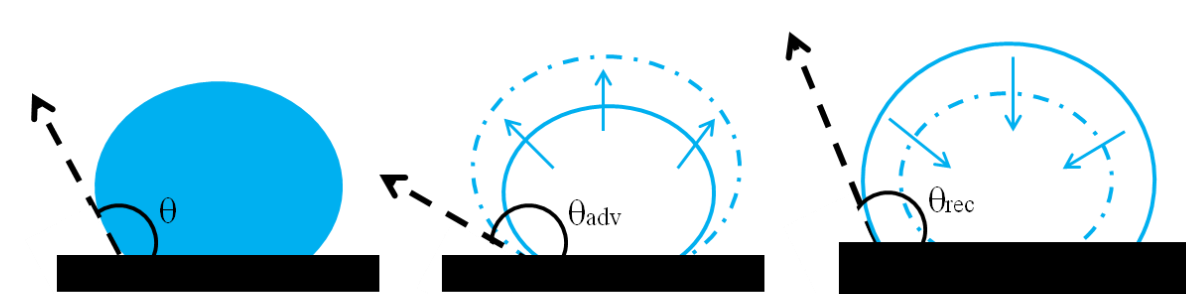

(a) (b) (c)

Figure 1-2: Schematic of (a) Static contact angle, (b) Advancing contact angle and (c) Receding contact angle. The liquid drops are sitting on a solid surface. In (b) and (c) the solid lines represent the present curvature of the liquid, while dash-dotted lines show the previous curvature before the drop expanded or contracted, respectively. The arrows indicate if the drop volume is increasing or decreasing.

Figure 1-2 illustrates the static, advancing and receding contact angles (CA). The difference between advancing and receding contact angle is referred to as contact angle hysteresis (CAH). Equilibrium contact angle lies between the two extremes of advancing and receding CA. Wetting characteristics (or behavior) of a surface towards a particular liquid are characterized by quantifying the advancing and receding CA of the drop. Advancing CA relates to the repellancy of the liquid towards the solid surface, while CAH points towards liquid mobility on the surface.

The extreme cases of CA on a surface are that of 0° (complete wetting) and 180° (non-wettable). Hence, lower the equilibrium CA the higher the wetting of the surface, and vice-versa. In research parlance, the surfaces lying towards the two ends of wetting spectrum are referred to as hydrophilic (completely wettable) and superhydrophobic (non-wettable). When the water equilibrium CA is less than 90° on a surface, the surface is said to be hydrophilic. In the case of water drop achieving an equilibrium CA between 90° and 150°, surface is referred to as hydrophobic. Superhydrophobic surfaces are those that exhibit both an equilibrium contact angle greater than 150° and low CAH. Figure 1-3 graphically illustrates possible wetting scenarios on surfaces and the respective contact angles they will exhibit.

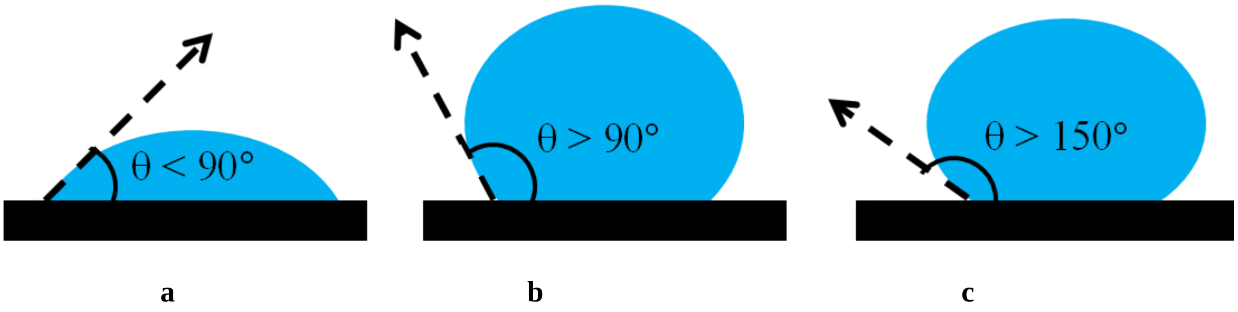

Figure 1-3: Schematic showing tentative contact angles for a water drop placed on a (a) hydrophilic, (b) hydrophobic and (c) superhydrophobic surface. Here, θ is the contact angle displayed on the surface.

1.2 Explaining Superhydrophobicity

Superhydrophobicity is defining the wettability of surfaces by leveraging surface chemistry (low surface energy) and surface morphology, such that surfaces exhibit water CA greater than 150° and low CAH. Combination of low surface energy and irregularities on surface helps augmenting liquids' surface tension and trapping air beneath the liquid drop, resulting in liquid shedding properties of the surface. The need for using the microtextured topography with low surface energy to achieve superhydrophobicity is detailed below.

1.2.1 Smooth surfaces

The drop forms a three phase contact line at the junction where it meets the solid surface. Interplay of interfacial surface energies between three phases (i.e. solid, liquid, and vapor) dictate the shape of the drop. This is portrayed by Young's equation [19], eq. 1-1, in which the equilibrium contact angle for a drop resting on an ideally smooth surface can be predicted theoretically as:

$$\gamma_{\mathrm{LV}}\cos\theta = \gamma_{\mathrm{SV}} - \gamma_{SL} \qquad \text{1-1}$$

Here, θ is the intrinsic or equilibrium CA of the surface whereas γ denotes the interfacial surface energy, with subscript referring to interface between phases denoted by solid (*S*), liquid (*L*) and vapor (*V*). In case of liquid phase being water and vapor phase being air, it can be seen from eq. 1-1 that contact angle can be lowered by increasing the surface energy of the solid component (γ_{SV}), since surface tension of water in air (γ_{LV}) is constant and defined. Lowest surface energy until now has been reported for closely packed CF_3 groups, and water contact angle on its smooth surface has been reported to be ~119° [20]. Hence, superhydrophobicity cannot be achieved by a smooth surface.

1.2.2 Rough surfaces

Textured surfaces help achieve higher contact angles, and two models by Wenzel [21] and Cassie [22] have been put forward to explain this phenomenon.

- **Wenzel's Model**

Wenzel [21] described the model for a drop resting on a rough surface with liquid penetrating fully into the asperities, as depicted in Figure 1-4.

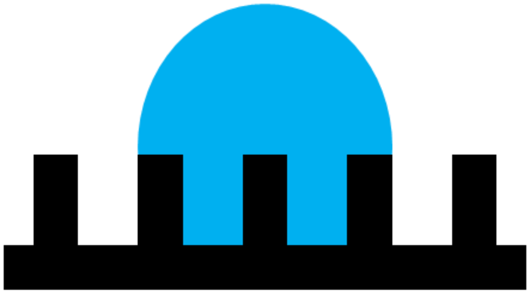

Figure 1-4: Schematic illustrating Wenzel model on a rough surface with water drop penetrating into asperities. For simplicity, regular geometry is shown here.

The contact angle (θ_w) on a rough surface in such a case is given by Wenzel equation:

$$\cos\theta_w = r\cos\theta \qquad \text{1-2}$$

Here, *r* is roughness factor and is calculated as ratio of actual surface area to projected surface area. Also, θ is the contact angle on a corresponding smooth surface. For a smooth surface, *r* will be equal to 1, and Wenzel equation (eq. 1-2) is transformed to Young's equation (eq. 1-1). Considering a rough surface, roughness *r* will always be larger than unity. This makes the CA (θ_w) greater than the corresponding angle on smooth surface, if $\theta>90°$. In case of hydrophilic ($\theta<90°$) substrates the CA decreases. Alone, as shown in Section 1.2.1, surface chemistry is able to achieve a maximum CA of 120°. Hence, roughness and chemistry are used in tandem to increase hydrophobicity.

- **Cassie's Model**

When the liquid sits suspended on the asperities, and does not penetrate them leaving air pockets embedded beneath the drop, the situation is described by Cassie's model [22-23]. In cases where liquid partially impregnates the surface topographical features, it is described as composite Cassie state. This is depicted in Figure 1-5, and written as eq. 1-3 for a two component system.

$$\cos\theta_c = f_1 \cos\theta_1 + f_2 \cos\theta_2 \qquad 1\text{-}3$$

where θ_c is apparent CA, f_1 and f_2 being surface fractions of respective materials; θ_1 and θ_2 are smooth surface for material 1 and material 2 respectively.

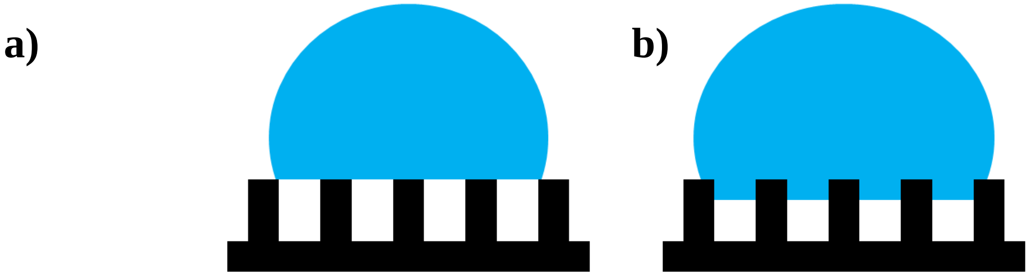

Figure 1-5: Schematic illustrating a) Cassie state on a rough surface with water drop trapping the air into asperities, b) Composite Cassie state where liquid has partially penetrated into the asperities.

If the second component material is air (as is the case in this thesis), θ_2 is 180° and hence the Cassie equation, eq. 1-3, is then:

$$\cos\theta_c = f_1 \cos\theta_1 - f_2 \qquad 1\text{-}4$$

Another form of Cassie equation prevalent in literature is shown in eq. 1-5. Traditionally, original form of Cassie equation (Eqs. 1-3 and 1-4) has been misinterpreted [23] and surface fraction f_2 was taken to be (1-f_1) and substituted in eq. 1-4.

$$\cos\theta_c = f\cos\theta_1 - (1 - f) \qquad \text{1-5}$$

This equation (eq. 1-5) is only valid when the liquid is not penetrating into the corrugated surface, and is resting on flat tops. Equation 1-5 has still been used for wide variety of topographies e.g. pyramidal, hemispherical where a degree of liquid penetration into surface topography will be present. Milne and Amirfazli [23] put forward a comprehensive viewpoint on Cassie equation, its use cases and how it has traditionally been used (as *popular* form, eq. 1-5) and used as defined originally by Cassie and Baxter (as *original* form, eqs. 1-3 and 1-4).

There also have been two schools of thought regarding Cassie equation toward calculating the surface fractions (f_1 and f_2), whether areal density (area covered by drop) or line density (three phase contact line) should be used to calculate the surface fractions [28-32]. This aspect is detailed in Section 2.3.1.

1.3 Predicting Wettability

While in Wenzel state, surfaces have high CAH and drop generally remains immobile on the surface even on application of a large tilting angle to the surface. Drop in Cassie state is highly mobile and rolls easily with application of a slight tilting angle to the surface. There also have been surfaces reported in literature with high static CA, but having high CAH and hence not being superhydrophobic [24-25]. Hence, determination of dynamic wetting scenario (CAH) is crucial to gauge surface superhydrophobicity, as most of the applications are sustained by drop having a highly mobile state on the surface. CAH is understood to arise as a result of surface heterogeneities, both chemical and topographical [21, 22, 33, 34]. Studies have been performed using thermodynamic aspects but predicting dynamic phenomenon remains incomplete due to complex nature of CAH [26-27]. Neumann and his coworkers [33-35] stated that "Models ascribing contact angle hysteresis to features of the solid surface such as roughness and heterogeneity may well be applicable in certain situations, but not on carefully prepared films of polymeric materials." Studies also show the inadequacies of existing Cassie and Wenzel models, as discrepancies have been observed between experimental CA and theoretically predicted CA [36-37]. Furthermore, Cassie, Wenzel and Young's equations all predict equilibrium CA, and dynamic scenarios (CAH) are not predicted.

Hence a look into Cassie equation was taken in this thesis on its ability to predict/estimate dynamic wetting scenarios. Both *original* and *popular* forms of Cassie equation (eqs. 1-4 and 1-5) were used and evaluated, incorporating both line and area density viewpoints.

1.4 State of the art of durability of superhydrophobic surfaces

Superhydrophobicity is achieved by a combination of surface energy and surface roughness. Surface energy is influenced by the topmost molecular layer of the surface. Mechanical wear on SHS can induce changes in both surface chemistry and surface topography by "planarizing" or "clogging" the surface roughness features and producing inhomogeneous surface energy sites, hence affecting superhydrophobicity. Alternate path of researchers to robust or "scratch-resistant" SHS has been finding materials and diverse ways to fabricate surfaces which are able to preserve their superhydrophobicity [38-40]. Surfaces fabricated with these new materials/methodologies were abraded to test their mechanical stability [41], and CAs (in some cases CAH) reported in literature.

Novel materials have been fabricated which show remarkable superhydrophobic robustness towards different environmental factors. D'Acunzi *et al.* [38] used a novel methodology towards robustness with core-shell colloids, which had a Polystyrene core and a porous silica shell. Multilayer SHS were formed by sedimentation and on exposure to Tetrahydrofuran (THF), Polystyrene leaked out through the porous silica shell to form bridges with neighboring colloids to impart mechanical strength to the film. Robustness of films was checked by a simple finger scratching method, and was found to be able to resist the friction. Yan *et al.* [39] fabricated Poly(alkylpyrrole) films whose superhydrophobicity was intact even after being immersed in various organic solvents and oils (acetone, ethanol, olive oil) for 2 hours. Han *et al.* [40] fabricated PAH/PAA-coated ZrO_2 nanocomposite coatings which showed remarkable hardness of 2.15 GPa in nanoindentation tests. Verho *et al*. [41] provided a comprehensive review into durability aspects of SHS, highlighting the fragility of microscopic roughness present on most SHS. After the roughness on topography is damaged, there is no effective way to restore it fully. They also pointed to the diversity of wear testing and characterization methods currently prevalent in the literature, and instead suggested that one standard testing procedure would be beneficial for quantitative assessment. Other methods of increasing durability include using of self-healing materials [42-43]. Recently, Nosonovsky *et al.* [44] took a novel approach of metal matrix composites (MMC) with hydrophobic reinforcement in the bulk. Copper-graphite and Aluminum-graphite MMCs were prepared, and chemically etched thereby changing the topography. It was observed that hydrophobicity of the surfaces increased after the chemical etching. Here, chemical etching could be thought of simulating the wear, which also changes the topography analogously.

Researchers have conducted mechanical durability tests on SHS too, sometimes generic abrasion tests and also tests suitable to a particular application, e.g. laundering tests for fabrics. Zimmerman *et al.* [13] who tested abrasion resistance of polyester fabrics coated with polymethylsilsesquioxane nanofilaments on a textile friction analyzer (TFA). In TFA, an oscillating (1.25 Hz with 20mm stroke) perpendicular force was applied on the stationary fabric [45]. Force applied with TFA simulated skin contact (5 N, 7.8 kPa) over 1450 cycles of wear. Water shedding angle increased from 2° to 25° for a 13µl water drop. Vollmer *et al.* [46-47] characterized SHS durability by sand abrasion test, wherein sand grains of varying diameter (100 µm – 300 µm) were dropped from a height on a 45° tilted SHS. SHS were functionalized by chemical vapor deposition (CVD) silanization in both the cases. Bell *et al.* [48] fabricated self-similar "ecdysiastic" SHS from functionalized copper particles and tested their abrasion resistance by use of abrasive paper (100 grit, ca. 150 µm particle size) and conventional double cut (10 teeth per cm) metal working files. Self-similarity of the surfaces preserved the superhydrophobicity even after 0.5 mm of the surface was filed. Low density recycled polyethylene (LDPE) SHS were abraded manually by hand gloves with differing abrading properties, and with a reciprocating abrader under 32.0 kPa having stroke length of 4 cm and 8 cm s^{-1} linear abrading speed [49]. These surfaces were able to withstand 2520 abrasion cycles without having any effect on static CA (160°) or slip angle, with static CA dropping to 140° after 6520 wear cycles. Wong *et al.* [50] studied abrasion resistance of perfluorosilane coated pyramidal silicon SHS with nano-scale roughness features. SHS were subjected to abrasion against a Technicloth wipe for a desired distance under a load of 3.45 kPa, and also by dropping sand from a height of 30 cm for 30 seconds on a 45° tilted substrate. They systematically studied static CA and CAH evolution as Technicloth abrasion distance increased, and observed a loss of superhydrophobicity with increasing abrasion distance. Li *et al.* [51] abraded polyurethane SHS with equipment similar to TFA, with applied pressure of 2945.7 Pa and reciprocating motion of 18 cm s^{-1}. Although static CA evolution characterized as wear cycles increased and 10% decrease in CA was documented, CAH was not reported. Similar abrasion tester method was used by Okada *et al.* [52] and a decrease in static CA leading to loss in superhydrophobicity (160° to <130°) was observed with increasing the rubbing frequency, but CAH was not reported. Similarly, Xue *et al.* [53] tested abrasion of their fluorinated SHS under a load of 10 kPa for abrasion length of 30 cm at speed of 3 cm s^{-1}. CA and sliding angle was reported as a function of wear cycles. Saini *et al.* [54] improvised by abrading silane functionalized SHS with a drill mounted abrader rubbing against SHS in rotary motion, which was also being pressed by a weight. Loss of hydrophobicity was observed with increasing cycles for different samples. Chen *et al.* [55] scoured the SHS underwater by fixing them onto ends of rotor and rotating it at 3700 rpm for varying time period. Here, it is pertinent that CAH was not reported. Researchers [56, 57] have also tested durability of SHS by using a standard test conforming to the AATCC (American Association of Textile Chemists and Colorists) Test Method 61–2006 where a fabric is laundered in a standard canister, but CAH changes were not reported. Dowling *et al.* [58] tested wear resistance of coatings by submerging SHS in water containing abrasive silicon carbide (SiC) particles, and stirring up the mixture with help of an ultrasonic probe. Again, CAH was not reported.

A study investigating durability of polypropylene surfaces was reported recently in literature [59], which suggested using multi-scale roughness for increased superhydrophobic robustness. Various polypropylene surfaces with double hierarchies (micro/nano scale roughness on square pillars) were abraded with pin-on-disk type tribometer by applying pressure and also wearing the

SHS. Static CA and CAH were reported at incrementally increasing pressure values. It was reported that double hierarchical (micro roughness on micro pillars) SHS were better able to retain superhydrophobicity under pressure and wear tests, than SHS with nanoscale roughness on microscale pillars. Wang *et al.* [60] used a standardized abrasion test (ASTM D4966) and washing durability test (Australian Standard - AS 2001.1.4) on polyester fabrics coated and functionalized with different polymers. In abrasion test, the sample was abraded by using an abradant placed still on a surface and sample mounted on a dynamic spinning disk and also applying pressure. Washing durability test was conducted by spinning the fabric in a washing machine with detergent containing water. Wang *et al.* reported that tests showed the surfaces retained superamphiphobicity, but important metric of CAH was not provided.

Majority of the SHS, as described above, lose their superhydrophobicity after a mild mechanical wear. Studies were inadequate in terms of reporting CAH [51, 52, 55, 58, 60], an important parameter for analyzing superhydrophobicity. Majority of the studies detailed above were suited towards a specific purpose of testing the SHS fabricated with a novel technique and not addressing fundamental issues concerning superhydrophobicity (effect of topography on wetting). Hence, majority of the studies done until now were not systematic in correlating wetting characteristics (CA and CAH) and surface topography as a SHS underwent abrasion. The abrasion procedure used in majority of studies discussed above was prone to contaminating surfaces, affecting surface chemistry, and may have had a directional wear pattern. This potentially affected and biased the CAs. Sand abrasion methods used in some studies [45, 46, 50] increased susceptibility to surface contamination. Researchers also imparted superhydrophobicity to the surface by use of a fluorinated polymer coating [47, 50]. Abrasion can remove this coating exposing the bulk material underneath, introducing a site of chemical heterogeneity (in terms of differing chemistry from neighboring material), which affects the wetting properties. Hence, combined effects of change in roughness and surface chemistry were producing a change in the wetting characteristics.

The two components of superhydrophobicity (chemistry and topography) need to be studied separately to gain an in-depth knowledge of the individual effect of each on wetting. Understanding changes in topography (and chemistry) as a surface wears, and simultaneously tabulating wetting behavior is pertinent to fundamental investigation of superhydrophobicity. Also, a contamination free abrasion method having unbiased pattern, conforming to accepted standards in other research fields needs to be transferred over to be used on SHS. Mitigating several of above mentioned aspects was of interest in this thesis.

1.5 Scope and Contribution of this Thesis

The fundamental investigation of superhydrophobicity and widely used models i.e. Wenzel and Cassie model, is still open and under discussion. Although areal density approach toward calculating Cassie equation parameters (f_1 and f_2) has been questioned, no alternative model or equation has been put forward for calculating CA on line density basis. Promise of predicting dynamic scenarios conclusively remain elusive. Until now, other surface topography descriptors have been neglected and focus has been mainly on average roughness and/or root mean square roughness. As topography plays an important role in achieving superhydrophobicity, these parameters cannot uniquely detail topography. Determination of surface fractions (f_1 and f_2) has not been done experimentally on an irregular topography. Surface topography has not been related to wetting characteristics. Furthermore, the important question of SHS durability has been neglected until recently [41, 59, 60, 44, 61]. These collective open questions form the crux of this thesis.

Lack of good experimental data on abrasion of SHS has been an impediment to a more thorough understanding of durability. To the best of our knowledge, this is the first systematic investigation detailing evolution of wetting, topography and surface roughness parameters as a SHS abrades. Surface roughness was the continually changing factor, and surface chemistry changes during wear were maintained constant. A contamination free random (non-directional) pattern wear method was used to abrade surfaces. Cassie model was used as a starting point to predict dynamic scenarios, and a gamut of surface roughness parameters and wetting characteristics were simultaneously analyzed. Surface topography parameters and wetting behavior were at the forefront, while analyzing durability of SHS. Calculation of Cassie equation (both *original* and *popular*) parameters on both area and linear density basis, and hence prediction of water penetration depths on SHS was done by direct confocal imaging of surface topography. After analyzing trends between wetting and roughness parameters, relevant roughness parameters were identified that would potentially help in predicting the potential mobility of a drop on a surface. These unique surface topography descriptors can be used in future to fabricate surfaces having durable topography.

The abrasion methodology was identified using surface topography data and an algorithm was developed to be applied on analogous artificial terrains. Diverse fields of tribology and superhydrophobicity have been brought together in developing an algorithm for abrading artificial terrains and finding surface roughness parameters after each iteration. This time efficient approach will help in simulating abrasion and finding long term wear effects on topography without the need of physical abrasion on the surfaces, and corresponding ability of predicting wetting behavior.

In this thesis, plasma etched polytetrafluoroethylene (PTFE) surfaces were abraded incrementally for a duration of time. Wetting characteristics (CAH), surface topography and surface topography descriptors were simultaneously captured after each wear iteration. Surface topography was imaged using surface electron microscopy (SEM), and surface roughness parameters were captured using confocal scanning microscopy (CSM). Advancing and receding CA, used as wettability characteristics, were measured using Axisymmetric Drop Shape Analysis (ADSA).

Focus of present research was finding surface parameters that can be helpful in predicting adhesion and mobility of a liquid on a surface, which in turn will help in designing durable superhydrophobic surfaces. Also, another issue of main interest was to identify the surface topographical descriptors that were inadequate in uniquely describing the topography. Computational modelling of the abrasion process on PTFE SHS used in this study, such that the abrasion algorithm can be scaled up to predict abrasion of any topography, will help in designing robust and durable future SHS. The result of this thesis will be important to industry and academia alike to further the understanding of wetting in conjunction with topography, and help maximizing the durability of SHS for potential widespread commercial adaptation.

1.6 Summary

The main aims of this study are:

- Highlight inadequacies of present durability studies done on SHS.
- Study effect on wettability upon change in surface topography; while keeping surface chemistry constant.

- Develop an abrasion methodology to do such a study and also develop a way to monitor surface topography in a quantitative way; such that a comparison between wettability and surface topography can be made.
- Establish an algorithm simulating the abrasion.

References

1. R. Fürstner, W. Barthlott, C. Neinhuis, and P. Walzel, “Wetting and Self-Cleaning Properties of Artificial Superhydrophobic Surfaces,” *Langmuir*, vol. 21, no. 3, pp. 956–961, Feb. 2005.
2. A. J. Scardino, H. Zhang, D. J. Cookson, R. N. Lamb, and R. de Nys, “The role of nano-roughness in antifouling,” *Biofouling*, vol. 25, no. 8, pp. 757–767, Aug. 2009.
3. J. Chapman and F. Regan, “Nanofunctionalized Superhydrophobic Antifouling Coatings for Environmental Sensor Applications-Advancing Deployment with Answers from Nature,” *Advanced Engineering Materials*, vol. 14, no. 4, pp. B175–B184, Apr. 2012.
4. B. Bhushan, Y. C. Jung, and K. Koch, “Self-Cleaning Efficiency of Artificial Superhydrophobic Surfaces,” *Langmuir*, vol. 25, no. 5, pp. 3240–3248, Mar. 2009.
5. I. Sas, R. E. Gorga, J. A. Joines, and K. A. Thoney, “Literature review on superhydrophobic self-cleaning surfaces produced by electrospinning,” *Journal of Polymer Science Part B: Polymer Physics*, vol. 50, no. 12, pp. 824–845, Jun. 2012.
6. A. J. Meuler, J. D. Smith, K. K. Varanasi, J. M. Mabry, G. H. McKinley, and R. E. Cohen, “Relationships between Water Wettability and Ice Adhesion,” *ACS Appl. Mater. Interfaces*, vol. 2, no. 11, pp. 3100–3110, Nov. 2010.
7. S. A. Kulinich and M. Farzaneh, “How Wetting Hysteresis Influences Ice Adhesion Strength on Superhydrophobic Surfaces,” *Langmuir*, vol. 25, no. 16, pp. 8854-8856, Aug. 2009.
8. L. Mishchenko, B. Hatton, V. Bahadur, J. A. Taylor, T. Krupenkin, and J. Aizenberg, “Design of Ice-free Nanostructured Surfaces Based on Repulsion of Impacting Water Droplets,” *ACS Nano*, vol. 4, no. 12, pp. 7699-7707, Dec. 2010.

9. A. J. Meuler, G. H. McKinley, and R. E. Cohen, “Exploiting Topographical Texture To Impart Icephobicity,” *ACS nano*, vol. 4, no. 12, pp. 7048–7052, 2010.
10. L. Cao, A. K. Jones, V. K. Sikka, J. Wu, and D. Gao, “Anti-Icing Superhydrophobic Coatings,” *Langmuir*, vol. 25, no. 21, pp. 12444–12448, Nov. 2009.
11. W. Choi, A. Tuteja, S. Chhatre, J. M. Mabry, R. E. Cohen, and G. H. McKinley, “Fabrics with Tunable Oleophobicity,” *Advanced Materials*, vol. 21, no. 21, pp. 2190-2195, Jun. 2009.
12. S. S. Chhatre, A. Tuteja, W. Choi, A. Revaux, D. Smith, J. M. Mabry, G. H. McKinley, and R. E. Cohen, “Thermal Annealing Treatment to Achieve Switchable and Reversible Oleophobicity on Fabrics,” *Langmuir*, vol. 25, no. 23, pp. 13625–13632, Dec. 2009.
13. J. Zimmermann, F. A. Reifler, G. Fortunato, L.-C. Gerhardt, and S. Seeger, “A Simple, One-Step Approach to Durable and Robust Superhydrophobic Textiles,” *Advanced Functional Materials*, vol. 18, no. 22, pp. 3662-3669, Nov. 2008.
14. N. J. Shirtcliffe, G. McHale, M. I. Newton, and Y. Zhang, “Superhydrophobic Copper Tubes with Possible Flow Enhancement and Drag Reduction,” *ACS Applied Materials & Interfaces*, vol. 1, no. 6, pp. 1316-1323, Jun. 2009.
15. G. McHale, N. J. Shirtcliffe, C. R. Evans, and M. I. Newton, “Terminal velocity and drag reduction measurements on superhydrophobic spheres,” *Applied Physics Letters*, vol. 94, no. 6, p. 064104, 2009.
16. F. Mumm, A. T. J. van Helvoort, and P. Sikorski, “Easy Route to Superhydrophobic Copper-Based Wire-Guided Droplet Microfluidic Systems,” *ACS Nano*, vol. 3, no. 9, pp. 2647–2652, Sep. 2009.

17. P. Joseph, C. Cottin-Bizonne, J.-M. Benoît, C. Ybert, C. Journet, P. Tabeling, and L. Bocquet, “Slippage of Water Past Superhydrophobic Carbon Nanotube Forests in Microchannels,” *Physical Review Letters*, vol. 97, no. 15, Oct. 2006.
18. G. Londe, A. Chunder, A. Wesser, L. Zhai, and H. Cho, “Microfluidic valves based on superhydrophobic nanostructures and switchable thermosensitive surface for lab-on-a-chip (LOC) systems,” *Sensors and Actuators B: Chemical*, vol. 132, no. 2, pp. 431–438, Jun. 2008.
19. T. Young, “An Essay on the Cohesion of Fluids,” *Philosophical Transactions of the Royal Society of London*, vol. 95, pp. 65–87, Jan. 1805.
20. T. Nishino, M. Meguro, K. Nakamae, M. Matsushita, and Y. Ueda, “The Lowest Surface Free Energy Based on $-CF_3$ Alignment,” *Langmuir*, vol. 15, no. 13, pp. 4321–4323, Jun. 1999.
21. R. N. Wenzel, “Resistance of solid surfaces to wetting by water,” *Ind. Eng. Chem*, vol. 28, no. 8, pp. 988–994, 1936.
22. A. B. D. Cassie and S. Baxter, “Wettability of porous surfaces,” *Trans. Faraday Soc.*, vol. 40, p. 546, 1944.
23. A. J. B. Milne and A. Amirfazli, “The Cassie equation: How it is meant to be used,” *Advances in Colloid and Interface Science*, vol. 170, no. 1–2, pp. 48–55, Jan. 2012.
24. M. Jin, X. Feng, L. Feng, T. Sun, J. Zhai, T. Li, and L. Jiang, “Superhydrophobic Aligned Polystyrene Nanotube Films with High Adhesive Force,” *Advanced Materials*, vol. 17, no. 16, pp. 1977–1981, Aug. 2005.

25. X. Song, J. Zhai, Y. Wang, and L. Jiang, “Fabrication of Superhydrophobic Surfaces by Self-Assembly and Their Water-Adhesion Properties,” *The Journal of Physical Chemistry B*, vol. 109, no. 9, pp. 4048–4052, Mar. 2005.
26. W. Li and A. Amirfazli, “A thermodynamic approach for determining the contact angle hysteresis for superhydrophobic surfaces,” *Journal of Colloid and Interface Science*, vol. 292, no. 1, pp. 195–201, Dec. 2005.
27. N. A. Patankar, “Hysteresis with Regard to Cassie and Wenzel States on Superhydrophobic Surfaces,” *Langmuir*, vol. 26, no. 10, pp. 7498–7503, May 2010.
28. C. W. Extrand, “Contact Angles and Hysteresis on Surfaces with Chemically Heterogeneous Islands,” *Langmuir*, vol. 19, no. 9, pp. 3793–3796, Apr. 2003.
29. D. F. Cheng and T. J. McCarthy, “Using the Fact that Wetting Is Contact Line Dependent,” *Langmuir*, vol. 27, no. 7, pp. 3693–3697, Apr. 2011.
30. L. Gao and T. J. McCarthy, “How Wenzel and Cassie Were Wrong,” *Langmuir*, vol. 23, no. 7, pp. 3762–3765, Mar. 2007.
31. G. McHale, “Cassie and Wenzel: Were They Really So Wrong?,” *Langmuir*, vol. 23, no. 15, pp. 8200–8205, Jul. 2007.
32. M. Nosonovsky, “On the Range of Applicability of the Wenzel and Cassie Equations,” *Langmuir*, vol. 23, no. 19, pp. 9919–9920, Sep. 2007.
33. C. N. C. Lam, R. H. Y. Ko, L. M. Y. Yu, A. Ng, D. Li, M. L. Hair, and A. W. Neumann, “Dynamic Cycling Contact Angle Measurements: Study of Advancing and Receding Contact Angles,” *Journal of Colloid and Interface Science*, vol. 243, no. 1, pp. 208–218, Nov. 2001.

34. C. N. C. Lam, R. Wu, D. Li, M. L. Hair, and A. W. Neumann, “Study of the advancing and receding contact angles: liquid sorption as a cause of contact angle hysteresis,” *Advances in Colloid and Interface Science*, vol. 96, no. 1–3, pp. 169–191, Feb. 2002.
35. C. N. C. Lam, N. Kim, D. Hui, D. Y. Kwok, M. L. Hair, and A. W. Neumann, “The effect of liquid properties to contact angle hysteresis,” *Colloids and Surfaces A: Physicochemical and Engineering Aspects*, vol. 189, no. 1, pp. 265–278, 2001.
36. N. J. Shirtcliffe, S. Aqil, C. Evans, G. McHale, M. I. Newton, C. C. Perry, and P. Roach, “The use of high aspect ratio photoresist (SU-8) for super-hydrophobic pattern prototyping,” *Journal of Micromechanics and Microengineering*, vol. 14, no. 10, pp. 1384–1389, Oct. 2004.
37. D.-H. Jung, I. J. Park, Y. K. Choi, S.-B. Lee, H. S. Park, and J. Rühe, “Perfluorinated Polymer Monolayers on Porous Silica for Materials with Super Liquid Repellent Properties,” *Langmuir*, vol. 18, no. 16, pp. 6133–6139, Aug. 2002.
38. M. D’Acunzi, L. Mammen, M. Singh, X. Deng, M. Roth, G. K. Auernhammer, H.-J. Butt, and D. Vollmer, “Superhydrophobic surfaces by hybrid raspberry-like particles,” *Faraday Discussions*, vol. 146, p. 35, 2010.
39. H. Yan, K. Kurogi, H. Mayama, and K. Tsujii, “Environmentally Stable Super Water-Repellent Poly(alkylpyrrole) Films,” *Angewandte Chemie International Edition*, vol. 44, no. 22, pp. 3453-3456, May 2005.
40. J. T. Han, Y. Zheng, J. H. Cho, X. Xu, and K. Cho, “Stable Superhydrophobic Organic−Inorganic Hybrid Films by Electrostatic Self-Assembly,” *The Journal of Physical Chemistry B*, vol. 109, no. 44, pp. 20773-20778, Nov. 2005.

41. T. Verho, C. Bower, P. Andrew, S. Franssila, O. Ikkala, and R. H. A. Ras, “Mechanically Durable Superhydrophobic Surfaces,” *Advanced Materials*, vol. 23, no. 5, pp. 673-678, Feb. 2011.
42. Y. Li, L. Li, and J. Sun, “Bioinspired Self-Healing Superhydrophobic Coatings,” *Angewandte Chemie International Edition*, vol. 49, no. 35, pp. 6129–6133, Aug. 2010.
43. X. Wang, X. Liu, F. Zhou, and W. Liu, “Self-healing superamphiphobicity,” *Chemical Communications*, vol. 47, no. 8, p. 2324, 2011.
44. V. Hejazi and M. Nosonovsky, “Wear-Resistant and Oleophobic Biomimetic Composite Materials,” in Green Tribology, M. Nosonovsky and B. Bhushan, Eds. Berlin, Heidelberg: Springer Berlin Heidelberg, 2012, pp. 149–172.
45. L.-C. Gerhardt, N. Mattle, G. U. Schrade, N. D. Spencer, and S. Derler, “Study of skin-fabric interactions of relevance to decubitus: friction and contact-pressure measurements,” *Skin Research and Technology*, vol. 14, no. 1, p. 77-88 Jul. 2007.
46. X. Deng, L. Mammen, H.-J. Butt, and D. Vollmer, “Candle Soot as a Template for a Transparent Robust Superamphiphobic Coating,” *Science*, vol. 335, no. 6064, pp. 67–70, Dec. 2011.
47. X. Deng, L. Mammen, Y. Zhao, P. Lellig, K. Müllen, C. Li, H.-J. Butt, and D. Vollmer, “Transparent, Thermally Stable and Mechanically Robust Superhydrophobic Surfaces Made from Porous Silica Capsules,” *Adv. Mater.*, vol. 23, no. 26, pp. 2962–2965, Jul. 2011.
48. I. A. Larmour, G. C. Saunders, and S. E. J. Bell, “Compressed Metal Powders that Remain Superhydrophobic after Abrasion,” *ACS Applied Materials & Interfaces*, vol. 2, no. 10, pp. 2703-2706, Oct. 2010.

49. Q. F. Xu, B. Mondal, and A. M. Lyons, "Fabricating Superhydrophobic Polymer Surfaces with Excellent Abrasion Resistance by a Simple Lamination Templating Method," *ACS Applied Materials & Interfaces*, vol. 3, no. 9, pp. 3508-3514, Sep. 2011.
50. Y. Xiu, Y. Liu, D. W. Hess, and C. P. Wong, "Mechanically robust superhydrophobicity on hierarchically structured Si surfaces," *Nanotechnology*, vol. 21, no. 15, p. 155705, Apr. 2010.
51. C. Su, Y. Xu, F. Gong, F. Wang, and C. Li, "The abrasion resistance of a superhydrophobic surface comprised of polyurethane elastomer," *Soft Matter*, vol. 6, no. 24, p. 6068, 2010.
52. T. Yanagisawa, A. Nakajima, M. Sakai, Y. Kameshima, and K. Okada, "Preparation and abrasion resistance of transparent super-hydrophobic coating by combining crater-like silica films with acicular boehmite powder," *Materials Science and Engineering: B*, vol. 161, no. 1-3, pp. 36-39, Apr. 2009.
53. X. Zhu, Z. Zhang, X. Men, J. Yang, K. Wang, X. Xu, X. Zhou, and Q. Xue, "Robust superhydrophobic surfaces with mechanical durability and easy repairability," *Journal of Materials Chemistry*, vol. 21, no. 39, p. 15793, 2011.
54. G. Saini, K. Sautter, F. E. Hild, J. Pauley, and M. R. Linford, "Two-silane chemical vapor deposition treatment of polymer (nylon) and oxide surfaces that yields hydrophobic (and superhydrophobic), abrasion-resistant thin films," *Journal of Vacuum Science & Technology A: Vacuum, Surfaces, and Films*, vol. 26, no. 5, p. 1224, 2008.
55. Z. Cui, Q. Wang, Y. Xiao, C. Su, and Q. Chen, "The stability of superhydrophobic surfaces tested by high speed current scouring," *Applied Surface Science*, vol. 254, no. 10, pp. 2911-2916, Mar. 2008.

56. Q. Gao, Q. Zhu, Y. Guo, and C. Q. Yang, “Formation of Highly Hydrophobic Surfaces on Cotton and Polyester Fabrics Using Silica Sol Nanoparticles and Nonfluorinated Alkylsilane,” *Industrial & Engineering Chemistry Research*, vol. 48, no. 22, pp. 9797-9803, Nov. 2009.
57. B. Deng, R. Cai, Y. Yu, H. Jiang, C. Wang, J. Li, L. Li, M. Yu, J. Li, L. Xie, Q. Huang, and C. Fan, “Laundering Durability of Superhydrophobic Cotton Fabric,” *Advanced Materials*, vol. 22, no. 48, pp. 5473-5477, Dec. 2010.
58. C. E. Nwankire, G. Favaro, Q.-H. Duong, and D. P. Dowling, “Enhancing the Mechanical Properties of Superhydrophobic Atmospheric Pressure Plasma Deposited Siloxane Coatings,” *Plasma Processes and Polymers*, vol. 8, no. 4, pp. 305-315, Apr. 2011.
59. E. Huovinen, J. Hirvi, M. Suvanto, and T. A. Pakkanen, “Micro–Micro Hierarchy Replacing Micro–Nano Hierarchy: A Precisely Controlled Way To Produce Wear-Resistant Superhydrophobic Polymer Surfaces,” *Langmuir*, vol. 28, no. 41, pp. 14747–14755, Oct. 2012.
60. H. Wang, H. Zhou, A. Gestos, J. Fang, H. Niu, J. Ding, and T. Lin, “Robust, electro-conductive, self-healing superamphiphobic fabric prepared by one-step vapour-phase polymerisation of poly(3,4-ethylenedioxythiophene) in the presence of fluorinated decyl polyhedral oligomeric silsesquioxane and fluorinated alkyl silane,” *Soft Matter*, vol. 9, no. 1, p. 277, 2013.
61. D. Ebert and B. Bhushan, “Transparent, Superhydrophobic, and Wear-Resistant Coatings on Glass and Polymer Substrates Using SiO_2, ZnO, and ITO Nanoparticles,” *Langmuir*, vol. 28, no. 31, pp. 11391–11399, Aug. 2012.

Chapter 2 - Wetting performance of Worn Superhydrophobic surfaces

2.1 Introduction

Superhydrophobic surfaces (SHS) show equilibrium contact angle greater than 150°, and low contact angle hysteresis (CAH). Low surface energy and micropatterned topography help liquids achieve low adhesion and a greater mobility on SHS. Superhydrophobic surfaces have several potential applications, and in last 15 years significant boom has been observed through increase in research publications [1 - 6].

Natural examples of SHS include lotus leaves, water striders etc. Understandably, natural SHS withstand wear and tear, inclement weather conditions, adverse temperature changes, etc. and in order to survive they need to retain their superhydrophobicity. Being biological entity, wax can be regenerated by lotus leaves and partial superhydrophobicity can be recovered [12 - 13], while water strider legs are also considerably durable [14 - 16]. Such a property has been mimicked by artificially fabricated self-healing SHS to a limited degree, but they lack abrasion resistance and are not durable [17].

While abhesive fluoropolymer coatings have enjoyed commercial success as non-stick cookware [18-19], SHS presently are untapped; despite various reported wide-ranging applications they have not made commercial inroads for widespread use in everyday life. Among other factors hindering the wide usage of SHS (large scale reproduction barriers, cost, etc.), prominent amongst them is their durability. The durability problem of SHS was highlighted in one of the earlier works in late 80’s, where author acknowledges the erosion of superhydrophobicity imparting coating as a serious problem [20]. Durability is limited by the inherently delicate nature of microtextured topography present on SHS, and mild mechanical wear on these surfaces results in loss of superhydrophobicity, as depicted in Figure 1-1.

Hence, the research progress of superhydrophobic surfaces has been hindered in two significant ways: a) Commercial applications have remained scarce, and b) fundamental understanding of dependence of wettability on surface topography has not been investigated fully. Along with significant research progress on other parallel realms, like finding durable materials and robust fabricating methodologies, durability should also be tackled with prominence. This thesis intends to bring forward the durability aspect and the surface topography dependence of superhydrophobicity to the forefront.

The majority of studies done to date have remained inadequate in addressing the durability aspect of SHS, and only until recently researchers have started addressing this aspect [7-11]. These studies, although addressing mechanical resistance of the surfaces, did not systematically connect wettability to topography/chemistry, the two foundations of superhydrophobicity. The primary motivation of the studies was fabricating SHS with novel techniques, and then the secondary motivation of testing surface robustness was addressed through a mechanical test. Hence, how the wetting characteristics were affected by change in topography was not the focus for many of the studies. The surfaces used were functionalized by using a fluorinated coating, and abrasion/mechanical strength tests done had the potential to affect surface chemistry. Hence, one of the purposes of this thesis was to understand wettability changes happening upon enacting a change in surface topography. This chapter addresses this aspect by demonstrating how the surface topography was affected by the wear, using quantitative methods and physical imaging of the surface. Wetting characteristics were also simultaneously tabulated.

In this thesis, SHS with random coniferous topography were abraded with a contamination free abrasion methodology which generated random non-directional wear pattern. Surface chemistry and topography both affect the wetting of the surface, but in this thesis only the effect of change in surface topography on wetting was considered. Surface chemistry changes were eliminated by use of a hydrophobic polymer bulk. Topography changes and wetting behavior were simultaneously monitored, in form of surface roughness descriptors and contact angle hysteresis (CAH), respectively. This helped in correlating topography to wetting, and would potentially help fundamental understanding of superhydrophobicity and in predicting liquid mobility on topography.

2.2 Experimental Methods

2.2.1 Fabrication of Surfaces

SHS were fabricated by plasma etching of an intrinsically hydrophobic material, polytetrafluoroethylene (PTFE). Hydrophobic bulk eliminates the need for fluorinated surface coating and allows to exclusively monitor the effect of change in surface topography on wetting characteristics. Surface chemistry of a SHS with bulk hydrophobic polymer will always remain consistent after abrasion, as depicted in Figure 2-1. Hence, wetting data will not be biased by a change in surface chemistry allowing correlating changes in topography to wetting characteristics.

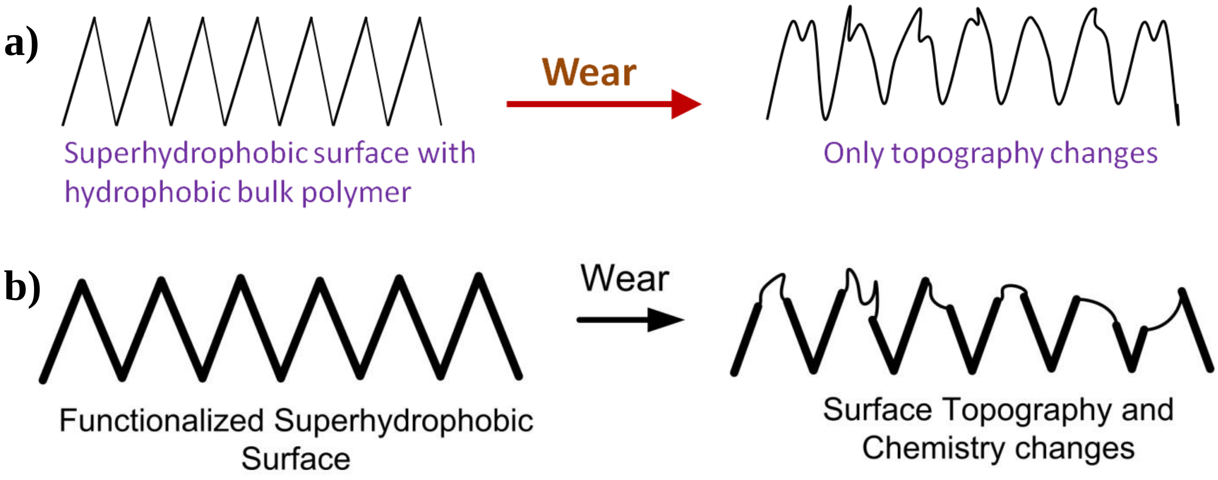

Figure 2-1: Schematic illustrating abrasion on, a) Hydrophobic bulk SHS which eliminates studying changes in surface chemistry, and allows to focus only on surface topography, while b) a SHS functionalized by a low surface energy coating resulting in both the surface topography and chemistry change. In (b), bold topography signifies the coating imparting superhydrophobicity to the surface, while thin lines signify the polymer exposed having a different surface energy.

Experimental details to fabricate the superhydrophobic PTFE surfaces used in this study have been described in detail elsewhere [21]. The samples were prepared by scientists at the Leibniz Institute of Polymer Research, Dresden, Germany (IPF). In brief, 3×3 cm^2 PTFE foils (PTFE Nünchritz GmbH, Nünchritz, Germany) were drilled[1], then cleaned with $CHCl_3$ in ultrasonic bath for 10 minutes, and plasma etched for 10 minutes in a stainless steel cylindrical vacuum chamber (diameter 250 mm, height 250 mm) with process conditions of: 10 sccm oxygen flow, pressure of 2×10^{-2} mbar, and effective radio frequency (RF) power of 200 W. The samples were again cleaned for 10 minutes in an ultrasonic bath having $CHCl_3$. Experimental conditions used in plasma etching were such that PTFE surface was chemically modified to a

---

[1] Two holes were drilled on the sample, 0.5 cm from the breadth wise edge, and 1.5 cm from the length wise edge

minor degree and only a small amount of oxygen was incorporated on the surface [21]. Figure 2-2 shows the SEM of the fabricated surfaces.

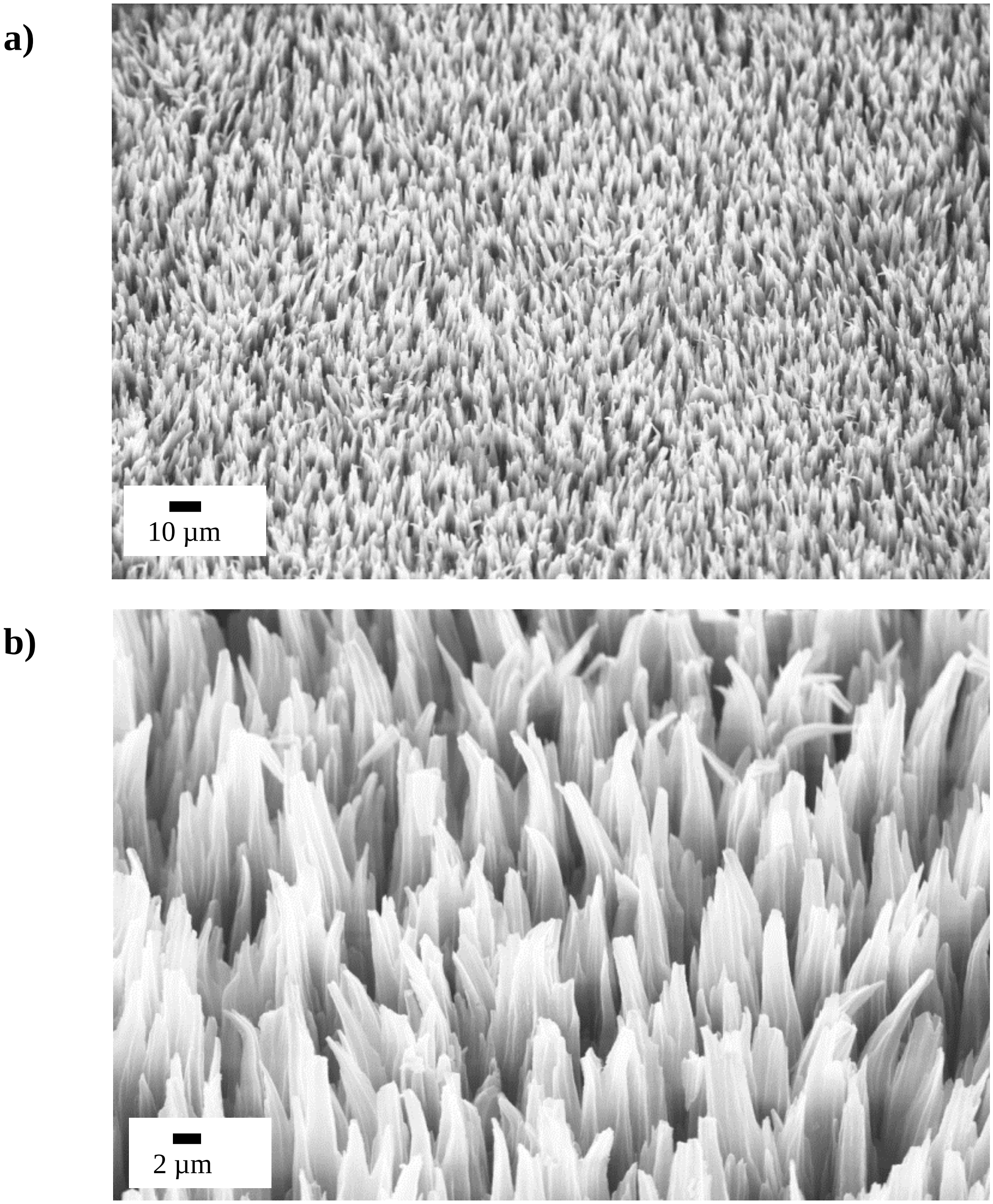

Figure 2-2: a) SEM of unworn plasma etched Teflon sample, and b) higher magnification view.

2.2.2 Abrading the surfaces

Abrasion experiment was designed based on standard test specification ASTM F735-06 (Standard Test Method for Abrasion Resistance of Transparent Plastics and Coatings using the Oscillating Sand Method) [22]. Mechanical wear on surfaces was done by abrading with inert glass beads (20-30 mesh size, 4-5 Mohs hardness, Manus abrasive systems, Edmonton, Canada) on an in-house modified gyrotory shaker (Model G2, New Brunswick Scientific Co. Inc., New Jersey, USA). This set-up allowed for control on wear (i.e. revolutions per minute), abrasive material and its amount while generating a random wear pattern on the sample surface. On the gyrotory shaker a customized steel sheet metal tray (25.4 cm × 25.4 cm × 5.08 cm, 3200 ml capacity) with walls on each side was built to confine the abrasive material. Also, bottom plate of tray had a recessed area (4.45 cm × 4.45 cm) to affix the sample flush with bottom of tray, see Figure 2-3. This prevented sample edges from interfering in the motion of abrading material (glass beads). PTFE samples were placed flat at the bottom of the gyrotory shaker while 2 liters of glass beads (3.8 cm glass bed depth), used as abrading material, covered the samples fully. Glass beads were inert and left no residue on surfaces and hence produced little to no contamination of sample surface (verified by SEM). Also, the bead size was sufficiently large not be lodged into any of the asperities on the PTFE SHS. Abrasion tests are done at room temperature, and during the abrasion experiment a significant increase in surface temperature was not expected which can influence surface chemistry. Moreover, PTFE has a melting point of 327° C [23], and this temperature cannot be achieved during machinery operating conditions described in this thesis.

Here, it is essential to address the question of surface contamination which can influence surface chemistry. Essential is the choice of the abrading material. Abrasion tests performed using sand showed that sand particles were physically lodged on the sample surfaces even after ultrasonication in various solvents. Also, discoloration of the sample surfaces was observed after wear. This was a pointer towards foreign matter present on the surfaces. Owing to the highly varying nature of sand particles, aggressive wear was observed on the surfaces. Hence, sand was not used. When using glass beads, no surface discoloration was observed for the period of wear done in this thesis. SEM verification was done and after surface cleaning procedure, no external matter was found to be present on the surface. Steel surface cannot be abraded, owing to the higher hardness than the glass beads. After each abrasion test, glass beads were carefully collected in a glass beaker already having 10-15 litres of glass beads. This ensured to keep the diameter of the glass beads consistent between different tests. Besides, owing to the nature of the study undertaken, it was not important to have these factors under minute control. Quantitative surface chemistry measurements (FTIR and XPS) were not possible on the surface, owing to the nature of the surface topography.

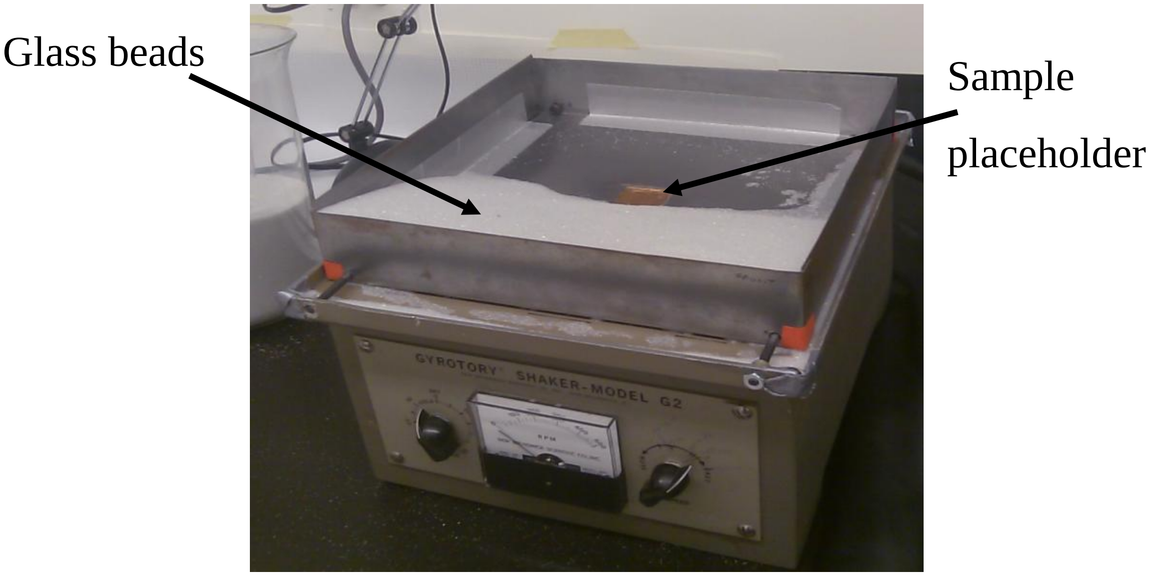

Figure 2-3: Gyrotory shaker set-up for abrading the surface. It allows for control over amount of wear, abrading material and generates unbiased random wear pattern on a surface. For demonstration purposes of sample holder, the glass beads are only partially filled in the image shown.

2.2.3 Surface Topography and Wetting Characterization

Non contact and top down confocal imaging was used to resolve surface topography and measure surface topography descriptors of the samples. Carl Zeiss Axio-700 confocal scanning microscope (CSM) having a white light source (400 nm – 700 nm) was used for this purpose. 100X objective (Epiplan-Neofluar 100x/0.75 M27, Carl Zeiss, Germany) with image field of 117.36 × 94.9 μm and 0.16 μm lateral resolution was used for all the measurements. Surface topography data was processed with inbuilt Carl Zeiss software to obtain various surface topography descriptors and other measurements like surface area, etc. MATLAB® was also used to attain relevant topography data by obtaining topography as a heightmap matrix (1280×1024). Row/column resolution for matrix was dependant on the objective used (dx=dy=0.091μm for 100X). Also, the data was processed further to filter noise, details about which are given in Appendix A. The topography obtained after filtering was compared with SEM images to ensure fidelity.

Surface imaging was also done with Carl Zeiss LEO 1430 scanning electron microscope (SEM). Before taking SEM, a gold layer of ~10 nm was deposited on the sample surface.

Contact angles were measured with an in-house equipment and processed with ADSA [24]. Contact angles were always measured with deionized (DI) water using sessile drop method. A water filled syringe was mounted below the surface through the holes (drilled while fabricating). The syringe was then driven to create a drop on the surface. Water was pumped into the drop at the rate of 0.5 µl/s, and CAs were measured at interval of one second as drop volume increased from 20 µl to 60 µl, and contact line advanced across the surface. Advancing CA was then calculated as an average of these entire individual CAs measured. Water was then withdrawn at a rate of 0.5 µl/s from this 60 µl volume water drop until it reached volume of 20 µl, and CAs were measured at interval of one second as the contact line receded across the surface. Receding CA was then calculated as an average of these entire individual CAs measured at each interval.

2.2.4 Experimental Procedure

Plasma etched Teflon SHS were worn in varying intervals of three minutes for a total duration of up to 180 minutes (varied for different samples) on a gyrotory shaker at 250 rpm. Rotation speeds lower than 250 rpm wear PTFE SHS slowly, while speeds greater than 250 rpm were aggressive. After each wear interval, abraded surfaces were rinsed gently with DI water and ultrasonicated for 15 minutes in 100% ethanol to remove any contaminants on the sample surface. The surfaces were air dried afterwards. It was seen that the cleaning procedure was efficient in removing any physically stuck contaminants. Dynamic contact angles (advancing and receding CA), CSM, and SEM measurements were taken after each wear duration. Figure 2-4 details the experimental procedure using a flow chart.

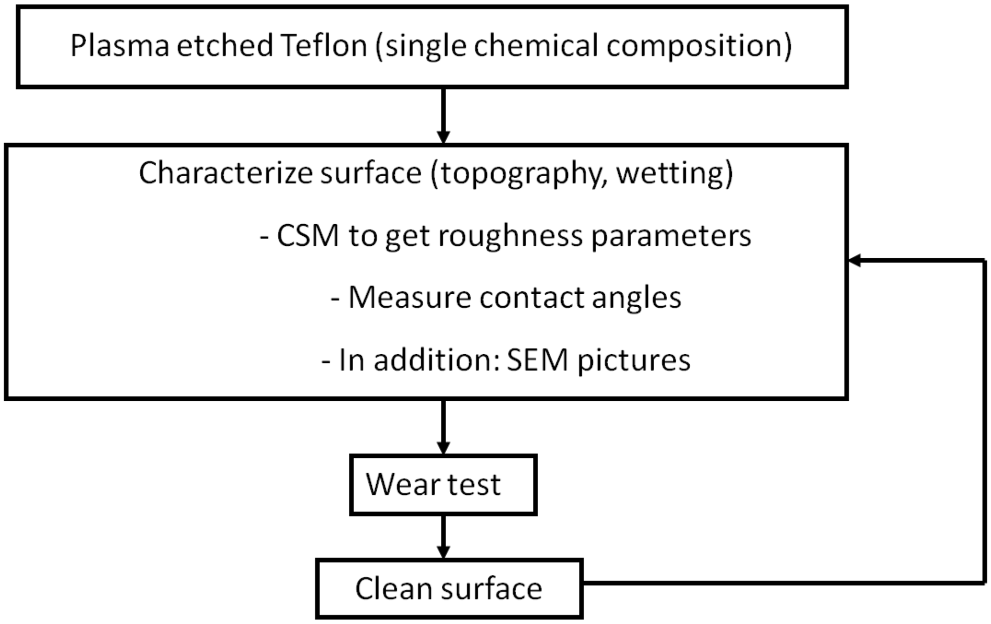

Figure 2-4: Flowchart of experimental procedure. SHS were abraded and cleaned of contaminants. Topography and wetting were then characterized by CSM and CAH, respectively.

Figure 2-5 shows the sample divisions and the relevant respective characterizations done. The need for segregating the sample into two regions arises due to the need for depositing conductive gold layer on the surface for SEM characterization. Due to the difficult to remove nature of the gold layer, without chemically modifying the sample surface, sample cutouts were used for SEM. Hence, the sample was divided into parts to help achieve the purpose of collecting various data (see Figure 2-5).

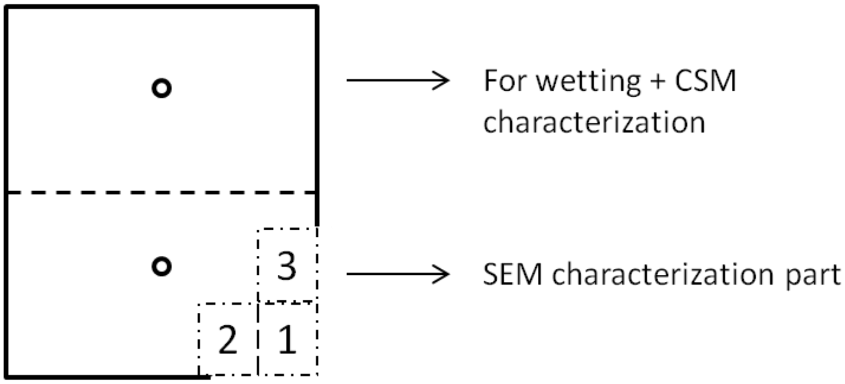

Figure 2-5: Schematic showing regions of sample and respective characterization done. The holes signify the place where syringe is inserted from the bottom for ADSA CA measurements. Numbered portions 1, 2, and 3 in the lower right corner signify the sample portions which were systematically cut out after each wear duration. The image is not to scale, and length and breath of the sample was 3cm each.

After the sample was worn for a duration of time (and also for unworn surface), wetting characterization (advancing and receding CA) and confocal scanning were done around the upper hole of sample (Figure 2-5). Care was taken such that CSM and CAs were all measured on the same position on the sample; this ensured that the parameters (surface descriptors, wetting characteristics) collected through each measurement (CSM, SEM, and CAs) were correlated and representative of each other, and kept the data comparison consistent. CSM was taken at three different areas around the hole to better help in understanding the variation and homogeneity in the surface topography. The lower part of the sample in Figure 2-5 was used to help visualize the topography by SEM. A small portion was systematically cut-out from the sample (number 1, 2, 3 etc. in Figure 2-5) for this purpose.

2.3 Cassie equation

Equilibrium contact angles can be theoretically predicted from Cassie – Baxter relationship [25-26], shown in eq. 2-1.

$$\cos\theta_c = f_1 \cos\theta_1 + f_2 \cos\theta_2 \qquad \text{2-1}$$

Here, f_1 and f_2 denote total area fraction of material 1 and 2, respectively, with θ_1 and θ_2 being the equilibrium CAs on smooth surface of material 1 and material 2, respectively. For a case when air is the second component, eq. 2-1 reduces to eq. 2-2, as $\theta_2 = 180°$ for air, as was the case in this thesis.

$$\cos\theta_c = f_1 \cos\theta_1 - f_2 \qquad \text{2-2}$$

This equation will also be referred to as *original* form of Cassie equation in this study.

Equation 2-3 is another form of Cassie's equation which has been propagating through literature [27].

$$\cos\theta_c = f\ \cos\theta - (1 - f) \qquad \text{2-3}$$

In eq. 2-3, f is the solid fraction, which is the ratio of the projected surface area that is wetted by the drop compared to the total projected surface area under the drop. This equation will also be referred to as *popular* form of Cassie equation in this thesis.

Equation 2-1 is as originally defined by Cassie and Baxter, and is valid universally if a liquid is in Cassie regime, whereas equation 2-3 is valid only when liquid does not penetrate the asperities, and/or is only sitting on the top of surface features with flat tops. A comprehensive look into these equations (eqs. 2-2 and 2-3) can be found in a recent study [27].

CSM mapped the surface topography and exact coordinates of relief features are known, this data can be used to calculate the Cassie equation parameters (f, f_1 and f_2). Conventionally, Cassie equation parameters are calculated on an area density basis i.e. whole topography under the drop influences the CA. So, in area density basis the data for calculating Cassie parameters was collected from a broad area field of 117.36 × 94.9 μm, which was reasonable considering the size of the drop (20 – 60 µl). An alternate view exists in literature [38, 39, 40, 41, 42], that only the topography at the triple phase contact line between liquid, solid and vapor phases influences the contact angle. Although the traditional view of calculating f_1 and f_2 on an area density basis was questioned, no alternative equation to predict Cassie CAs on line density basis was proposed. Hence, Cassie equation (eqs. 2-2 and 2-3) was used to predict CAs on line density basis too.

Equation 2-4 shows the *original* Cassie equation based on linear density basis, where all parameters were defined analogous to eq. 2-2 on line density basis, and l in subscript signifies that the parameters are contact line based. Equation 2-5 shows the line density version of the *popular* form of Cassie equation (eq. 2-3). Herein too, all the parameters were also calculated similar to eq. 2-3 but on a line density basis.

$$\cos\theta_{cl} = f_{1l}\cos\theta_1 - f_{2l} \qquad \text{2-4}$$

$$\cos\theta_{cl} = f_l\cos\theta + f_l - 1 \qquad \text{2-5}$$

In this thesis, both versions of Cassie equation (eqs. 2-2 and 2-3) were used and the parameters were calculated on the basis of line and area densities. Equation 2-2 and 2-3 were used in case of area density basis, and eqs. 2-4 and 2-5 were used for line density purposes.

Original and *popular* forms of Cassie equation give predictions for equilibrium contact angle. No specific equation exists in literature regarding prediction of dynamic wetting situations.

Equations that have been put forward and examined in literature until now derive from *original* Cassie equation [28-31]. They were not used in this thesis, as there are associated caveats with using of these equations regarding the topography, etc., which unnecessarily complicates the examination. Neumann and his coworkers [32- 34] stated that "Receding contact angles on a dry surface are experimentally as well conceptually inaccessible". Hence, predicting mobility is an arduous task. Many previous studies have also used dynamic CAs in lieu of static CA in Cassie equation [35-37]. Noting above viewpoints, both *original* and *popular* Cassie equations were used for dynamic CA scenarios in this thesis. Advancing and receding CAs were substituted in place of equilibrium CAs in both forms (*original* and *popular*) of Cassie equation.

Presently, theoretical calculations of Cassie contact angles have been done majorly on flat top pillars and it is assumed that the liquid does not penetrate into asperities [36]. This assumption does not hold true on surfaces which deviate from flat top geometry e.g. pyramid, hemispherical top, conical needles; where water will partially impregnate the surface topography [27]. To predict Cassie contact angles (θ_c), area fraction of air-solid interface (f_1), liquid- air interface (f_2) and CA on smooth surface (θ_1) must be known. Developing a methodology to calculate various area fractions (f_1, f_2) is more significant in these cases to be able to predict CAs with a degree of confidence. For the first time, to the best of authors knowledge, this study calculated Cassie equation parameters (f_1, f_2) by mapping topography of the surface using CSM.

2.3.1 Calculating Cassie equation parameters

Confocal scanning microscopy allows for non-contact spatial resolution of surface topography. CSM maps surface topography and gives output in the form of height profiles at each point on the surface. Hence intra-peak distances, height and depth of peaks amongst other parameters (like average roughness, Skewness, summit density etc.) can be calculated, directly enabling the calculation of Cassie equation parameters (f, f_1, and f_2).

CSM is a top-down imaging technique, and one potential problem can be shadowing of features, as shown in Figure 2-6. This introduces a possibility of introducing artifacts into surface topography data collected by CSM. This can potentially affect the calculation of Cassie equation parameters, and also the magnitude of surface roughness descriptors. Figure 2-2 shows only a minor percentage of bent pillars on PTFE SHS surfaces, which allows for minor possibility of CSM data “contamination” on surfaces used in this thesis. Hence, the effect on Cassie equation parameters and surface roughness descriptors will be minor. Alternatively, CSM is the most suitable way forward in the situation where one wants to map topography of the surface without damaging it, as was critical in this study.

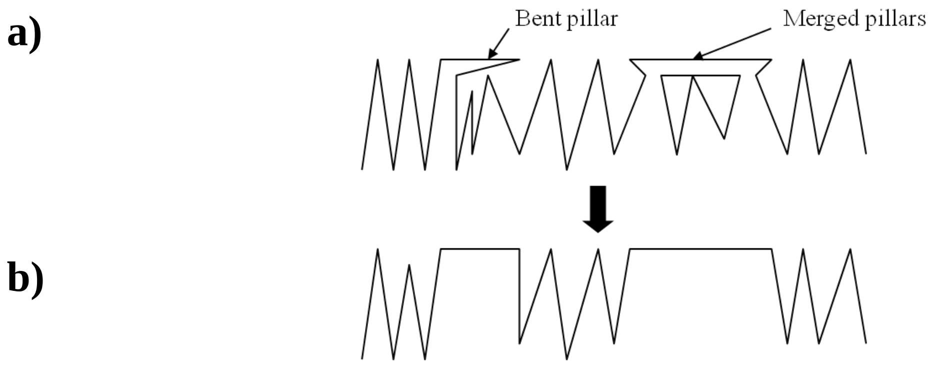

Figure 2-6: a) Side view of a surface containing needle-like geometry. It shows possibility of bent and conjoined pillars. b) Side view of the surface, as will be viewed by CSM.

Figure 2-7 (on page 42) shows a 3D topography of plasma etched PTFE surface mapped by CSM, and corresponding snippet of a heightmap matrix. Using mapped height data, Cassie equation parameters were evaluated by assuming a water penetration depth into the asperities on the surface. For calculating CAs with Cassie equation (*original* and *popular* form), it was assumed that, (1) liquid interface between asperities on the surface does not sag and is flat, (2) the liquid does not strictly follow the topography, and, (3) edge effects on the TPCL are neglected. Figure 2-8 (On page 43) demonstrates these assumptions, and also visualization of Cassie equation parameters is given along with. It is to be noted, that as the water penetration depth will increase, the surface area in contact with topography will increase. Using data processing software (Axio CSM 700 software, version 1.4.2.6), surface area above this penetration depth, projected surface area by the peaks above the penetration depth, and total area of the solid was found. As shown in Figure 2-9 (on page 44), a liquid penetration depth was chosen (5%, 10%, 15% in this case) on a surface and with increasing penetration depth, topography in contact with liquid increases hence changing the Cassie equation parameters. In Figure 2-9, liquid penetration depth is shown by corresponding topographical peak, and corresponding 3D figures show the topography in contact with liquid. For area density calculation of Cassie equation parameters, the topography spanning the whole CSM image of 117.36 × 94.9 μm was used. The parameters were calculated on all three different areas imaged on a particular sample and averaged, with error being the standard deviation between three calculations.

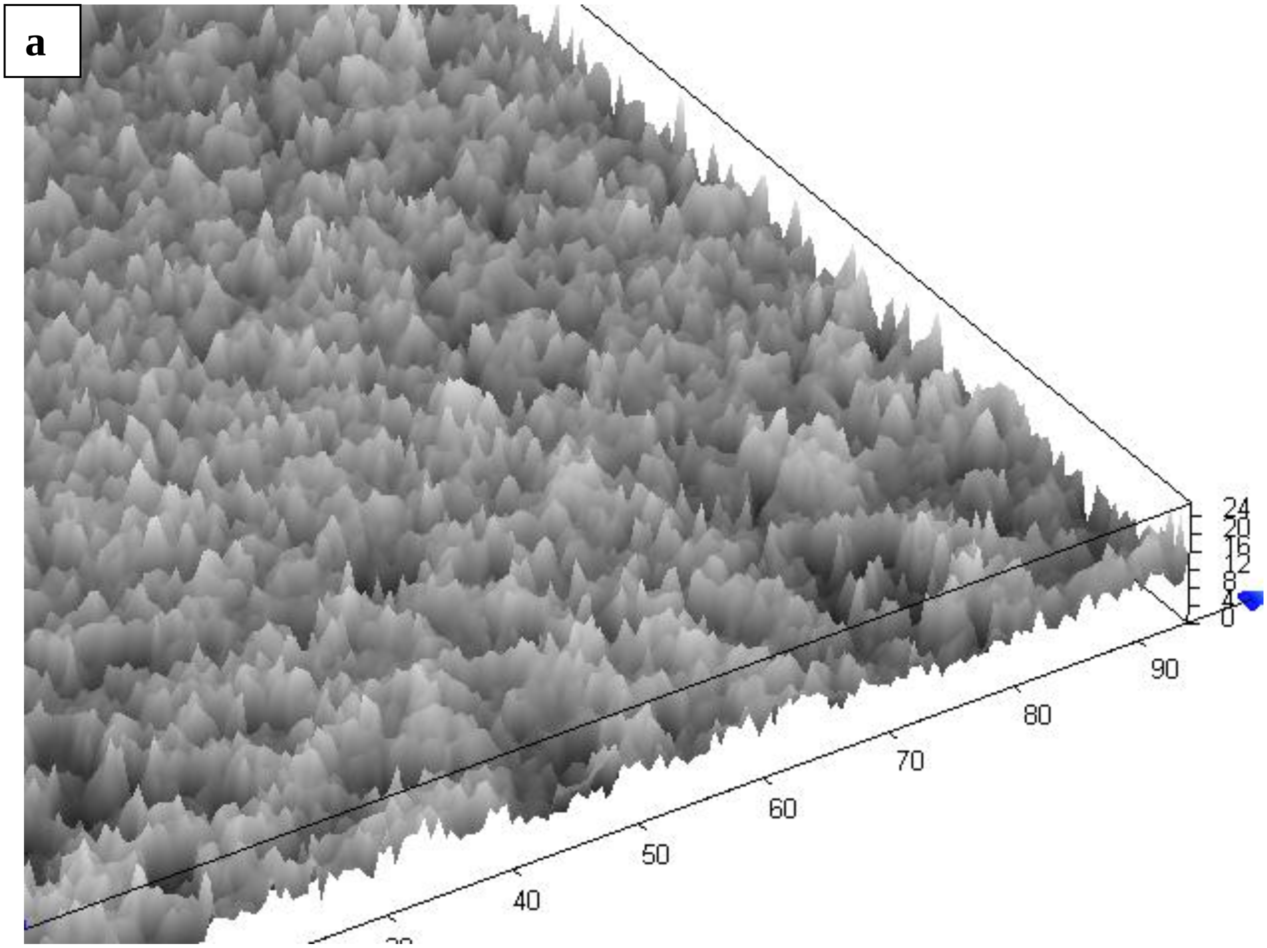

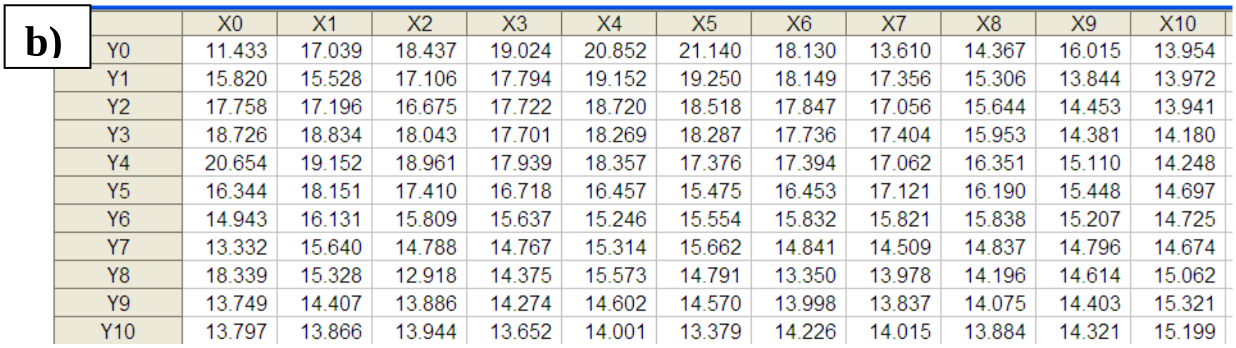

	X0	X1	X2	X3	X4	X5	X6	X7	X8	X9	X10
Y0	11.433	17.039	18.437	19.024	20.852	21.140	18.130	13.610	14.367	16.015	13.954
Y1	15.820	15.528	17.106	17.794	19.152	19.250	18.149	17.356	15.306	13.844	13.972
Y2	17.758	17.196	16.675	17.722	18.720	18.518	17.847	17.056	15.644	14.453	13.941
Y3	18.726	18.834	18.043	17.701	18.269	18.287	17.736	17.404	15.953	14.381	14.180
Y4	20.654	19.152	18.961	17.939	18.357	17.376	17.394	17.062	16.351	15.110	14.248
Y5	16.344	18.151	17.410	16.718	16.457	15.475	16.453	17.121	16.190	15.448	14.697
Y6	14.943	16.131	15.809	15.637	15.246	15.554	15.832	15.821	15.838	15.207	14.725
Y7	13.332	15.640	14.788	14.767	15.314	15.662	14.841	14.509	14.837	14.796	14.674
Y8	18.339	15.328	12.918	14.375	15.573	14.791	13.350	13.978	14.196	14.614	15.062
Y9	13.749	14.407	13.886	14.274	14.602	14.570	13.998	13.837	14.075	14.403	15.321
Y10	13.797	13.866	13.944	13.652	14.001	13.379	14.226	14.015	13.884	14.321	15.199

Figure 2-7: a) Mapped CSM 3D topography of the plasma etched PTFE sample, shown in Figure 2-2. b) A snippet of the corresponding heightmap matrix, showing the height coordinates of the topographical features stored as a 2D array.

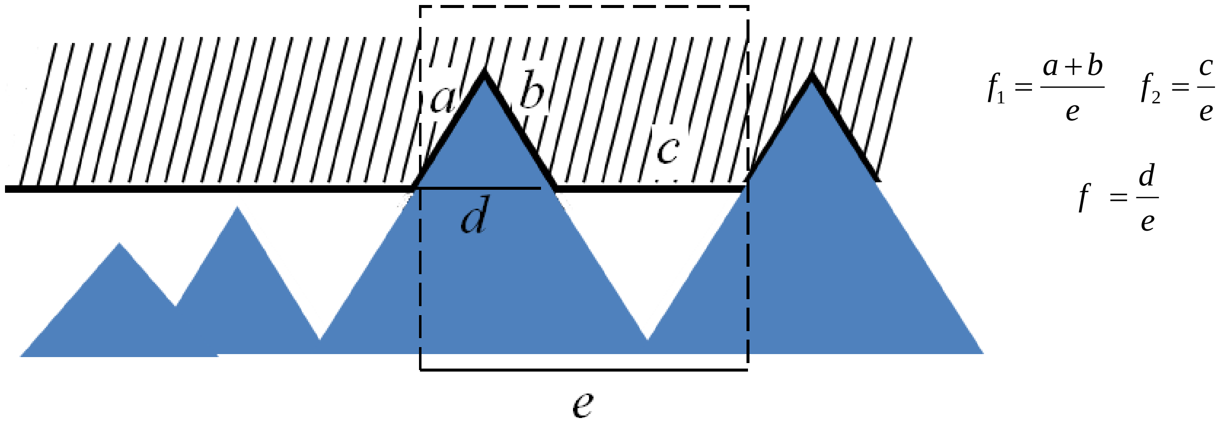

Figure 2-8: Illustration of liquid on a SHS. Blue (dark in print) denotes solid, while liquid is the cross-hatched area above the surface. Liquid-vapor and solid-liquid interfaces of drop are denoted by the bold black line. Shown are the assumptions that liquid-air interface does not sag, and does not follow the surface topography, as it should have otherwise touched the peaks on the left. Also, the TPCL on each of peaks follows the liquid-vapor interface strictly. Also shown is how the parameters used in Cassie equation 2-2 and 2-3 are defined.

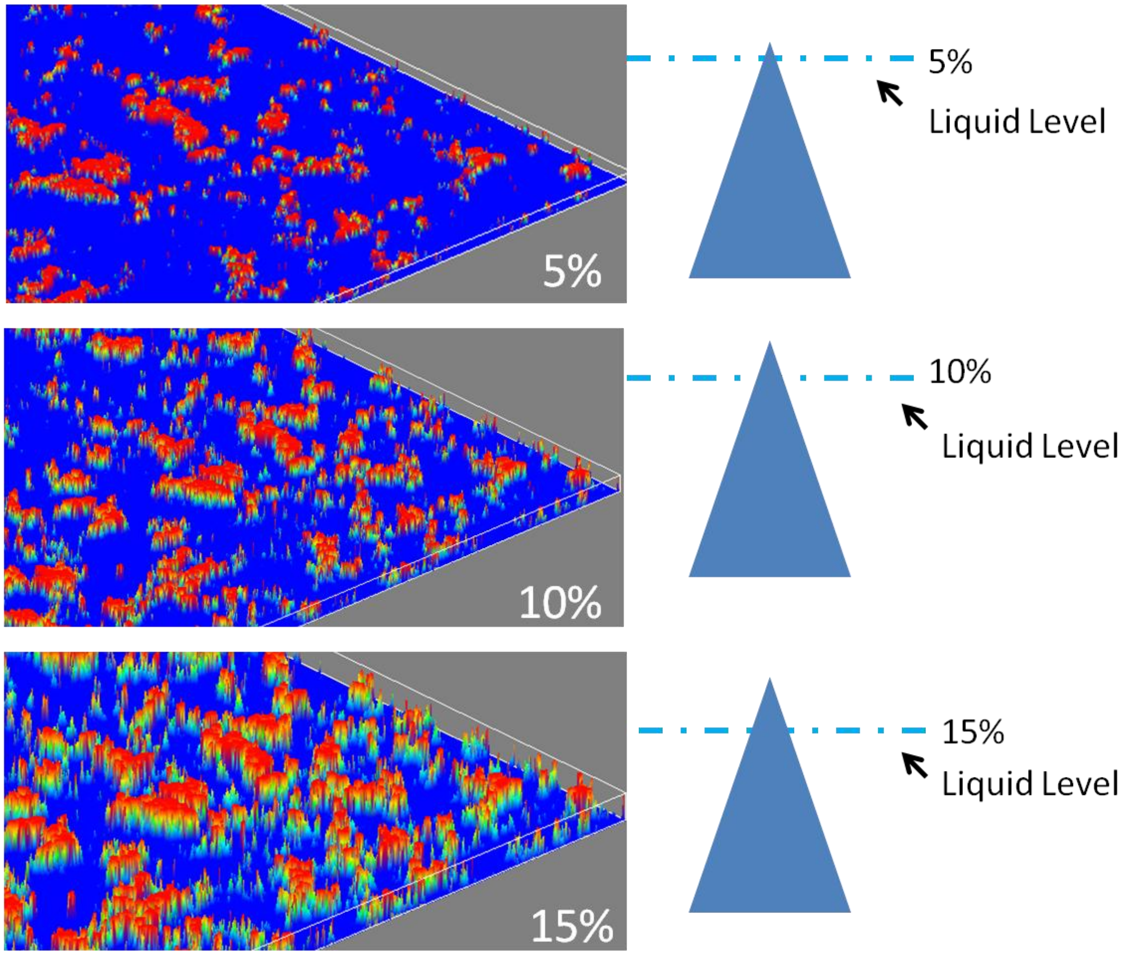

Figure 2-9: CSM 3D topographical map showing solid surface area in contact with liquid, depending upon absolute penetration depth. Water-air interface is signified by blue (Dark in print). Red/green (light in print) is the solid surface area in contact with water. Adjacent solid figures elucidate the water penetration depth on surface peaks. Dash-dotted blue line signifies water-air interface.

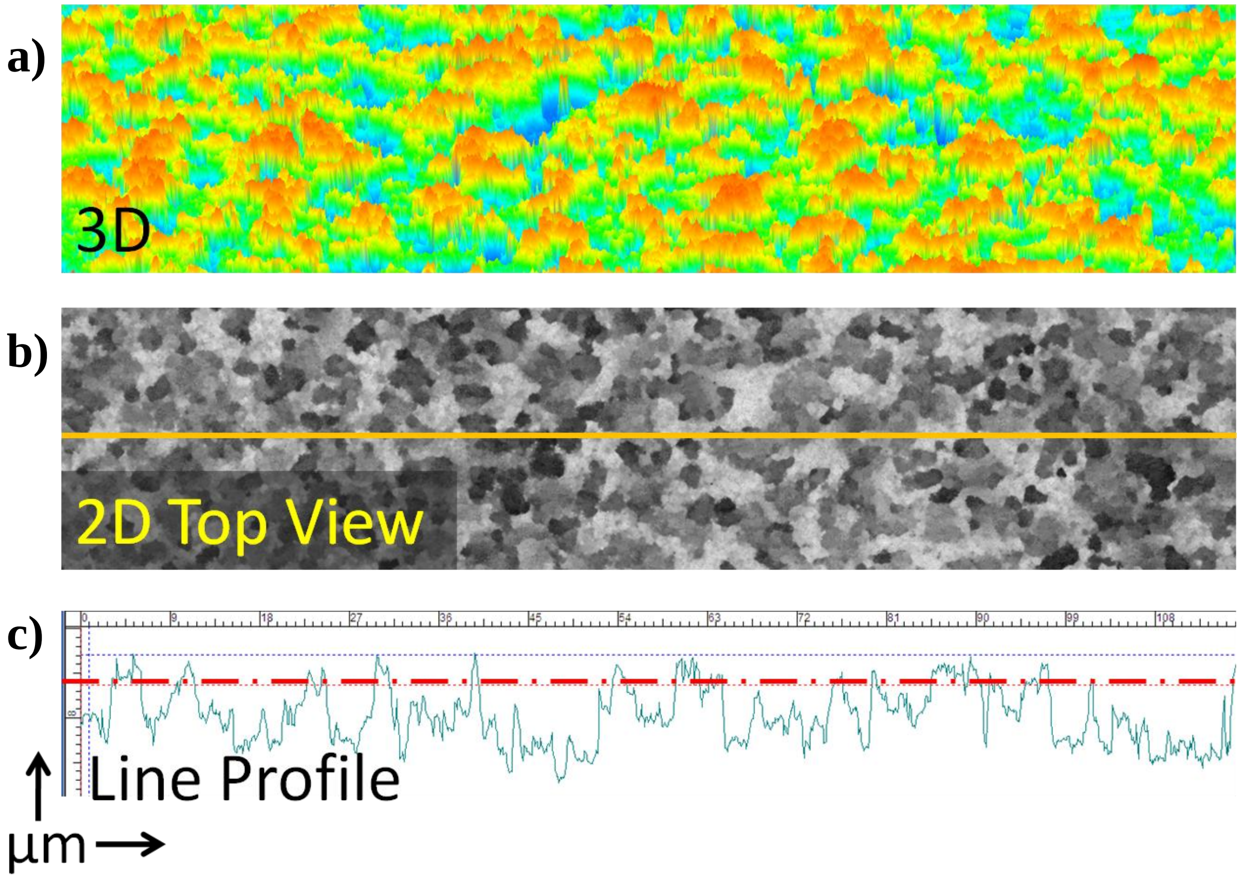

Figure 2-10: Finding Cassie equations parameters on linear density basis. a) 3D map of a plasma etched surface, b) 2D top view of (a), the line signifies the three-phase contact line on surface, and c) line profile on the TPCL shown in (b). In (c), dash-dotted red (dark in print) line signifies the penetration depth.

Figure 2-10 shows how the Cassie parameters were calculated based on linear density. On a sample, vertical and horizontal lines of one pixel width and entire length of CSM image was chosen as a representation of what drop may “see” as contact line on topography, as shown in Figure 2-10 (b). Width of this pixel varies according to the objective used; 0.09 µm for 100X objective and 0.90 µm for 20X objective. These values were chosen to be based upon resolving power of the measurement device, as TPCL is dependent upon system being studied [43] and this was not the focus of this study. Figure 2-10 (c) shows the line profile for the single pixel width line, and based upon liquid penetration depth, parameters were calculated for eqs. 2-4 and 2-5. Cassie parameter f_1 was the ratio of total length of the surface in contact with liquid and total projected length of the line, while f_2 was the ratio of total length of the surface (on the selected line only) in contact with air and total projected length of the line. On each sample, on each of the three CSM data sets for a particular wear interval, three individual horizontal and vertical line CAs were calculated using eq. 2-4 and 2-5 as shown in Figure 2-11. These individual measurements were then averaged to find one combined CA. 10% and 15% penetration depth CAs on line basis were calculated and 5% was skipped; since penetration of 5% produced an insignificant number of conjoined pixels on the topography that touched the water interface on line density basis and hence calculation of parameters was difficult.

Different penetration i.e. 5%, 10%, 15% gives different values of f, f_1, and f_2, and these parameters can be computed from the CSM data, as described in Figure 2-9. Comparing these theoretically calculated CAs with the experimentally observed CAs one can estimate the liquid penetration depth on the sample. Intrinsic Contact angle of 120° for Teflon was used in Cassie equations (Eqs. 2-2, 2-3, 2-4 and 2-5). The left-hand side of Cassie equations becomes indeterminate, if its value is above -1. So Cassie equation was bounded between 120° and 180°. Lower bound is at 120° because of the intrinsic CA of Teflon, the lowest any form of Cassie equation will be able to predict irrespective of the penetration depth.

Wenzel equation (eq. 1-2) was also used to theoretically predict CAs, and the roughness factor (r) was calculated using CSM data, total surface area was calculated on whole mapped topography while the projected area was simply the area of the image. Data was calculated on all three sample areas for a surface, and then averaged with standard deviation conveying the error.

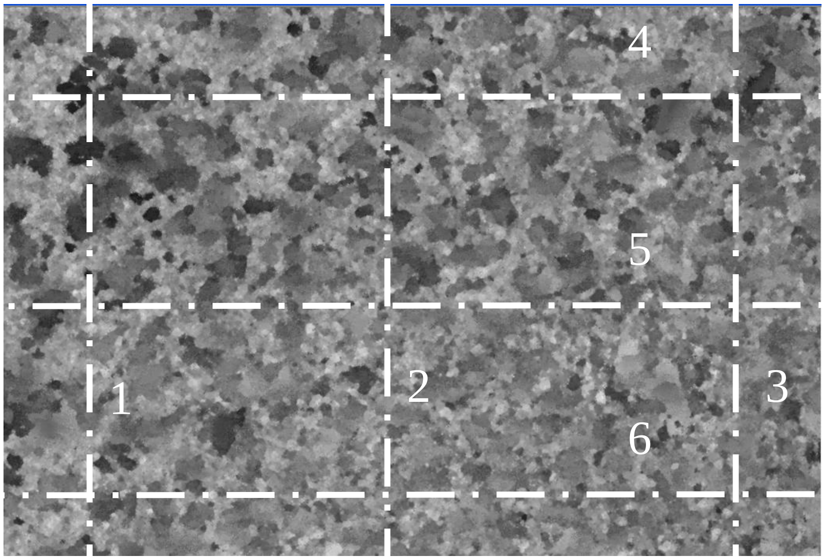

Figure 2-11: Top view of a surface, showing what a drop may see on topography as a contact line (dash-dot). Three vertical (namely 1, 2, and 3) and three horizontal lines (namely 4, 5, and 6) are selected for calculating line contact angles. The lines are selected randomly on the surface and are one pixel wide.

2.4 Results and Discussions

Figure 2-2 shows the PTFE SHS, fabricated by plasma etching, and the coniferous structures are ~11 µm tall. Advancing and receding CAs were both ~160°±3°, with no observed CAH. Abrasion was then performed on these PTFE surfaces as detailed in Section 2.2.4. It is pertinent here that, abrasion is a very stochastic phenomenon and this should be kept in mind as the data is generated and understood; as such trends maybe more valid than, at times, absolute values. Another factor to keep in mind is that plasma etching process used in this thesis does not let one to directly control the topography (unlike a photolithographic method) of the surface, and hence surfaces fabricated under the same conditions can show variations in height of the coniferous structures. In this study, topography is referred by a terminology analogous to waves. Longer wavelength refers to waviness (macrotexture) and shorter wavelength refers to roughness (fine topographical features). Figure 2-12 demonstrates this using an example surface having periodic sinusoidal features, and the modeled line profiles using MATLAB®. The line profiles were not physically measured, rather modeled to simplify the demonstration.

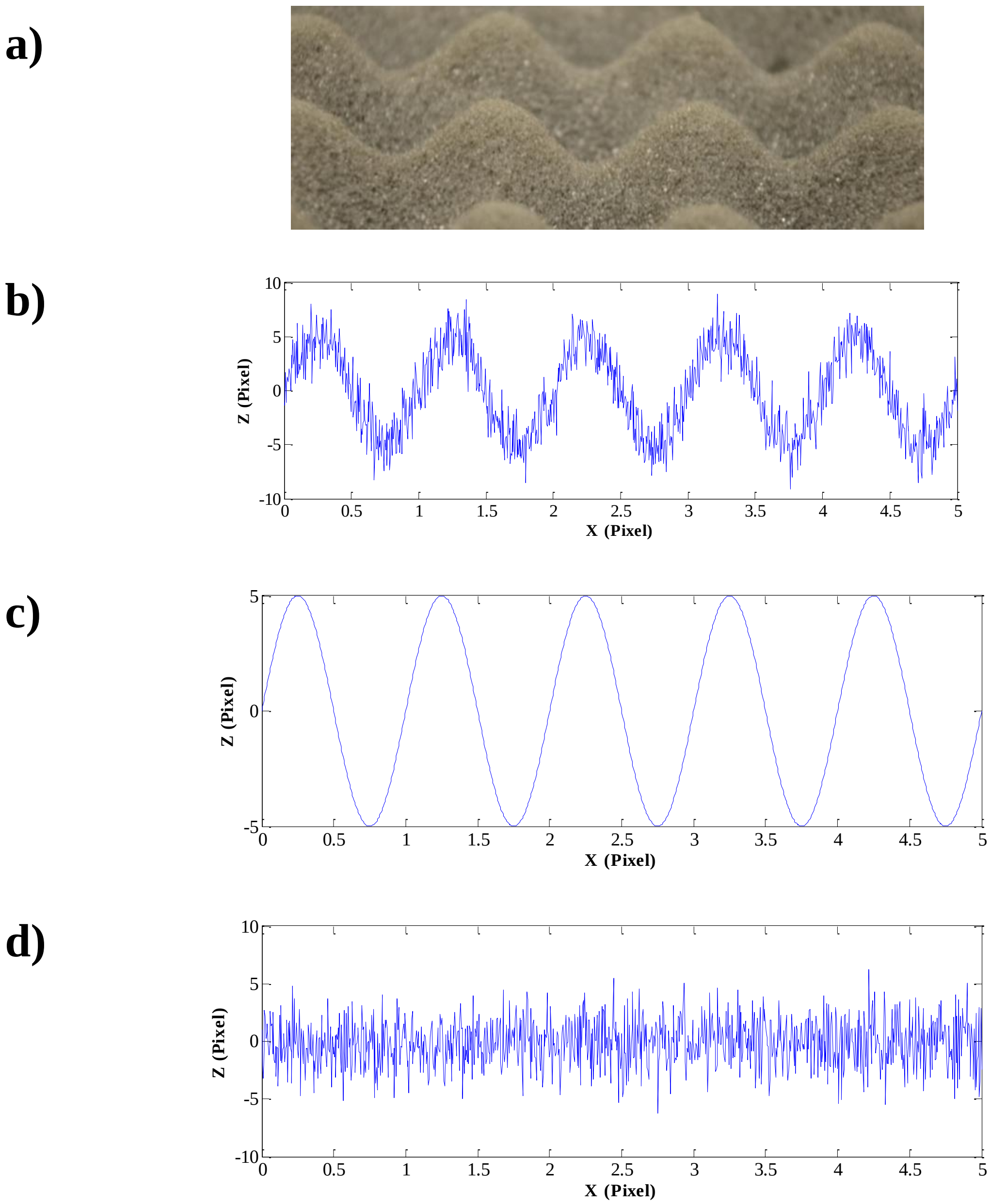

Figure 2-12: Demonstrating longer and shorter wavelengths of the surface using, a) Surface having sinusoidal undulations, b) Model (not actual) line profile on the surface computed using MATLAB, c) Waviness of the profile demonstrating longer wavelength of the surface, (d) Roughness of the surface demonstrating the high frequency component of the surface.

2.4.1 Topographical Evolution of Surfaces under Abrasion

SEM images in Figure 2-13 show the decrease in surface features (valleys and peaks) as a PTFE surface wears.

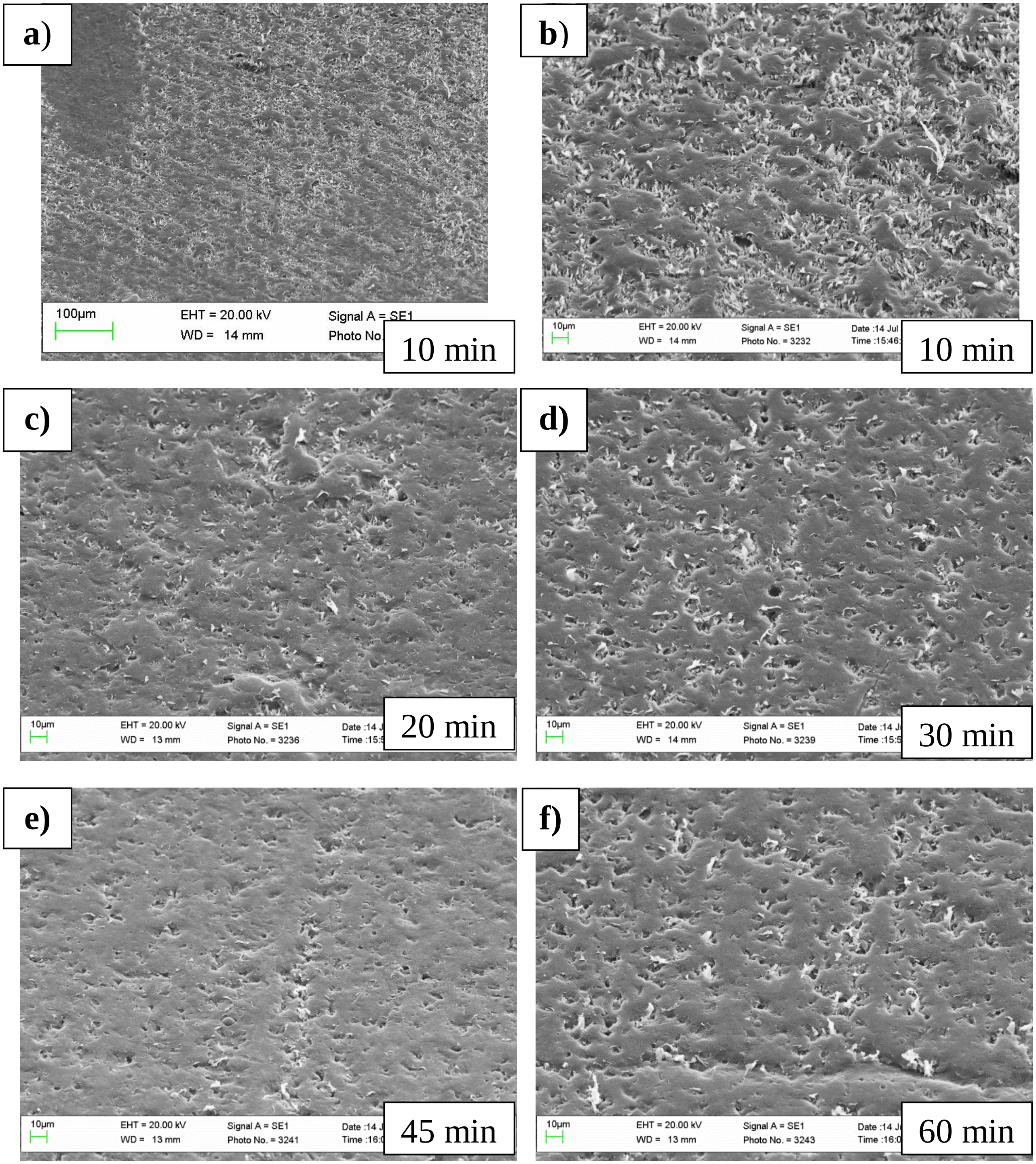

(continued on next page)

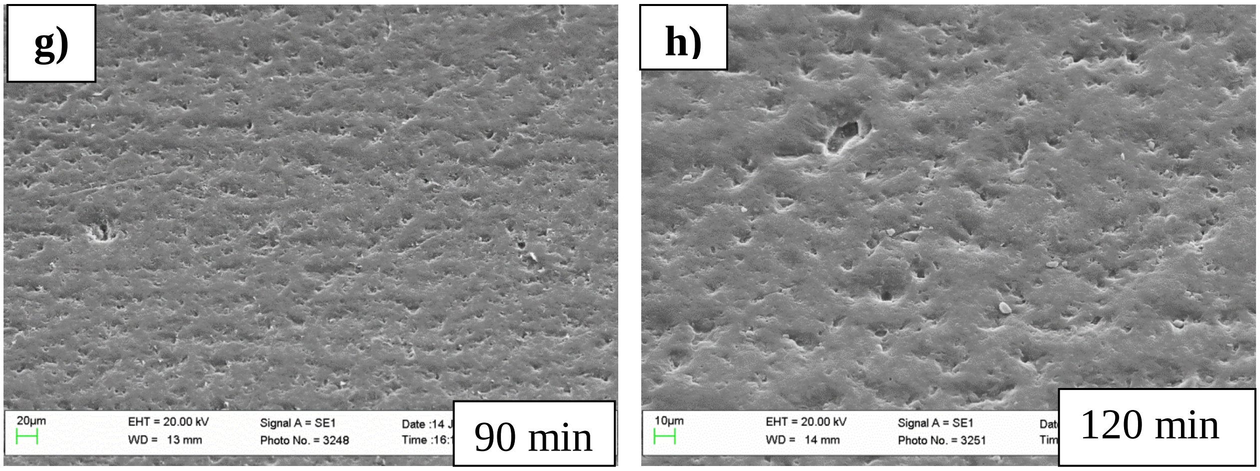

Figure 2-13: SEM of sample 1 being worn at 250 rpm for different durations of time. Inset shows the cumulative time a surface has been worn. Fig. (a) also shows the regional dependancy of wear.

Figure 2-13 (a) shows the regions with different wear rates, with edges in lower and upper left side in particular having faster rate of abrasion as signified by a number of flat regions compared to rest of the sample. This gradient in wear emphasizes the stochastic nature of wear phenomenon. This effect can be due to regions having different rotational speed of abrading material near the edges. This can occur probably due to even a minor interference of the metal edge of the recessed slot, or simply due to inherent corrugations on the intrinsic PTFE sheet. Also, since the abrading material rotates in an undefined random way on the gyrotory shaker, regional wear pattern change was expected.

Regions in which peaks are dominant decrease progressively with increase in wear time. At 10 minutes (Figure 2-13b), peaks and the valleys on the surface occupy roughly equal area, and by 20 minutes (Figure 2-13c) the surface is already dominated by plateaus. At 45 minutes (Figure 2-13e) longer surface wavelength components have started to become dominant, and at 120 minutes (Figure 2-13h), they dominate completely. It is pertinent to mention here that Figure

2-13 (d) and Figure 2-13 (f) show a similarity in surface wear condition although wear times are different, due to the random regional wear pattern on the surfaces.

Above, topographical evolution was evaluated after long wear intervals, now focusing on short wear intervals and seeing affect on topography after minutes of undergoing mechanical abrasion. Figure 2-14 shows the sample 2 at different wear intervals after being worn at 250 rpm. Figure 2-14 (a) shows the small number of randomly distributed patches of flattened PTFE peaks, and as the wear time increases the surface is progressively flattened, as shown in Figure 2-14 (e), (f), (g), and (h). The parallel streaks in Figure 2-14 (h) and (e) might be due to the corrugations of the original PTFE sheet which was plasma etched.

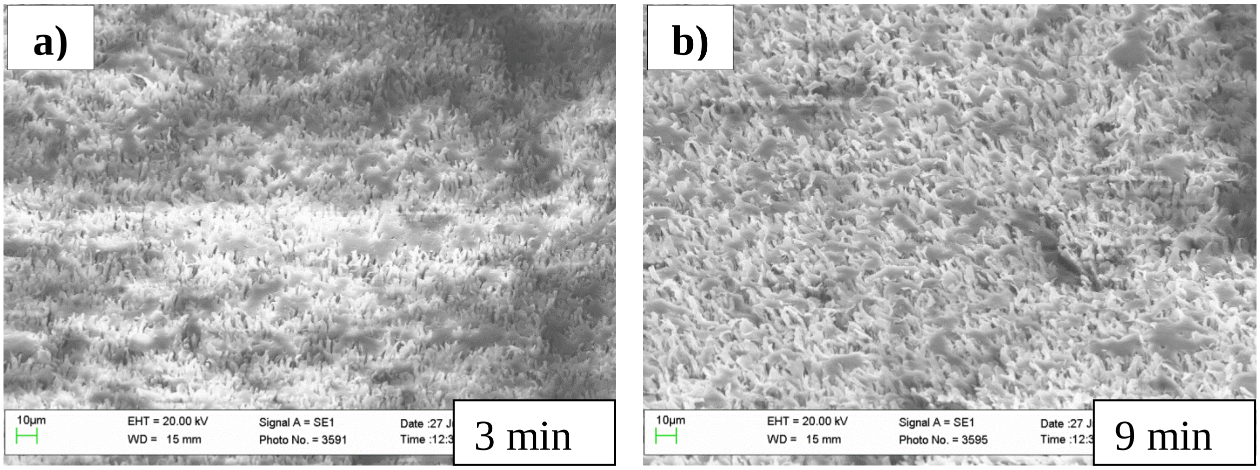

(continued on next page)

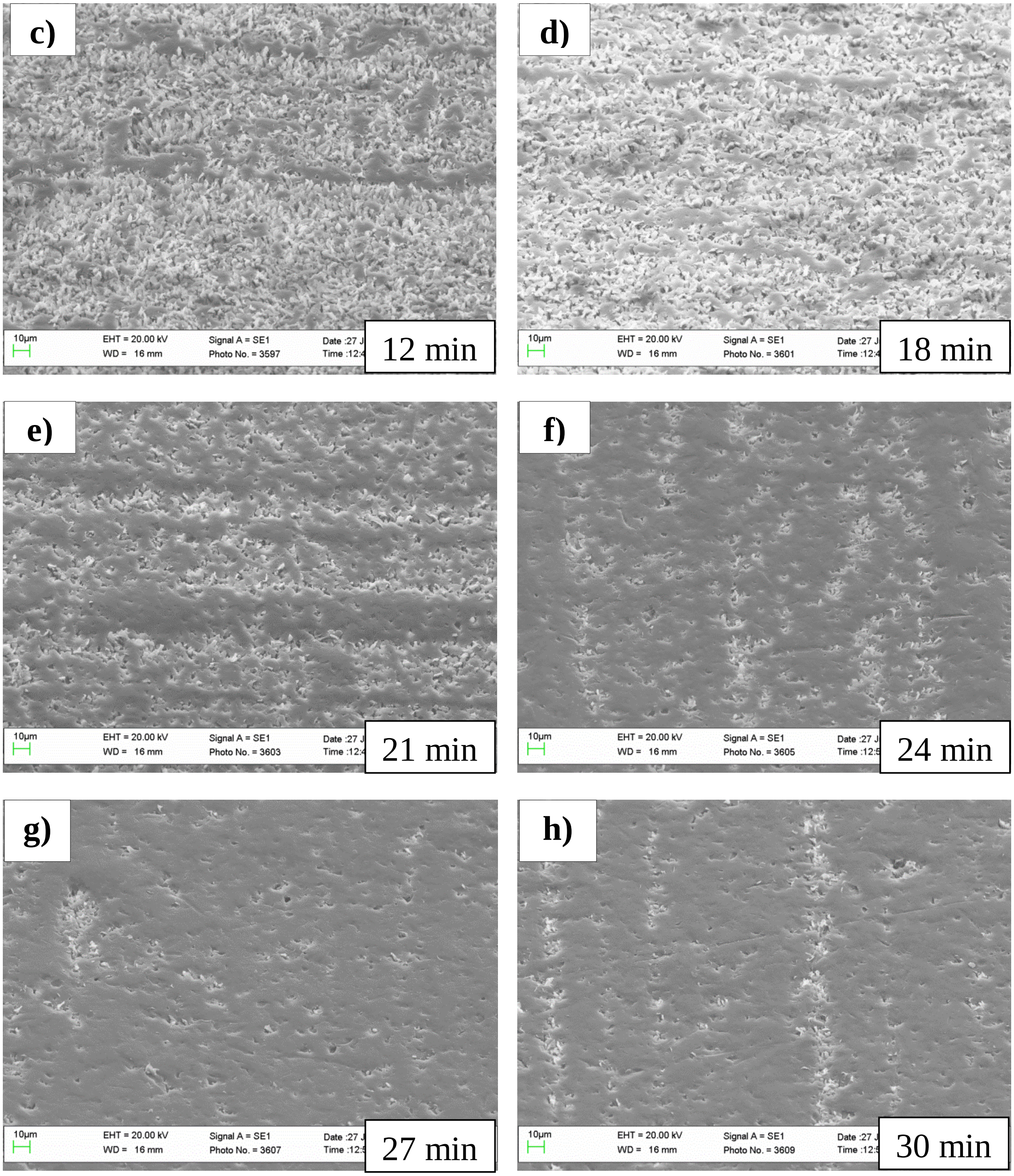

Figure 2-14: SEM of sample 2 as it is worn at 250 rpm. Inset shows the time a sample has been worn.

SEM images Figure 2-13 (b) and Figure 2-14 (b) show a similarity in the wear pattern due to a number of flat regions and surrounding peaks. Figure 2-14 (b) will evolve similar to Figure 2-13 (b) as the surface wears further, keeping in mind the stochastic nature of wear. This is validated by Figure 2-13 (c) and Figure 2-14 (e), the wear time after which the surfaces in whole register a significant increase in plateaus. Also, from Figure 2-14 (e) and Figure 2-14 (d), it can be seen that wear pattern is different even though wear time difference is small showing the obvious time dependence of surface wear, and how a small wear time plays a significant role. Figure 2-14 (e) has identical wear pattern to Figure 2-13 (c), showing consistency among different samples with respect to wear behavior, and that the surface texture was able to typically sustain nearly 20 minutes of abrasion before flattening.

Figure 2-15 shows the initial wear evolution of PTFE surfaces after undergoing wear in short intervals of 30 seconds, to detail how the surface peaks were affected in initial wearing time. It can be seen that the tip of peaks were immediately affected (Figure 2-15 b), and hence as wear time increases the peak tops continue to erode and flatten. It can be seen that at some regions, only the peak tops were affected (Figure 2-15 b, d and f), while at some regions whole group of peaks were eroded (Figure 2-15 c and e). This exemplifies the stochastic wear nature, and aggressive wear can be seen in Figure 2-15 (c) and (e) compared to Figure 2-15 (d) and (f), respectively. As wear time increases, peak tops were nearly abraded as can be seen between 3 and 6 minutes of wear (Figure 2-15 f, g and h), and topography after wear time of 12 minutes consists of local flat regions (Figure 2-15 i and j). These flat islands were analogous to those on other samples (Figure 2-13 b and Figure 2-14 b), and demonstrate the consistent intergroup behavior of wear on PTFE surfaces.

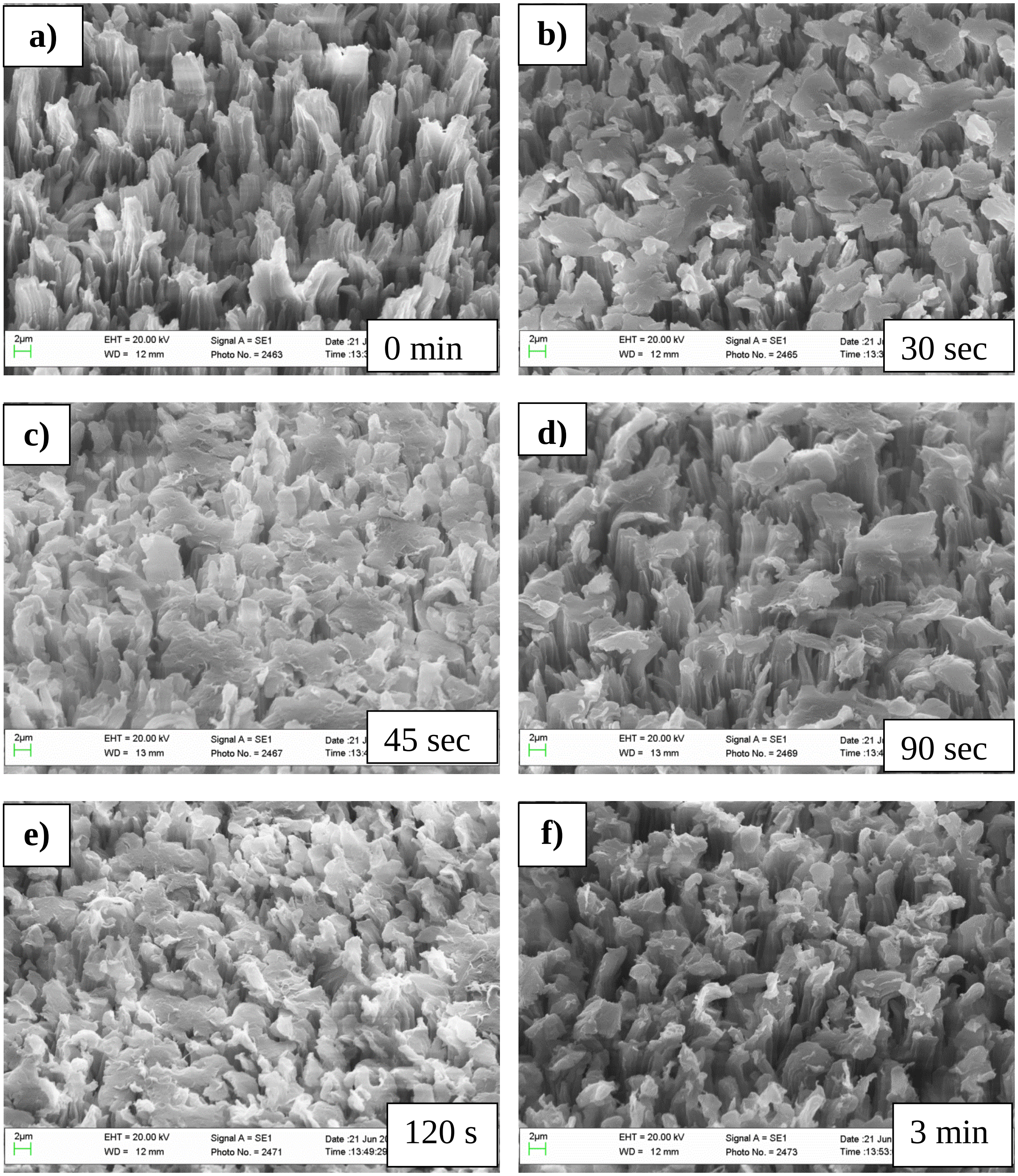

(continued on next page)

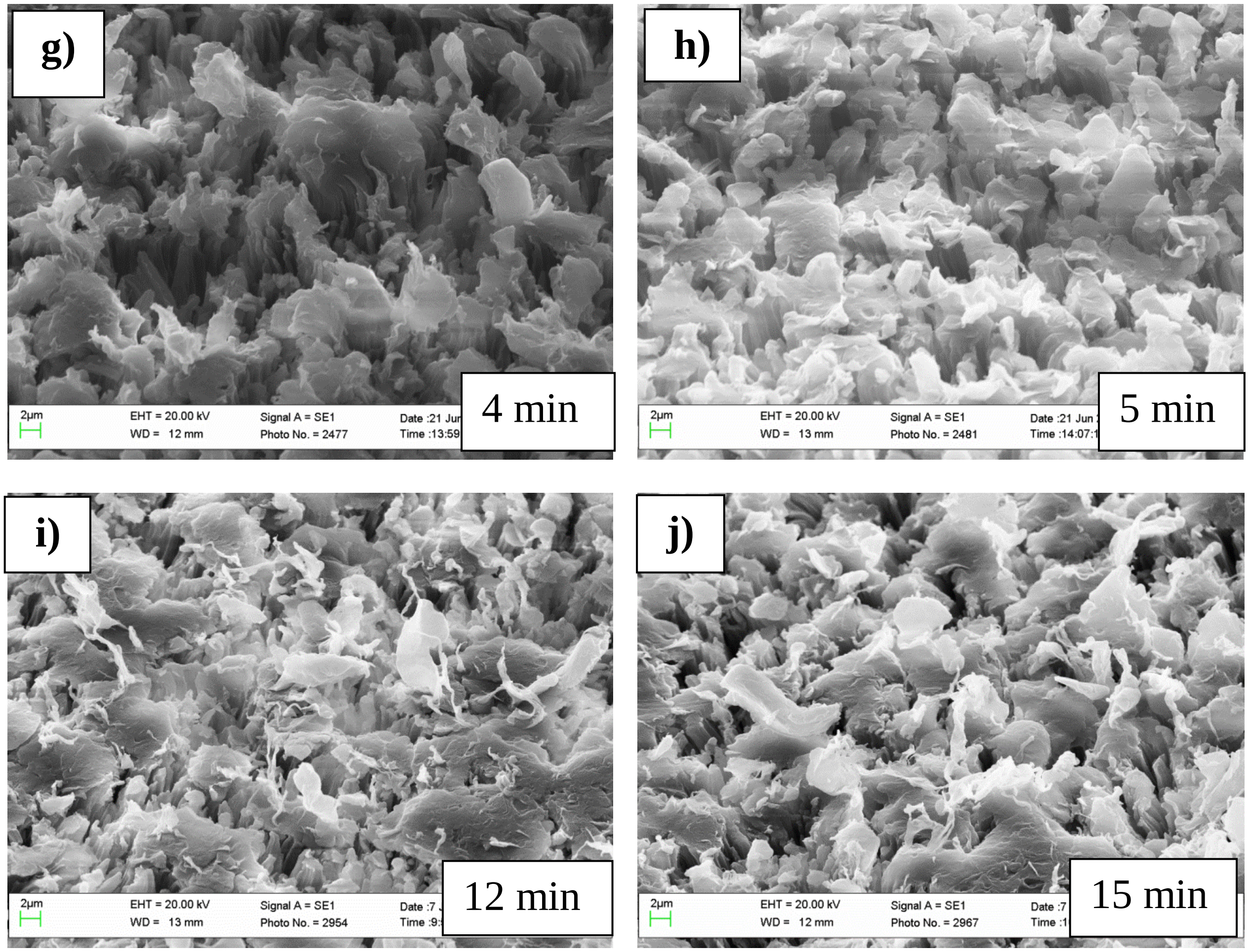

Figure 2-15: SEM of sample 3 being worn at 250 rpm for different durations of time. Inset shows the cumulative time a surface has been worn.

SEM images in Figure 2-13, Figure 2-14, and Figure 2-15 show that the PTFE surfaces were randomly abraded in an undefined distinct pattern by the gyrotory shaker, if the abrasion conditions are kept the same. Sometimes, the difference in surface topology among various regions on the same sample can arise due to the random regional wear behavior. The evolution of the wear pattern with time was consistent among the different samples of the same surface. Also, the wear pattern evolved consistently within the samples, with area under the peaks decreasing and area under the valleys increasing and the wear pattern developing homogeneously barring regions prone to be influenced by regional wear behavior. The surface topography starts flattening between 18 and 21 minutes as witnessed in sample 1 and 2. Note that the term “flat” is used here (i.e. this chapter) in a comparative sense to what was the initial texture of the surface.

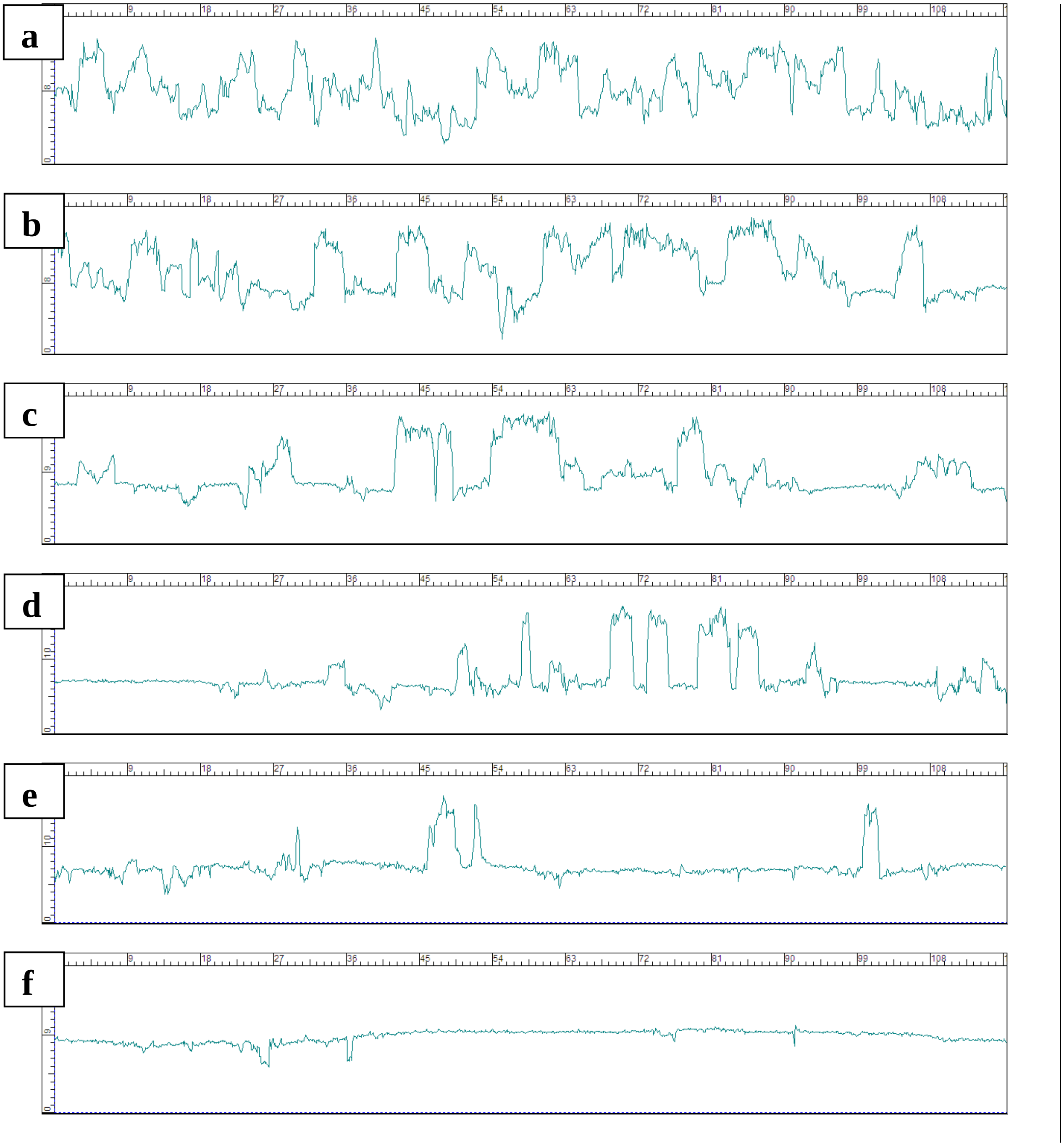

Figure 2-16: Surface profiles for (a) unworn, (b) 3 min, (c) 12 minutes, (d) 18 minutes, (e) 21 minutes and (f) 27 minutes worn samples evaluated from CSM data. The profiles are for sample 2.

Quantitative physical comparison of worn surface topography can be done on the samples by evaluating CSM data. Figure 2-16 (a) shows that the initial unworn surface topography as a line profile over the whole width of area imaged by CSM. Initial surface topography was composed of closely spaced peak features distributed homogeneously. SEM image of unworn surface in Figure 2-2 also shows the tightly packed peaks. The height distribution is also shown in Figure 2-18 (a) as a height histogram. The average peak height on the surface was (12.87 ± 2.99) µm.

As the surface wears the peaks start to become flat, as can be seen in height profile in Figure 2-16 (b) and also shown in SEM images, e.g., Figure 2-14 (a). The average peak height after 3 minutes of wear on the surface was (7.07 ± 3.39) µm, approximately a 50% decrease from original surface distribution, where initial peaks were ~12 µm. This shows that most peaks were affected as wear starts, and the highest peaks have their tops shaved and hence skewing the height distribution (Figure 2-18b). Similar behavior was seen in Sample 3, where peaks tops were flattened in initial wear time and shown in Figure 2-15 (b), (c), (d), (e), and (f). SEM image in Figure 2-14 (a) shows the small patches of flattened peaks. From CSM height profiles, like the one given in Figure 2-16 (b), the average length of the flat area was found to be ~10.6 µm. This was calculated by taking 35 samples on line profiles collectively, on all 3 different CSM measurements for the same surface. The heights lying in lower 5% (<3.72 µm) were considered as nearly being flat (i.e. lying on the same horizontal plane). The minimum recorded length of a flattened patch was 3.9 µm, and maximum 21.7 µm. In Figure 2-14 (a), and also illustrated again in Figure 2-17, it can be seen that large numbers of flat patches are close to the average length of ~10 µm, with some flat patches stretching to ~22 µm.

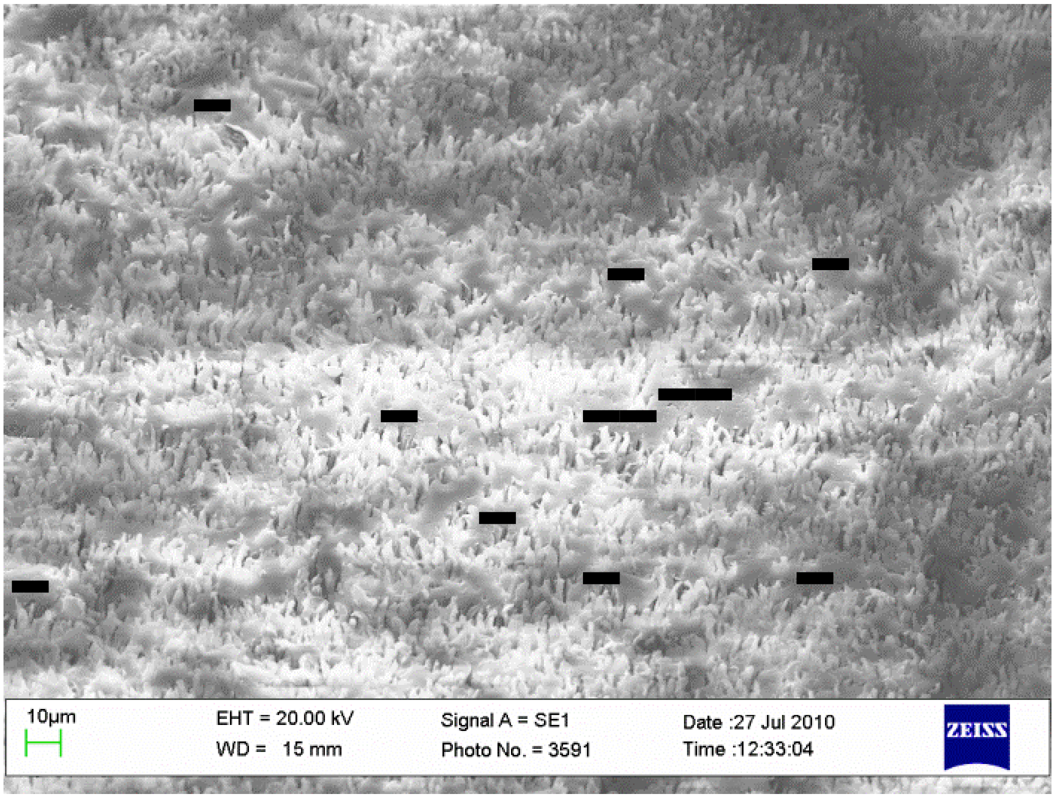

Figure 2-17: Illustrating the length of flattened patches on sample 2 SEM, worn for 3 minutes. The small black bars have length of 10 µm, and larger bars are of length 20 µm. It can be seen that surface has large number of flattened patches with 10 µm length, and some of them extend to 20 µm.

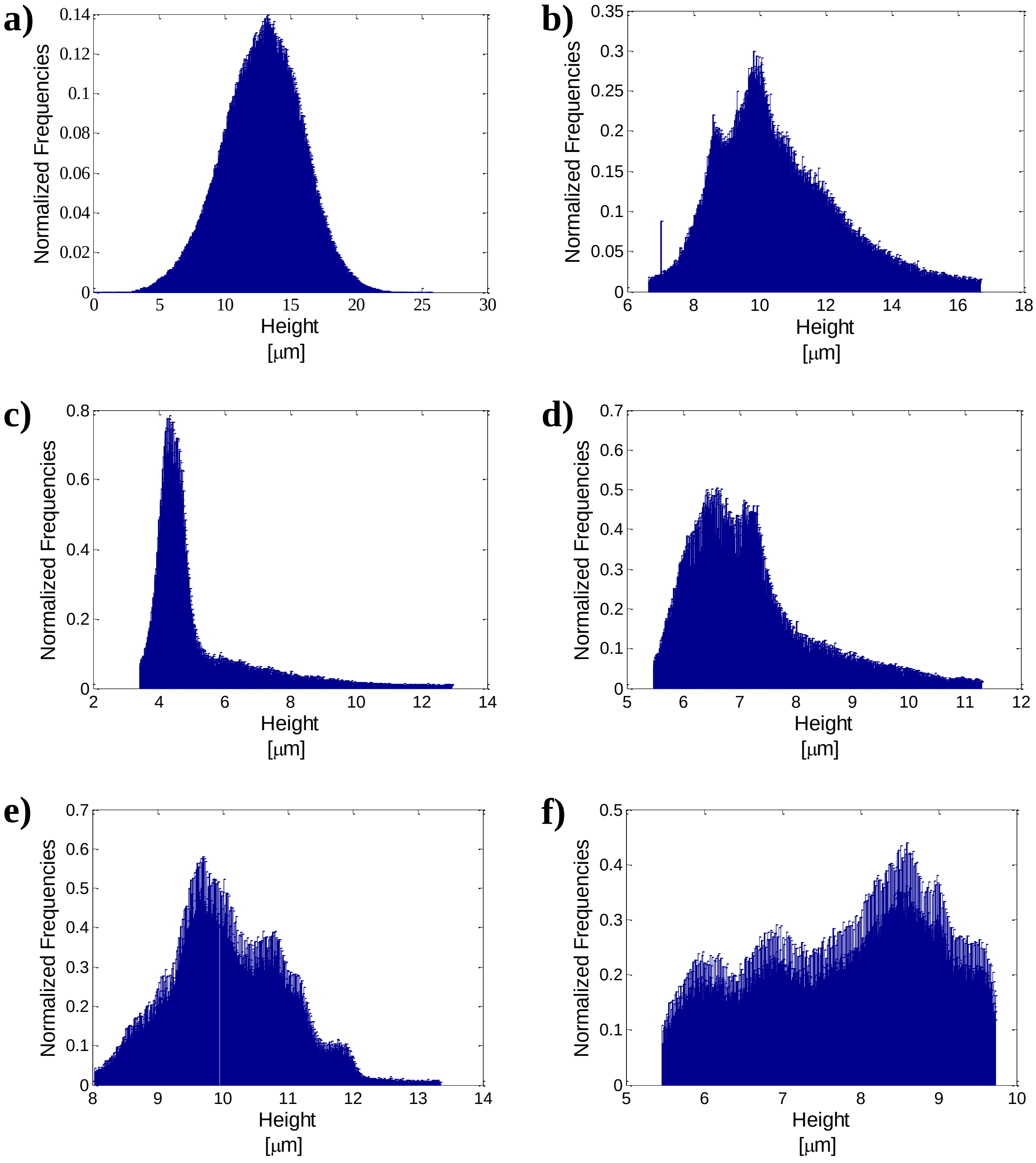

Figure 2-18: Normalized histograms for (a) unworn, (b) 3 min, (c) 12 min, (d) 18 min, (e) 21 min, and (f) 27 minutes worn samples evaluated from CSM data (Sample 2). It can be seen that height distribution starts as Gaussian, becomes positively skewed Poisson distribution, and then becomes lognormal distribution with high peaks and low valleys removed.

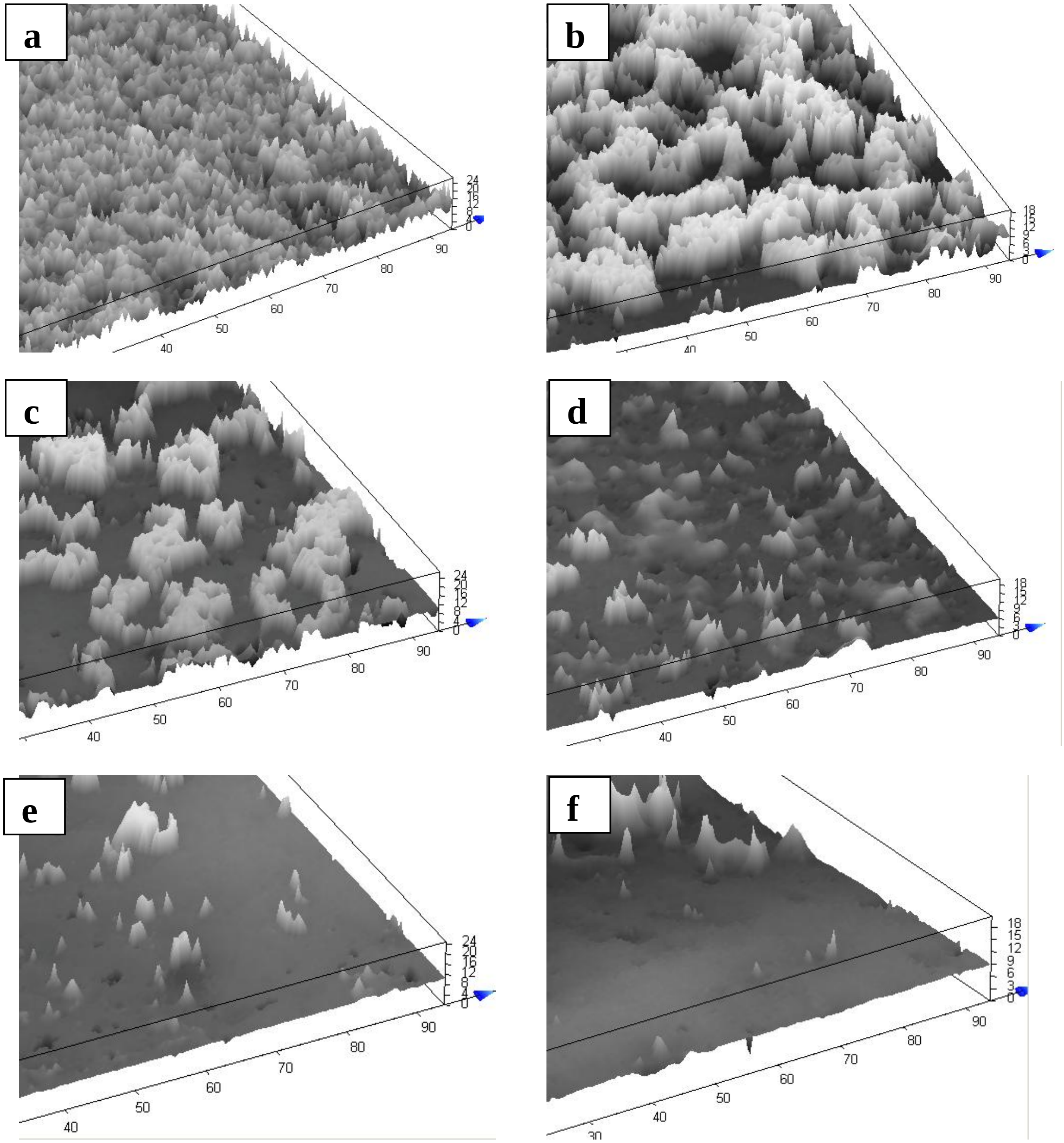

Figure 2-19: Visualizing surface topography evolution in 3D using CSM data for (a) unworn, (b) 3 min, (c) 12 minutes, (d) 18 minutes, (e) 21 minutes, and (f) 27 minutes worn samples. The corresponding height profiles are displayed in Figure 2-16. The plotted data is for sample 2. The data underwent noise filtering to remove artificial peaks and valleys. Example of artificial valleys, before and after noise removal can be seen in Appendix A.

Also as shown in Figure 2-18 (b), the histogram height distribution shows a positive skew due to peaks being shaved after abrasion as described previously and shown in Figure 2-14 (a) and Figure 2-16 (b) for sample 2 and 3 respectively. Figure 2-19 helps visualize the 3D topography evolution of worn surfaces, plotting the graphs using CSM data. The topography change after 18 minutes (Figure 2-19 d) of abrasion is visible clearly.

To give an interlude, one of the aims of this section is to validate the topographical data mapped using CSM, and that the noise filtration done on the data is able to generate results matching the physical condition on the surfaces. Line profiles are being used to calculate heights profiles and match the plateau regions with the areas mapped on SEM. Further a more quantitative granularity is being added by using height histograms. The purpose is to add redundancy in the measurements done, and to make sure the results derived were correct. This is essential as the rest of the thesis majorly depends upon this quantitative data, hence the in-depth look being undertaken in this Section.

The histogram height range in Figure 2-18 (c) is same as of 3 min histogram in Figure 2-18 (b), but the number of peaks have decreased and the area under valleys have grown significantly for Figure 2-18 (c). This difference can be seen in height profile (Figure 2-16c), where the flattened areas have increased, with peaks becoming scarce. Height profiles in Figure 2-16 (c) closely resemble the topography in SEM Figure 2-14 (c), as large number of flattened peak tracts averaging ~25 µm in length can be seen in the SEM. From CSM line profile (Figure 2-16 c), the average length of the flat area was found to be ~24.2 µm (calculations done based on methodology discussed previously). In Figure 2-18 (d) histogram range is ~5.46 µm to ~9.72 µm and Figure 2-16 (f) shows a flat surface with minor rough undulations (i.e. surface wavelength is dominated by low frequency components with minor number of high frequency components).

These progressive line profiles show that the peak heights are consistently decreasing. The curvature in the height profile (Figure 2-16 f) shows the long component of wavelength dominating, and is also the reason for probability increase, seen as a hump between~ 8 µm to ~9 µm in histogram (Figure 2-18 d). Importantly, it has to be noted that the major change of topography is after ~18 minutes of abrasion, as shown in Figure 2-14 (d) and (e) and quantitatively demonstrated in Figure 2-16 (d) and (e), and the topography progressively flattens afterwards. Similarly, Appendix B.1.1 contains the analysis for Sample 4.

The progressive evolution of surface topography as shown through Figure 2-16 (and Figure B-1), and Figure 2-18 (Figure B-2) is same for the samples. First, the peak tops are affected, which skews the histogram distribution. Afterwards, regions on the surface star getting affected and getting flattened with islands increasing in size as abrasion time increases, with histograms continuing the skewing trend as peaks are still dominant. After 18-21 minutes of abrasion, significant number of peaks abrade with histogram showing a return back to nearly Gaussian distribution but with reduced peak height. As wear is further continued, surface becomes completely flat, and major wavelength component of the surface dominates and hence the histogram shows a nearly skewed Poisson distribution.

From Figure 2-18 (and Figure B-2), starting from a nearly Gaussian distribution with wide height distribution among valleys and peaks, the height distribution becomes positively skewed (Figure 2-18b and Figure B-2b) for both the samples as they wear. When the surface becomes nearly flat with rough undulations (low frequency component of the surface) and the histogram returns to normal distribution but with a very narrow height distribution (Figure 2-18d and Figure B-2d). The above discussion shows that the surface topography changes consistently among samples despite stochastic nature of wear. The minor differences in the histograms are due to different height distribution in the starting unworn sample, but the evolution of heights with abrasion shows the same trend for all samples.

Figure 2-20 and Figure 2-21 show the normalized height distribution histograms for different wear intervals plotted on one graph, for two samples. The wear intervals were chosen to show the immediate and long term effect of wear on topography, and possible identical wear intervals for each sample were compared in these histograms. It can be seen that all the surfaces start as nearly Gaussian height distribution, with sample 4 (Figure 2-21 b)having broad range of normal height peaks, and sample 2 (Figure 2-20 b) having large number of high peaks. The height magnitude of peaks in sample 2 is also large compared to sample 4. After 3 minute (10 min for Sample 1) of wear, all height histograms register a decrease in number of peaks and a reduced peak height. After long time wear of nearly 27 minute (15 minutes for Sample 3), the surface is dominated by what were once the valleys on the unworn surface, for all the samples (Sample 3 will also evolve such that the peaks are abraded). Hence also illustrating the flatness of the surface. The initial distribution of the heights on the sample 4 makes the heights and valleys wear off in the nearly symmetrical fashion, as the peaks above 6 µm appear to be scattered among each other closely and hence are abraded equally.

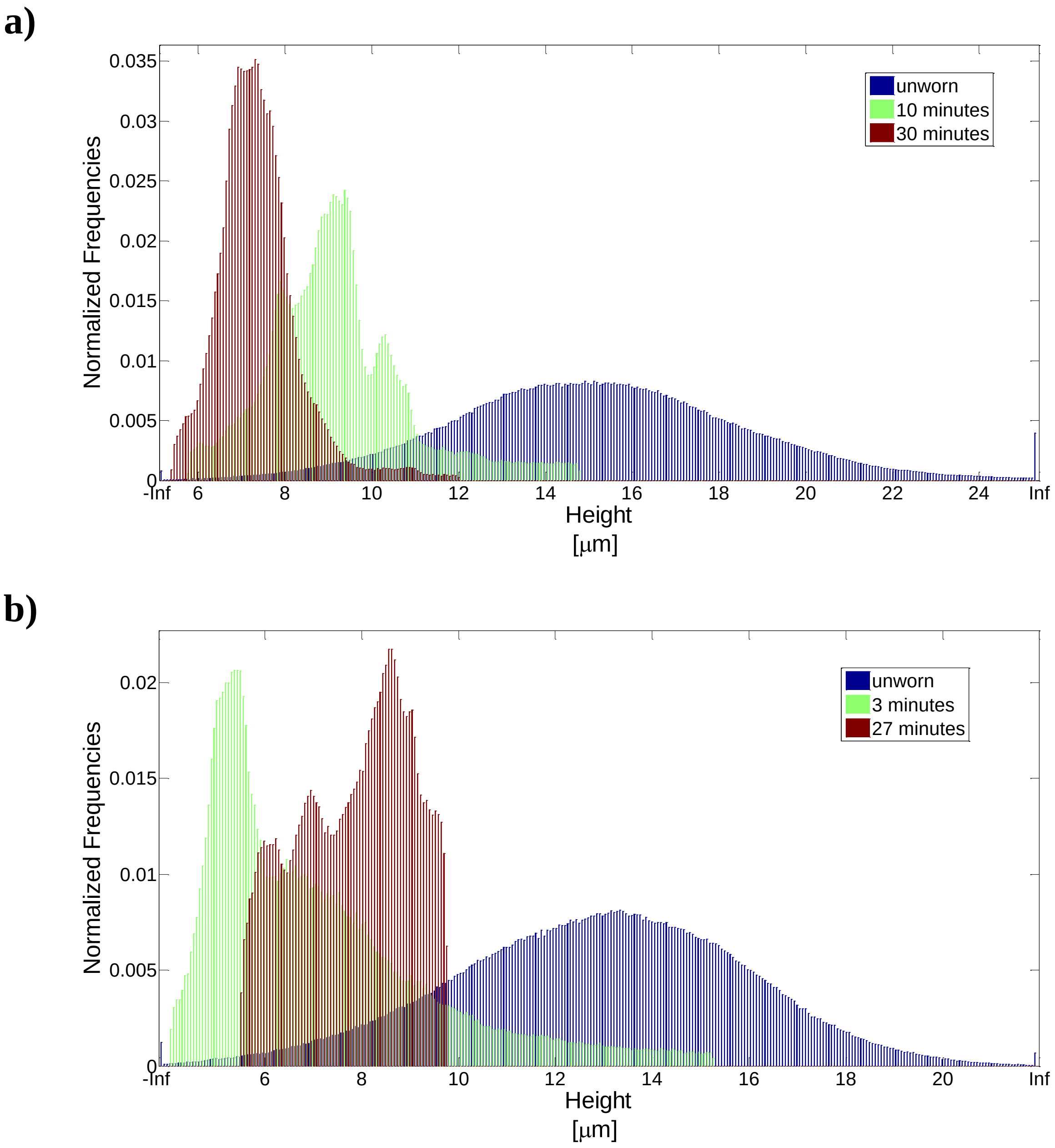

Figure 2-20: Comparing height distribution in (a) Sample 1, and (b) Sample 2 at nearly identical and three different wear durations. Normalized histograms have been evaluated from CSM data. The data has undergone noise filtering to remove artificial peaks and valleys.

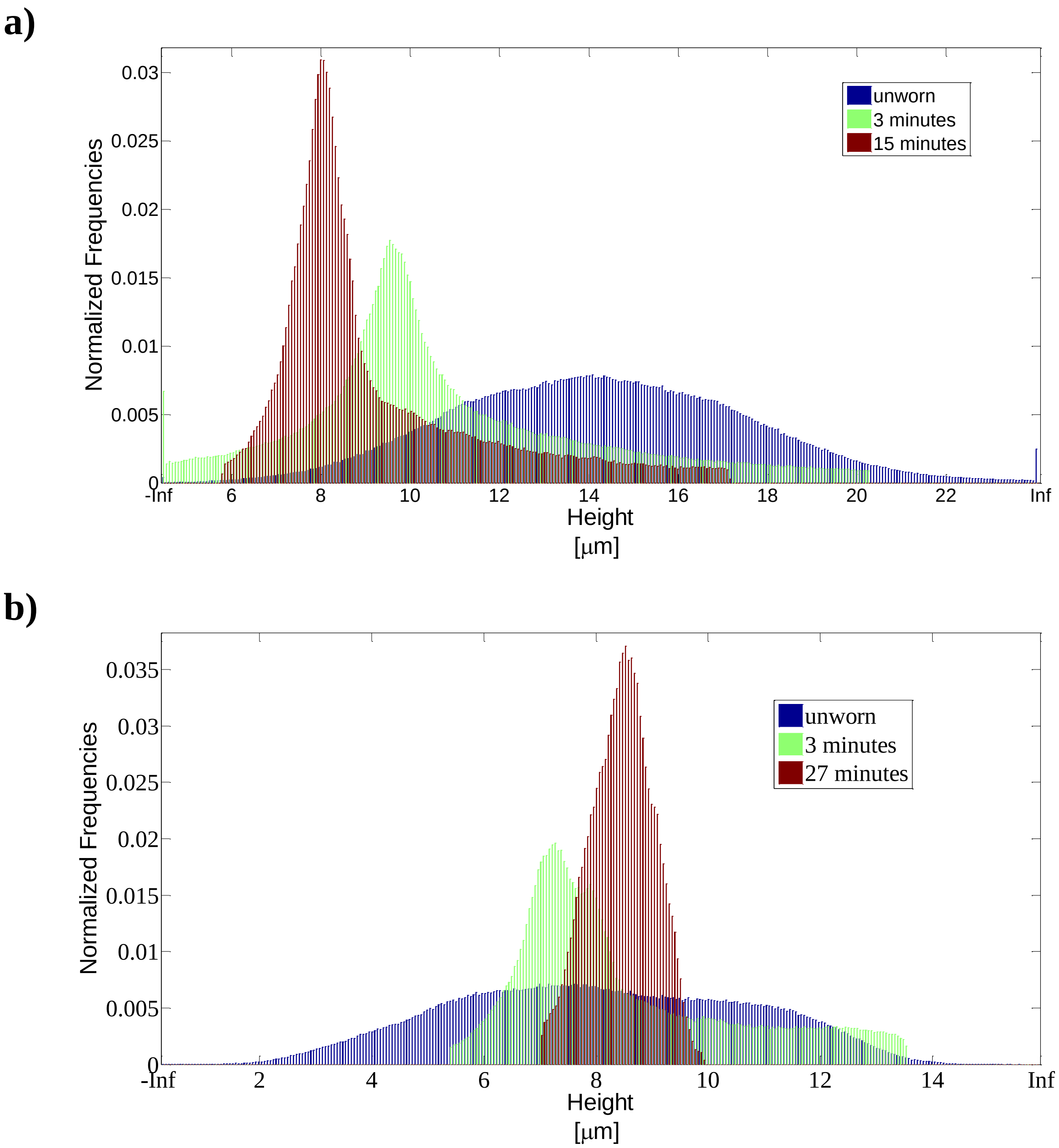

Figure 2-21: Comparing height distribution in (a) Sample 3, and (b) Sample 4 at at nearly identical and three different wear durations. Normalized histograms have been evaluated from CSM data. The data has undergone noise filtering to remove artificial peaks and valleys.

CSM height data helped to quantitatively evaluate the change in roughness and surface features as surface topography abraded. SEM also helped in verifying and supporting the CSM data, and both were consistent with each other. The abrasion method chosen was also consistent among all the samples, albeit minor differences did exist due to stochastic nature of phenomenon being studied. Thus the CSM data was used for further qualitative measurements of various surface roughness descriptors. Also, no contamination of surfaces due to external detritus, or lodged glass beads was observed. This can further attest the fact that no probable changes in surface chemistry happened due to foreign media.

2.4.2 Wetting Characteristics of Worn Surfaces

One of the motivation of this study was to understand the repellency and mobility of a liquid on the surface as it undergoes changes in topography due to wear. Advancing CA helps understanding the adhesion/repellency on the surface, and CAH serves as an indicator to liquid mobility. In this section, wetting characteristics of PTFE SHS are detailed, as surfaces were abraded and topography gradually changed.

Figure 2-22 and Figure 2-23 (Sample 1, 2, 3, 4 and 5) show the wetting characteristics on various surfaces as they wear. Figure 2-22 shows the wetting characteristics in initial stages of wear for sample 3. The CA hysteresis jumped at 690 s (11.5 min) until 780 s (13 min), and then dropped back to ~10°. SEM images in Figure 2-15 show the corresponding surface topography change. It can be seen that initially the peaks were spread out and as the surface was eroded, the peaks had their tops shaved off and also their “packing density” became compact. This can be seen in Figure 2-15 (a), (c), (f) and (h), as the surface is abraded tops were shaved and the peaks seem to get compacted. CA hysteresis jumps at around 690 s, the SEM at 720 s, Figure 2-15 (i) shows that peaks have been abraded off and their “packing density” is compact. Also, little shards of

Teflon are protruding from the surface. Surface in Figure 2-15 (j) at 15 minutes was in same condition as Figure 2-15 (i), but the CAH at this point is <10°. It is to be noted here that, the advancing CA during the whole wear duration remain near constant at 160°, showing that repellency was not affected but instead mobility was as the surface topography changes. This is in accordance with findings by Rühe *et al.* [29] which stated that liquids in Cassie state on a SHS exhibit advancing CA independent of roughness and topography, while receding CAs are more suspect to be affected by surface topography. They cited additional works by Dettre and Johnson [44], and Morra [45] in support of their arguments. Data on PTFE SHS surfaces also supports this argument that receding CA contribute towards CAH, while advancing CA remains relatively constant.

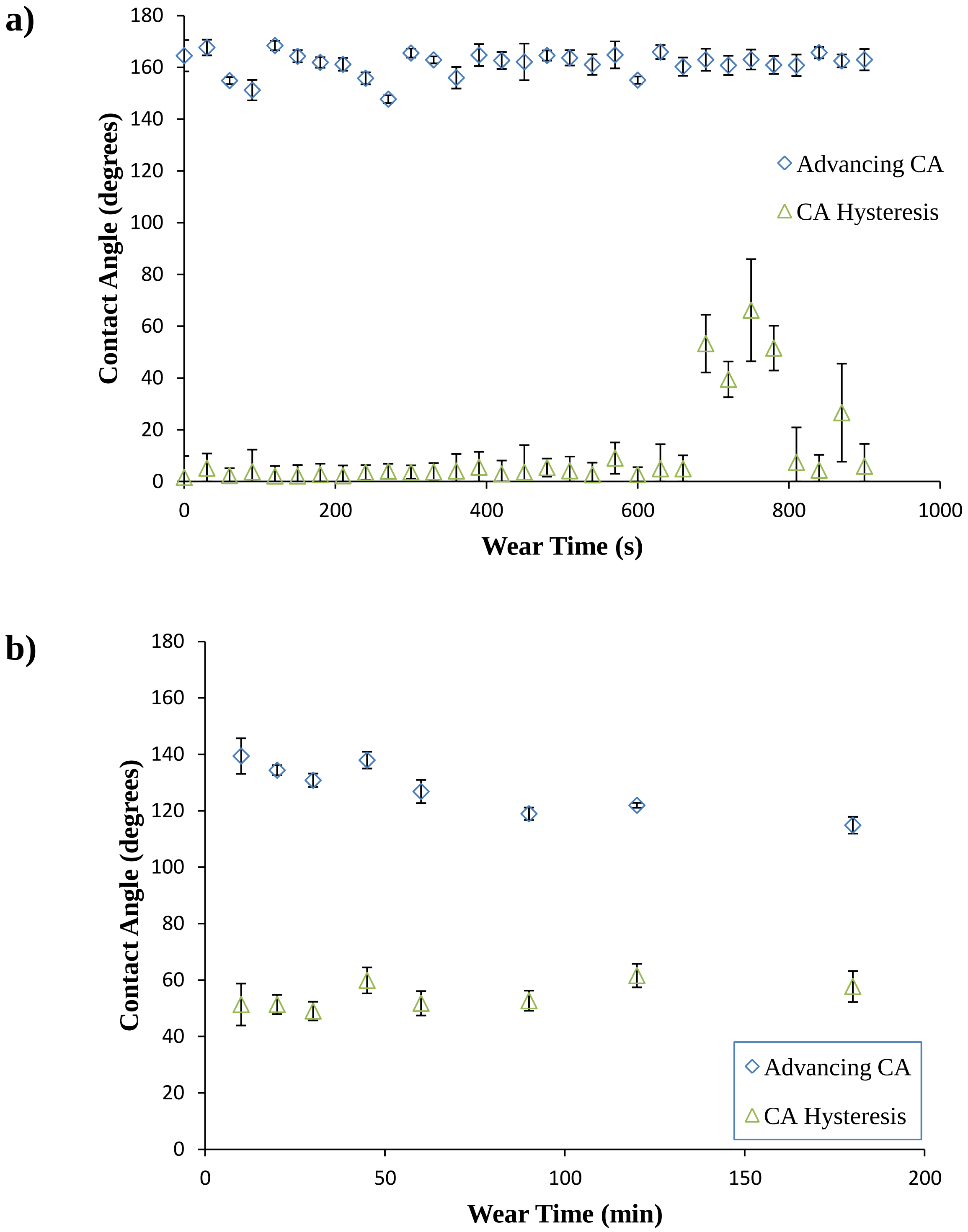

Figure 2-22: Wetting data on plasma etched PTFE surface, for a) sample 3, in the initial stages of wearing, and b) Sample 1, long term wear wetting data.

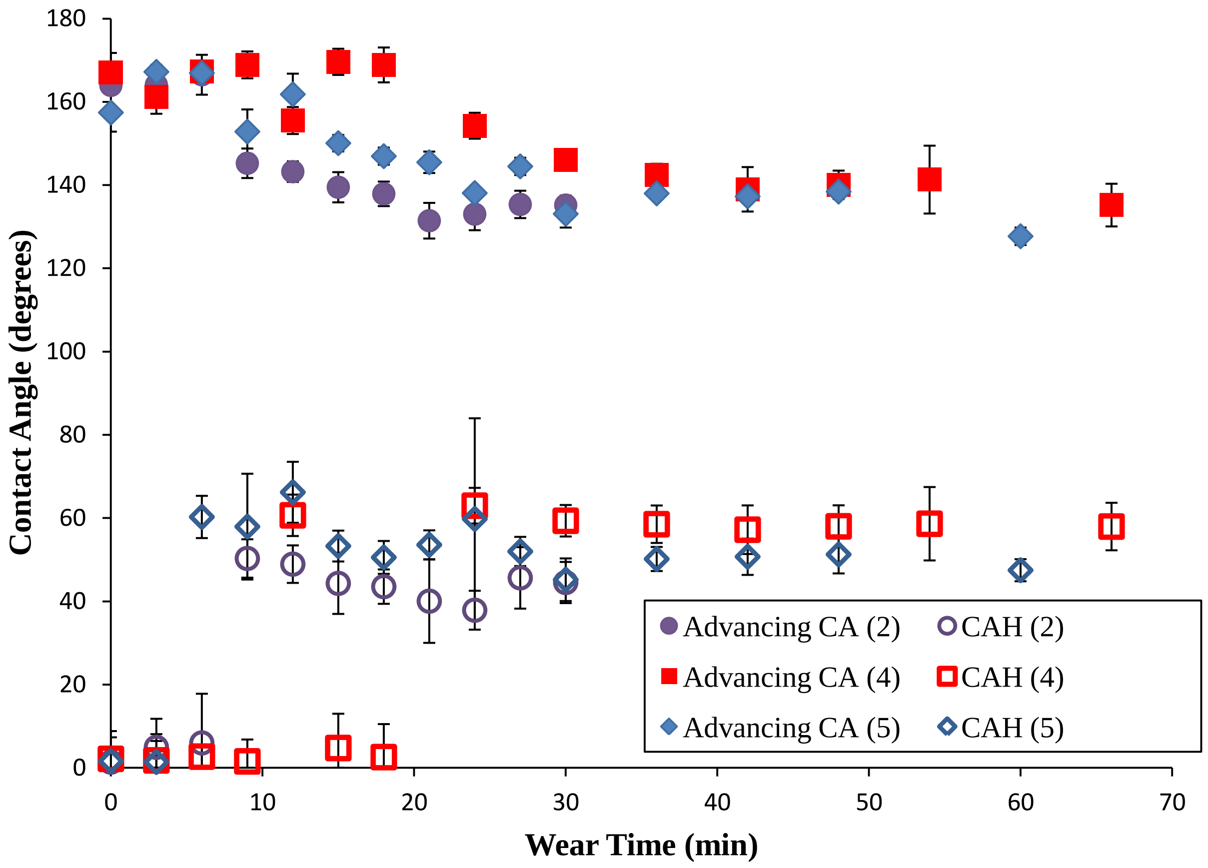

Figure 2-23: Wetting data on various plasma etched PTFE surfaces. In the legend, the numbers in the brackets indicate the sample number.

Figure 2-22 depicts the wetting characteristics on a surface worn for long duration of time. The CA hysteresis for the sample has already risen to 51° after 10 minutes of abrasion, and stays nearly constant with increment of only 6° after 3 hours of abrasion. Advancing contact angle decays with gentle slope and reaches 115°, the intrinsic contact angle for smooth surface of Teflon. Figure 2-13 (b) shows that after 10 minutes of wear, the surface peaks were largely flat. The CAH difference after 15 minutes of abrasion between this sample and one described earlier (Figure 2-22, sample 3) probably arise due to the fact that wear is stochastic phenomenon, and hence surface topography can be affected differently. This is probable explanation, as surface chemistry was not affected, as glass beads were inert and surface was thoroughly cleaned after abrasion. SEM images shown in previous section also did not show any lodged glass beads, or any extraneous detritus.

From Figure 2-22, it can be deduced that water remains mobile on the surface in initial period (until 650 seconds) of abrasion. From Figure 2-15 and Figure 2-22, the surface effectively repels water while the peaks are still dominant, and tentatively as the peaks started (Figure 2-22 b) to flatten to a greater extent, the mobility of the water drop was compromised. Figure 2-22 and Figure 2-22 (b) show this behavior too, as the mobility jumps at different wear time for both surfaces.

Figure 2-23 shows the water advancing CA's and CAH on the surfaces with respect to wear time. It can be seen that CAH rises after 9 minutes, and 6 minutes of wear for sample 2 and 4, respectively. For sample 5, CAH rises momentarily at 12 minutes but then drops back to <10° and finally rises after 24 minutes. This behavior was observed in Figure 2-22 too, for sample 3. This can probably indicate a presence of a transition band where both high and low CAH can be seen simultaneously depending upon surface particulars. For sample 5 wear time of 24 minutes will be taken as when the hysteresis jumps, as it was permanent. The advancing CA, and CAH follow the same trend (except CAH jump times) for all the samples (shown in Figure 2-23) except the difference between CAs at various wear times. SEM images in Figure 2-14 (e) and (f) show that the surface for sample 2 starts becoming completely flat after 27 minutes of wear time, and the wetting data for all samples show close behavior between contact angles after this point. This can be due to topography not affecting CAs to a major degree after the peaks have already flattened. Additionally, Figure 2-13 (c) also shows the sample 1 becoming flat ~20 minutes, and the mobility of water on the surface has already decreased, as shown in Figure 2-22 (b) the liquid drop at this point is in high state of immobility.

Advancing CA decreases with a gentle slope, ultimately reaching intrinsic CA (120°) on the smooth Teflon surface with longer wear times for all the sample surfaces, as shown in Figure 2-23.

Also, the CAH jumps in between (690 s) and then drops (810 s) for sample 3, pointing towards a existence of zone with ambiguous mobility characteristics (Figure 2-22). Water mobility on the surface is typically lost when the surface peak tops start flattening generally after ~5-10 minutes of wear. Figure 2-24 quantifies this by using normalized histograms at the wear time at which surface loses mobility. Sample 1, 2, 3, and 4 (Figure 2-24 a, b, c, and d, respectively) show similarity in height distribution with nearly identical height bandwidth for the topography, and surface dotted with small number of high peaks. Sample 5 (Figure 2-24c) on the contrary shows a surface height distribution containing majorly flat surface, and with miniscule number of high peaks. Hence, the topography at CAH jump cannot be subjectively quantified by physical condition of topography or height measurements alone, and various topography descriptors should be evaluated. This is one of the subjects discussed in depth in Chapter 3.

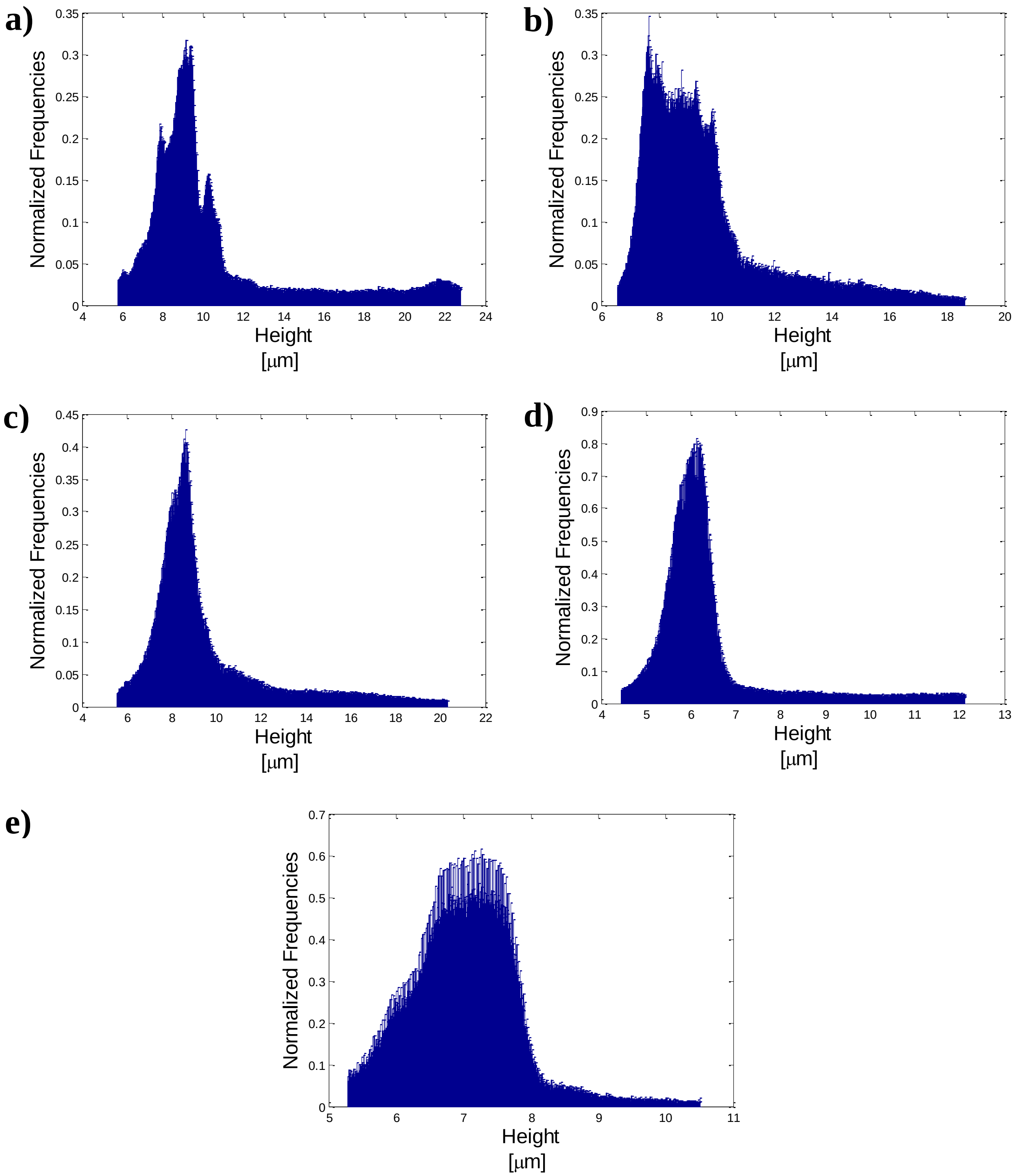

Figure 2-24: Normalized histograms for the samples when the hysteresis jumps, (a) Sample 1 at 10 minutes, (b) Sample 2 at 9 minutes, (c) Sample 3 at 690 seconds, (d) Sample 4 at 6 minutes, and (e) Sample 5 at 24 minutes.

In this section, wetting behavior of surfaces as they wear was shown, and the corresponding surface topography was also related. CAH was majorly due to increasing of the receding CA, while advancing CA remained unaffected after a time of wear. This was also consistent with findings of Rühe *et al.* [29], which found that advancing angles were relatively immune to changes in surface geometry compared to receding angles.

The exact delineation point where the mobility decreases cannot be gauged from this data or the fact that if even such a point exists after which the mobility decreases universally for all the samples. This is due to the difficult nature of predicting the topography according to wear intervals on different samples, and due to stochastic nature of wear. Hence, rather than looking into absolute topographical relief features, various surface topographical trends should be evaluated. The point when CA hysteresis jumps and hence the mobility for the drop decreases, and conversely adhesion increases, will not be constant for all the surfaces, since topography and abrasion is random, hence instead a zone can exist in which CAH rises. This zone will be identified in Chapter 3, where a look into corresponding surface roughness characteristics is also undertaken. Wetting behavior in conjunction with surface topography descriptors are discussed in Chapter 3.

2.4.3 Predicting Wettability

Previously, topography and wetting behavior of surfaces was discussed as surfaces were abraded. It is important to predict wettability as it is the paramount parameter of superhydrophobcity, and in this section, a look into behavior of Cassie equation regarding its ability to predict wetting characteristics is undertaken.

To predict CA theoretically, various penetration depths were chosen between 5% and 15% of unworn surface height (Figure 2-9). Surface was considered to span between the highest peak and lowest valley, and the penetration depth was calculated as a percentage of this height. The height data was already available through CSM. The absolute values of penetration depths, as shown in Table 2-1, were calculated based upon unworn topography of the sample and its contact angle. This absolute value was propagated to the entire set of abraded surfaces for finding various f, f_1, and f_2 values on worn samples. The absolute values based upon unworn topography were used, as otherwise for surfaces abraded for longer durations having flat topography, the penetration depths were in *nm* range, which would have rendered further CA predictions meaningless.

Table 2-1: Penetration depth (in μm) corresponding to various percentage of penetration depth for Sample 2 to 5[2].

Sample	**5% depth (μm)**	**10% depth (μm)**	**15% depth (μm)**
2	0.60 ± 0.02	1.20 ± 0.03	1.81 ± 0.07
3	0.80 ± 0.05	1.60 ± 0.07	1.98 ± 0.12
4	0.55 ± 0.07	1.11 ± 0.07	1.73 ± 0.05
5	0.57 ± 0.04	1.15 ± 0.04	1.67 ± 0.06

Table 2-2 shows the various percentage penetration depths and their corresponding absolute values on a plasma etched Teflon surface (sample 3) on both area and line density basis. Equation 2-2 and 2-3 parameters (f, f_1, and f_2) were calculated at each penetration depth for a

---

[2] Sample 1 penetration depth was not calculated due to the surface losing superhydrophobicity in first wear interval, and hence Cassie equation would not have been relevant

typical surface. This sensitivity analysis was done to theoretically predict the CA, and match it with the experimentally measured CA, which would help estimate the liquid penetration depth on the surface. In calculation of CAs both Cassie equations (Eq. 2-2 and 2-3) were used. The merit of using equation 2-3 is explained later.

Table 2-2: Cassie equation parameters calculated on area and linear density basis for various penetration depths, for sample 4.

	Penetration depth (μm)	f_1	f_2	f
Area	5% (0.55 μm)	0.150	0.978	0.018
	10% (1.10 μm)	0.603	0.933	0.093
	15% (1.65 μm)	1.081	0.888	0.167
Linear	10% (1.10 μm)	0.154	0.966	0.027
	15% (1.65 μm)	0.360	0.931	0.068

Contact angles predicted by Cassie equation (both forms) on unworn PTFE surface on area density basis are shown in Figure 2-25. As shown, *original* Cassie equation remains indeterminate on all the samples; however symbols at 180° were placed to indicate this matter i.e. cosθ was larger than -1, hence CA was indeterminate (not predictable). *Popular* form of Cassie equation was able to predict CAs with increasing penetration depth, and ~10% was the predicted penetration depth for the samples, pointing towards nearly ~1.10 μm water penetration into surface topography for unworn PTFE SHS. The maximum error observed between predicted CAs (10% penetration) and experimental CAs was 3.90% for *popular* form of Cassie equation. Figure 2-26 shows the predicted CAs by Cassie equation (both forms) on linear density basis. It can be seen that original form of Cassie equation remain indeterminate, while ~10% penetration depth broadly agrees with the experimentally observed CAs. The maximum error observed between predicted CAs (10% penetration) and observed CAs was 4.58% for *popular* form of Cassie equation.

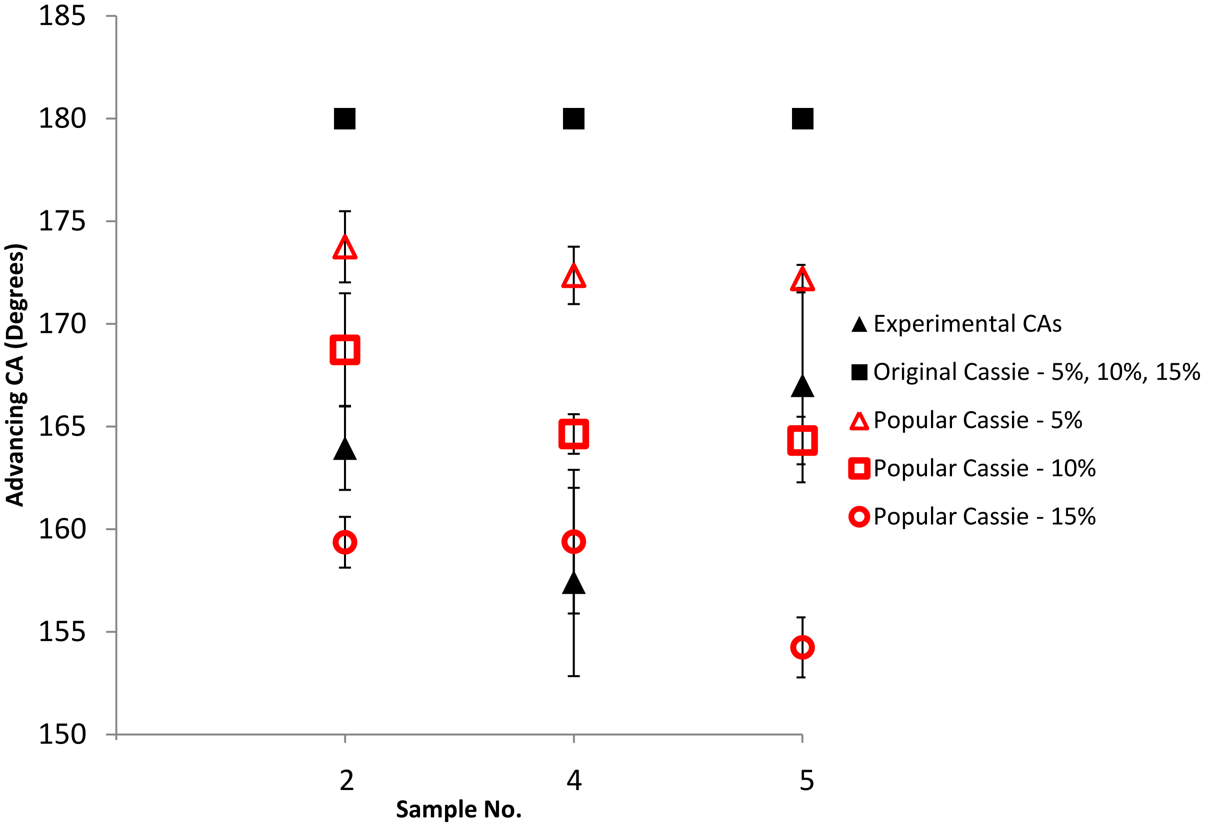

Figure 2-25: Predicted Cassie CAs for PTFE SHS on an area density basis. Original Cassie equation remains indeterminate for any amount of penetration, while popular Cassie equation is able to predict advancing CA for an unworn surface.

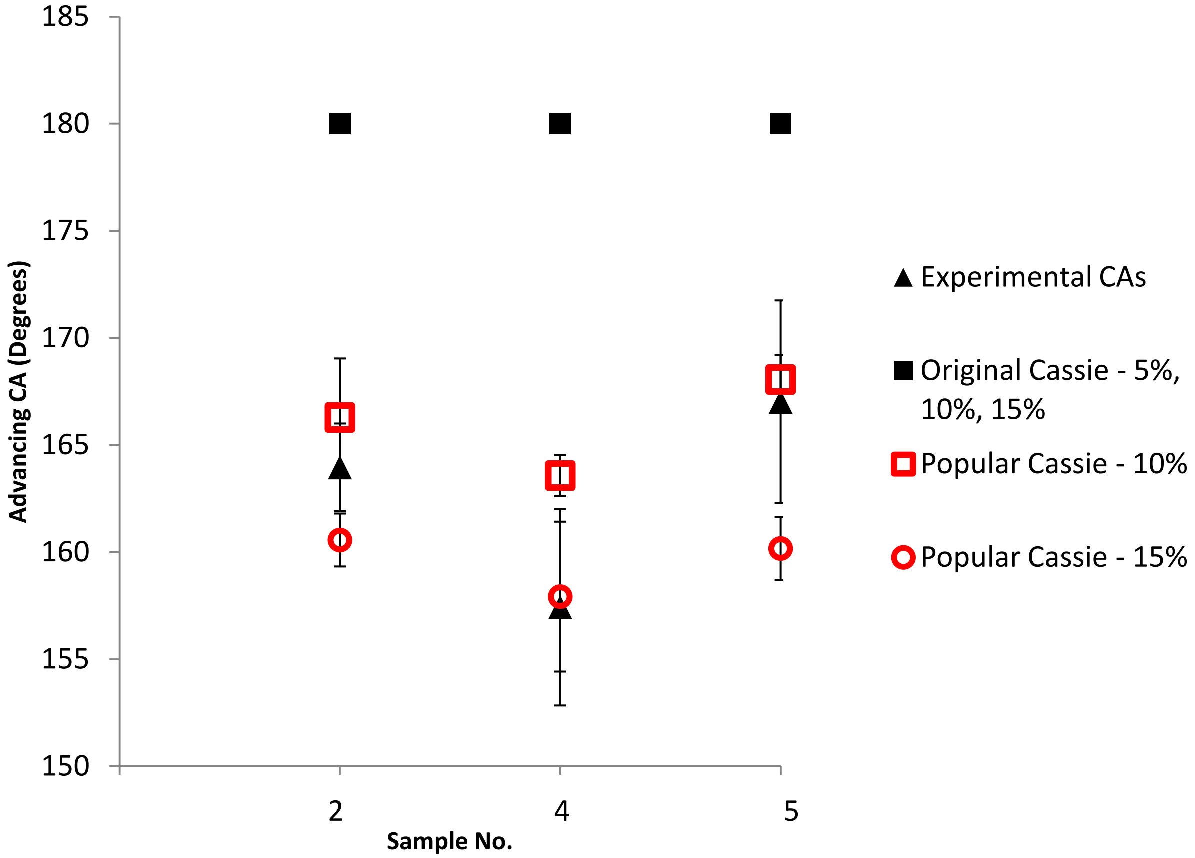

Figure 2-26: Cassie CAs on linear density basis as a surface wears for plasma etched PTFE surfaces. As can be seen 15% penetration with equation (2) is able to predict CA.

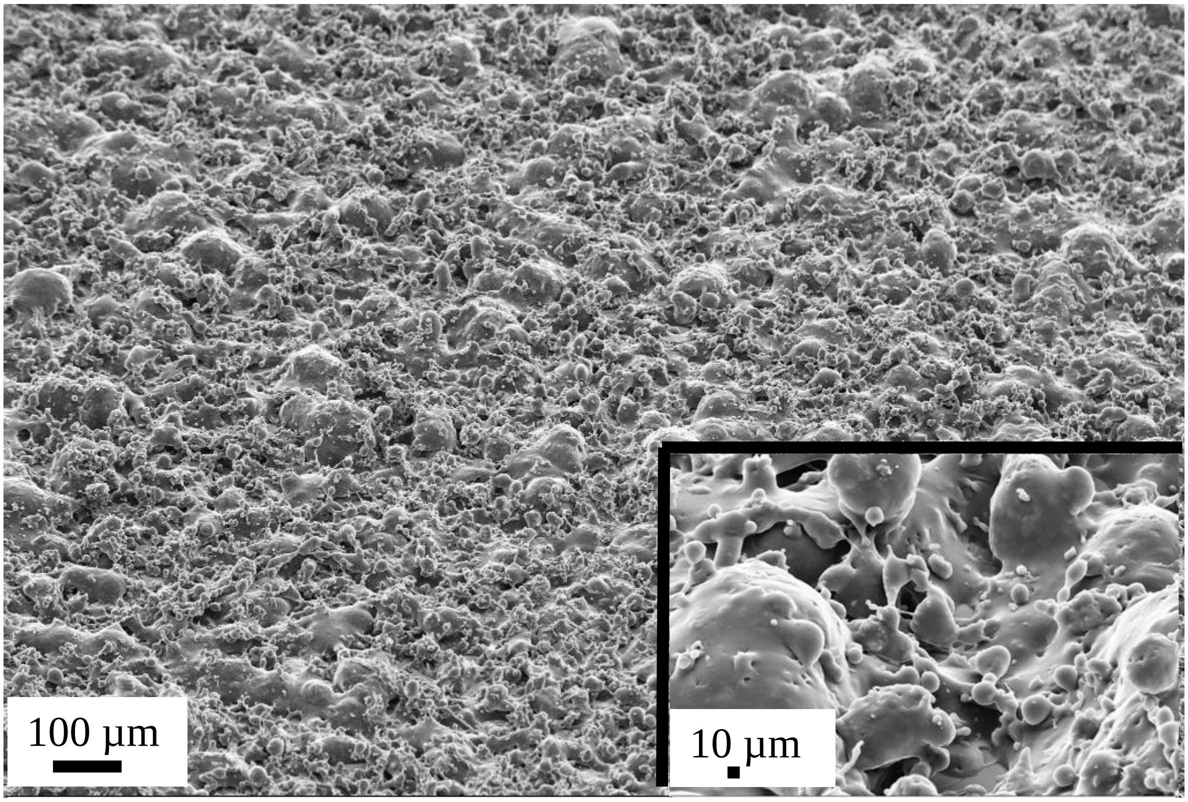

Figure 2-27: SEM of Teflon-Nanoclay spray coated sample. Inset shows a zoomed in view.

To see if both forms of Cassie equations can predict CAs for another random geometry structure, measurements were done on another random geometry surfaces fabricated by spray coating Teflon-nanoclay mix used in our earlier study [46]. Figure 2-27 shows the SEM of the topography present on the sample. Advancing CA on this surface was 156.34°±2.91° and CAH was 9.64° ± 8.13°. This random topography presents curved tops and not pointed micro-structures and hence is a good alternative to test applicability of eqs. 2-2 and 2-3.

Contact angles predicted by using eqs. 2-2 and 2-3 on both area density and line density basis, are shown in Figure 2-28 and Figure 2-29, respectively. As can be seen, eq. 2-2 results in indeterminate values for various levels of penetration depths on both line and area density basis.

As penetration depth changes, *f* changes and eq. 2-3 hence behaves as a “fitting equation” giving Cassie CA values. On area and linear density basis, 15% penetration on surfaces was successful in predicting CAs within error range of ±7°. This error number can be reduced by increasing the penetration percentage further, but was not done in the thesis as the error was relatively less, keeping in mind the nature of study undertaken.

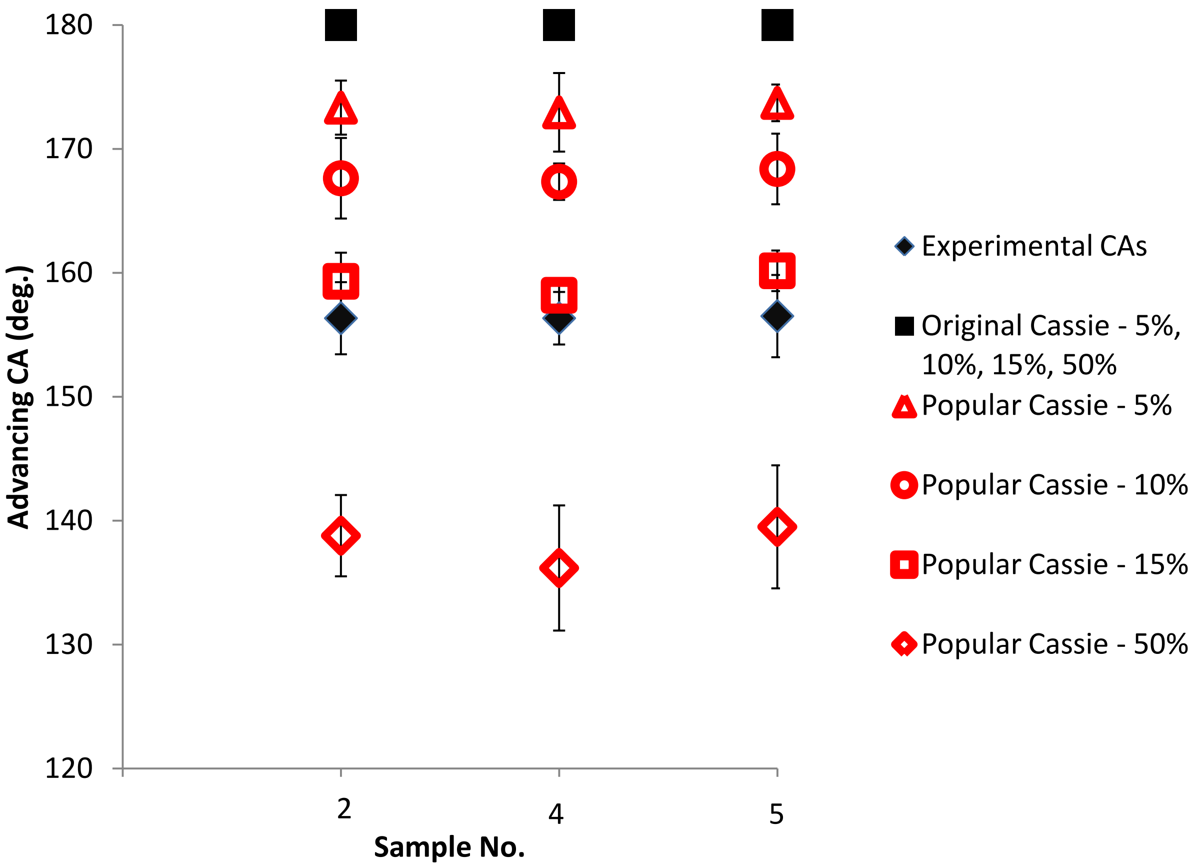

Figure 2-28: Predicted Cassie CAs on area density basis for different penetration percentages on Teflon-Nanoclay spray coated sample. Original Cassie equation remains indeterminate for all penetration depths.

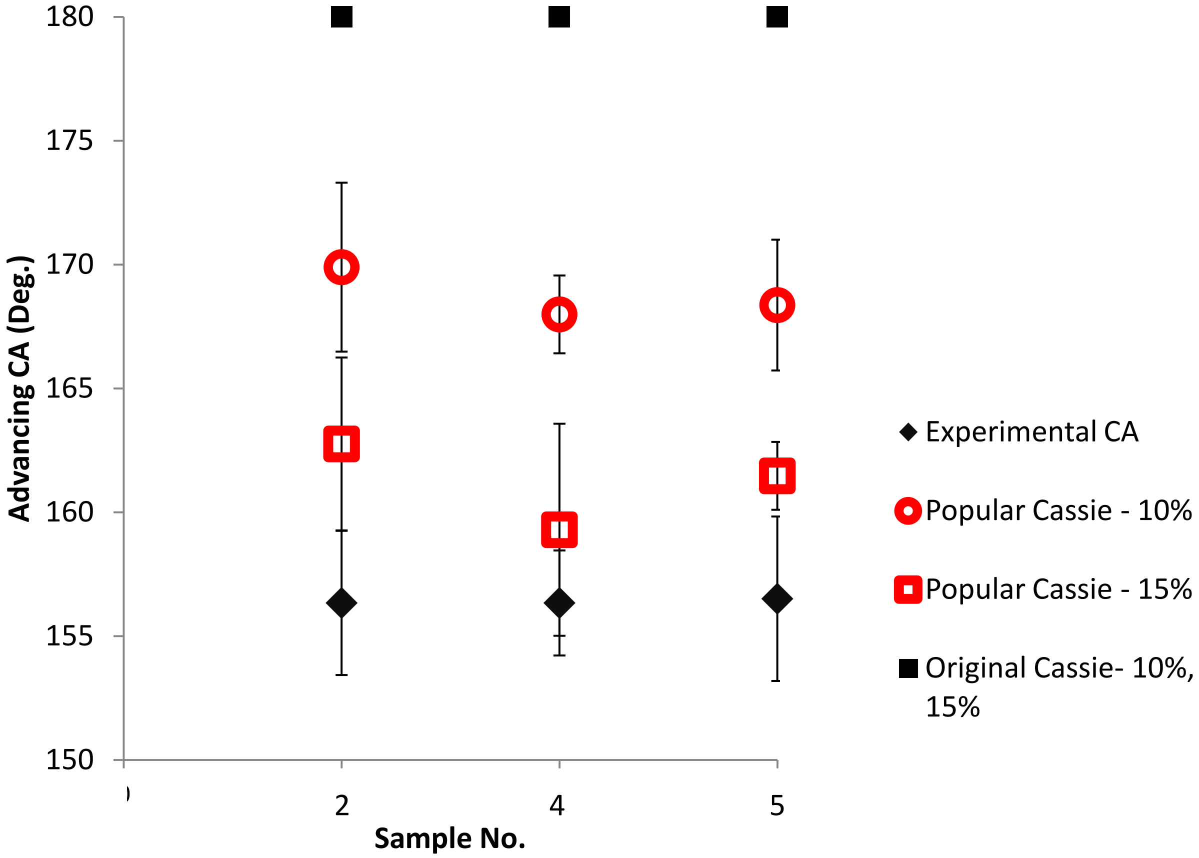

Figure 2-29: Predicted Cassie CAs on linear density basis for different penetration percentages on Teflon-Nanoclay spray coated sample. Original Cassie equation remains indeterminate for all penetration depths.

Above, only unworn surfaces have been evaluated. Next, CAs for *worn* plasma etched Teflon surfaces were predicted with popular and original Cassie equation on area density basis, as line density would also have given similar results. Penetration depths on the samples are listed in Table 2-1, and were used for all wear interval topographies. Figure 2-30 shows the calculated contact angles for different penetrations using eqs. 2-2 and 2-3. It can be seen that using eq. 2-3, 10% penetration depth broadly agrees with measured advancing contact angles providing an estimation of liquid penetration theoretically. It is to be noted here that eq. 2-2, *original* Cassie equation, fails to predict advancing CA for any of the penetration depth while popular equation is able to predict CAs for all of the samples. Similarly for other samples, shown in Figure 2-31, it was found that the penetration depth varied from 7% to 12% (~1.2-1.5 µm). Hence, the *popular* form of Cassie equation works well as a fitting parameter equation on worn surfaces too, and probably explains its widespread usage in literature [27].

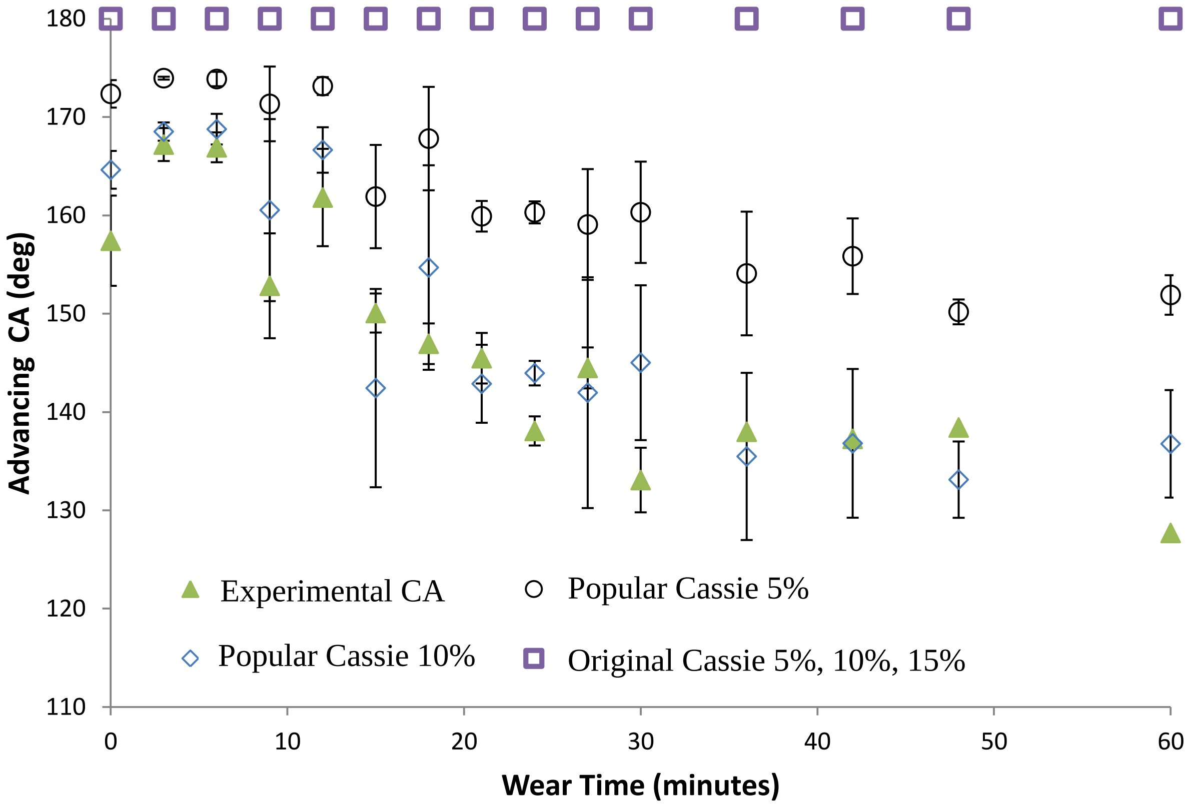

Figure 2-30: Comparison of contact angles calculated using original and popular Cassie equation with measured contact angles on Sample 4. For graphical clarity only two penetration depths (5% and 10%) are shown. Open symbols show the predicted CAs, while closed symbol signify the experimental advancing CA. Error bars show standard deviation.

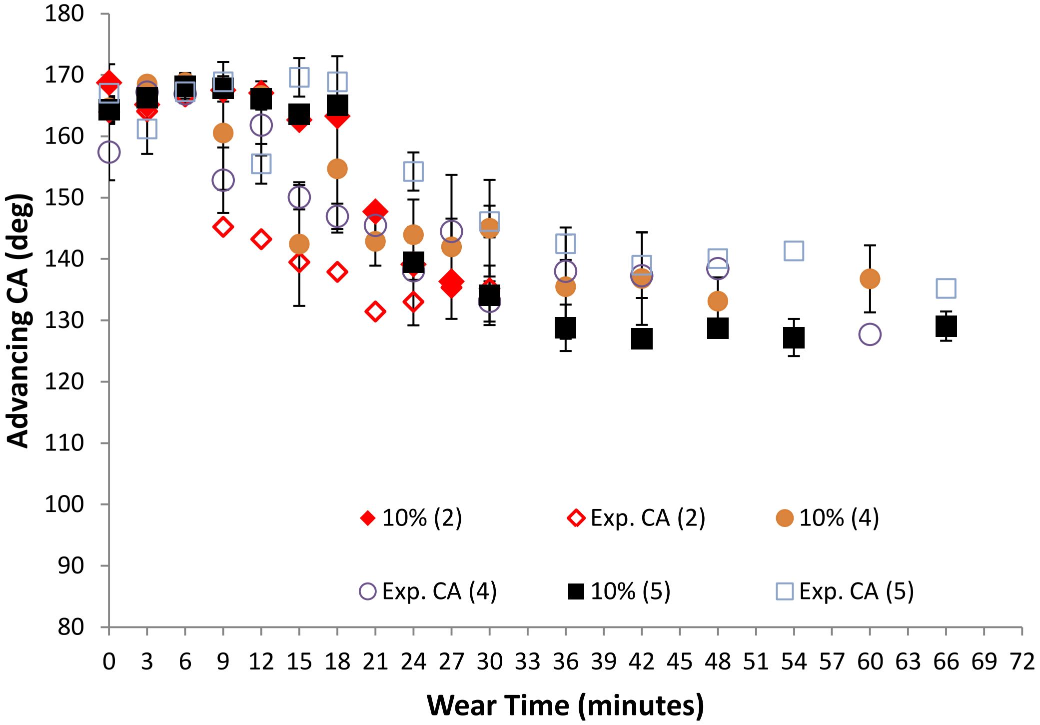

Figure 2-31: Prediction of CA behavior with popular Cassie equation for worn plasma etched PTFE samples. Only 3 samples are plotted for brevity. Original Cassie equation remains indeterminate for all values of percentage penetration. Closed symbols represent experimentally observed CAs, while open symbols are CAs predicted by Cassie equation on an area density basis. Number in legend parenthesis represents the sample number.

Based upon above discussion, it can be seen that *original* Cassie equation results in indeterminate CA values for all samples, on both area and line basis. While *popular* Cassie equation gave identical results on all the samples for both topographies, on both area and line basis. The percentage penetration depth was same for both area and line density basis, and error between experimental and predicted CAs was 1.1% - 2.5%. Hence, eq. 2-3 can serve as a “fitting equation” for random geometry surfaces to predict advancing CAs. This, probably, also explains the extensive use of *popular* Cassie equation (eq. 2-3) in literature, as it has been successful in predicting CAs until now although it misinterprets Cassie's original definition and thermodynamic basis for its definition [27]. Anomalies have also been reported in predictions by *popular* Cassie equation too [47].

Receding angles cannot be predicted by any of the equations, as they were in the range of 90° when surfaces lost their superhydrophobicity, and minimum CA predictable by Cassie equation is 120°. This is also shown in Figure 2-32. Increasing the penetration depth progressively will also be unhelpful as lower bound of Cassie equation is 120°, predicting CA of 90° is not possible. Hence, predicting mobility of the surface remains elusive with any equation in the form of the Cassie equation.

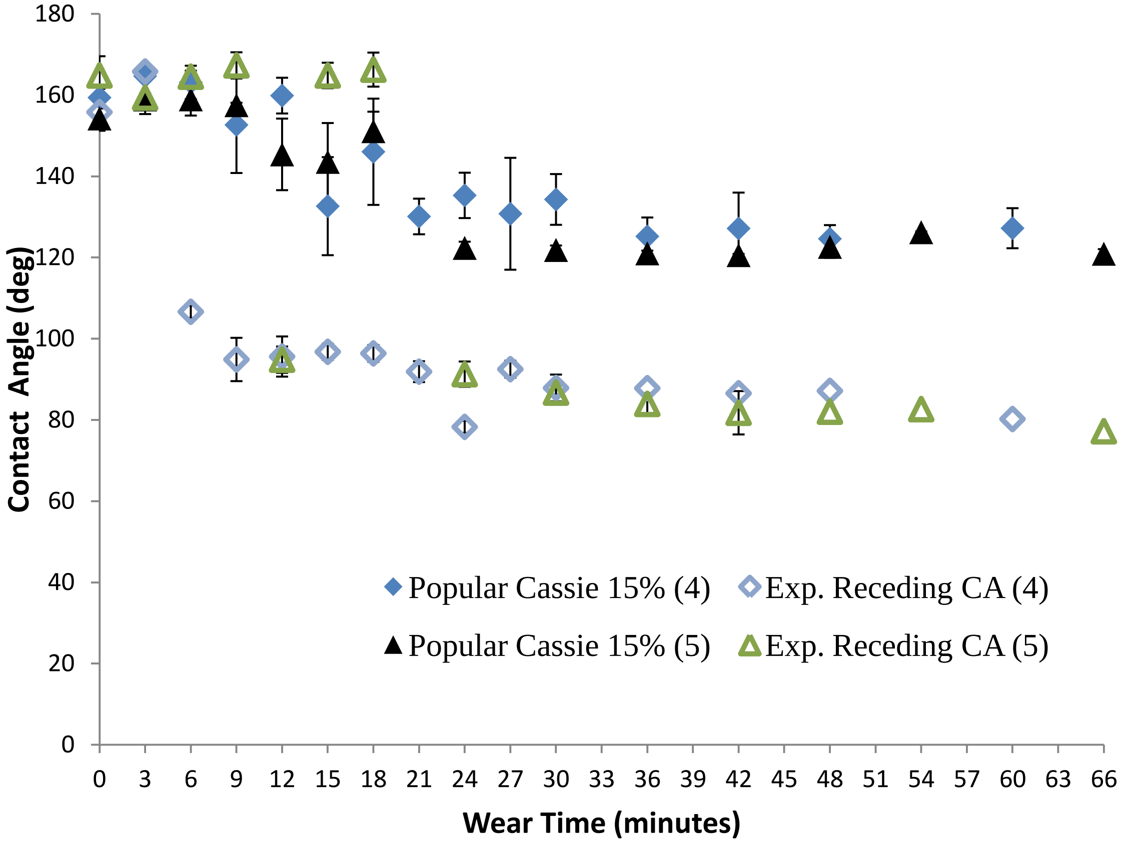

Figure 2-32: Prediction of receding CA behavior with popular Cassie equation for plasma etched PTFE samples. Original Cassie equation remains indeterminate for all values of percentage penetration. The number in the legend parenthesis refers to the sample number.

On progressive abrasion of surfaces, the superhydrophobicity was lost, and probably water was in Wenzel state after the surfaces were fully flat. Hence, CAs were also calculated according to Wenzel equation. Figure 2-33 show the CAs predicted by Wenzel equation, and as can be seen, Wenzel equation is also inadequate for predicting receding CAs.

So, in this section it was shown that *popular* Cassie equation behaves the same way for line parameters as it does for the area parameters. By estimating liquid penetration percentage on

SHS, CAs could be predicted. *Original* Cassie equation remained indeterminate on random topography surfaces on both area and line density basis. Receding CAs could not be predicted by either form of Cassie equation, and also by Wenzel equation.

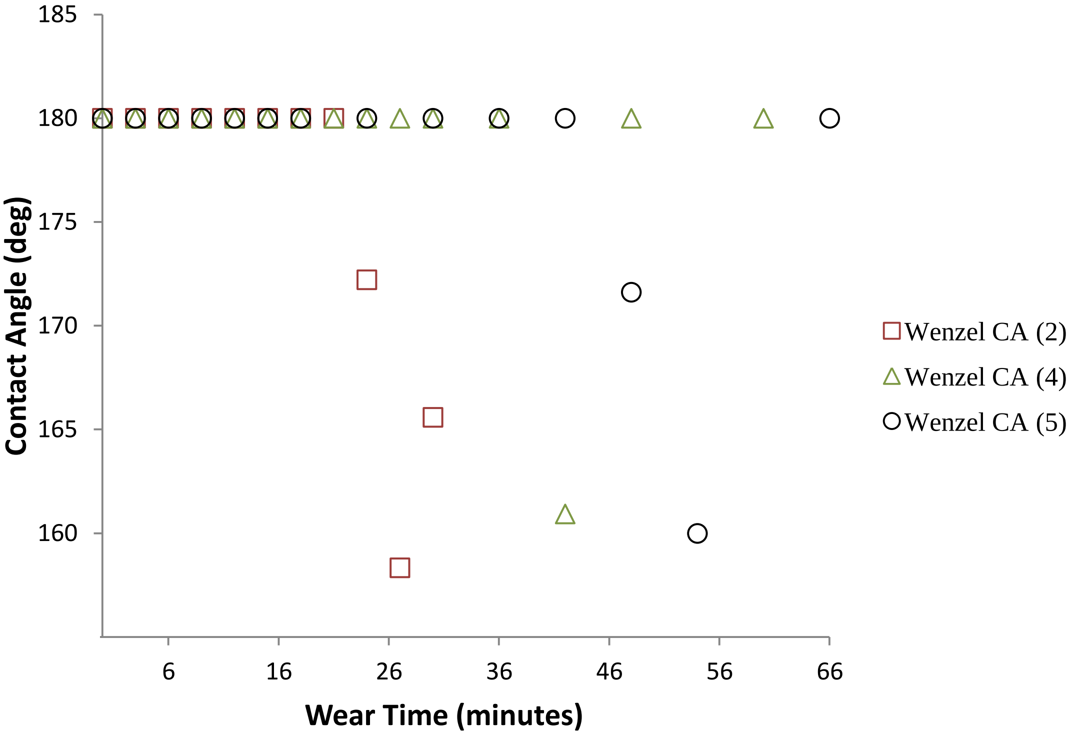

Figure 2-33: Prediction of CA behavior according to Wenzel equation. The number in the legend parenthesis refers to the sample number. For brevity, only three samples out of five are shown.

2.5 Prediction of wear behavior

In previous section, it was shown that although adhesion/repellency of a liquid can be predicted by popular Cassie equation used as a "fitting equation", predicting mobility (receding CA) still remained elusive. In this section, an examination of data to see if intermediate advancing CAs (lying between unworn and fully worn surface topography) can be predicted based on topography characteristics of unworn and long term worn surface.

The correlation was done on basis of interpolating either *f* values, and simply doing a linear fit between advancing CAs (at unworn and long time worn topography), shown in Fig. 2-34. Interpolating *f* values (10% penetration depth) of intermediate wear times based upon unworn and long time worn surface *f* values, predicted CA within ±10° to experimental CAs with 75% accuracy (based upon all the samples). While a simple linear fit based upon unworn and long time worn surface was successful in predicting CAs 70% of the time within an error range of ±5°. Based on this, linear fit is probably a viable method which can be used for predicting intermediate advancing CAs, simply based upon advancing CAs of unworn and long time worn surface. Figure 2-35 shows the comparison between advancing CAs predicted by eq. 2-3 and linear fit between two end points. It can be seen that the linear fit has more probability of predicting CAs close to the measured CAs than by using eq. 2-3. This is valid for all other data sets of the same surface (sample 3, 4, and 5). It is notable to mention here that a straight line fit was chosen here, because the CAs were to be predicted based on only two data points i.e. unworn and long time worn wetting condition.

Hence, having wetting characteristic at unworn plasma etched PTFE surface and long time worn surface, can also be used as a primary method to predict adhesion of the drop (advancing CAs) at any intermediate wear time within reasonable error limits of CA. This method should be used with caution as the surfaces in this study followed a generally continuous decreasing slope and hence linear fit was able to reasonably model the advancing CAs. This method will fail when data does not slope linearly. Nevertheless, it can be a model that can be studied on other topographies and can remove abrading multitude of samples to predict advancing CAs in intermediate region between unworn and long term worn topography.

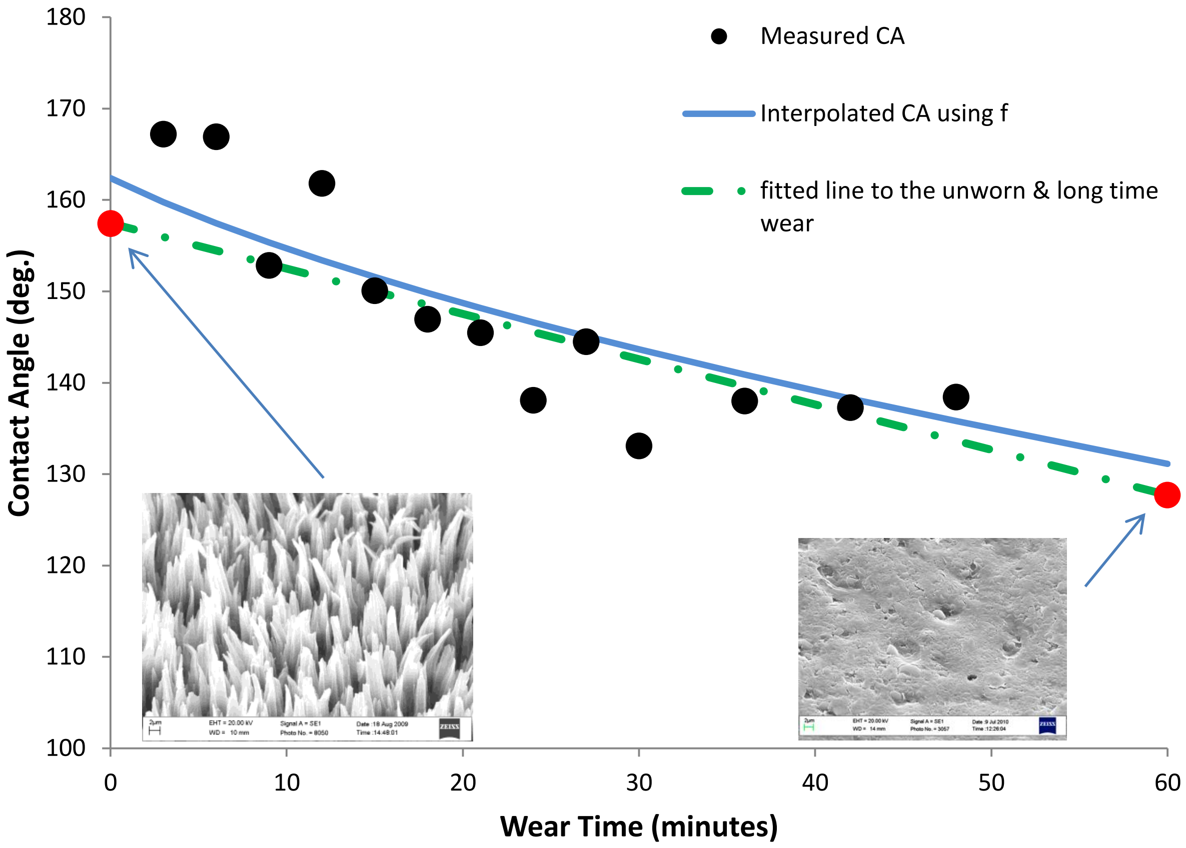

Figure 2-34: Predicting intermediate wetting behavior of plasma etched PTFE surface by using unworn and long term behavior characteristics. Advancing CAs are calculated by interpolating *f* parameter based on values of *f* at unworn and long term wear. Linear fit between unworn and long term wear is also shown. With respect to interpolation, linear fit is consistently giving good results predicting intermediate advancing CAs.

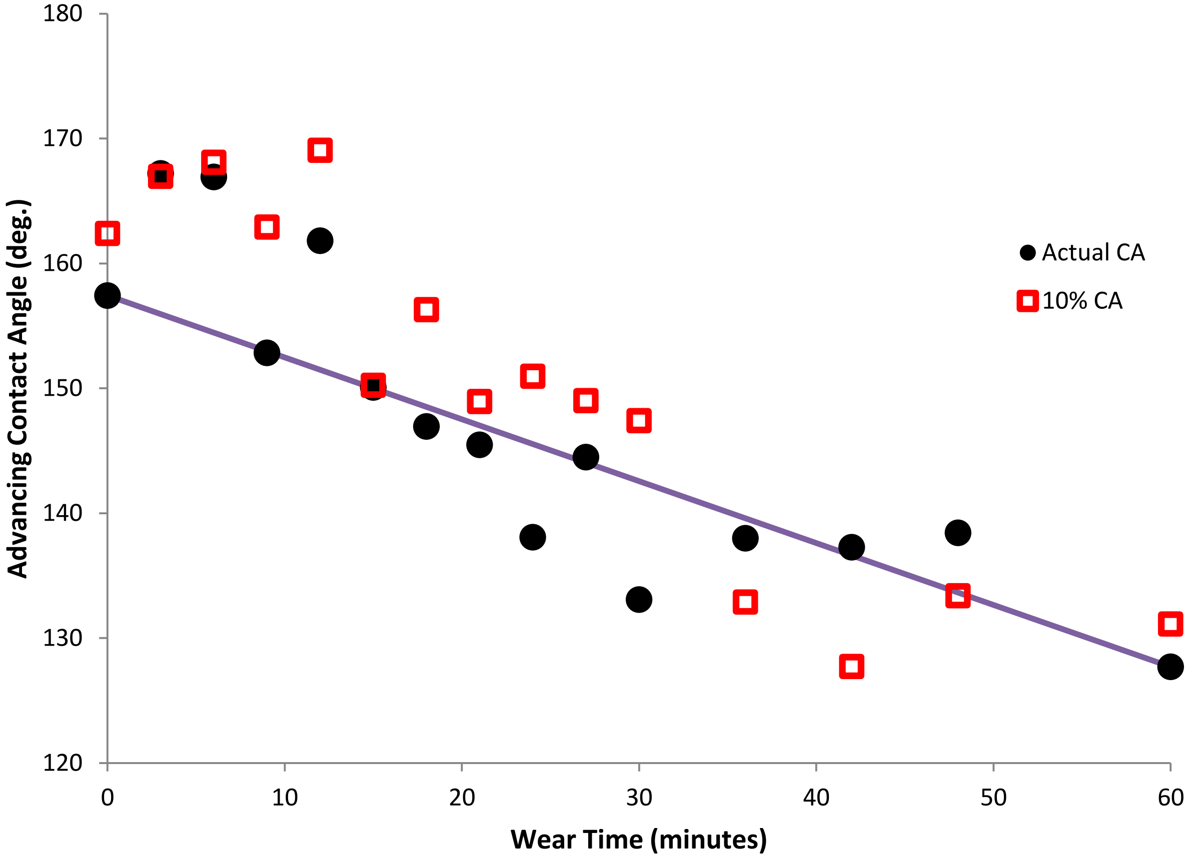

Figure 2-35: Correlating Wetting and wear of plasma etched PTFE surfaces by comparing the linear fit with 10% penetration CAs predicted by popular Cassie equation. With comparison to popular Cassie equation, linear fit is consistently better (and 'accurate') at predicting intermediate advancing CAs.

2.6 Summary

An abrasion methodology which abrades a surface in random unbiased fashion has been presented. A quantitative way of monitoring surface topography has also been described. With the help of height histograms and line profiles, it was shown that the abrasion happening on surfaces is although stochastic, but consistent among different samples. Wettability data showed that wear increased the receding CA, but the jump times were not consistent among different samples, and sometimes after initial increase the values decreased after further wear. Excessive wear resulted in final large increase in contact angle hysteresis. Advancing CA showed a progressive decrease as wear time increased, and became nearly constant to achieve advancing CA close to that of intrinsic smooth PTFE surface. It was shown that both *original* and *proper* form of Cassie equation lacks the ability to predict liquid mobility on the surfaces. *Original* Cassie equation was also unable to predict advancing CAs, while *proper* Cassie equation was able to predict the advancing CAs after assuming of a penetration depth for the liquid on the surface asperities. While receding CAs could not be predicted by any form of Cassie equation. Therefore the focus of the next chapter is probing the surface texture parameters as a way towards explaining the surface wettability.

References

1. Z. Guo, W. Liu, and B.-L. Su, “Superhydrophobic surfaces: From natural to biomimetic to functional,” *Journal of Colloid and Interface Science*, vol. 353, no. 2, pp. 335–355, Jan. 2011.
2. Y. Y. Yan, N. Gao, and W. Barthlott, “Mimicking natural superhydrophobic surfaces and grasping the wetting process: A review on recent progress in preparing superhydrophobic surfaces,” *Advances in Colloid and Interface Science*, vol. 169, no. 2, pp. 80–105, Dec. 2011.
3. L. Chen, G. Yang, and S. Wang, “Air-Grid Surface Patterning Provided by Superhydrophobic Surfaces,” *Small*, vol. 8, no. 7, pp. 962–965, Apr. 2012.
4. B. Balu, A. D. Berry, D. W. Hess, and V. Breedveld, “Patterning of superhydrophobic paper to control the mobility of micro-liter drops for two-dimensional lab-on-paper applications,” *Lab on a Chip*, vol. 9, no. 21, p. 3066, 2009.
5. M. Nosonovsky and B. Bhushan, “Superhydrophobic surfaces and emerging applications: Non-adhesion, energy, green engineering,” *Current Opinion in Colloid & Interface Science*, vol. 14, no. 4, pp. 270–280, Aug. 2009.
6. C.-H. Xue, S.-T. Jia, J. Zhang, and J.-Z. Ma, “Large-area fabrication of superhydrophobic surfaces for practical applications: an overview,” *Science and Technology of Advanced Materials*, vol. 11, no. 3, p. 033002, Jun. 2010.
7. T. Verho, C. Bower, P. Andrew, S. Franssila, O. Ikkala, and R. H. A. Ras, “Mechanically Durable Superhydrophobic Surfaces,” *Advanced Materials*, vol. 23, no. 5, pp. 673-678, Feb. 2011.

8. X. Deng, L. Mammen, H.-J. Butt, and D. Vollmer, “Candle Soot as a Template for a Transparent Robust Superamphiphobic Coating,” *Science*, vol. 335, no. 6064, pp. 67–70, Dec. 2011.
9. Y. Xiu, Y. Liu, D. W. Hess, and C. P. Wong, “Mechanically robust superhydrophobicity on hierarchically structured Si surfaces,” *Nanotechnology*, vol. 21, no. 15, p. 155705, Apr. 2010.
10. V. Hejazi and M. Nosonovsky, “Wear-Resistant and Oleophobic Biomimetic Composite Materials,” in Green Tribology, M. Nosonovsky and B. Bhushan, Eds. Berlin, Heidelberg: Springer Berlin Heidelberg, 2012, pp. 149–172.
11. D. Ebert and B. Bhushan, “Transparent, Superhydrophobic, and Wear-Resistant Coatings on Glass and Polymer Substrates Using SiO_2, ZnO, and ITO Nanoparticles,” *Langmuir*, vol. 28, no. 31, pp. 11391–11399, Aug. 2012.
12. K. Koch, B. Bhushan, H.-J. Ensikat, and W. Barthlott, “Self-healing of voids in the wax coating on plant surfaces,” *Philosophical Transactions of the Royal Society A: Mathematical, Physical and Engineering Sciences*, vol. 367, no. 1894, pp. 1673-1688, May 2009.
13. C. Neinhuis, K. Koch, and W. Barthlott, “Movement and regeneration of epicuticular waxes through plant cuticles,” *Planta*, vol. 213, no. 3, pp. 427-434, Jul. 2001.
14. K. Liu and L. Jiang, “Bio-inspired design of multiscale structures for function integration,” *Nano Today*, vol. 6, no. 2, pp. 155-175, Apr. 2011.
15. X. Yao, Q. Chen, L. Xu, Q. Li, Y. Song, X. Gao, D. Quéré, and L. Jiang, “Bioinspired Ribbed Nanoneedles with Robust Superhydrophobicity,” *Advanced Functional Materials*, vol. 20, no. 4, pp. 656–662, Feb. 2010.

16. J. Zhang, X. Sheng, and L. Jiang, “The Dewetting Properties of Lotus Leaves,” *Langmuir*, vol. 25, no. 3, pp. 1371–1376, Feb. 2009.

17. Y. Li, L. Li, and J. Sun, “Bioinspired Self-Healing Superhydrophobic Coatings,” *Angewandte Chemie International Edition*, vol. 49, no. 35, pp. 6129-6133, Aug. 2010.

18. P. Thomas, “The use of fluoropolymers for non-stick cooking utensils,” *Surface Coatings International*, vol. 81, no. 12, pp. 604-609, Dec. 1998.

19. H. P. Tannenbaum, Fluoropolymer non-stick coatings, U. S.Pat. No. 6,761,964, 2002.

20. F.G. Reick, Toys and games using super-hydrophobic surfaces, U.S.Pat. No. 4,199,142, 1980.

21. S. Minko, M. Müller, M. Motornov, M. Nitschke, K. Grundke, and M. Stamm, “Two-Level Structured Self-Adaptive Surfaces with Reversibly Tunable Properties,” *Journal of the American Chemical Society*, vol. 125, no. 13, pp. 3896-3900, Apr. 2003.

22. ASTM Standard F735-06, "Standard Test Method for Abrasion Resistance of Transparent Plastics and Coatings Using the Oscillating Sand Method," ASTM International, West Conshohocken, PA, 2003, http://www.astm.org/Standards/F735.htm.

23. “Fluoropolymer Comparison - Typical Properties.” Internet: http://www2.dupont.com/Teflon_Industrial/en_US/tech_info/techinfo_compare.html, [accessed Dec. 12, 2012]

24. A.W. Neumann, R. David, Y. Zuo. *Applied Surface Thermodynamics*. New York: CRC Press, 2011, pp. 107 – 282.

25. A. B. D. Cassie and S. Baxter, “Wettability of porous surfaces,” *Trans. Faraday Soc.*, vol. 40, p. 546, 1944.

26. A. B. D. Cassie, “Contact angles,” *Discuss. Faraday Soc.*, vol. 3, p. 11, 1948.

27. A. J. B. Milne and A. Amirfazli, “The Cassie equation: How it is meant to be used,” *Advances in Colloid and Interface Science*, vol. 170, no. 1–2, pp. 48–55, Jan. 2012.
28. C. W. Extrand, “Model for Contact Angles and Hysteresis on Rough and Ultraphobic Surfaces,” *Langmuir*, vol. 18, no. 21, pp. 7991–7999, Oct. 2002.
29. C. Dorrer and J. Rühe, “Advancing and Receding Motion of Droplets on Ultrahydrophobic Post Surfaces,” *Langmuir*, vol. 22, no. 18, pp. 7652–7657, Aug. 2006.
30. R. Dufour, M. Harnois, V. Thomy, R. Boukherroub, and V. Senez, “Contact angle hysteresis origins: Investigation on super-omniphobic surfaces,” *Soft Matter*, vol. 7, no. 19, p. 9380, 2011.
31. K.-Y. Yeh, L.-J. Chen, and J.-Y. Chang, “Contact Angle Hysteresis on Regular Pillar-like Hydrophobic Surfaces,” *Langmuir*, vol. 24, no. 1, pp. 245–251, Jan. 2008.
32. C. N. C. Lam, R. H. Y. Ko, L. M. Y. Yu, A. Ng, D. Li, M. L. Hair, and A. W. Neumann, “Dynamic Cycling Contact Angle Measurements: Study of Advancing and Receding Contact Angles,” *Journal of Colloid and Interface Science*, vol. 243, no. 1, pp. 208–218, Nov. 2001.
33. C. N. C. Lam, R. Wu, D. Li, M. L. Hair, and A. W. Neumann, “Study of the advancing and receding contact angles: liquid sorption as a cause of contact angle hysteresis,” *Advances in Colloid and Interface Science*, vol. 96, no. 1–3, pp. 169–191, Feb. 2002.
34. C. N. C. Lam, N. Kim, D. Hui, D. Y. Kwok, M. L. Hair, and A. W. Neumann, “The effect of liquid properties to contact angle hysteresis,” *Colloids and Surfaces A: Physicochemical and Engineering Aspects*, vol. 189, no. 1, pp. 265–278, 2001.

35. R. Dufour, M. Harnois, V. Thomy, R. Boukherroub, and V. Senez, “Contact angle hysteresis origins: Investigation on super-omniphobic surfaces,” *Soft Matter*, vol. 7, no. 19, p. 9380, 2011.
36. B. He, J. Lee, and N. A. Patankar, “Contact angle hysteresis on rough hydrophobic surfaces,” *Colloids and Surfaces A: Physicochemical and Engineering Aspects*, vol. 248, no. 1–3, pp. 101–104, Nov. 2004.
37. B. He, N. A. Patankar, and J. Lee, “Multiple Equilibrium Droplet Shapes and Design Criterion for Rough Hydrophobic Surfaces,” *Langmuir*, vol. 19, no. 12, pp. 4999–5003, Jun. 2003.
38. C. W. Extrand, “Contact Angles and Hysteresis on Surfaces with Chemically Heterogeneous Islands,” *Langmuir*, vol. 19, no. 9, pp. 3793–3796, Apr. 2003.
39. D. F. Cheng and T. J. McCarthy, “Using the Fact that Wetting Is Contact Line Dependent,” *Langmuir*, vol. 27, no. 7, pp. 3693–3697, Apr. 2011.
40. L. Gao and T. J. McCarthy, “How Wenzel and Cassie Were Wrong,” *Langmuir*, vol. 23, no. 7, pp. 3762–3765, Mar. 2007.
41. G. McHale, “Cassie and Wenzel: Were They Really So Wrong?,” *Langmuir*, vol. 23, no. 15, pp. 8200–8205, Jul. 2007.
42. M. Nosonovsky, “On the Range of Applicability of the Wenzel and Cassie Equations,” *Langmuir*, vol. 23, no. 19, pp. 9919–9920, Sep. 2007.
43. A. Amirfazli and A. W. Neumann, “Status of the three-phase line tension: a review,” *Advances in Colloid and Interface Science*, vol. 110, no. 3, pp. 121–141, Aug. 2004.
44. R. H. Dettre and R. E. Johnson, “Contact Angle Hysteresis II. Contact Angle Measurements on Rough Surfaces,” in *Contact Angle, Wettability, and Adhesion*

(Advances in Chemistry Series), vol. 43, F. M. Fowkes, Ed. Washington, D.C.: American Chemical Society, 1964, pp. 136–144.

45. M. Morra, E. Occhiello, and F. Garbassi, “Contact angle hysteresis in oxygen plasma treated poly (tetrafluoroethylene),” *Langmuir*, vol. 5, no. 3, pp. 872–876, 1989.
46. D. Barona and A. Amirfazli, “Producing a superhydrophobic paper and altering its repellency through ink-jet printing,” *Lab on a Chip*, vol. 11, no. 5, p. 936, 2011.
47. H. Y. Erbil and C. E. Cansoy, “Range of Applicability of the Wenzel and Cassie−Baxter Equations for Superhydrophobic Surfaces†,” *Langmuir*, vol. 25, pp. 14135–14145, Dec. 2009.

Chapter 3 - Characteristics of Surface Topography Descriptors on worn Surfaces

In Chapter 2, surfaces were worn and their wetting characteristics and the topography behavior after each wear interval was investigated. Reported in this chapter are the surface topography descriptors. They will be evaluated in comparison to Chapter 2 results with respect to surface topography.

3.1 Introduction

Surface topography is a critical aspect of achieving superhydrophobicity, besides surface chemistry. When surfaces undergo physical changes with respect to topography, different wettability behavior is expected. To help ascertain the wettability changes, it needs to be related to topography changes. Topographical changes happen in various ways, like steepening of surface slope, which physical imaging e.g. SEM cannot describe properly. Hence, to properly describe topography quantitatively surface texture parameters have been defined in literature [1-8]. Surface texture parameters are mathematical way of describing different topographical aspects. Since describing topography is a complex process, a single parameter is ascribed to a unique aspect of topography e.g. maximum peak height, S_t, describes the highest point on the surface. A set of combinations of parameters is able to quantitatively cover the topography as comprehensively as possible. These topographical descriptors are now used as a standard to define surface texture [9]. Surface roughness parameters have been described on two and three dimensional (2D and 3D) basis. In 2D, roughness parameters are calculated over a single line measurement, while 3D parameters incorporate whole surface area. In this thesis, 3D surface parameters were calculated, as they are more realistic in describing the overall surface topography [1].

Surface roughness descriptors have found invariable use in literature (especially in tribology), e.g. wearing studies have been done on polymer surfaces [10-11], and surface roughness parameters have been used to describe roughness in relation to wetting [12-13]. The mapping of the surface texture has been typically done by both non-contact and contact methods, i.e. optical and stylus [14], presenting both strengths and limitations compared to each other. Confocal scanning microscopy (CSM) has gained traction in literature to monitor topographical changes in a non contact way [15-19]. Confocal profilometer prevents damage occurring to the surface, a potential problem with stylus measurement methods. Hence, CSM was used to quantify surface morphology in this thesis.

CSM mapped topography was used to compute surface roughness parameters. These parameters helped monitor topography changes taking place after a surface was worn for a wear interval. Hence, this quantitative way of describing topography was used to relate changes in topography with changes in CA. Since the wear was stochastic, as described in Chapter 2, hence the trends in roughness parameters are more important than absolute values.

Procedure for PTFE SHS fabrication, abrasion and subsequent surface topography data collection is documented in Chapter 2. The aim of this chapter is to see the behavior of surface topographical descriptors on worn surfaces, and if they can be used to describe wetting behavior of a liquid on a surface. Multitude of surface roughness parameters were collected, and their relevancy was examined; only select 3D roughness parameters were persisted with. This is one of the first study to investigate systematically various 3D surface roughness parameters on abraded SHS, and correlate with wetting characteristics.

Wetting on surfaces is directly related to the topography, and surface roughness parameters are a quantitative way to evaluate topography. Hence, the wetting characteristics will be overlaid and compared with wetting data to see, if the trends correlate to each other. One should also keep in mind that surface roughness parameters may sometimes be more accurate in predicting trends in an interval of wear, rather than the entire wear process. In this thesis, only individual (and not as a group or combination of parameters) roughness parameter trends were compared, for their ability to predict wetting.

3.2 Evaluating surface descriptor parameters

Various compiled surface descriptor parameters are evaluated in this section for their ability to describe topography. All the parameters were calculated according to their mathematical formulas given in literature [20-21], on the whole area topography mapped by CSM ($117.36 \times 94.9\ \mu m^2$). Chapter 2 outlined all the experimental details, the abrasion methodology followed, and how the topography was mapped. As a reminder again, the wear procedure on surfaces was stochastic, and hence sometimes trends will be more meaningful than the absolute magnitude of the parameters.

3.2.1 Average and RMS Roughness

Average roughness (S_a) is the arithmetic mean of the surface heights relative to the mean line. It is given by Eq. 3-1. Root mean square (RMS) roughness (S_q) is the root mean square roughness evaluated over complete topography (Eq. 3-2). In the underlying equations, Z(x,y) is the amplitude at (x,y) point relative to the central mean line, while *a* indicates whole surface area integral.

$$Sa = \iint_a |Z(x,y)| \; dx \, dy \qquad 3\text{-}1$$

$$Sq = \sqrt{\iint_a \left(Z(x,y)\right)^2 \; dx \, dy} \qquad 3\text{-}2$$

These parameters give an overall measure of the distribution of the topography. Both of these parameters remain indistinct in differentiating peaks or valleys, since only the height *magnitude* is considered in parameter, a valley will be "seen" as a peak. Also, a few outlier heights can bias both of these parameters heavily [12, 20, 21]. It has been documented that average and RMS roughness are not distinctive roughness parameters to help categorize topographies uniquely, and two different topographies can show similar value [12]. Also, both of these parameters are known to correlate strongly, with S_q having more significance in statistics as it describes standard deviation of the distribution of surface heights [3, 20]. Below, both average and RMS roughness for worn PTFE SHS have been investigated. As shown in Chapter 2, the peaks started to diminish as the surface starts to wear progressively, eventually resulting in flattening of the surface. Hence the average and RMS roughness should decrease too, as they are dependent on height magnitudes.

Figure 3-1 shows the average roughness trend of the surfaces. As can be seen, all the surfaces show the same trend for the average roughness. Figure 3-1 (a) shows the average roughness behavior of long term, 180 minutes, worn surface. Long term wear behavior follows the exact same trend as by other three surfaces (Sample 2, 4, and 5). Figure 3-1 (b) shows the average roughness behavior in the initial period of abrasion. It can be seen that the surface (Sample 3) follows the same trend, albeit the values have larger magnitudes than other samples and show a significant amount of error. As, can be seen Sample 3 shows a somewhat constant value of average roughness until starting 6 minutes of abrasion, and also a significant amount of error in this abrasion period. After this, the values show a consistent decrease according to trends for previous samples, with the error having decreased significantly.

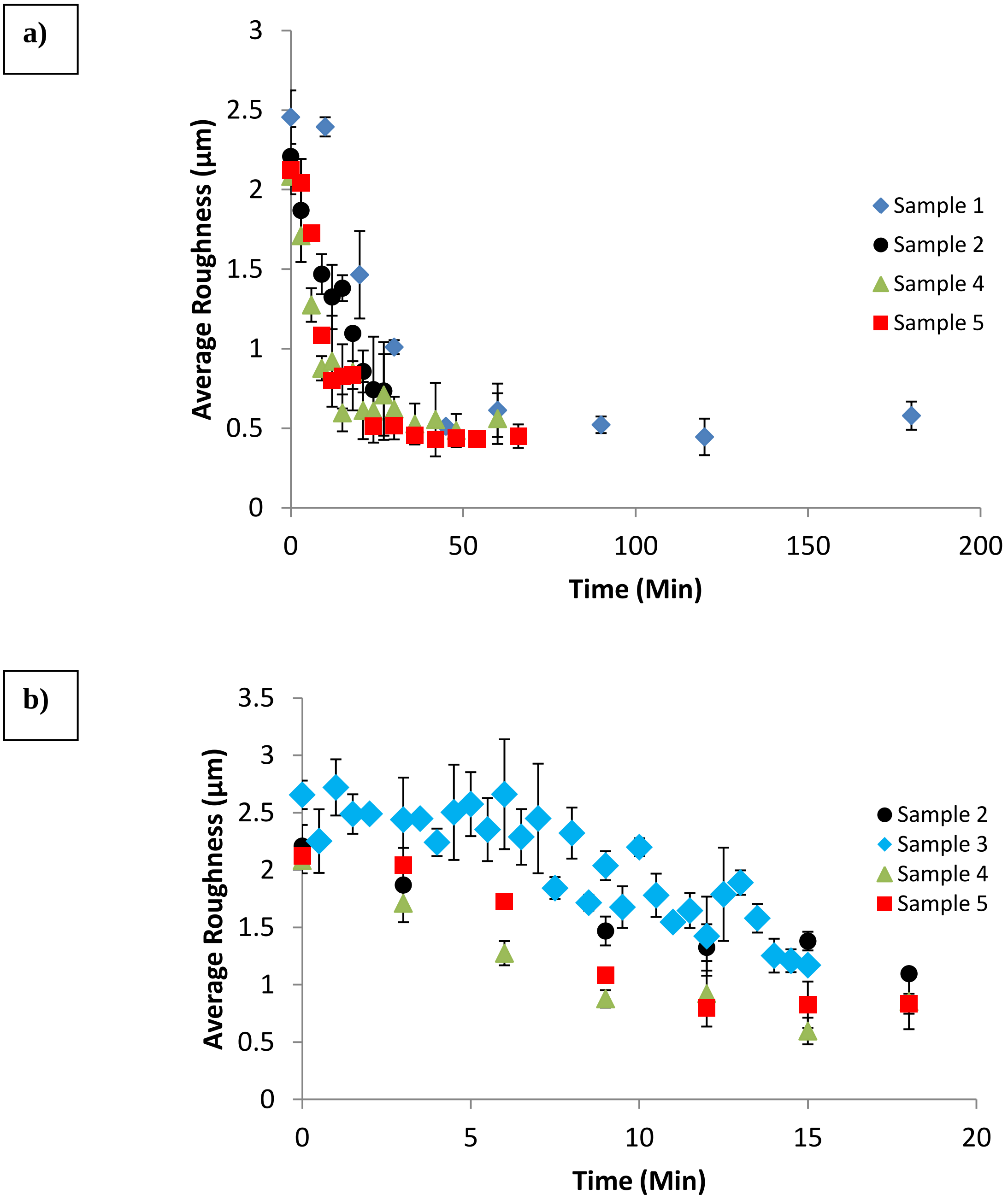

Figure 3-1: Average roughness for PTFE worn surfaces, a) showing the long term behavior, for a period of 180 minutes, and b) short term behavior in initial 18 minutes of abrasion.

As shown in Figure 3-2, average and RMS roughness follow the same trend with minor difference in magnitude, for the same surface (sample 2). This difference is (0.59 ± 0.07) for values upto 21 minutes, and (0.21 ± 0.01) for last two wear intervals (24 and 27 min). The standard deviations show the strong correlation between RMS and average roughness values. This correlation was observed for all the other surfaces too (Sample 1, 3, 4 and 5). This agrees with the literature [3, 20], and hence these values are analogous. Since, RMS roughness is more statistically meaningful, only it is used henceforth in this study.

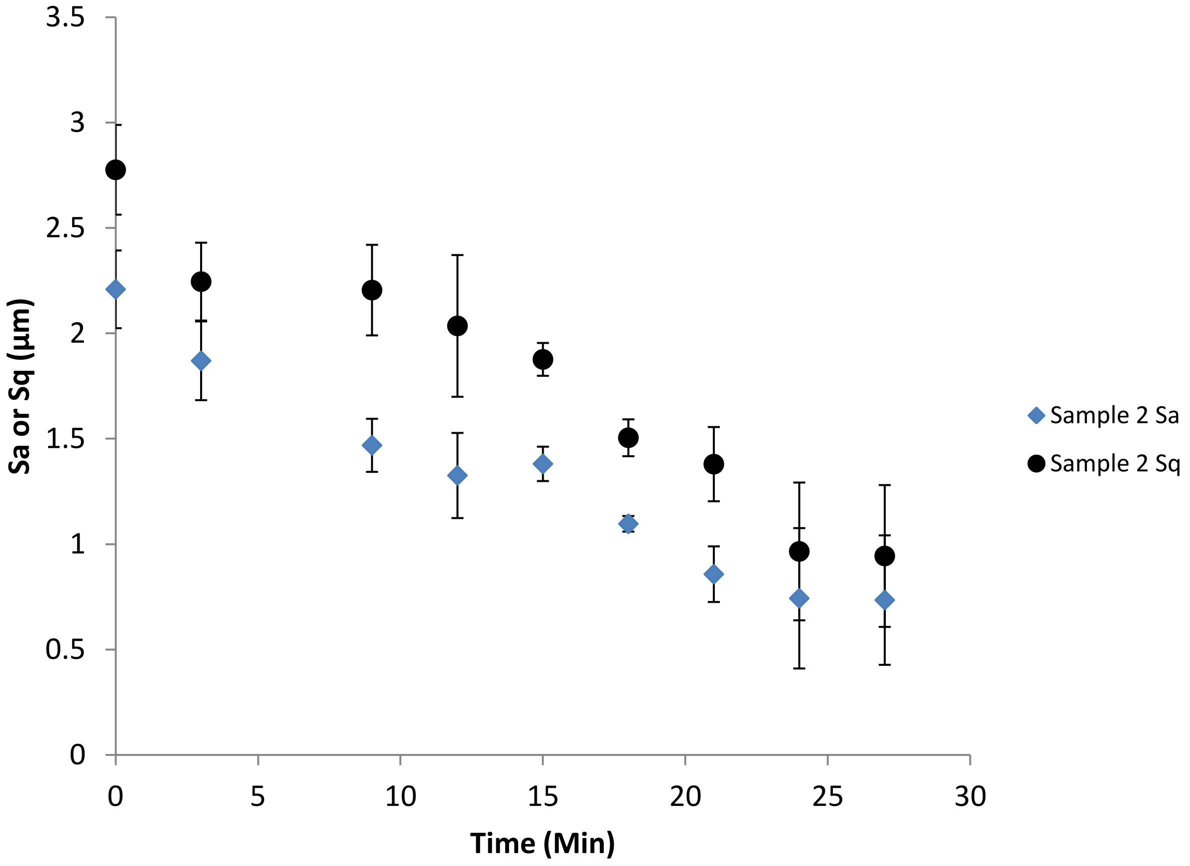

Figure 3-2: Comparing RMS and average roughness for sample 2. It can be seen that the trends for each wear interval are exactly the same.

Figure 3-3 (a) shows the RMS roughness behavior of the three surfaces abraded for under an hour, and also shows the long term wear behavior of one of the surface (Sample 1). Figure 3-3 (b) shows the behavior in initial period of abrasion. Magnitudes and error differ among different surfaces (Sample 1 – 5), but all the surfaces follow the same trend, notwithstanding the time period of wear. This shows that the abrasion among different surfaces was consistent, with varying amounts of error pointing towards stochastic nature of wear. Also, roughly the same magnitude of average and RMS roughness for unworn surfaces shows that the height distribution was nearly the same.

The slope for RMS roughness curve, shown in Figure 3-3(a), is decreasing roughly linearly until 24 minutes, and then it follows a very mild decreasing slope. For sample 2, SEM images in Figure 2-14 show that the surface was abundant with peaks until 18 minutes of wear time and the peaks were being shaved off progressively. The RMS roughness curve in Figure 3-3 (a) shows an aggressive decline for sample 2, showing that flattening of peaks is having an adverse effect on surface roughness as expected. Sample 2 surface has started flattening (peaks have diminished) at 24 minutes wear time (Figure 2-14f), and by 27 minutes peaks have totally flattened (Figure 2-14g). For sample 2, it is apparent in Figure 3-3 (a) that the RMS roughness value for 24 and 27 minutes wear time lie in close vicinity of each other. Also after 24 minutes the slope decreases in gentle manner than during the pre-24 minute wear time, for both sample 4 and 5. This is also validated by surface height data from CSM, as shown in Figure B-1 (f) for sample 4. At 27 minutes, the peaks distribution has diminished in relation to unworn peak surface distribution for samples 2 and 4. This analysis was shown with example of only one surface, but applies equally and similarly to all the other surfaces (sample 1, 3, 4 and 5). After abrasion for 30 minutes, since the surface has flattened, as expected the RMS roughness values remains constant for Sample 2, 3, 4 and 5 as shown in Figure 3-3 (a).

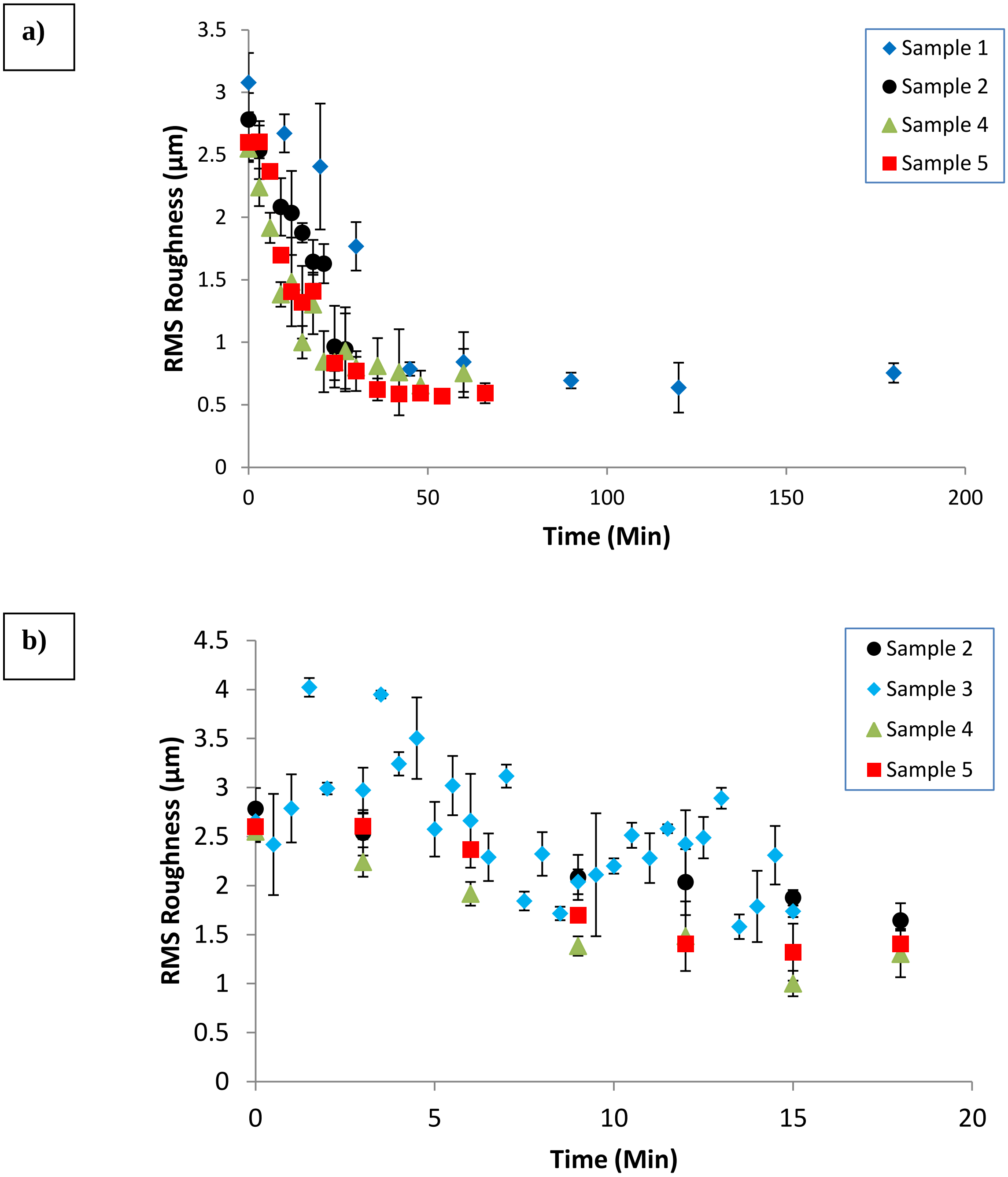

Figure 3-3: RMS roughness for PTFE worn surfaces, showing the a) long term wear behavior, of 180 minutes, and b) short term behavior in initial 18 minutes of abrasion.

Since one of the motives was to predict mobility by use of surface topography descriptors, by corresponding the RMS roughness data to wetting characteristics. Since, advancing CAs can be predicted with a degree of confidence using *popular* Cassie equation as shown in Chapter 2, only receding CAs were compared with various surface descriptors. RMS roughness shows the same trend for all the samples, but the mobility (rec. CA) for different samples is affected at different wear times for individual samples (Figure 2-23). Hence, maybe RMS roughness is not a suitable parameter to predict the CAH trend. To evaluate this idea better, CAH and RMS roughness were compared by plotting on same graph, for individual samples. Only 3 samples, worn for upto an hour were chosen, as the trends for all samples were same, but these 3 samples (2, 4 and 5) had consistent wear intervals. Resulting graph is shown in Figure 3-4 for Sample 2, while graphs for sample 4 and 5 are provided in Appendix B.2.1 (Figure B-3). In Figure 3-4, the CAH jump is at 9 min, and at 3 min the surface is in superhydrophobic state. RMS roughness values for both wear intervals (3 and 9 min) are nearly the same (2.24 ± 0.18, and 2.20 ± 0.21). Similar inconsistent correlation between RMS roughness and CAH was observed for Sample 4 and 5 (see Appendix B.2.1). Hence RMS roughness is not a strong indicator of mobility.

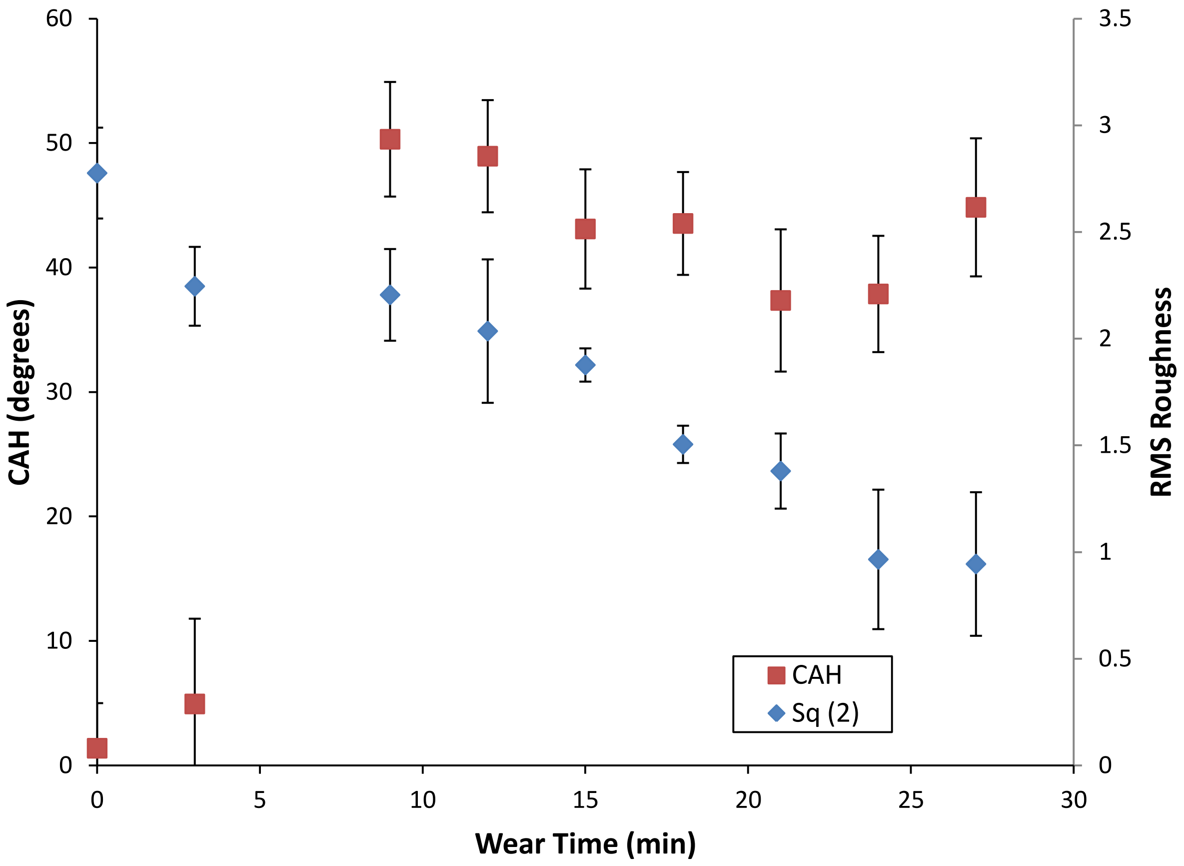

Figure 3-4: Comparing CAH and RMS roughness for sample 2.

Also, if comparing repellency (adv. CA) for the surfaces (Figure 2-23), advancing CA in nearly constant in the initial wearing period (until 9 min), and starts decreasing gently afterwards, with becoming constant afterwards (after 30 min). RMS roughness slope on the contrary does not align with this behavior. The slope is aggressively decreases in the initial wearing period, while advancing CA remains constant.

Hence, the RMS roughness is not an able parameter to be used as an indicator towards liquid mobility on surface. This is due to it being a general parameter, which is not determinate of any peculiar aspect of topography, rather gives a measure of height variations. Different topographies can exhibit same values of both average and RMS roughness parameters, and are not able to identify the topography uniquely. For example, a surface having peaks and its exact negative surface, containing valleys, will have the same average roughness and RMS roughness. Among themselves, RMS and average roughness are redundant parameters. Hence, to distinguish and characterize surfaces additional parameters should be considered.

Also, until now average roughness or root mean square (RMS) roughness has been at the forefront, and their use is nearly universal while describing topography, in majority of SHS literature [22-29]. As shown, they are ambiguous roughness parameters in relating to CAH, and also not fully sufficient to describe topography. Hence in this thesis various other 3D roughness parameters [20, 21] have been evaluated.

3.2.2 Skewness

Skewness (S_{sk}) measures the asymmetry of the profile about the mean line. Equation 3-3 is the mathematical representation of Skewness.

$$Ssk = \frac{1}{Sq^3} \iint_a \left(Z(x,y)\right)^3 \, dx \, dy \qquad \text{3-3}$$

Zero Skewness signifies perfect symmetry about the mean line, this is exhibited by a Gaussian surface. Surface having disproportionate number of high peaks will exhibit positive Skewness (a shaped surface), while a surface having predominant plateau with deep valleys will exhibit a negative Skewness (a honed surface). Figure 3-5 graphically illustrates Skewness for different topographies. It is sensitive to outliers (high peaks and deep valleys). Skewness describes shape of the surface height distribution [20-21]. Smallest S_{sk} value points towards a surface least dominated by peaks. Literature review in field of superhydrophobicity shows that this parameter has been used, albeit seldomly compared to S_a, to characterize surface topography [30-33].

Zhang *et al.* [33] used Skewness as a factor to correlate to antireflective property of superhydrophobic boehmite films. Bhushan *et al.* [30, 32] used Skewness to characterize difference between topography i.e. microbumps and nanobumps on various leafs. Kulinich *et al.* [31] used Skewness to monitor surface topography during icing/deicing cycles on superhydrophobic surfaces, and found that Skewness decreased as surface progressively became more flat. In this thesis, Skewness is used extensively to monitor surface topography and also its correlation with wetting.

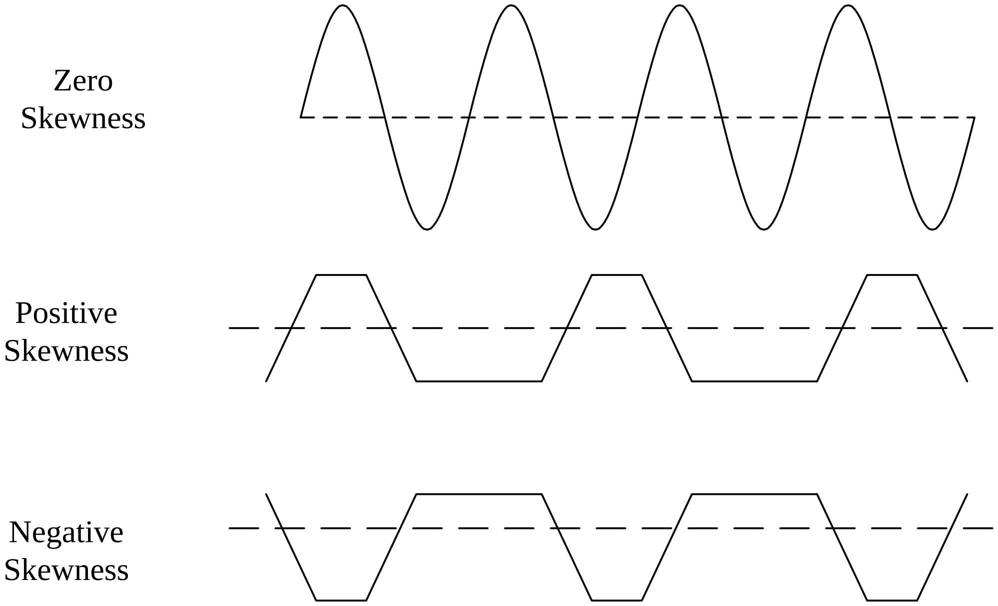

Figure 3-5: Schematic showing surface profile and the corresponding theoretical Skewness. The dashed lines serve as a visual guide to identify mean height values.

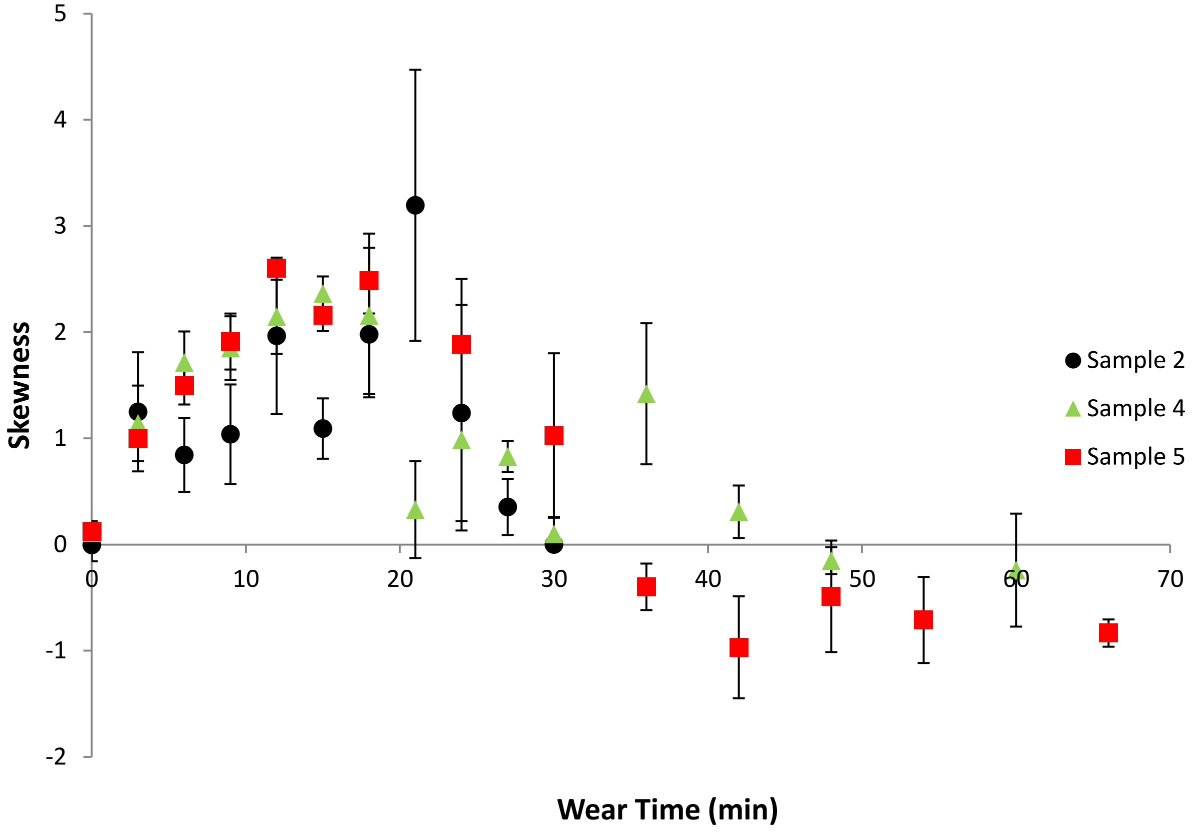

Figure 3-6: Evolution of Skewness as a surface wears. Error bars show the standard deviation in the parameter.

Figure 3-6 shows the graph of the evolution of the Skewness parameter for three surfaces (Sample 2, 4 and 5). It can be seen that the trend is same for all the surfaces. Large error in some values of Skewness can be due to its sensitivity to large peaks and deep grooves. Similar trend is shown by sample 1 and 3 (see Appendix B.2.2). In the discussion below, sample topography is evaluated with respect to Skewness behavior.

1) Starting value of ~0 for all the surfaces shows that surface height distribution is symmetric and not skewed. This can mean, surface is flat or surface has equal distribution of high peaks and low valleys. This observation can be supplemented using RMS

roughness data. Figure 3-3 (a) shows high RMS roughness for unworn surface (for all samples), which rules out possibility for a smooth surface.

2) As surface is wearing, Skewness increases positively showing that peaks are becoming scarce. As Figure 2-14 (a) (Also Figure 2-13 (b) and Figure 2-15 (b) for Sample 1 and 3 respectively) show that top of peaks are shaved off, flat plateaus start appearing, but valleys are not affected, as also shown in Figure 2-14 (b). This shows that Skewness should be positive, as peaks have decreased compared to initial surface. Skewness shows positive slope until 20 minutes and is highest at this point, showing high random distribution of peaks.
3) After 24 minutes, Skewness decays indicating scarce peaks than before, and increasing plateaus. Figure 2-14 (d) (and Figure 2-13 d) show that this is indeed the case.

Skewness can be divided in three regimes, as shown in Figure 3-7. Regime 1, when wear is starting and peaks are aplenty until 9-12 minutes. This also shows us that majority of peaks are able to resist abrasion until 9 minutes, as shown in Figure 2-14 (b) and Figure 2-15 (b). In this zone Skewness is continuously increasing. Regime 2 has more random disproportionate distribution of peaks and large flat patches are on surface until 21-24 minutes, as shown in Figure 2-14 (c) and Figure 2-15 (c). Skewness in this region increases mildly and then starts to decrease. Regime 3 signifies the region when peaks are decaying and surface is becoming flattened, as illustrated by Figure 2-14 (d) and Figure 2-15 (d). In regime 3, with increasing wear time surface becomes completely flat and long wavelength features of surface topography dominate. This leads to Skewness being near zero but on negative side signifying plateaus with insignificant number of valleys. In Figure 3-3 (a) until 21-24 minutes, i.e. regime 1 and 2 for Skewness, RMS roughness shows negative slope. After 24 minutes, i.e. regime 3 for Skewness, RMS roughness has almost constant slope in Figure 3-3 (a). Absolute values of Skewness should not be used to predict the regimes, as shown in Figure 3-6, sample 4 Skewness values at 3 and 24 minute of abrasion are nearly same although topographies are different. Hence, magnitude alone should not be used to predict the Skewness regime, rather evolution of the parameter should be known. So a change in slope of Skewness curve can help distinguish regime change, and how the wear is affecting the surface (i.e. surface topography).

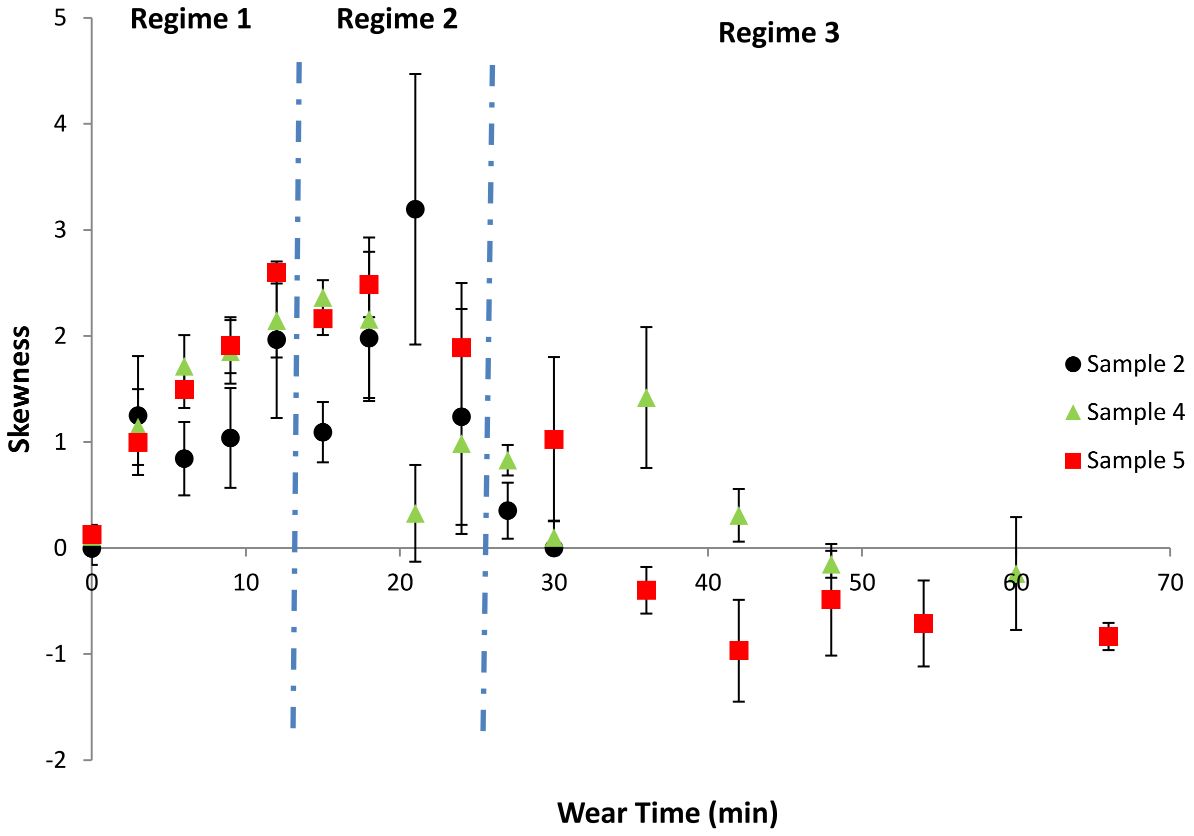

Figure 3-7: Skewness evolution and regimes for PTFE worn surfaces. Error bars show the standard deviation in the parameter. Dash dotted line is a visual guide to elucidate the regime boundaries.

Skewness is now compared to CAH data, and if any regimes can indicate the mobility on the surface. Figure 3-8 compares the CAH with Skewness values for sample 2, 4 and 5. Comparing

CAH in regime 1 (discussed previously), sample 2 and 4 lose superhydrophobicity while sample 5 still retains it. In regime 1, until 9 minutes, Skewness was increasing, with surface having plenty of peaks. In regime 2, from 9 to 24 minute, all the surfaces definitely saw an increase in CAH. Hence, seeing CAH behavior in regime 3 is redundant since liquid mobility has been lost previously in regime 2. Sample 4 Skewness increased until 18 minutes, while CAH rose at 6 minutes. Sample 5 shows CAH and Skewness increase at and until 21 minutes. This observance can help predict the region where the surface liquid mobility will be lost, but by looking at slope of Skewness curve. CAH displayed at 6 and 66 minutes for sample 5 is different, but the Skewness magnitude is roughly the same.

a)

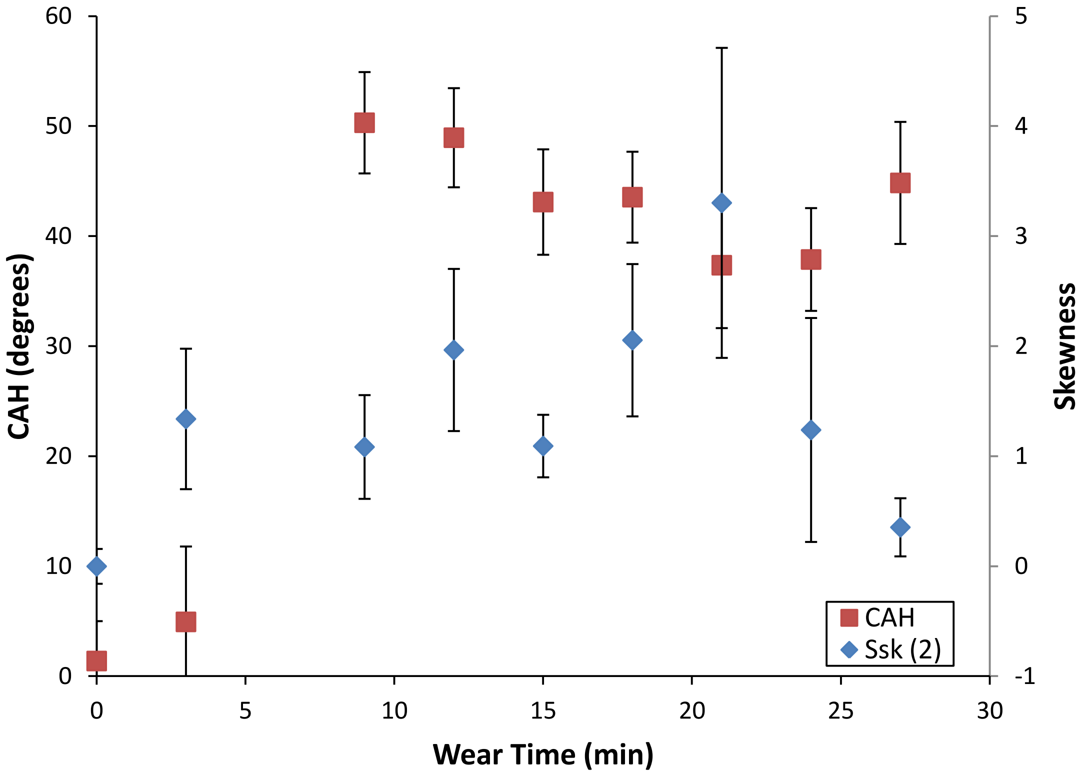

(Continued on next page)

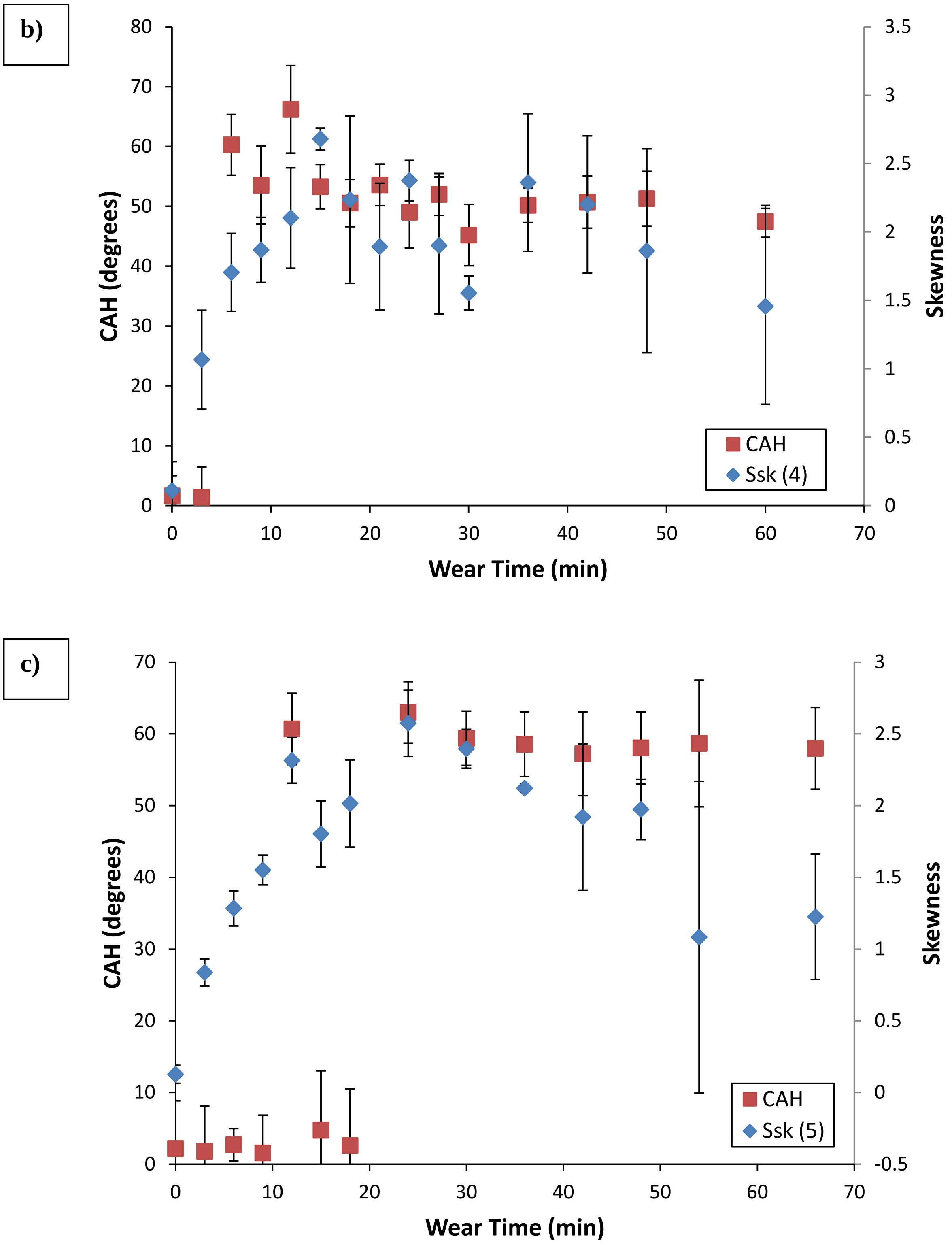

Figure 3-8: Comparing Skewness to CAH for samples (a) 2, (b) 4, and (c) 5.

The point of interest here is the Skewness at the wear time when the CAH was lost for different surfaces. Looking at the different Skewness-CAH comparison curves, it can be seen that CAH is lost when the slope of Skewness curve is still increasing (regime 1 and 2). Sample 2 Skewness increases until roughly 21 minutes, while CAH increased at 9 minutes. Similar inconsistent behavior for RMS roughness and CAH correlation was seen for samples 4 and 5. Hence, Skewness magnitudes in solitude cannot be used as a good predictor of the surface CA behavior, although Skewness curve slope can be used to predict the zone where the surface has high probability of losing liquid mobility.

For sample 2, SEM images in Figure 2-14 and CSM data in Figure 2-16 (Figure B-1 for sample 4) show that topographies at 3 and 24 minutes are different, although Skewness magnitudes are nearly same. Same observations can be made for other samples too, i.e. different topographies show same Skewness magnitudes. To distinguish between different wear times, corresponding RMS roughness data should be taken into account. Also, the Skewness evolution as a whole should be considered to gauge the predominance of peaks or valleys on topography, and slope should be used to determine wear condition on the surface. Exact observation of CAH jump points is difficult, due to the nature of the undertaken study, but Skewness curve slope is also helpful in predicting liquid mobility decrease zone.

3.2.3 Kurtosis

Kurtosis helps evaluate “peakedness” or “flatness” of the surface profile relative to normal distribution. A surface having normal distribution (Gaussian) has Kurtosis of 3, while surface with many high peaks and deep valleys shows Kurtosis greater than 3, and a surface with few peaks and valleys shows Kurtosis less than 3. Spread of surface height distribution can be characterized by Kurtosis. Equation 3-4 shows the mathematical representation of Kurtosis. Figure 3-9 illustrates it graphically.

$$Sku = \frac{1}{Sq^4}\iint_a \left(Z(x,y)\right)^4 \, dx \, dy \tag{3-4}$$

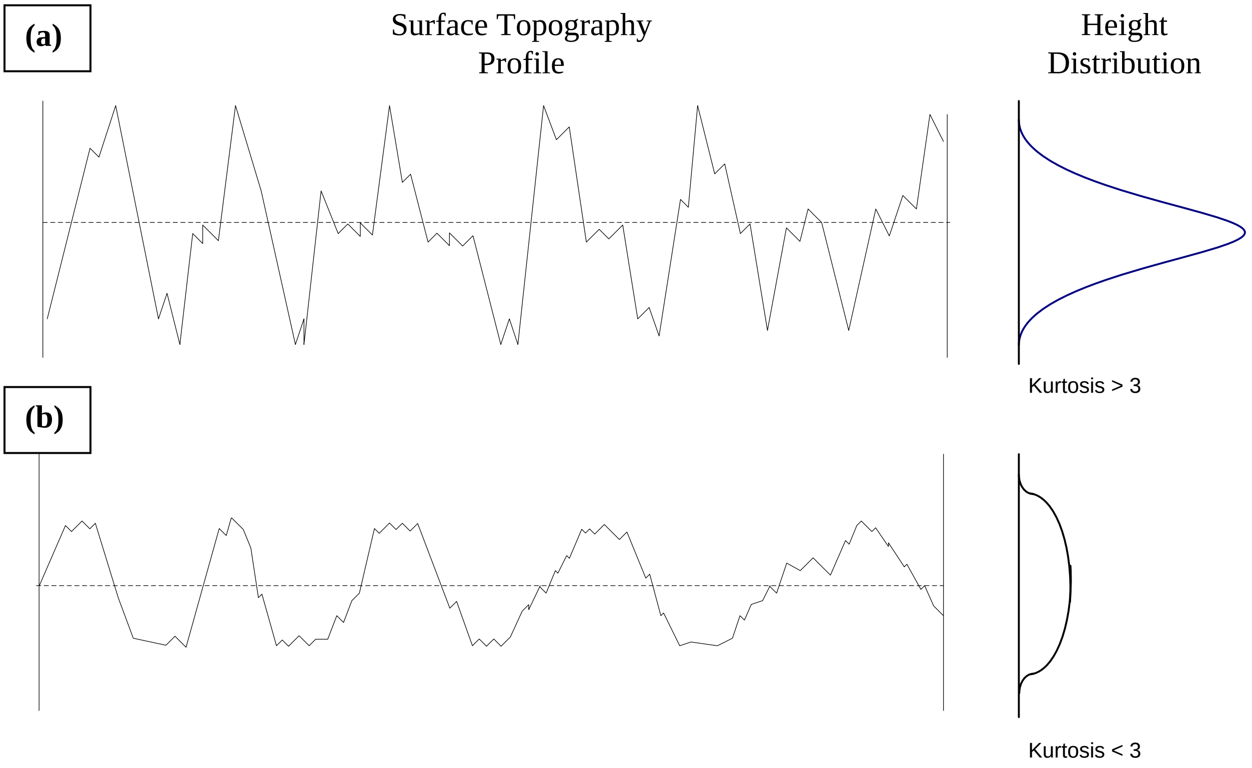

Figure 3-9: Schematic showing surface topography and corresponding Kurtosis. The height distribution curve in (a) is leptokurtic (“skinny”) distribution, while (b) has platykurtic (plateau like) distribution. The dashed line represents the central line average of the surface heights. Adapted from [20].

Figure 3-10 shows the Kurtosis of surfaces as they are worn. As can be seen, all the surfaces follow the same trend. Kurtosis trends for sample 1 and 3 are shown in Appendix B.2.3. The trends remain consistent in the initial minutes of wearing for all samples (Figure 3-10), and also as a surface is worn for long and short time duration (Figure B-6).

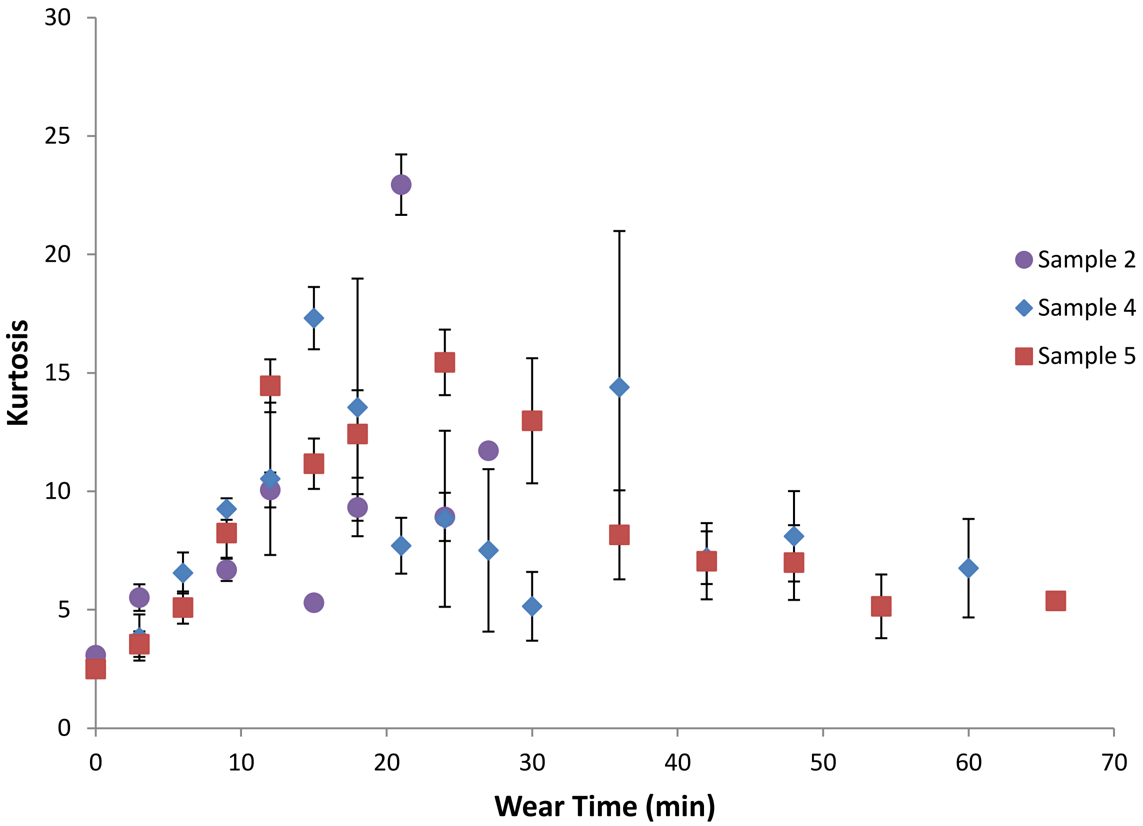

Figure 3-10: Evolution of Kurtosis as a surface wears. Error bars show the standard deviation in the parameter.

Also, the regimes 1, 2, and 3 as defined in Skewness section are transferred over to Kurtosis for comparison. If the Kurtosis values do not give reasonable and defined trends in these regimes, new regimes will be defined for Kurtosis. Large error in some values of Kurtosis can be due to its sensitivity to outliers and spikes. As the trends for all samples are the same, with minor variation at times, only sample 2 trend is discussed below.

1) Kurtosis value for the surfaces is increasing unequivocally in regime 1 (as defined in Skewness section), as it should be because of presence of high peaks on the surface. In regime 1, contact angle hysteresis remains nearly constant at ~3°. Also, from SEM

images for sample 2 (Figure 2-14), the majority of the area is still covered by peaks and valleys in regime 1. Height distribution histograms in Figure 2-18 show that the peaks although not dominant are a significant portion of the heights on the surface, and the height distribution is showing increase in “spikiness”, implying that Kurtosis will be increasing in this regime.

2) As the wear enters regime 2, all the peaks are getting affected and their height is decreasing which affects the Kurtosis and it is wavering, but can be seen as nearly constant. The standard deviation in this regime is very high, illustrating the locally varying nature of topography at different points when the peaks have started to become affected. SEM images Figure 2-14 (b), (c) and (d) physically show the topography change in this regime. CSM data in Figure 2-16 (c) and Figure B-1 (c) illustrate the onset of the regime, and the topography difference is apparent in Figure 2-16 (f) and Figure B-1 (f) with majority of peaks being flattened.
3) In regime 3, Kurtosis decreases as the plateaus on the surface are increasing, and becomes nearly constant as wear time increases. The slope in this regime is mild, contrary to the slope in regime 1. This is because the majority of peaks have been flattened, as they are the parameters that affect Kurtosis. Also, wetting data in Figure 2-23 (both adv. CA and rec. CA) shows a very gentle slope in this regime, with a tendency to remain constant, showing that topography has already undergone majority of the changes in previous wear time.

Kurtosis never shows a value below 3, as can be seen from surface topography histograms (Figure 2-18 and Figure B-2) that the shape characteristics of height distribution never strictly achieves a platykurtic shape, but instead retain the “pointy” shape. Figure 3-11 show the CAH and Kurtosis comparison on the same graph. As can be seen CAH is lost in regime 1 for sample 2 and 4, while in regime 2 for sample 5. Also, when the CAH increases the Kurtosis values for all the samples are different. Kurtosis for sample 2 was (6.63 ± 1.34), sample 4 (6.21 ± 0.77), and for sample 5 (11.70 ± 2.41). Besides, for sample 2 (Figure 3-11) there is not a significant variation at the point where hysteresis jumps by a large amount (9 min).

a)

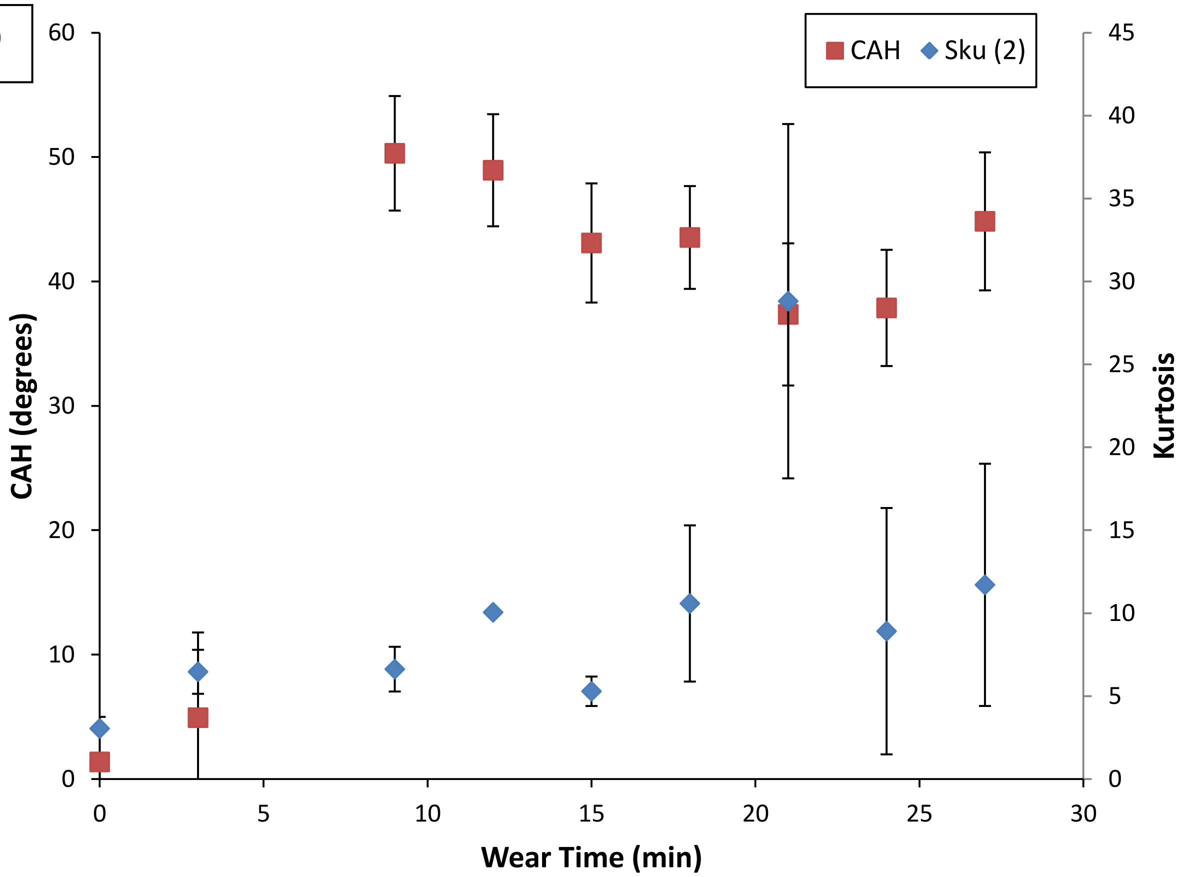

(Continued on next page)

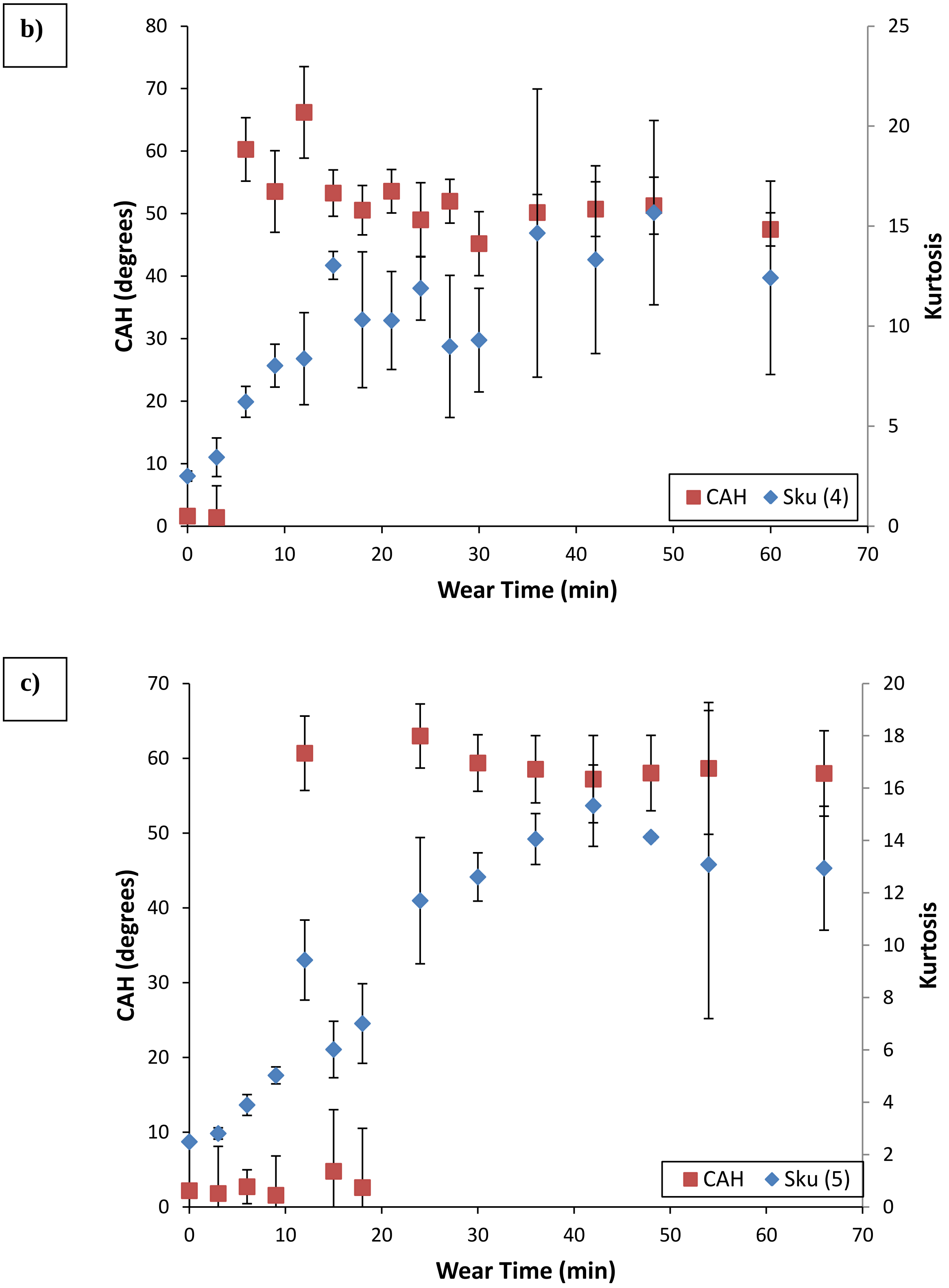

Figure 3-11: Comparing Kurtosis to CAH for, (a) Sample 2, (b) Sample 4, and (c) Sample 5.

This shows that predicting liquid mobility on the surface based on magnitudes is considerably difficult; instead zones can be known where liquid mobility is reduced. The zone is typically while Kurtosis value is increasing i.e. regime 1, and sometimes during initial wear time in regime 2. These regimes can typically be identified by change of slope of the curve. Skewness and Kurtosis align up with each other (in terms of regimes), and can supplement each other. The hindrance is that given the value for both of these parameters, one will not be able to identify the regime (1, 2, 3, etc.) without using any other quantitative method (height profile or SEM). This is due to the fact that certain values for both Skewness and Kurtosis are prone to fall in all three regimes. Hence, a combination of RMS roughness, Skewness and Kurtosis will be able to roughly predict the regime the surface is in, and also be able to predict the topography of the surface. This agrees with King *et al.* [34], that this set of parameters is most suitable to characterize height profile of the surface. Note that the study in [34] did not study concern with wetting but with surface metrology research. Evolution of all the parameters should be considered, and a prediction should not be made based upon magnitude of parameters alone.

In their present individual form, both Skewness and Kurtosis are unable to predict either CAH with a degree of confidence, but instead a rough estimate is possible. Various roughness descriptors can be combined and computed as a group to gain a complete understanding of wetting characteristics. Also, an empirical relationship can be found between various surface roughness descriptors such that it corresponds to change in wetting characteristics.

3.2.4 Other Height Parameters

Parameters discussed earlier (RMS roughness, Skewness and Kurtosis) are typically classified as amplitude parameters, that are able to define height distribution of the topography. Other height parameters in this group are (a) Maximum peak height (S_p), (b) Maximum valley depth (S_v), and

(c) Maximum height of the surface (S_z). For graphs and analysis of these parameters, refer to Appendix B.2.4.

These three parameters are not informational and statistically significant, since they are singularities on the topography and tend to be not repeatable. If topography contains outliers, the values reported can be misleading. Hence, these parameters were not considered in this thesis.

3.2.5 Hybrid Parameters

Hybrid parameters are a family of surface descriptor parameters that help in characterizing topographical amplitude and spatial information [35]. Slope of the surface, curvature of the peaks, interfacial area, summit density is some of the information gained from these parameters. Evaluating hybrid parameters can be beneficial as spatial spacing of peaks is important criteria for superhydrophobicity [36-39].

The parameters in this family relevant to this study are:

(a) RMS Surface Slope (S_{dq}): It is a measurement of slopes on the topography, and can be used to differentiate surfaces having same average or RMS roughness. Surface amplitude and spacing mutually affect S_{dq} value. Mathematical representation of Sdq is given by:

$$Sdq = \sqrt{\frac{1}{L_x L_y}\int_0^{L_x}\int_0^{L_y}\left(\frac{\partial Z(x,y)}{\partial x}\right)^2 + \left(\frac{\partial Z(x,y)}{\partial y}\right)^2} \qquad 3\text{-}5$$

(b) Summit density (S_{ds}): It is defined as number of peaks per area for a given texture. A point above all of its nearest neighbors is considered a peak in here. In this study, since topography is evaluated as a heightmap, so a peak is a local maxima among 8 immediate neighboring height pixels. A high summit density can reflect high number of peaks points available for the liquid drop, while a low summit density can be a detriment towards high liquid mobility. This parameter can help developing an optimum density of peaks necessary for superhydrophobicity.

(c) Mean summit curvature (S_{sc}): This parameter averages the curvature of each summit over whole area. Summit curvature can help in determining the wear on the surface, as peak points are immediately affected on a texture. The curvature is defined as:

$$Ssc = \frac{1}{N}\iint_{Summit\ Area} \{\left(\frac{\partial^2 z\,(x,y)}{\partial x^2}\right) + \left(\frac{\partial^2 z\,(x,y)}{\partial y^2}\right)\} dxdy \qquad 3\text{-}6$$

Figure 3-12, Figure 3-13 and Figure 3-14 show these parameters graphically, on each wear duration for sample 2, 4 and 5. RMS surface slope (Figure 3-12) shows a continuous decrease, akin to RMS roughness graph, with a high degree of error in the measurements until 30 minutes of wear. Since the starting surfaces have finely spaced peaks, so the texture slope in general direction will be in fact high. The high degree of error points towards the highly anisotropic nature of texture. As the surface peaks decrease, the features start to become widely spaced and hence the RMS slope also shows a decrease. This parameter cannot be used to provide mobility correlation, since the trend is same as RMS roughness, and all the samples follow the same trend but CAH jump times for these samples were different. This parameter can be used to predict the anisotropic and isotropic nature of topography, as shown by initial values and high error compared to final flat surface values and low error.

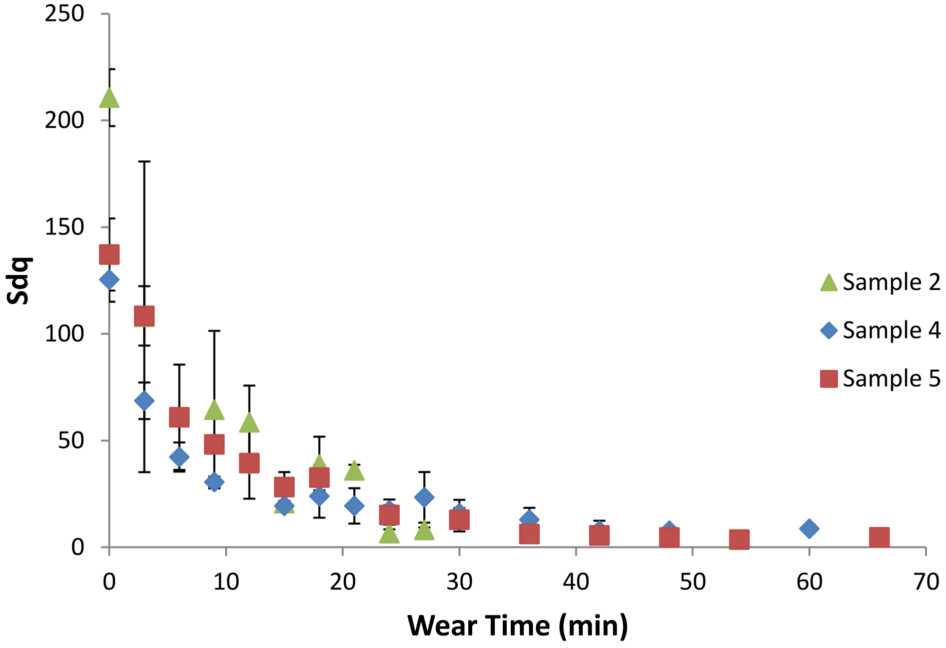

Figure 3-12: Evolution of RMS surface slope (S_{dq}) as a surface wears. Error bars show the standard deviation in the parameter.

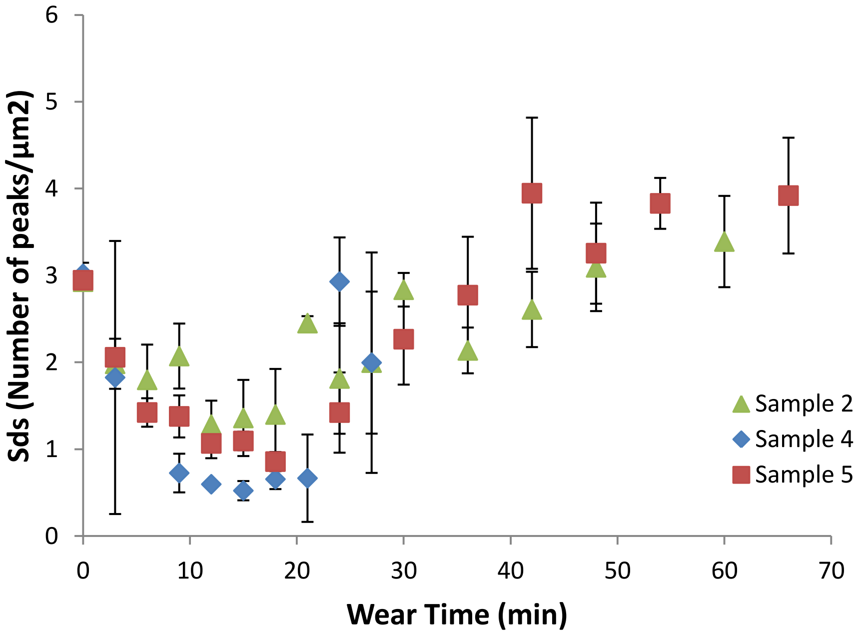

Figure 3-13: Evolution of summit density (S_{ds}) as a surface wears. Error bars show the standard deviation in the parameter.

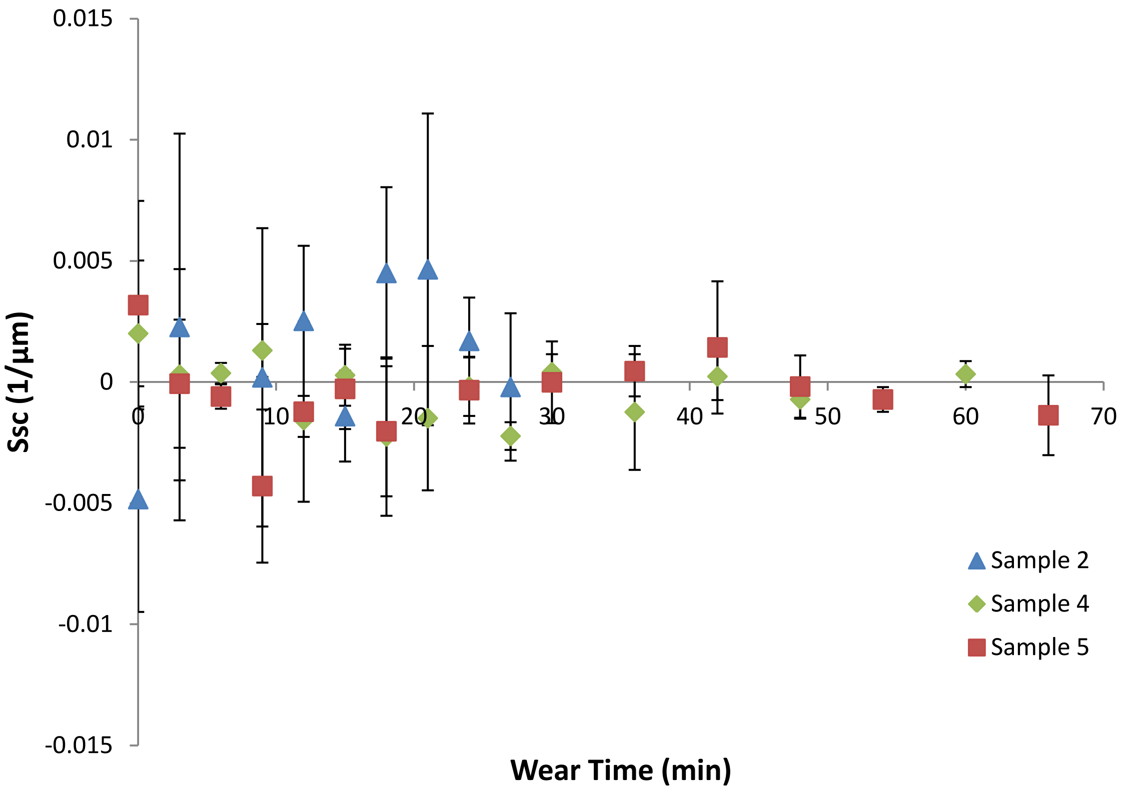

Figure 3-14: Evolution of mean summit curvature (S_{sc}) as a surface wears. Error bars show the standard deviation in the parameter.

Summit density, as plotted in Figure 3-13, shows an interesting trend. Initial number of peaks is high, and as expected continues to decrease with increasing wear on surface until 21 minutes. After that it shows an increasing trend. The decreasing trend is expected, and manifests the findings of Chapter 2. The increasing trend is because of the definition of the peak. Since after 21 minutes the surface is majorly flat and the peaks, as defined here, will increase as the surface progressively flattens more. The major wavelength of the surface also contributes towards this increasing number of summit density. Hence, the valid region to be considered is until the values starts rising. Initial high value is immediately affected as shown by 3 min wear interval, suggesting peaks decrease immediately. CAH jump time for sample 2 was 9 minutes, sample 4 was 24 minutes and for sample 5 was 6 minutes. The respective summit densities at these wear times are all different, suggesting the correlation with liquid mobility on a surface might be weak. Sample 4 values from 9 minute onwards show nearly constant value; hence an optimum value of summit density conducive to high liquid mobility cannot be suggested. Additionally, high summit density might also suggest an increased number of pinning points for the drop, compromising liquid mobility on the surface. Combining summit density with RMS slope can tell about the behavior of the surface topography, but high error in RMS slope prevented the analysis.

Summit curvature can predict the available contact area. Figure 3-14 plots summit curvature for various samples. As can be seen, the data has large error for all of the wear intervals. The error can be a result of definition of the peak and sampling interval, where a number of false peaks can be identified as described in literature [40-42], and no meaningful result can be discerned from this data.

Hence, hybrid parameters in solitude are not able to add any meaningful spatial information, but can be used in conjunction with other roughness parameters to gain a better understanding of the surface topography.

3.2.6 Functional Parameters

Amplitude parameters discussed in earlier sections give general description of the topography, giving the height variation of the structures. Functional parameters are used to characterize functional properties of the surface [3, 21]. The functional properties of the surface include material and void volume that is enclosed by the contacting surface of the material, this can help in evaluating the how wear will affect the contacting surface, and the fluid retention capability of the surface. Functional properties are important to find out for the purpose of this study as they can give a measure of liquid that would be in contact with peaks after each wear interval. Hence, they can be used as a secondary measure of finding penetration depth on surfaces. The parameters calculated in this section are, (a) Reduced peak height (S_{pk}), (b) Core roughness depth (S_k), (c) Reduced valley depth (S_{vk}), (d) Peak material portion (S_{mr1}) and (e) Valley material portion (S_{mr2}).

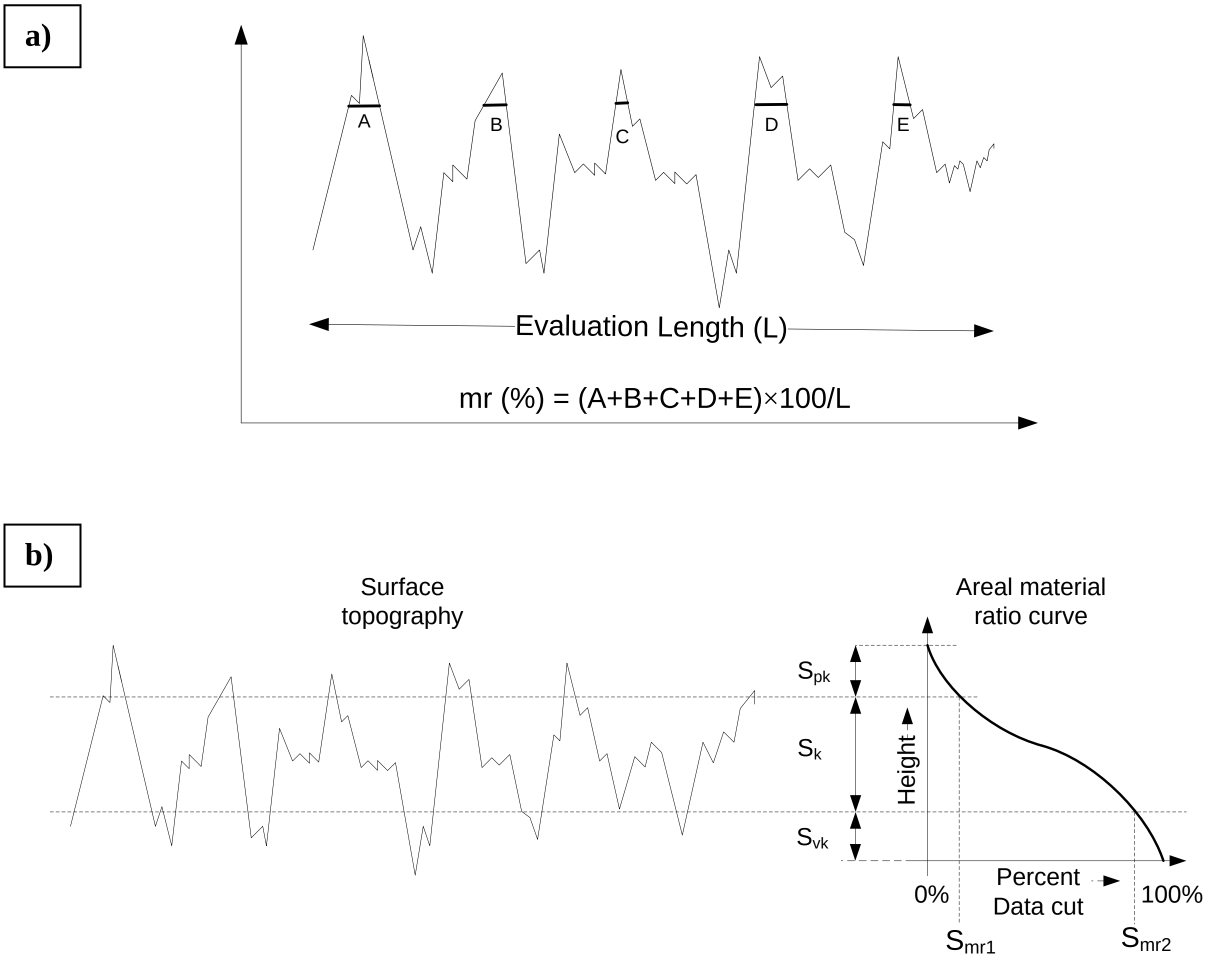

Figure 3-15: (a) Illustration showing how material area ratio is calculated on a surface topography, and (b) schematic of the calculation of parameters showing the surface topography and corresponding material ratio (mr) curve.

Figure 3-15 illustrates how these parameters are calculated on surface topography. Material ratio parameter (Figure 3-15 a) is a parameter that helps simulate the wear taking place on a surface by providing a bearing surface for the abrading material. Material ratio is calculated by visualizing a flat lapping plate (parallel to the horizontal datum) resting on the peaks. As the peaks are abraded, the flat lapping plate moves down the topography hence increasing the contact surface. The material ratio (also referred to as "percent data cut") is expressed as ratio of the contact area (bearing length) to the evaluation cross sectional area, and is expressed as percentage. Limitations of material ratio include: (a) It ignores surface topography of the abrading material, and (b) the crests are truncated by a straight line making it an unrealistic possibility. Despite these limitations, material ratio curve can still help gauge the performance of the surface topography and can be correlated to wear performance. Hence, this section is devoted to finding correlation between surface topography and these functional parameters.

Figure 3-15 (b) illustrates various functional parameters, based upon material ratio curve. The highest point and lowest point in the topography forms the height bounds of material ratio curve. Height corresponding between 10% and 90% of the percent data cut, is called the core roughness depth (S_k). It signifies the topography stripped off its peaks and valleys, where the significant material percentage of a surface lies. Reduced peak height, S_{pk}, is a measure of the peak height above the core roughness depth. It signifies the contact area available for a liquid, solid, abrader etc. when coming in initial contact with the surface. S_{Mr1}, peak material portion, represents the peak material area percentage associated with S_{pk}, and signifies the percentage of the surface material prone to be removed during initial period of wear. Reduced valley depth, S_{vk}, is a measure of the valley depth below the core roughness representing the nominal height of the material which can entrap material detritus and fluid. Valley material portion, S_{Mr2}, is the percentage of the surface (i.e., 100%-S_{Mr2}) comprising of deep valleys associated with S_{vk} [21].

Figure 3-16 shows the parameter evolution with increasing wear time for all the surfaces. Long and short time wear evolution of parameters for sample 1 and 3 is shown in Appendix B.2.4. It can be seen that trends for all the samples is the same, and even the long and short term wear agrees with the general trend for other surface (Sample 2, 4 and 5).

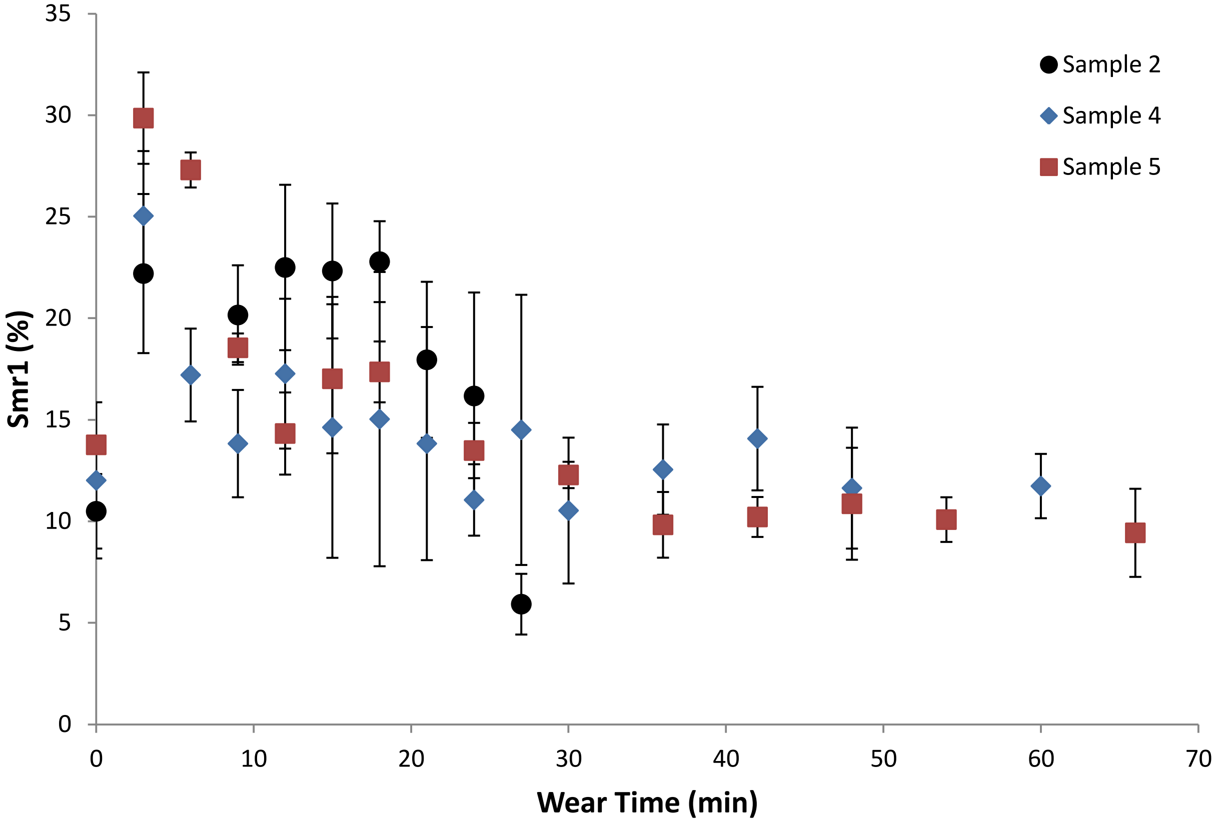

Figure 3-16: Evolution of S_{mr1} as a surface wears. Error bars show the standard deviation in the parameter.

If penetration depth is determined, S_{mr1} can give insight into the *projected* surface area the liquid may come in contact with. This can directly help compute the *popular* Cassie equation parameter, *f*, and help predict CAs. The S_{mr1} increases immediately after the first period of wear on the surface, and then progressively decreases until it achieves a nearly constant value of 10%. The initial jump in the value signifies the sawing of the peaks during initial wear. The peak tops are abraded, exposing a flat surface (Figure 2-15 b-f), hence the 10% depth cut for calculating material ratio is deep into the surface which carries more bearing length weight than the upper portions of the peaks. This also points towards dense needle like geometry of the peaks, where the peak portions at the top carry considerably less weight and when the tops are abraded it leads to massive jump in contact area for the abrading material. Trend from 3 minute onwards, is that of a progressive decrease in peak material percentage. The trend was expected as the peak circumference has nearly squared after initial wear, and further wear just keeps on decreasing the number of peaks and increasing the plateaus. This results in decrease of the material percentage. As can be seen the S_{mr1} values have a lot of error in them, hence, computing projected area through S_{mr1} can introduce significant error affecting CA predictions. Additionally, CSM software can compute the projected area without any difficulty, so it is redundant to calculate projected surface area through S_{mr1}. Also, S_{mr1} in its present form is not useful, because as the wear increases liquid touches more than the upper 10% of the peak areas and hence S_{mr1} remains ill equipped to predict the projected surface area in contact with the liquid. Hence, this approach was not followed. S_{mr1}, can be used as a way to understand topographical features, for e.g. wear on a regular geometry rectangular topography will result in S_{mr1} having little variations between wear times.

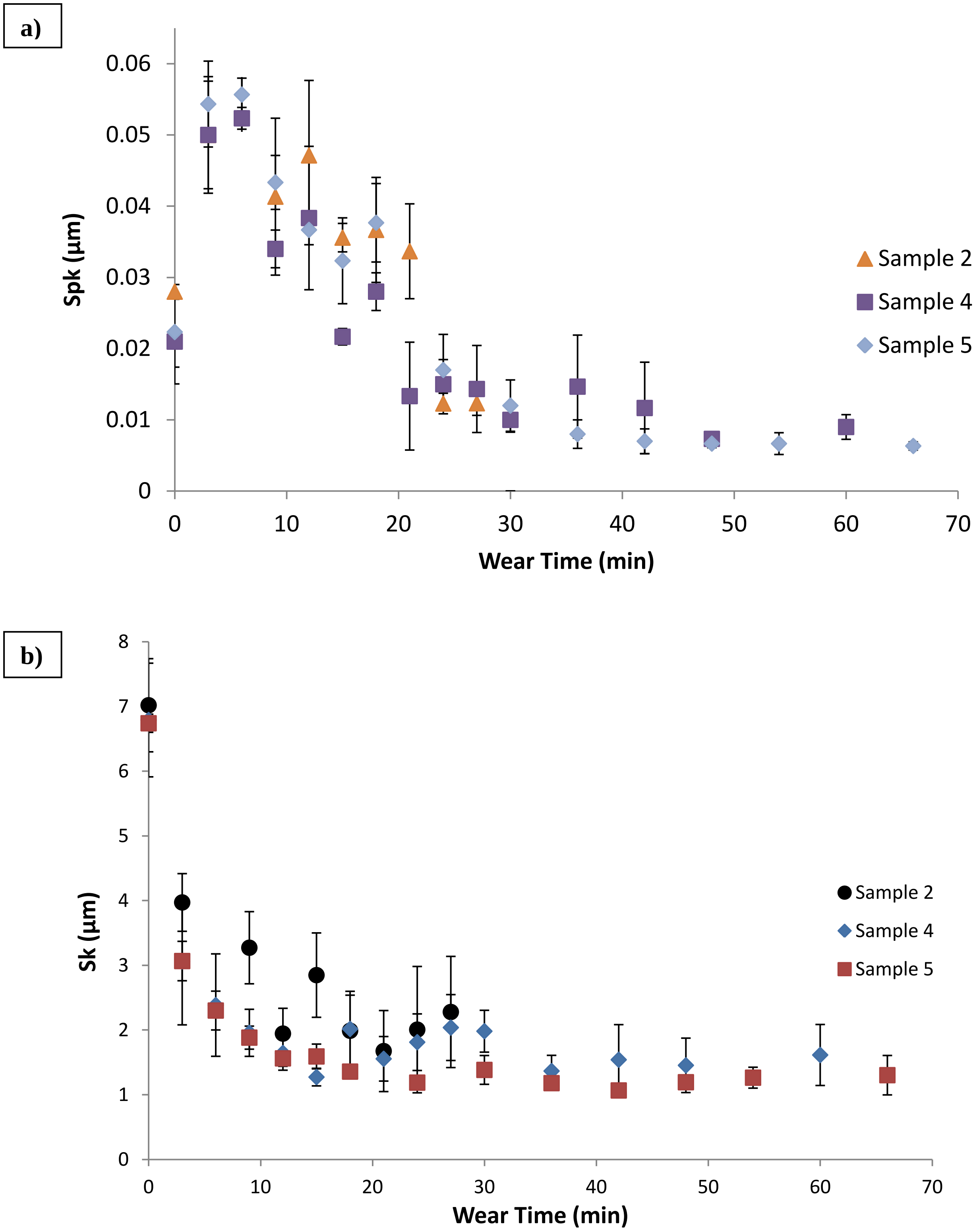

Figure 3-17: Evolution of, (a) S_{pk}, and (b) S_k, as a surface wears. Error bars show the standard deviation in the parameter.

S_{pk} and S_k (Figure 3-17) combined may help in determining the penetration of the liquid into the surface asperities. S_{pk} and S_k combined help in determining the bulk depth (Peak and core of the surface without the valleys) of the material, and potential asperity depth available to a liquid for penetration.

Figure 3-17 shows the evolution of various roughness parameters. Short and long term wear effect on both S_k and S_{pk} are shown in Appendix B.2.4. The trends for all the samples are the same, for all the parameters. S_k and S_{pk} follow the same trend as S_q, and decay slowly as expected due to wearing surface topography and hence decreasing of peak heights. The jump at 3 minutes for the S_{pk} is due to its relation with S_{mr1}. If a peak is assumed to be conical, the material ratio will keep on increasing as the frustum (top of the peak which is now flattened due to wear) distance decreases due to widening of the base. Hence the value of S_{pk} is directly affected. S_{pk} can be used in predicting liquid penetration into asperities. The limitations are non availability of real water penetration depth data to corroborate with, and the magnitude of the S_{pk} being almost negligible (maximum being 0.055 ± 0.002 µm). This can also signify that the surfaces contains an insignificant number of high peaks or outliers which brings down the S_{pk} magnitude. Hence, S_k can be a good predictor of the penetration depth, which represents majority of the peak heights since magnitude of S_{pk} is considerably small. But, predicting penetration depth with S_k can be a speculative task as it represents all of the bulk height, and does not give any specific penetration depth but a range of the surface heights. Hence, S_k also is not useful in helping to predict drop mobility.

Comparing the penetration depths that were predicted by popular Cassie equation in Chapter 2, to S_k values at the CAH jump points. The absolute penetration depths are given in Table 2-1 while Figure 3-17 (b) gives S_k values.

From Chapter 2, sample 4 absolute penetration depth of 1.11 µm gave a good comparison for theoretical Cassie angle with advancing angle. Hence from the S_k values (Figure 3-17 b) after 24 minutes of wear, drop has penetrated nearly 35% - 85% of the asperity depth, rendering it immobile. For sample 2, at 9 minutes of wear drop has penetrated 30% - 42% when the liquid mobility on the surface is lost. While for sample 5, CAH rises at 6 minutes of wear which gives a penetration percentage of 30% - 60%. The widely varying nature of penetration depths at CAH jump times suggest that S_k is not a reliable indicator of liquid mobility on surface topography tested in this thesis.

S_{mr2} (Figure 3-18) is relatively constant throughout its evolution, which is expected as the S_{vk} (Figure 3-19) decreases by a very minor quantity and hence base area of the conical peaks increases miserly. S_{vk} values are relatively constant at an almost negligible height of 0.02 ± 0.01 µm, hence these values cannot be used as an indicator towards drop mobility on the surface. Also, S_{vk} values need not be analyzed, since if drop impregnates surface to such a depth, it signifies a surface in Wenzel regime and hence an already immobile drop. Appendix B.2.4 shows the trends for S_{mr2} and S_{vk}, for surfaces worn for long and short time period. The trends remain the same as discussed above, and the conclusions/observations derived above stand.

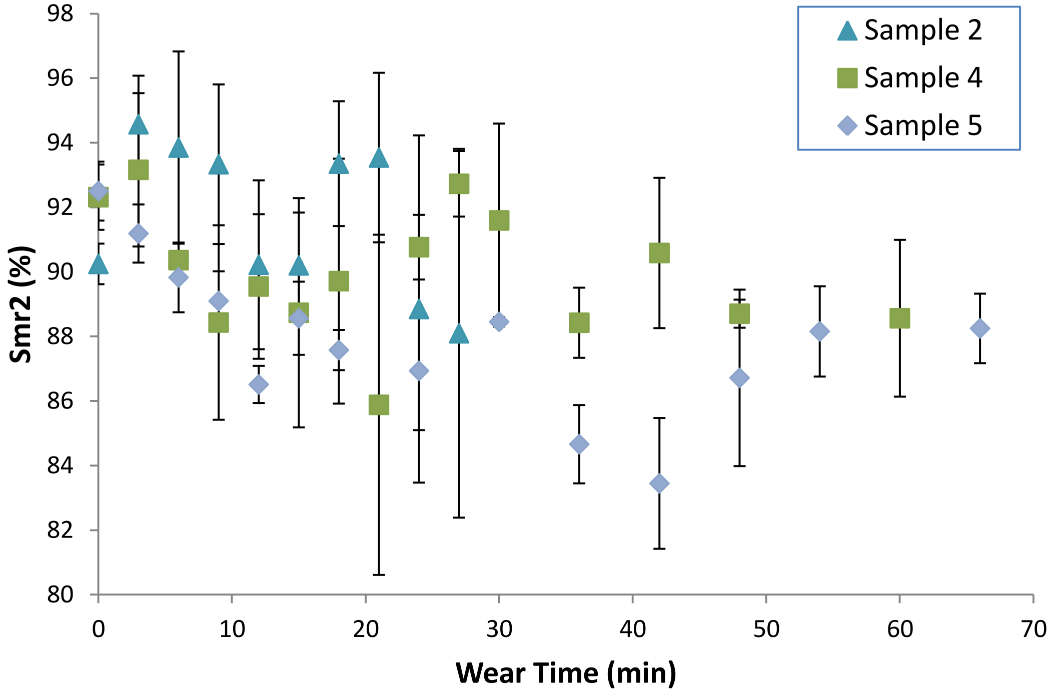

Figure 3-18: Evolution of S_{mr2} as a surface wears. Error bars show the standard deviation in the parameter.

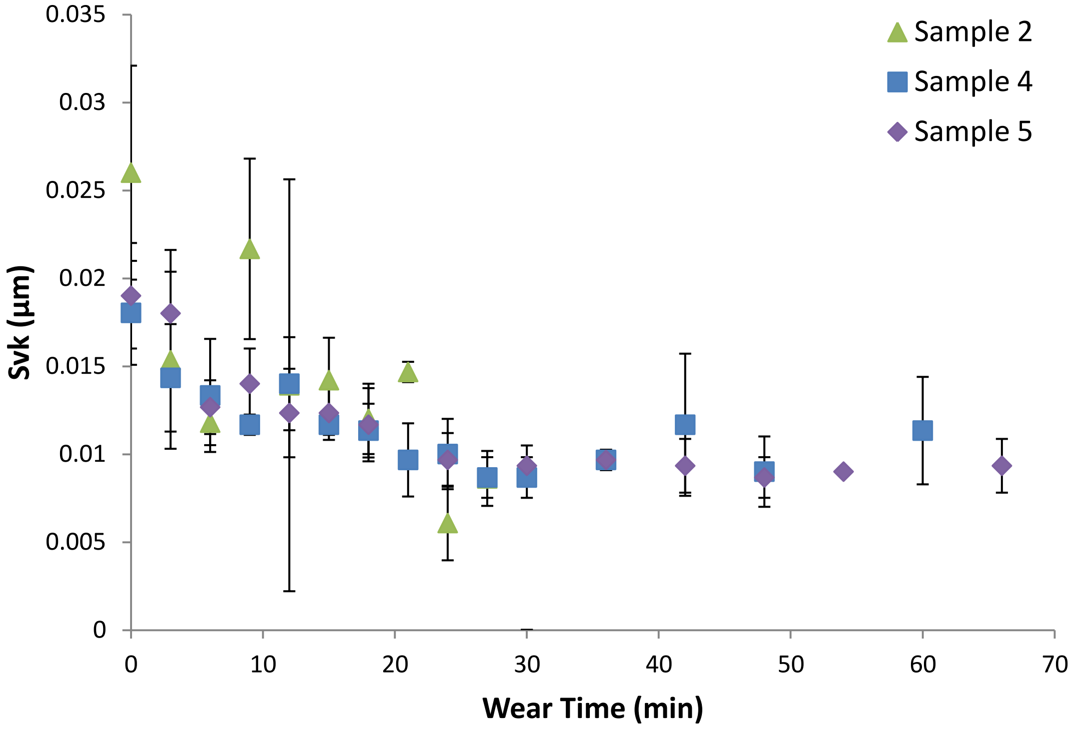

Figure 3-19: Evolution of S_{vk} as a surface wears. Error bars show the standard deviation in the parameter.

Functional parameters indicate how the surface height magnitudes are being affected by wear, which can also be predicted by average roughness and RMS roughness. They remain inconclusive in helping to predict liquid mobility on a surface, hence functional parameters were redundant on the random coniferous like topography studied in this thesis.

3.3 Summary

It was shown that surface texture parameters can be used to quantify the surface topography. A multitude of surface roughness parameters were calculated belonging to amplitude, spatial and functional families of texture parameters. The parameters were assessed in their capability to predict unique trends in the change in surface topography and wetting characteristics, and not wetting magnitudes. The change in graph trends was divided into various regimes. It was found that average roughness, Skewness and Kurtosis when used in conjunction are better equipped to tell about the changes occurring on surface topography.

While many of the parameters studied here show the same trend, and can substitute each other (as far as trend is concerned), but each may have a different sensitivity when used for another surface type, so it is good to have alternatives. However, the topic of study of different surface topographies experimentally and its effect on surface descriptors is out of scope of this thesis.

All of the parameters remain inadequate in their present form, i.e. in solitude, to predict absolute values of wetting data. But, surface roughness parameters can help signify the liquid mobility on surface depending on the regime in which the surface texture parameters lie. Since abrading physical surfaces is time consuming, the data remains inadequate to make meaningful conjectures, hence next chapter deals with development of abrasion algorithm for synthetic textures. This will generate significant amount of datasets for surface topography descriptors.

References

1. W. P. Dong, P. J. Sullivan, and K. J. Stout, “Comprehensive study of parameters for characterizing three-dimensional surface topography I: Some inherent properties of parameter variation,” *Wear,* vol. 159, no. 2, pp. 161–171, 1992.
2. W. P. Dong, P. J. Sullivan, and K. J. Stout, “Comprehensive study of parameters for characterizing three-dimensional surface topography II: Statistical properties of parameter variation,” *Wear*, vol. 167, no. 1, pp. 9–21, 1993.
3. W. P. Dong, P. J. Sullivan, and K. J. Stout, “Comprehensive study of parameters for characterising three-dimensional surface topography: III: Parameters for characterising amplitude and some functional properties,” *Wear*, vol. 178, no. 1, pp. 29–43, 1994.
4. T. Thomas, “Characterization of surface roughness,” *Precision Engineering*, vol. 3, no. 2, pp. 97–104, 1981.
5. M. Sedlaček, B. Podgornik, and J. Vižintin, “Correlation between standard roughness parameters Skewness and Kurtosis and tribological behaviour of contact surfaces,” *Tribology International*, vol. 48, pp. 102–112, Apr. 2012.
6. M. Sedlaček, B. Podgornik, and J. Vižintin, “Influence of surface preparation on roughness parameters, friction and wear,” *Wear*, vol. 266, no. 3–4, pp. 482–487, Feb. 2009.
7. K. N. Hansson and S. Hansson, “Skewness and Kurtosis: Important Parameters in the Characterization of Dental Implant Surface Roughness—A Computer Simulation,” *ISRN Materials Science*, vol. 2011, Article ID 305312, 6 pages, 2011.

8. K. K. Manesh, B. Ramamoorthy, and M. Singaperumal, “Numerical generation of anisotropic 3D non-Gaussian engineering surfaces with specified 3D surface roughness parameters,” *Wear*, vol. 268, no. 11–12, pp. 1371–1379, May 2010.
9. Surface Texture (Surface Roughness, Waviness, and Lay), ASME Standard, B46.1-2009.
10. N. S. Eiss and M. M. Bayraktaroglu, “The Effect of Surface Roughness on the Wear of Low-Density Polyethylene,” *A S L E Transactions*, vol. 23, no. 3, pp. 269–278, Jan. 1980.
11. R. Reizer, P. Pawlus, L. Galda, W. Grabon, and A. Dzierwa, “Modeling of worn surface topography formed in a low wear process,” *Wear*, vol. 278–279, pp. 94–100, Mar. 2012.
12. W. Li, Y. Diao, S. Wang, G. Fang, G. Wang, X. Dong, S. Long, and G. Qiao, “New roughness parameter for the characterization of regularly textured or ordered patterned superhydrophobic surfaces,” *Langmuir*, vol. 25, no. 11, pp. 6076–6080, 2009.
13. S. Semal, T. D. Blake, V. Geskin, M. J. de Ruijter, G. Castelein, and J. De Coninck, “Influence of Surface Roughness on Wetting Dynamics,” *Langmuir,* vol. 15, no. 25, pp. 8765–8770, Dec. 1999.
14. T. V. Vorburger, H. G. Rhee, T. B. Renegar, J. F. Song, and A. Zheng, “Comparison of optical and stylus methods for measurement of surface texture,” *The International Journal of Advanced Manufacturing Technology*, vol. 33, no. 1, pp. 110–118, 2007.
15. S. Adi, H. Adi, H.-K. Chan, P. M. Young, D. Traini, R. Yang, and A. Yu, “Scanning White-Light Interferometry as a Novel Technique to Quantify the Surface Roughness of Micron-Sized Particles for Inhalation,” *Langmuir*, vol. 24, no. 19, pp. 11307–11312, Oct. 2008.

16. G. Udupa, M. Singaperumal, R. S. Sirohi, and M. P. Kothiyal, “Characterization of surface topography by confocal microscopy: I. Principles and the measurement system,” *Measurement Science and Technology*, vol. 11, no. 3, p. 305, 2000.
17. A. Wennerberg, R. Ohlsson, B.-G. Rosén, and B. Andersson, “Characterizing three-dimensional topography of engineering and biomaterial surfaces by confocal laser scanning and stylus techniques,” *Medical Engineering & Physics*, vol. 18, no. 7, pp. 548–556, Oct. 1996.
18. B. Al-Nawas, K. A. Grötz, H. Götz, G. Heinrich, G. Rippin, E. Stender, H. Duschner, and W. Wagner, “Validation of three-dimensional surface characterising methods: Scanning electron microscopy and confocal laser scanning microscopy,” *Scanning*, vol. 23, no. 4, pp. 227–231, Dec. 2006.
19. M. D’Acunzi, L. Mammen, M. Singh, X. Deng, M. Roth, G. K. Auernhammer, H.-J. Butt, and D. Vollmer, “Superhydrophobic surfaces by hybrid raspberry-like particles,” *Faraday Discussions*, vol. 146, p. 35, 2010.
20. E. Gadelmawla, “Roughness parameters,” *Journal of Materials Processing Technology*, vol. 123, no. 1, pp. 133–145, Apr. 2002.
21. “3D Surface Texture Parameters.” Internet: www.michmet.com/Texture_parameters.htm, [accessed December 15, 2012].
22. H. Y. Erbil, A. L. Demirel, Y. Avci, and O. Mert, “Transformation of a Simple Plastic into a Superhydrophobic Surface,” Science, vol. 299, no. 5611, pp. 1377–1380, Feb. 2003.
23. C. Yang, U. Tartaglino, and B. N. J. Persson, “Influence of surface roughness on superhydrophobicity,” *Physical Review Letters*, vol. 97, no. 11, p. 116103, 2006.

24. J. Bravo, L. Zhai, Z. Wu, R. E. Cohen, and M. F. Rubner, “Transparent superhydrophobic films based on silica nanoparticles,” *Langmuir*, vol. 23, no. 13, pp. 7293–7298, 2007.
25. I. Woodward, W. C. E. Schofield, V. Roucoules, and J. P. S. Badyal, “Super-hydrophobic surfaces produced by plasma fluorination of polybutadiene films,” *Langmuir*, vol. 19, no. 8, pp. 3432–3438, 2003.
26. A. D. Tserepi, M. E. Vlachopoulou, and E. Gogolides, “Nanotexturing of poly (dimethylsiloxane) in plasmas for creating robust super-hydrophobic surfaces,” *Nanotechnology*, vol. 17, no. 15, p. 3977, 2006.
27. G. Zhang, D. Wang, Z. Z. Gu, and H. Möhwald, “Fabrication of superhydrophobic surfaces from binary colloidal assembly,” *Langmuir*, vol. 21, no. 20, pp. 9143–9148, 2005.
28. Y. Cui, A. T. Paxson, K. M. Smyth, and K. K. Varanasi, “Hierarchical polymeric textures via solvent-induced phase transformation: A single-step production of large-area superhydrophobic surfaces,” *Colloids and Surfaces A: Physicochemical and Engineering Aspects*, vol. 394, pp. 8–13, Jan. 2012.
29. A. Tuteja, W. Choi, M. Ma, J. M. Mabry, S. A. Mazzella, G. C. Rutledge, G. H. McKinley, and R. E. Cohen, “Designing superoleophobic surfaces,” *Science*, vol. 318, no. 5856, p. 1618, 2007.
30. B. Bhushan and Y. C. Jung, “Micro- and nanoscale characterization of hydrophobic and hydrophilic leaf surfaces,” *Nanotechnology*, vol. 17, no. 11, pp. 2758–2772, Jun. 2006.
31. S. A. Kulinich, S. Farhadi, K. Nose, and X. W. Du, “Superhydrophobic Surfaces: Are They Really Ice-Repellent?,” *Langmuir*, vol. 27, no. 1, pp. 25–29, Jan. 2011.

32. M. Nosonovsky and B. Bhushan, “Hierarchical roughness optimization for biomimetic superhydrophobic surfaces,” *Ultramicroscopy*, vol. 107, no. 10, pp. 969–979, 2007.
33. X. Zhang, M. Järn, J. Peltonen, V. Pore, T. Vuorinen, E. Levänen, and T. Mäntylä, “Analysis of roughness parameters to specify superhydrophobic antireflective boehmite films made by the sol–gel process,” *Journal of the European Ceramic Society*, vol. 28, no. 11, pp. 2177–2181, 2008.
34. T. G. King and T. A. Spedding, “Towards a rational surface profile characterization system,” *Precision Engineering*, vol. 5, no. 4, pp. 153–160, 1983.
35. W. Dong, P. Sullivan, and K. Stout, “Comprehensive study of parameters for characterising three-dimensional surface topographyIV: Parameters for characterising spatial and hybrid properties,” *Wear*, vol. 178, no. 1–2, pp. 45–60, Nov. 1994.
36. W. Li and A. Amirfazli, “Hierarchical structures for natural superhydrophobic surfaces,” *Soft Matter*, vol. 4, no. 3, pp. 462–466, 2007.
37. J. Shieh, F. J. Hou, Y. C. Chen, H. M. Chen, S. P. Yang, C. C. Cheng, and H. L. Chen, “Robust Airlike Superhydrophobic Surfaces,” *Advanced Materials*, vol. 22, no. 5, pp. 597–601, Feb. 2010.
38. B. He, N. A. Patankar, and J. Lee, “Multiple equilibrium droplet shapes and design criterion for rough hydrophobic surfaces,” *Langmuir*, vol. 19, no. 12, pp. 4999–5003, 2003.
39. M. Nosonovsky and B. Bhushan, “Roughness-induced superhydrophobicity: a way to design non-adhesive surfaces,” *Journal of Physics: Condensed Matter*, vol. 20, no. 22, p. 225009, 2008.

40. J. A. Greenwood. “Problems with Surface Roughness” in *Fundamentals of Friction: Macroscopic and Microscopic Processes*, 1st ed., I. L. Singer and H. M. Pollock, AA Dordrecht: Kluwer Academic Publishers, 1992, pp. 67.
41. B. Griffiths, “Surface Finish Characterization,” in *Manufacturing Surface Technology*, Elsevier, 2001, pp. 109–151.
42. W. Dong, P. Sullivan, and K. Stout, “Comprehensive study of parameters for characterising three-dimensional surface topographyIV: Parameters for characterising spatial and hybrid properties,” *Wear,* vol. 178, no. 1–2, pp. 45–60, Nov. 1994.

Chapter 4 - Modeling Abrasion on Random Geometry Synthetic Terrains

4.1 Introduction

Superhydrophobic surfaces (SHS) while presenting an enormous potential for numerous applications, also present challenge regarding their durability. To date many SHS lose liquid drop mobility after undergoing mild abrasion due to fragile topography present on them. In previous chapters, SHS were abraded progressively and evolution of wetting characteristics, surface topography and surface roughness parameters was investigated. The motive was to understand how wear affects the superhydrophobicity, and hence finding ways to maximize durability of SHS. This generated valuable data for surface roughness descriptors, understanding surface topographical changes as a surface abrades, and simultaneously helping monitor the advancing/receding contact angles. For a statistical investigation and a meaningful conjecture into correlation between surface roughness parameters and wetting characteristics, a substantially large number of datasets (surface parameters and wetting characteristics) are required. The process of abrading a surface and calculating surface roughness parameters is time intensive, and hence a good candidate to be studied in a simulated environment like artificial terrains by implementing an abrasion methodology. Some salient features of surfaces and abrasion procedure chosen in this study, as also detailed in previous chapters, are: a) Among different samples of similar surfaces the surface roughness parameters show the same trend albeit with different magnitudes, b) Surface topography was abraded randomly and the material was removed in an unbiased pattern, the methodology behind which is not complex and can be woven into an algorithm, and c) The only factor affecting the wetting data studied was surface topography and not chemistry. Hence, abrasion process can be modeled on artificial virtual terrains by replicating abrasion methodology and similar surface roughness parameter trends among similar surfaces. Abrasion algorithm can be an asset in finding the surface topography after duration of wear on various synthetic terrains, and how surface parameters are affected. Counter intuitively, as every physical terrain has a synthetic counterpart this can help evaluating physical surface durability too, helping to design SHS with improved wear resistance.

Abrasion on PTFE SHS studied previously was a stochastic phenomenon depending on many factors which cannot be mimicked to truest degree; hence the abrasion algorithm would not be an exact replication, but should be a good approximation of the probable abrasion of physical surfaces. The trends in surface roughness parameters will guide in helping review the performance of abrasion algorithm. This approach to simulate the abrasion based on roughness parameter behavior has been used in literature previously [1-2]. Ao *et al.* [1] used Skewness, Kurtosis, and RMS roughness behavior of physically abraded surfaces as pivot information to train an artificial neural network (ANN). This ANN was then used to simulate wear on surfaces, and predict roughness parameters. Jeng *et al.* [2] simulated wear on surfaces having different initial height distributions, and evaluated performance of Skewness and Kurtosis to establish the wear behavior of their model.

The computational approach can help faithfully replicate abrasion of coniferous-like random geometry PTFE surfaces, and also generate similar trends in surface topography descriptors. This eliminates the need to abrade multiples of surfaces, saving time and preparation of samples. Since the need ultimately is to integrate wetting characteristics with surface roughness parameters and find a correlation amongst them, the wetting characteristics will be calculated on actual surfaces and transported over to the analogous synthetic terrain. This can be done by dividing wetting characteristics into zones of varying drop mobility and seeing how the corresponding surface parameters behave in those zones. The behavior of surface roughness parameters on a synthetic terrain can then be integrated with the calculated roughness parameters on real physical surfaces, and divided into zones and hence assigned corresponding wetting characteristics. A computational approach can be successful on a varied number of surfaces, only requiring a small number of initial datasets (surface parameters and wetting characteristics) of actual surface abrasions to help calibrate and validate the algorithm. Although, it will be difficult to find advancing/receding contact angles at a given abrasion iteration on a synthetic terrain, it will be possible to determine the surface state with regards to drop mobility (i.e. high or low) which is as important and helpful.

Although abrasion on synthetic terrains has been simulated a number of times in literature [3-6], but only one publication has come to the knowledge of the author which uses synthetic surfaces in wetting studies. Torregrosa *et al.* [7] used synthetic terrains and roughened titanium surfaces to study the effect of resolution and scan size, to acquire the spatial information, on the roughness factor. Synthetic terrains were constructed using fractional Brownian motion technique [8]. Topography of titanium surfaces was acquired at different scan sizes, and resolutions using AFM and CSM. Resolution of the instrument was found to be the critical factor affecting roughness values, rather than scan sizes. This result was also validated using artificial terrain data, by varying the density of the spatial information and size of the topography. Using roughness factor to find Young's contact angle resulted in significant deviations with actual contact angle, found by authors to be ~15°. Hence, this work is one of the first studies which models physical abrasion on synthetic surfaces, to integrate the wetting data for synthetic and physical surfaces based upon roughness parameter trends.

This chapter details the developed methodology and characteristics of the abrasion algorithm. Abrasion methodology of PTFE SHS worn in previous chapters is studied and detailed to be applied on synthetic counterpart terrains. The algorithms available to generate synthetic terrain are also detailed. The artificial terrains will be used only for testing and validating the abrasion algorithm, while actual algorithmic abrasion will be done on already available virtual terrains of PTFE SHS surfaces available from CSM mapping. Critical analysis is presented with advantages and disadvantages of each of the terrains generated by respective terrain generation algorithms. The abrasion algorithm is then verified against various different synthetic terrains. Finally, previously abraded PTFE coniferous-like random geometry surfaces are inputted to the algorithm and resulting surface parameters are evaluated against results previously calculated by CSM on PTFE SHS. Figure 4-1 summarizes the methodology to be followed in this chapter.

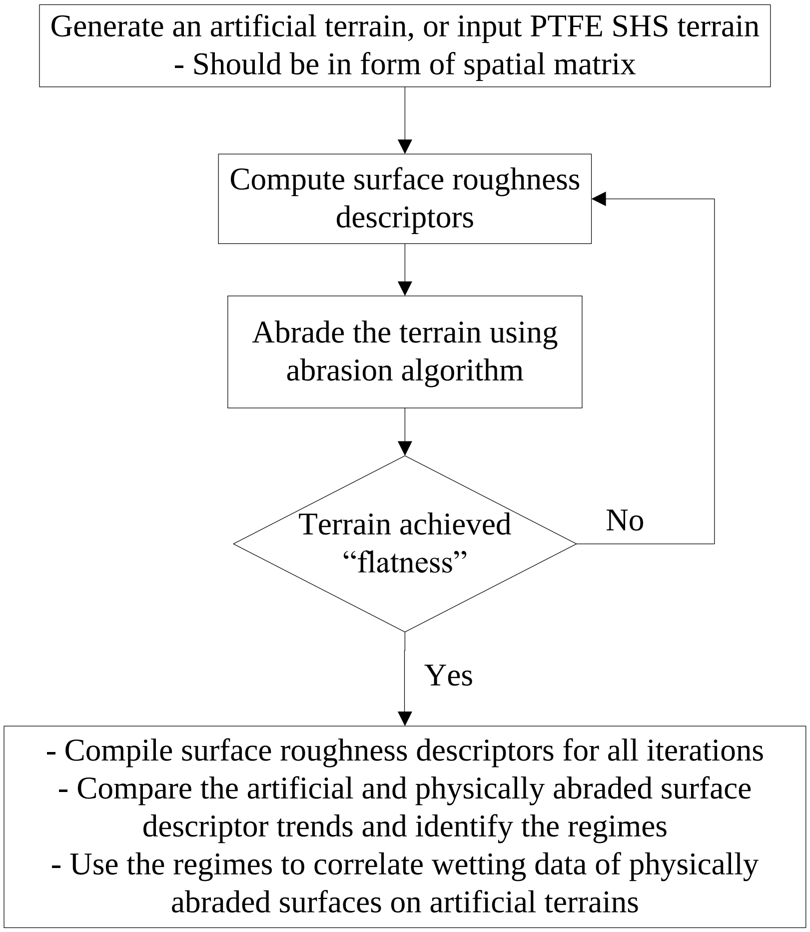

Figure 4-1 – Flowchart describing the abrasion process for abrading an artificial terrain.

4.2 Generating Random Terrains

Artificial terrain generation techniques help in realizing various types of surface topography. One prominent area of terrain generation is to provide a rich and entertainment focused user experience in various genres of computer video games which need fantasy inspired, combat arena, natural and other varied landscapes [9]. Architecture, urban infrastructure planning, and weather virtualization are some of the other areas where terrain generation finds applications [10]. A wide range of techniques available for terrain generation have been developed, differing in speed, ease of implementation, and ability to create terrains with differing level of detail [11]. They present numerous advantages and constraints over each other in their own realm. Some techniques are confined only to a certain limited variety of terrains [12-13], some allow limited control over output terrain and some techniques focus on generating realistic looking terrains. Torregrosa *et al.* [7] studied differences in predicted and observed wetting data, using synthetic and physical terrains to calculate effect of resolution and scan size of the acquired topography.

The terrains can be stored digitally in many different storage formats. The spatial height matrix can be stored in various data structures, e.g., regular in form of discrete square or rectangle grid, or an irregular triangular irregular network (TIN) [14-17]. Regular grid spatial matrix allows to process algorithmic iterations at a faster rate, but the storage cost of matrix is large and has a limited adoption to topographical structures [14-15]. Irregular data structures are able to adapt to the terrain (overhangs, caves, etc.), but have a complicated data structure making it difficult to adopt uniform abrasion algorithm iteration on the terrain. Hence, a regular matrix was chosen for this study due to ease of implementation, and suitability for applying an iterative abrasion algorithm.

Terrains can be digitally stored in a spatial height matrix, saving *z* elevation coordinates in a corresponding 2D plane scalar (*x*, *y*) grid. Limitations of choosing a regular grid spatial height matrix to generate a terrain are: a) Only one elevation per square grid limits generation of overhangs, caves or vertical structures (pillars, and cylinders); b) Terrain resolution is universal and resolution over a local area cannot be changed; and c) Grid representation of shapes that are rough (not square or rectangle, e.g. circle) is not easy. For this study, the random synthetic geometry to be generated will be free of overhangs, similar to the PTFE SHS surfaces studied. The resolution used can be tailored for a specific purpose, fine resolution can be used while generation terrain with coarse features and vice versa. Fine resolution can also help mitigating the problematic reproduction of circular relief features. Hence, keeping in view the capabilities and reservation about the limitations of regular spatial matrix regarding our specific purpose, in this study terrain relief features can be described by a set of elevation points placed at vertices of equally spaced plane rectangular array.

Modeling, measuring, and procedural are some of the terrain generation techniques [11]. In modeling, terrain is manually generated using 3D modeling software like 3D Studio MAX, Maya, etc. Herein, terrain visualization is dependent and limited on creativity and skill of the individual. Measuring techniques sample a real world terrain, and the captured data is conceptualized into a synthetic terrain. This technique produces realistic looking terrains, on a planetary (earth like landscape) scale. Procedural techniques make use of programming to generate terrains. Modeling technique was not used to generate terrains in this work, as the procedure is not time efficient. Modeling techniques require a substantial time to draw the terrain. Procedural technique allows for the generation of random geometry by control over precisely pre-defined variables, which are easy to understand and manipulate allowing control over synthetic terrain. Hence, procedural techniques were used to generate terrains in this thesis. Procedural techniques can be categorized into physical, spectral synthesis, and fractal techniques [11].

Differing landscapes on the Earth are a result of erosion processes. Physical procedural technique algorithms take inspiration from the underlying phenomenon in erosion to generate eroded terrains i.e. peak attrition by sand or water and settling the sediment in valleys. Output terrain is generally a realistic terrain [5]. In spectral synthesis, frequency components are converted into altitude over whole spatial scale by adding up trigonometric polynomials (fast Fourier transforms) at a range of different scales [18]. This technique is deficient in that it generates homogeneous periodic terrains and requires large computational time, and allows lesser control over the terrain features [11, 18]. This method is better for generating smooth terrains.

Fractal synthesis was used to generate complex, self similar virtual terrains [3, 19]. Fractal algorithm acts recursively upon a dataset to generate pattern which is self similar. Self similar terrain is magnification agnostic, and magnified subsets of terrain look similar to original terrain, irrespective of magnification [18, 20]. Due to the incorporated randomness, every different run of the algorithm generates a different terrain [11]. The drawback of this technique is limited control over terrain features, but terrain roughness can be controlled [3].

Terrains in this study were generated using two techniques, pseudo-measuring and fractal synthesis. Spatial elevation matrix for PTFE SHS that were abraded in previous chapters is already available through mapping done by CSM, as described in previous chapters. Hence, there was no need to develop or apply special measuring techniques to create terrain similar to coniferous-like random geometry PTFE SHS, implying the pseudo nature of the technique. Fractal synthesis was used to generate random terrains in this study due to speed and simplicity of implementation. Resulting terrains were inputted into abrasion algorithm for iterative abrasion; hence the speed of terrain generation can be a bottleneck in overall implementation. Combined with speed and easily implementable algorithms which provide control over roughness of generated terrain, fractal synthesis was used to generate terrains in this study for increased productivity.

MATLAB® was the coding environment used for fractal terrain generation and subsequent abrasion. The terrain was represented as M×N rectangular matrix, with value stored at (m, n) representing height of terrain at the point (m, n). The height values were stored as floating point numbers, giving a larger dynamic range.

4.2.1 Generating terrain - Diamond Square Algorithm

Multitude of procedural fractal terrain generation algorithms have been developed by researchers, e.g. [18, 21], and random midpoint displacement algorithm introduced by Fournier *et al.* [22] is one of the most widely used methods. Modified implementation of midpoint displacement method is Diamond square algorithm [21]. Diamond square algorithm derives its name from two steps performed as virtue of its implementation, the diamond and square step. It helps reduce the square and rectangular artifacts along the gridlines which can be seen while using midpoint displacement method.

This algorithm does not allow for local control of terrain i.e. specifying height range of specific peaks, or a particular feature cannot be designated to be generated at a particular point. Though for more control over the generated topography, the initial 2D array and first few passes can be seeded with values that will befit the desired topography. This drawback of the algorithm is not a hindrance in this study, as it allows for manipulation of surface roughness and surface height range (i.e. maximum height difference between peaks and valleys). This makes diamond square algorithm a suitable choice to generate random geometry synthetic terrains with varying surface roughness.

An initial 2D square array was chosen and the outermost corners were seeded with height values. These height values can be inputted manually and user defined, and also randomly generated though an algorithm. In Figure 4-2 (a), solid dots depict the seeded height values, with Figure 4-3 (a) showing the same with numerical values. The diamond step is then performed, which consists of averaging the height of the four neighboring corners of the square and adding a random number to the averaged value. This final value is height of the centre of the square, thus generating diamonds. The top view depicted in Figure 4-2 (b) by usage of dashed lines, shows the four faces of a diamond. Figure 4-3 (b) shows the diamond step with numerical values. The new values are shown by solid black dots, and open dots note the existing corner values. In the square step, the height of centre of diamonds created in previous iteration is set to average height of its neighbors and random noise is also added to this averaged value. Figure 4-2 (c) illustrates this by using arrows to point to the pixel created, and originating point is the height contributing pixel. Figure 4-3 (c) details the square step using numerical values. With each pass, more detail is added to the topography. The diamond and square steps are repeated until all the points in the grid have values assigned to them.

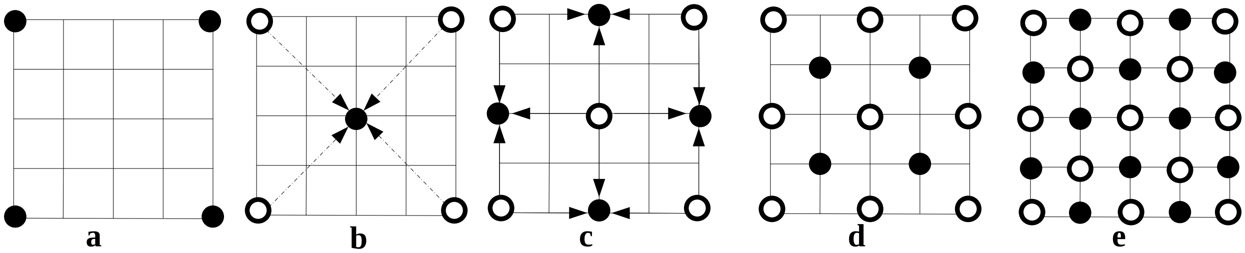

Figure 4-2- Graphical illustration of virtual terrain generation using diamond square algorithm. The grid represents the spatial 2-D heightmap. (a) shows the initial square seeded with predetermined height values, (b) and (d) show the diamond step, (c) and (e) illustrate square step. Solid black dots are the pixels with new values, the unfilled dots are pixels with existing values. Dashed lines in (b) are visual guides to generated diamonds. The originating point of arrow in (b) and (c) is the height contributing pixel. Figure adapted from [23].

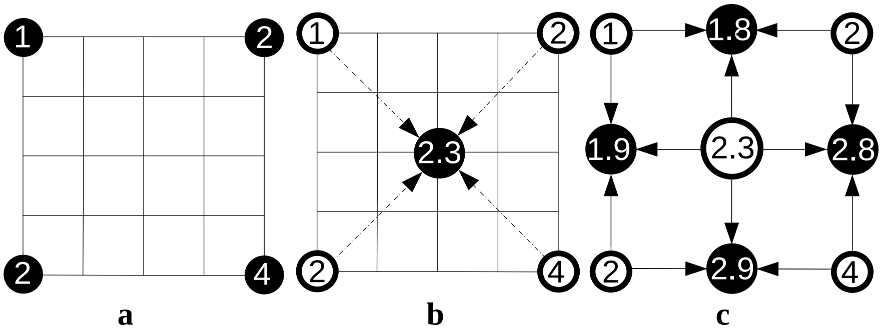

Figure 4-3 – Graphical illustration of virtual terrain generation using diamond square algorithm using numerical values. Only first three iterations are shown: a) initial seeded matrix with corner height values, b) diamond step, and c) square step.

The MATLAB® code for generating the terrain has been directly adapted from the one written by Alexander Carette [24], and appended in Appendix C. The code is distributed under GNU Lesser General Public License [25], which permits use of the code in software libraries. Some of the generated terrains with different roughness are shown in Figure 4-4.

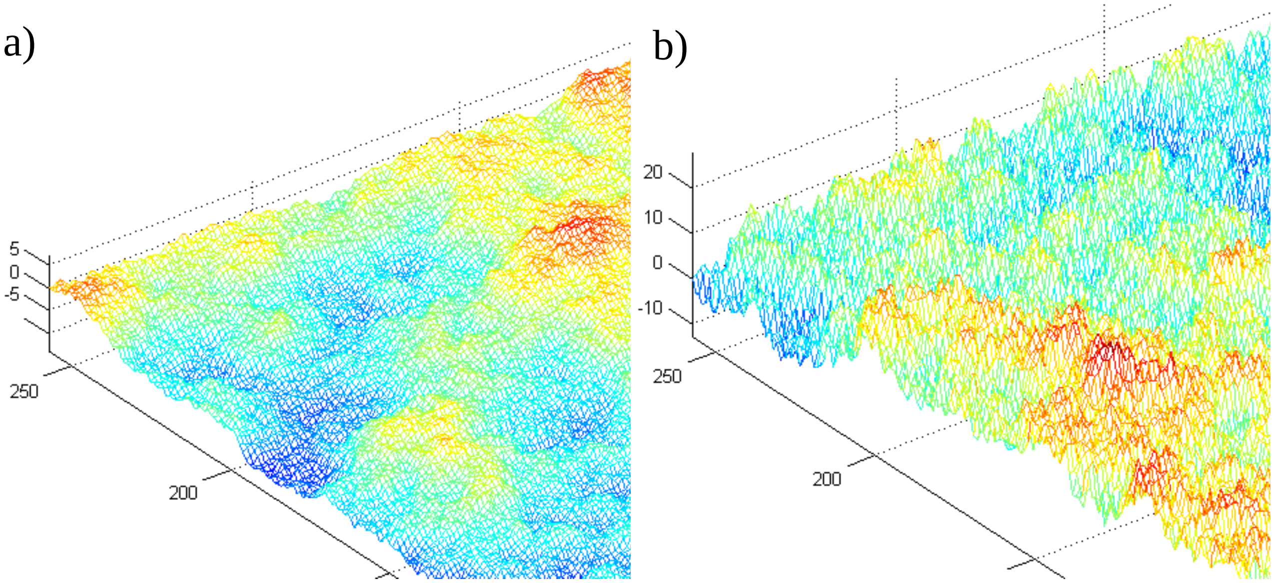

Figure 4-4 – Synthetic terrains generated by diamond square algorithm with a) lower , and b) higher surface roughness.

4.3 Abrasion algorithm methodology and implementation

Abrasion is generally defined as progressive irreversible removal of material from the body by mechanical action [26]. The removal of material happens by various methods of abrasion e.g. scratches, grinding, etc. The surface wear can vary according to the surface material composition and topography, abrading material and method, etc. Since the wear is dependent on many parameters, experimental observation of the wear process that was operating on the surface can help in better understanding. Understanding the wear methodology can then help to simulate the wear on virtual terrains too.

Erosion (Wind, hydraulic, rainfall, etc.) has previously been modeled on artificial terrain by various researchers [3, 5, 18]. Erosion algorithms cannot be applied in this study, as erosion is not similar to abrasion. Rain erosion will produce sharp peaks and erode valleys too, until sediment deposits. Wind erosion also results in sharp protrusions at varying height on the same peak. This difference in methodology makes implementation of erosion algorithms infeasible for terrains studied here.

Abrasion is an actively studied field and there have been various abrasion models proposed by researchers e.g. [26-28]. The complex nature of this tribological phenomenon renders the prediction ability of these abrasion models suitable to only select systems, as abrasion varies due to material being abraded and methodology being applied [26]. Besides, most of the models iterate and refine upon Archard's law of abrasive wear [29] which predicts volume of material removed by virtue of knowing coefficient of wear friction, pressure and sliding distance. Material volume removed would help in estimating the amount of wear and hence predict the topography. Since abrasion on SHS previously studied was anisotropic, this would require extensive investigation of contact surface force tensors and then various finite element methods would need to be applied to model abrasion on PTFE SHS [26]. This is a complicated strategy, and outside the scope of this study.

Instead, abrasion methodology on PTFE SHS, detailed in Chapter 2 was followed, as this would enable a simplified yet precise simulation of wear. Previously, in Chapter 2, coniferous-like random geometry surface were abraded, initial abrasion flattened the top portions of peaks, but some peaks were still unaffected. Further wear caused the surface to heavily abrade random peaks and then ultimately as abrasion time increased the whole surface flattened. All matter abraded is assumed to be detritus which does not adhere further to the surface. The abrasion algorithm should be pattern agnostic i.e. generate random wear pattern. Abrasion algorithm should be able to simulate this behavior, on a whole, with matching trends in surface roughness parameters. The abrasion process was stochastic, with definite trends identified in concurrent surface roughness parameters. Hence, the abrasion algorithm will not be able to closely replicate and shortcomings are expected to be present, but it will be approximate predictor of abrasion methodology and surface roughness parameter trends.

Segregating the artificial terrain on a peak based approach will be difficult, as identifying peaks mathematically will be problematic when a heightmap consists of closely situated height values. Instead of concentrating on individual peaks and abrading them, an algorithm which peppers the surface with negative values at random peaks will work very similar; a hypothesis of this study. This simplistic approach can help simulate random surface abrasion by acting on random selected heights, prioritize abrading peaks in initial iteration passes, and also include abrasion speed as a factor. Bigerelle *et al.* [30] describe an algorithm which emphasizes the height of the peak as a critical factor to its abrading probability. As the peak height increases, probability of resisting the abrasion decreases. The algorithm selects random height coordinates on the terrain, and abrades the heights depending on, if the probability is favorable. Hence, this algorithm is suitable for this study as it prioritizes peaks, no adherence of the material abraded is counted in the algorithm, and the abrasion process is random. One limitation of the algorithm, that is refined in this study, is the ability to differentiate between roughness from surface form error and waviness. Any surface consists of various different spectral frequencies, and surface waviness (longer wavelength) and surface roughness (short wavelength) are illustrated in Figure 4-5. The combination of the longer and short wavelength gives the profile of the surface. As the abrasion algorithm abrades surfaces based on their elevation, the lower wavelength peaks will always be prioritized and the roughness peaks based in valleys of lower wavelength peaks will be abraded later. Also, the abrasion algorithm does not preserve the waviness (major wavelength) of the surface and abrades it completely flat. Hence the need for the abrasion to iterate on roughness features, as the peaks on roughness features are already prioritized in the abrasion algorithm. Abrasion algorithm is refined to work only on surface roughness, and waviness is left intact.

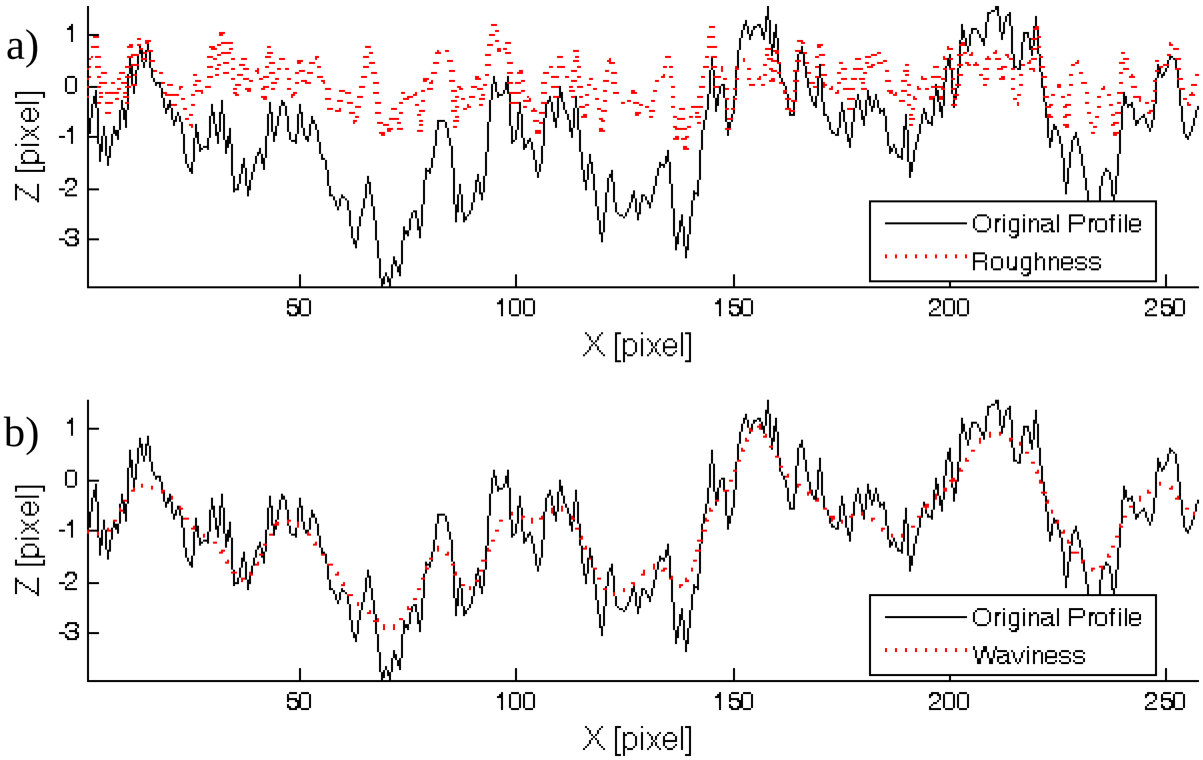

Figure 4-5 – Illustrating a) Surface roughness, and b) surface waviness with help of line profiles on a virtual terrain.

The algorithm refined and implemented in this study and originally detailed by Bigerelle *et al.* [30] is described in steps below. The contribution of this work is to making the algorithm aware of the waviness present on the surface, and hence abrasion flattens the surface preserving the waviness of the surface. Also, only 2D profile was abraded by Bigerelle *et al.* [30], but in this study abrasion algorithm is extended to 3D topographies.

1) A terrain is inputted to the algorithm in the form of 2D heightmap. A Gaussian filter is applied on this surface to extract the waviness of this surface. The original fractal surface is subtracted from this Gaussian curvature surface to obtain roughness. This spatial matrix is called roughness matrix.

2) On roughness matrix at each wear cycle, *c*, the value of $W_\lambda(x,c)$ is computed for each discretized pixel of height $z\ (x,\ c)$. Here, $R_t(c) = z_{max} - z_{min}$ for the surface, and $W_\lambda(x,c)$ is the probability of material located at position *x* and at height *z* to be eroded during a wear cycle *c*. λ is a real number here.

   $$W_\lambda(x,c) = 1- [(1-e^{-\lambda(Rt(c)-z(x,c)})/ (1-e^{-\lambda Rt(c)})]$$

   An exponential decay function was probably used by Bigerelle *et al.* [30] here to calculate resistance probability as the probability calculated will not scale linearly with height, and react to the height of the pixel with a greater magnitude.

3) Then, a random number k ϵ [0 ….. 1] is generated for each pixel point and compared with the value of $W_\lambda(x,c)$, at that pixel, previously calculated in step 2. If $k < W_\lambda(x,c)$, the pixel is abraded with height *Δh* (user defined) removed from the corresponding pixel on the original height matrix (and not from roughness matrix), and nothing is done, if $k > W_\lambda(x,c)$. Hence, this step adds randomness into the abrasion algorithm. Even if every pixel has high probability, not each pixel will be abraded.

   To add robustness to the abrasion algorithm, for a given number of initial cycles one is able to abrade only a percentage (*p*%, user defined number) of the peaks, and also value of *Δh* can be varied. *Δh* can range from *dh1* to *dh2* with a step size of *ddh* between each value, e.g. Δ*h= [dh1, dh1+ddh, dh1+2*ddh, … , dh]*. The abrasion algorithm then picks a value at random from the *Δh* matrix for each pixel, and at each iteration.

4) Repeat steps 1, 2, and 3 until desired.
5) After each iteration a number of roughness parameters are calculated, namely Sa, Sq, S_{sk}, S_{ku}, S_{sc}, S_{dq}, S_{dq6}, S_{dr}, S_{ds}, S_{td}, S_{tdi}, S_{rw}, S_{rwi}, S_{hw}, S_{fd}, S_{cl20}, S_{cl37}, S_{tr20}, S_{tr37}, S_{tr}, and S_{al}. All these parameters are saved in excel file after each iteration. Topography of surface after each iteration is also saved in an Excel file as a spatial matrix.

The abrasion algorithm was implemented as a graphical user interface (GUI) with back-end coding done in MATLAB®. Considering the number of input parameters involved in the algorithm, a GUI would help in smoothing the workflow. The code is appended in Appendix D.

4.4 Behavior characteristics of the abrasion algorithm

Determining the behavior of algorithm to different artificial terrains, and with different input parameters is important. The abrasion algorithm takes following parameters as input:-

1) Initial topography, in the form of a matrix containing heightmaps,
2) Number of abrasion iterations to be performed,
3) λ, a real number as defined in abrasion algorithm above
4) Δh, height to be abraded from a pixel at each iteration.

The abrasion algorithm can also be divided into two parts, with each part having different value of λ and only acting on a user defined percentage of total topography. Two part division of abrasion algorithm was done so as to see if the peaks needed to abraded with less intensity in the initial abrasion iterations.

4.4.1 Determining the algorithm envelope

As described above, the roughness parameter output depending on four input parameters. Hence, the interdependency of the parameters was examined by fixing one of the parameters and changing others. Ideal number of abrasions needed for surface to flatten also needed to be evaluated. Hence, ten random fractal surfaces generated by the diamond square algorithm with dimensions 257×257. All surface topographies were different, due to being generated by diamond square algorithm. The matrix dimensions are similar to the one given by spatial height matrix of CSM imaged surface using 100X objective. Four different values of λ were chosen as 2, 6, 10, and 100. This would help evaluating the impact of λ in surface abrasion, and hence the input values were chosen arbitrarily to gage the algorithm behavior. The height to be deducted from pixel heights, Δh, at each iteration was set in four groups, with small and large range of height variations: a) [1.40, 1.45, 1.50], b) [0.90, 0.95, 1.00], c) [0.40, 0.45, 0.50], d) [0.50, 0.55, 0.60, 0.65, 0.70… 1.50]. These four groups will help demonstrating how the Δh impacts the topography as it increases in smooth steps (groups a, b and c), and also if the Δh is randomly chosen from a large height variation as in group (d).

The results are shown in the form of graphs of surface roughness parameters below (Figure 4-6, Figure 4-7, and Figure 4-8) for $\lambda=2$, $\Delta h = [1.4, 1.45, 1.5]$. For the first 100 iterations a $\lambda=4$ was chosen, and it was acting on only 15% of the surface peaks, the values were chosen arbitrarily to gage their impact.

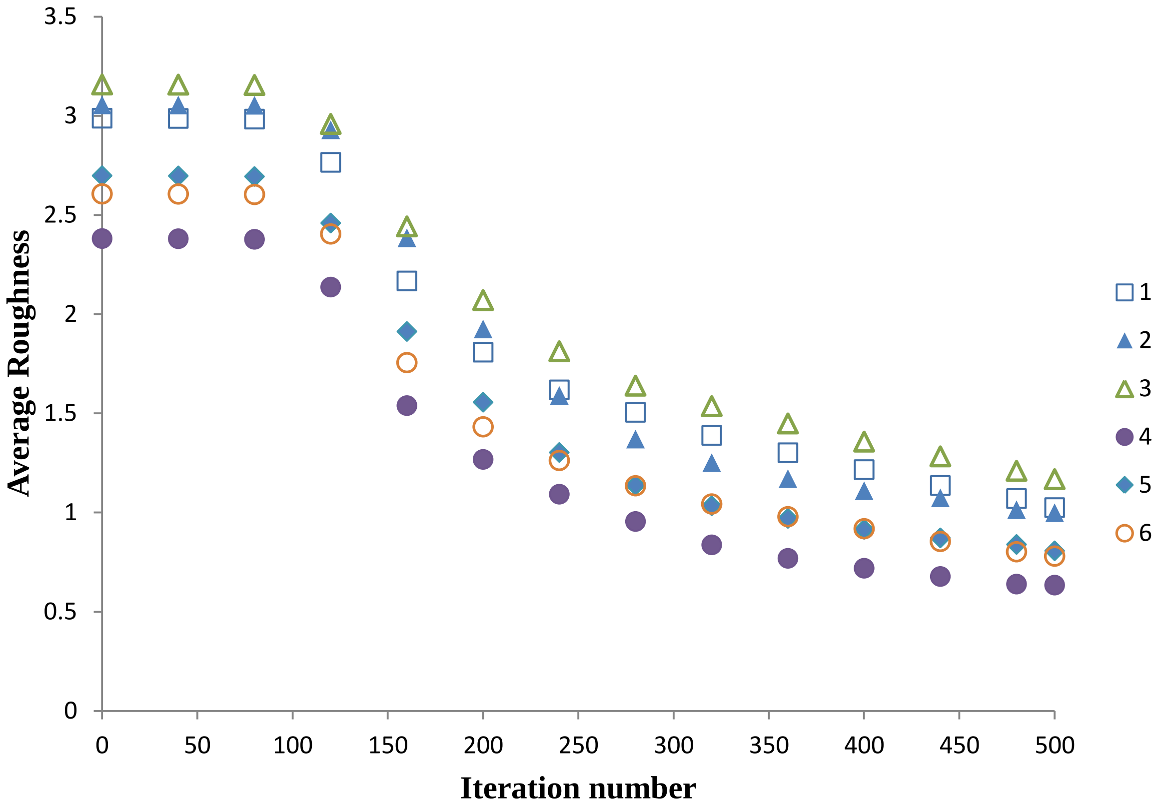

Figure 4-6- Average roughness of 6 random surfaces, after being abraded for 500 iterations. Only select samples and every 40th iteration has been plotted for better clarity.

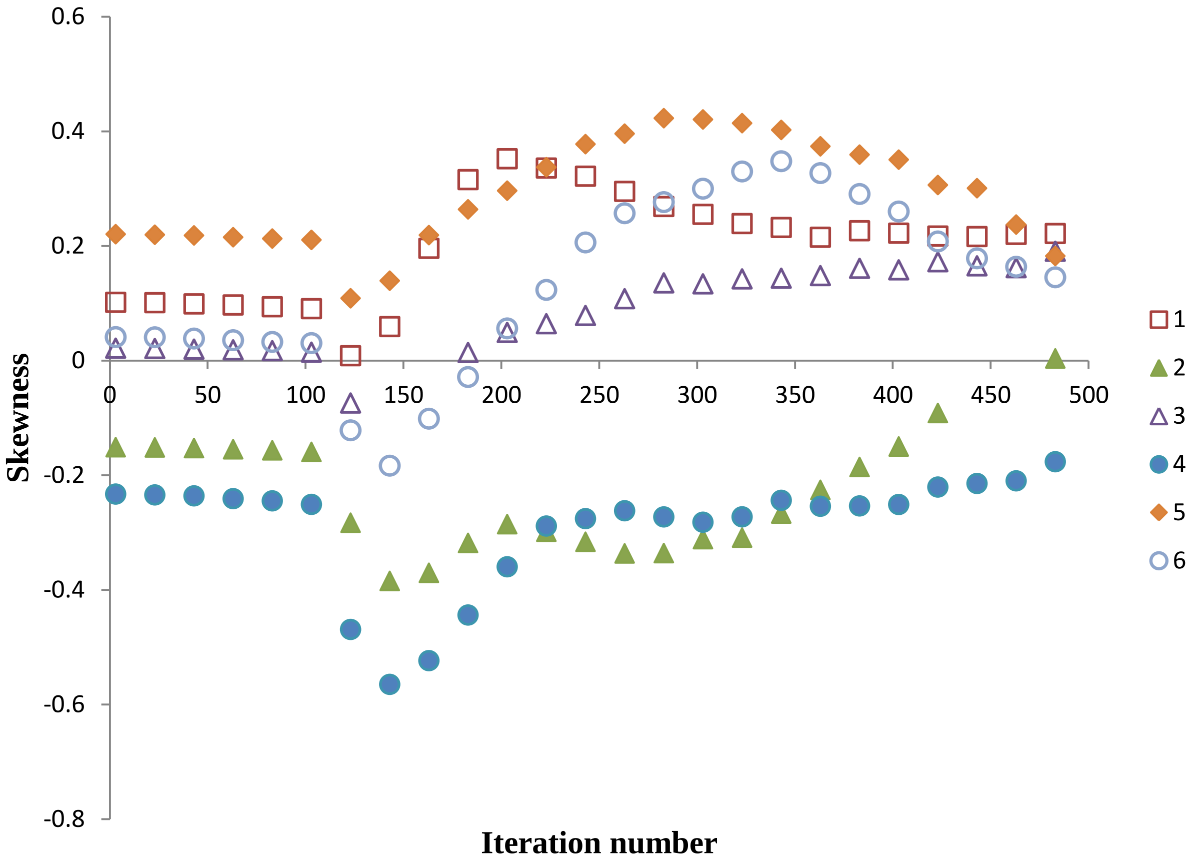

Figure 4-7- Skewness of 6 random surfaces, after being abraded for 500 iterations. Only select samples and every 20th iteration has been plotted for better clarity.

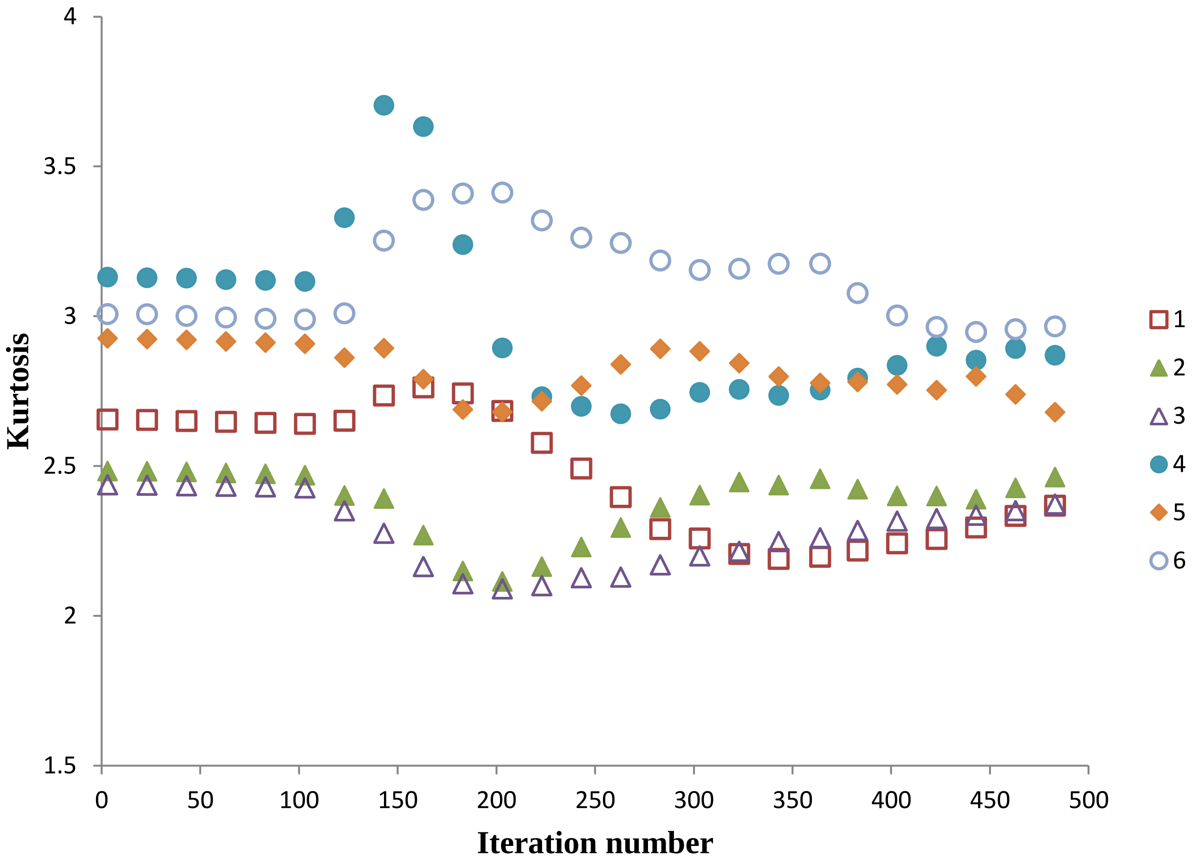

Figure 4-8- Kurtosis evolution of 6 random surfaces, after being abraded for 500 iterations. Only select samples and every 20th iteration has been plotted for better clarity.

Figure 4-6, Figure 4-7, and Figure 4-8 show an important aspect of the algorithm, that the surface roughness parameters are a property of initial surface that is inputted to the algorithm. It can be seen that the first 100 iterations produce a nearly constant values for all the parameters namely average roughness, Skewness, and Kurtosis. This was due to a combination of low value of lambda (4, compared to 2 for further iterations) and only abrading 15% fraction of the pixels. The parameter trends are expected as the height of the surface decreases minimally during initial 100 iterations, and hence minimum change occurs to topography. As the abrasion algorithm switches to λ=2, the surface parameters start varying at an increasing pace relative to first part of the abrasion algorithm. The average roughness trend decreases continually as the heights are progressively decreasing by the virtue to abrasion iterations. The Skewness and Kurtosis are topography dependent and behave accordingly, and trends cannot be predicted like average surface roughness. It is important to tune the number of iterations by looking at the surface topography after each iteration, as the trends cannot conclusively help identify when the surface topography has flattened or roughness is at minimum.

Only 3 surface roughness parameters have been shown here out of the calculated 27, as the other parameters were redundant in giving any information about topography changes, as discussed in the Chapter 3.

Each iteration takes 7 minutes on an Intel® Core i5 processor running at 2.33 Ghz with 4GB Random Access Memory (RAM), and 2 minutes on an Intel® Core i7 processor running at 2.67 GHz with 16GB RAM. The processing times are dependent on dimensions of the inputted initial topography to the abrasion algorithm. The times given here are for 1280 × 1024 spatial height matrix.

Above tests show how the abrasion algorithm provides unique surface parameter set for a unique surface topography. Next, the consistency of the abrasion algorithm was tested by feeding same surface topography ten times. If the algorithm reacts same for every surface, it would indicate the consistency. The input parameters were same as used for the previous test. Surface topographies are given names, surface A and surface B.

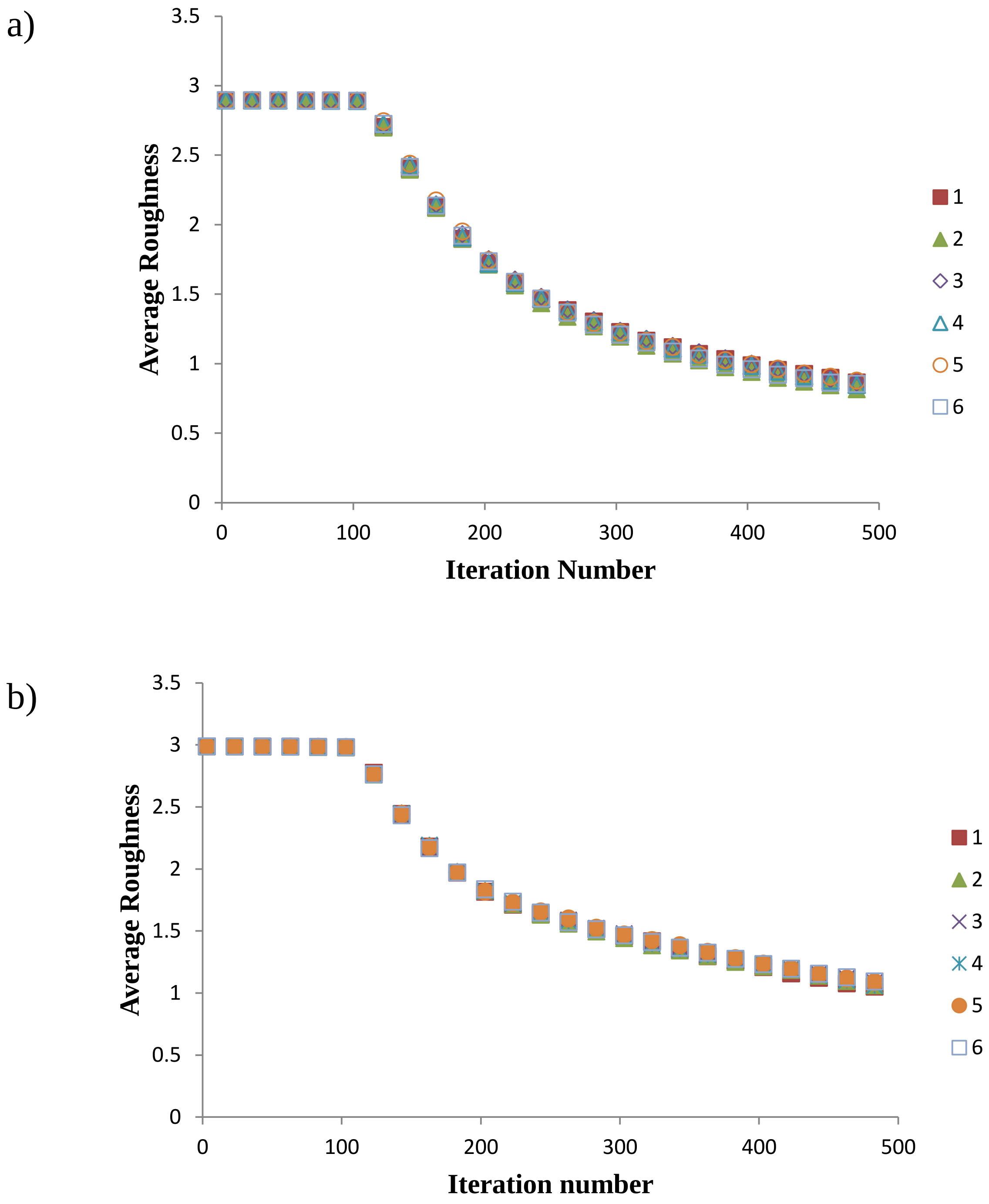

Figure 4-9 – Average roughness of a) Surface A, b) Surface B after undergoing 6 algorithmic abrasions. The legends show the abrasion number the surface is undergoing. Due to the magnitude being same for all the surfaces, only 6 abrasions have been plotted here.

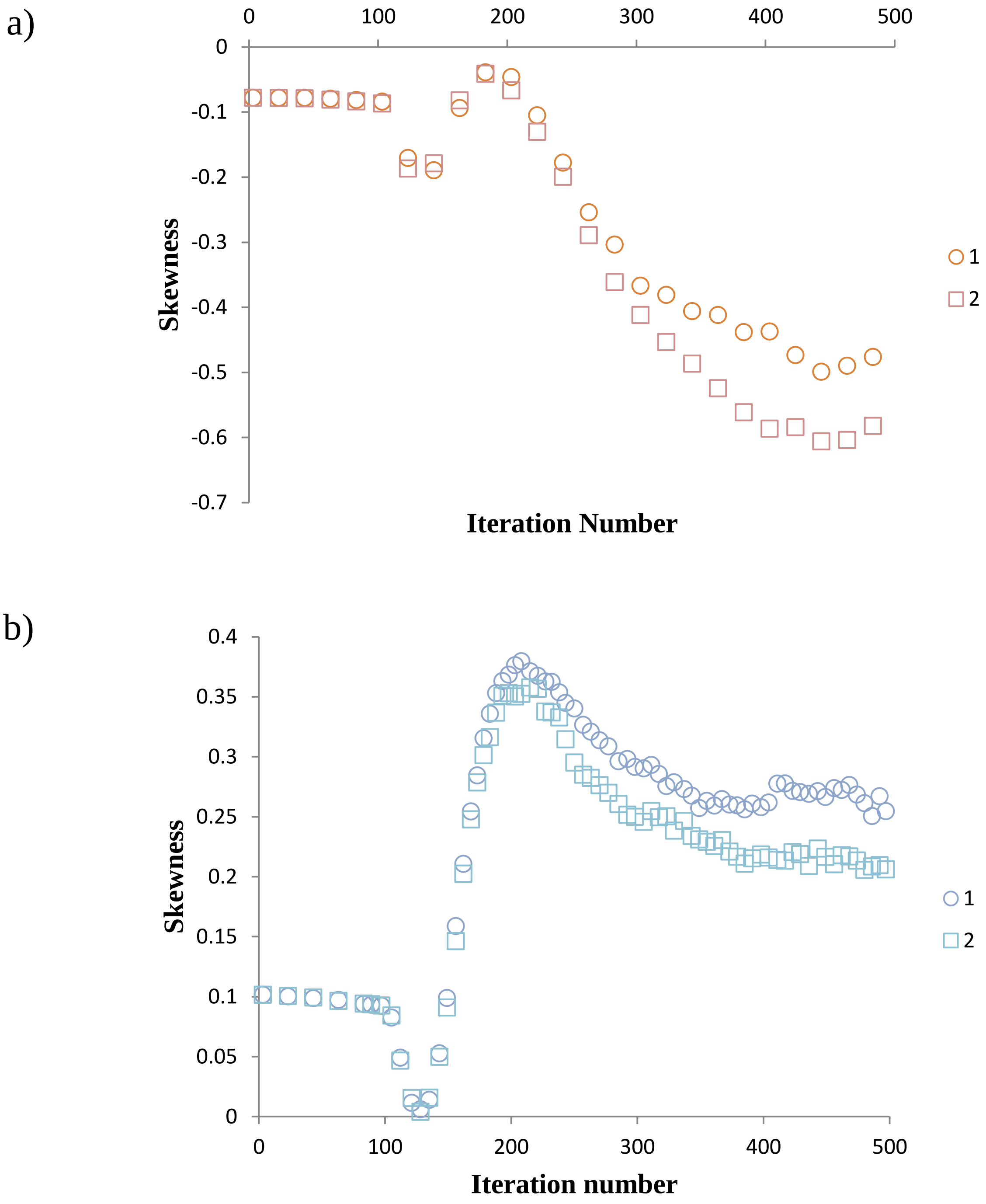

Figure 4-10 – Skewness of a) Surface A, b) Surface B after undergoing algorithmic abrasions. Only two surface abrasions, roughly the upper and lower bound of values, are shown for brevity. The legend shows the abrasion number.

a)

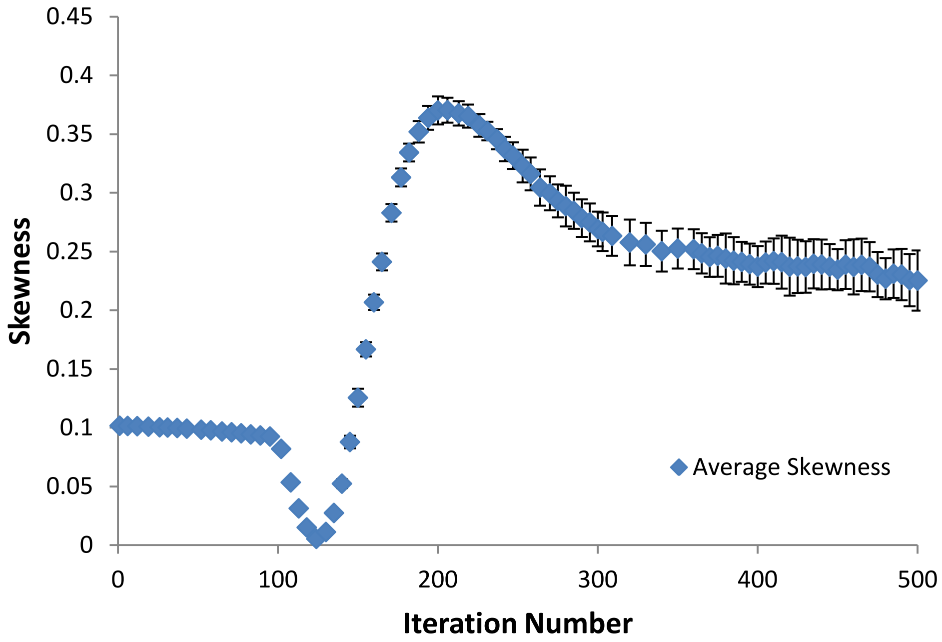

b)

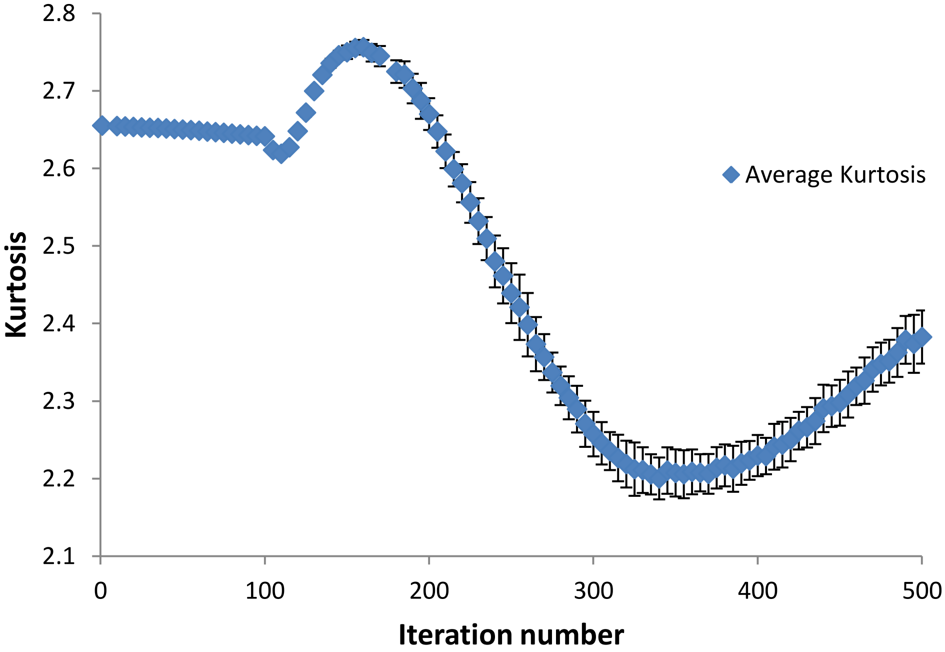

Figure 4-11 – a) Skewness, and b) Kurtosis for Surface B, after averaging all the ten abrasions. The abrasion algorithm was run for ten iterations on the surface B, and all the values were averaged. Error bars show the standard deviation.

Figure 4-9 shows the average roughness for two surfaces after abrading them ten times. All 10 surfaces abraded previously and shown in Figure 4-6, Figure 4-7, and Figure 4-8 were input to the abrasion algorithm ten times, and surface roughness parameters were recorded. Here only two surfaces were shown for brevity, as the results on all ten surfaces were similar. Figure 4-9 demonstrates how average roughness of the surfaces follows the exact same trend for all ten abrasion iterations. This shows how the surface is abrading consistently always, and abrasion algorithm works uniformly. Figure 4-10 (a) and (b) show the Skewness and Kurtosis for the surface, only the cases showing maximum and minimum deviation are shown. It can be seen there is no deviation until 300 iterations for both parameters, and even after that the deviation is not significant. Figure 4-11 shows this by averaging all the ten abrasion iterations of the surface B for Skewness and Kurtosis, the bars show the standard deviation. It can be seen that Skewness and Kurtosis do not change significantly until 300 iterations, and even after that the error is not significant with maximum being 0.027 for Skewness, and 0.042 for Kurtosis. The deviation after 300 iterations can be due to surface topography being abraded of peaks, and not the abrasion algorithm is iterating on the flat surface generation "noise".

These two tests show the uniqueness and consistency of abrasion algorithm. The abrasion is a function of the initial topography of surface, with surface parameters showing different trends accordingly if the input surface for each abrasion iteration was different. Within the same surface if it is abraded manifold, the abrasion consistent with the surface parameters of each abrasion iteration behaving consistently with same trends.

4.4.2 Finding ideal number of iterations, and calibrating λ and Δh values

Aside from surface topography, the surface roughness parameters are dependent on magnitude of the λ and Δh, and number of iterations should be calibrated as a time saving measure and observe when the surface topography has flattened. The abrasion algorithm is not topography aware and cannot detect a flat surface, and the effect of values of λ and Δh is not fully known. The combination of parameters previously described in Section 4.4.1 would help to determine how λ and the pixel values to be subtracted at each iteration (Δh) affect the roughness parameter trends. An indepth look into topography evolution after abrasion iterations would help calibrate number of iterations ideally needed for a given set of λ and Δh. Line profiles of the surface A are given below, all the profiles are for the same location on the topography.

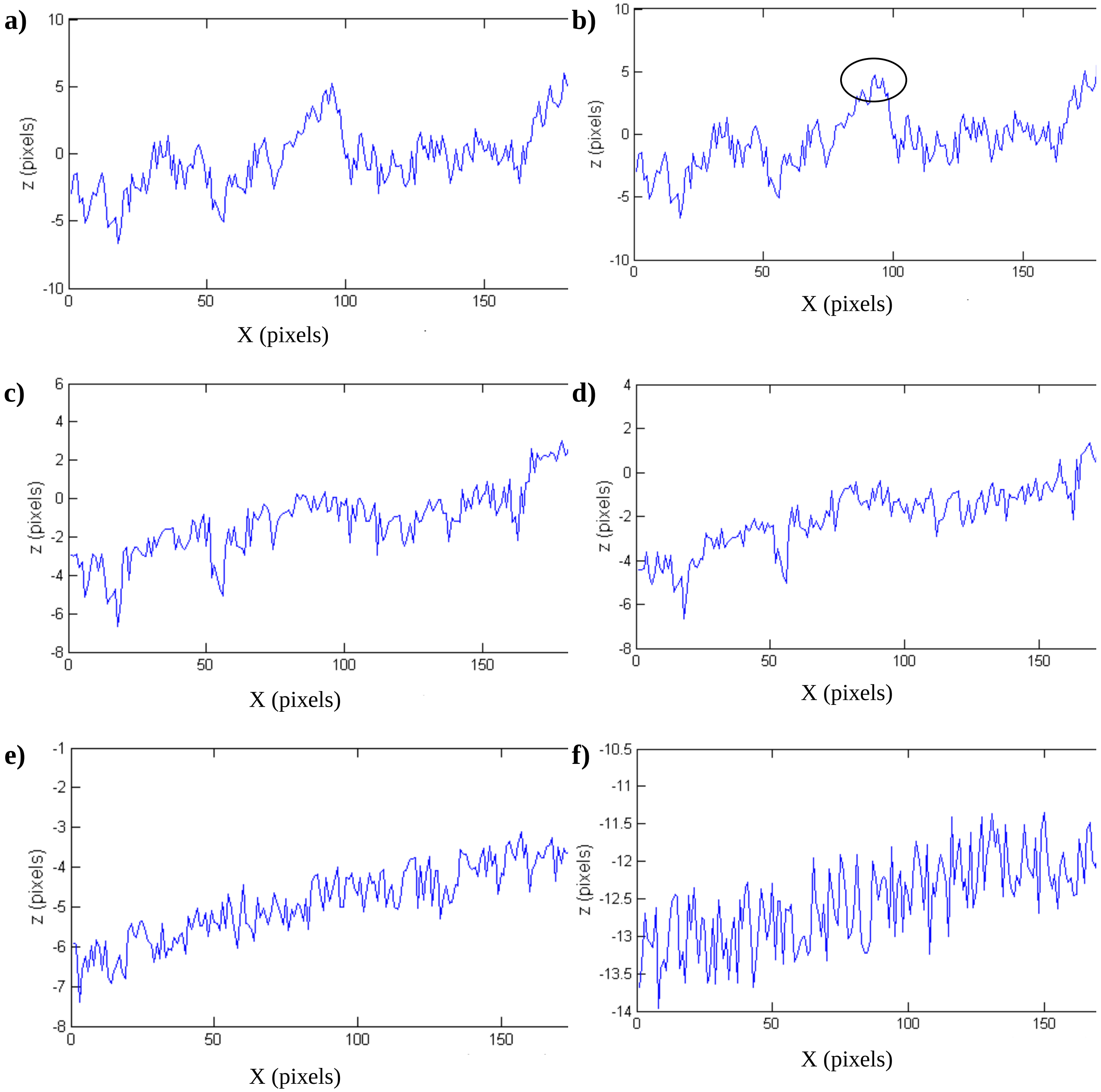

Figure 4-12 - Line profile for abraded surface (A) a) unworn, and after b) 100, c) 250, d) 300, e) 500, and f) 1000 iterations. The profiles are drawn at the same location. Abrasion parameters are: λ=10, and Δh= 1.4 - 1.5 pixels. The circled portion in (b) shows the only peak abraded after initial 100 iterations.

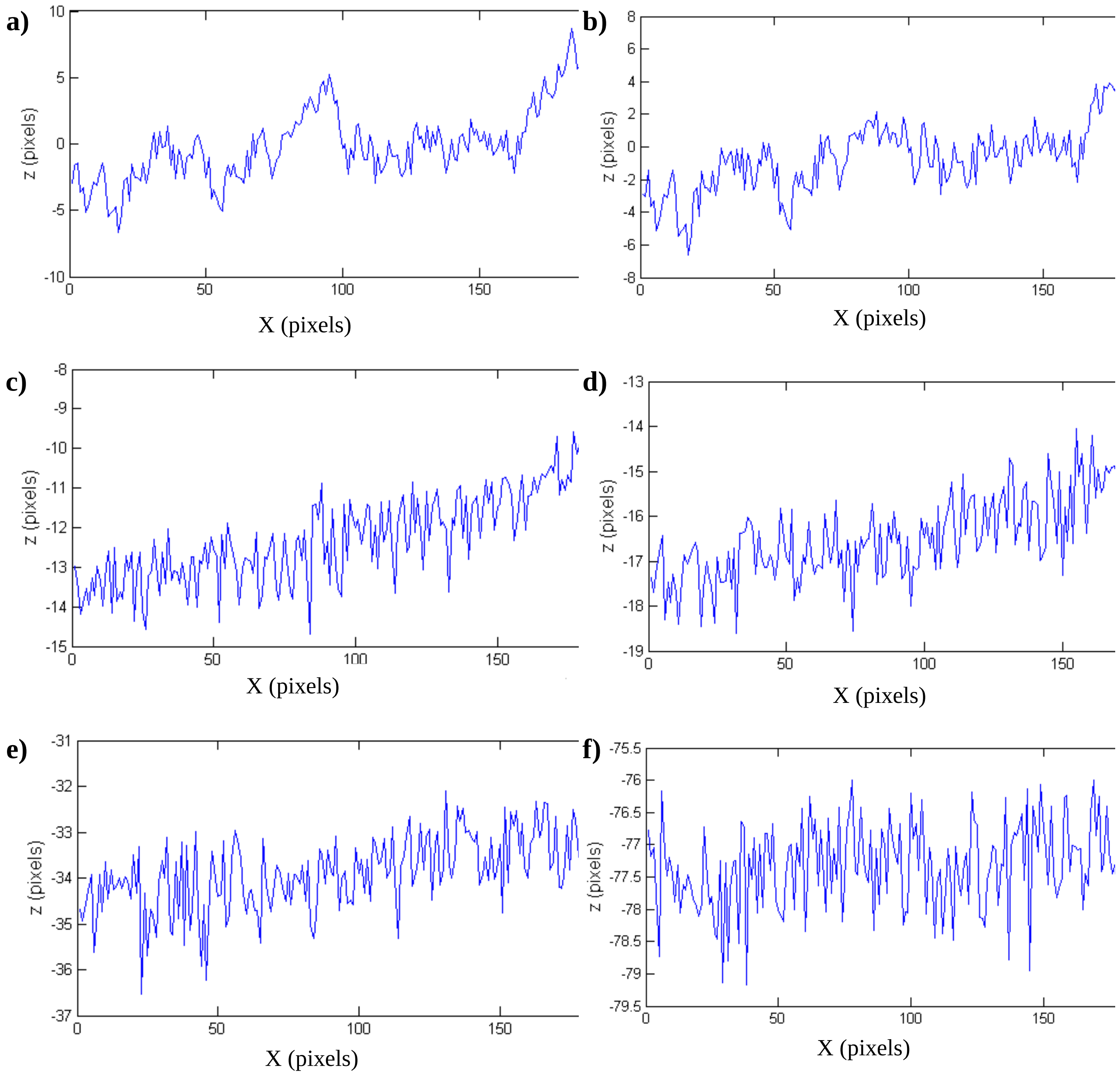

Figure 4-13 – Line profile for abraded surface A a) unworn, and after b) 100, c) 250, d) 300, e) 500, and f) 1000 iterations. The profiles are drawn at the same location. Abrasion parameters are: λ=2, and Δh= 1.4 - 1.5 pixels.

Surface A, generated by diamond square algorithm having dimension of 257 × 257, was abraded for 1000 iterations, with Δh= [1.40, 1.45, 1.50], and λ=10 for surface shown in Figure 4-12 and λ=2 for Figure 4-13. First 100 iterations were abrading only 30% of the surface area. Both figures show the line profiles at the same location of the surface after a set number of iterations. Comparing Figure 4-12 (a) and (b), it can be seen that only a minor height change results between column numbers 80-90, and encircled in Figure 4-12 (b). The minor change after 100 iterations is because the abrasion algorithm is working only on 30% of the total peaks. Figure 4-12 (c), (d) and (e) show the abrasion algorithm abrading the surface peaks, as line profiles show the appropriate decrease in peak height. The height profiles taken at different locations show the same trend. Comparing Figure 4-12 (a) and (e), the surface roughness has decreased to a minimum after 500 iterations, with Figure 4-12 (e) retaining prominently only the major slope of the surface. There will always be surface roughness after each iteration, and topography will not become ideal flat surface, as the Δh is subtracted after each iteration and only at selective random points. Figure 4-12 (a) through (e), the height of lower valleys remains roughly constant. As shown in Figure 4-12 (f), the next 500 iterations are adding "noise" to the surface, as reflected in the incrementally decreased height values and high roughness ("noise") of the surface. Hence, the last 500 iterations are not affecting the topography or surface roughness parameters significantly. Also, it should be noted that although the z – heights in Figure 4-12 and Figure 4-13 are in the negative, that is due to the value of the Δh chosen being aggressive, and also a combination of height of the initial surface.

In Figure 4-13, the surface abraded was the same as in Figure 4-12. Only difference was the factor λ, which was 2 instead of 10. As can be seen in Figure 4-13 (a) and (b), the first 100 iterations produced minor abrasion on the surface and only peaks are abraded. For next 150 iterations, the surface was nearly abraded flat with roughness along the major slope of surface, as shown in Figure 4-13 (c). The next 800 iterations from Figure 4-13 (d) through (f), are just adding noise to the surface and have similar slope but height magnitudes are decreasing. Hence from Figure 4-12 and Figure 4-13 it can be seen that abrasion is more severe for small values of λ, and becomes milder with increasing the λ. It takes 150 iterations with λ=2 for the surface roughness to decrease to a minimal, and with λ=10 surface flattens in 400 iterations. This excludes the first 100 iterations, as the effect on surface topography was minimal. Figure 4-12 (f) and Figure 4-13 (c) depict similar line profiles, and hence similar topography illustrating the abrasion severity achieved with lower value of λ. Also, the first 100 iterations which only act on a fraction of total peaks can be used to provide robustness to abrasion algorithm, in the case of surfaces where peaks only abrade mildly in initial time period. Although this step is not necessary for synthetic/physical terrains discussed in this thesis, as it takes considerably higher number of iterations and hence computation time without providing any adequate benefit as the roughness parameters remain nearly constant during this period.

Until now, only the effect of λ has been studied on the surface topography, now effect of Δh is compared by abrading ten surfaces generated by diamond square algorithm. Only one surface abrasion is shown here, but all the surfaces showed the same general trend. The surfaces were compared by using two values of λ (2 and 10) and three values of Δh. As previously described, Δh was chosen from a matrix of [0.40, 0.45, 0.50], [0.90, 0.95, 1.00] and [1.40, 1.45, 1.50]. The effects on surface topography are shown by virtue of line profiles on the same location among different abrasions.

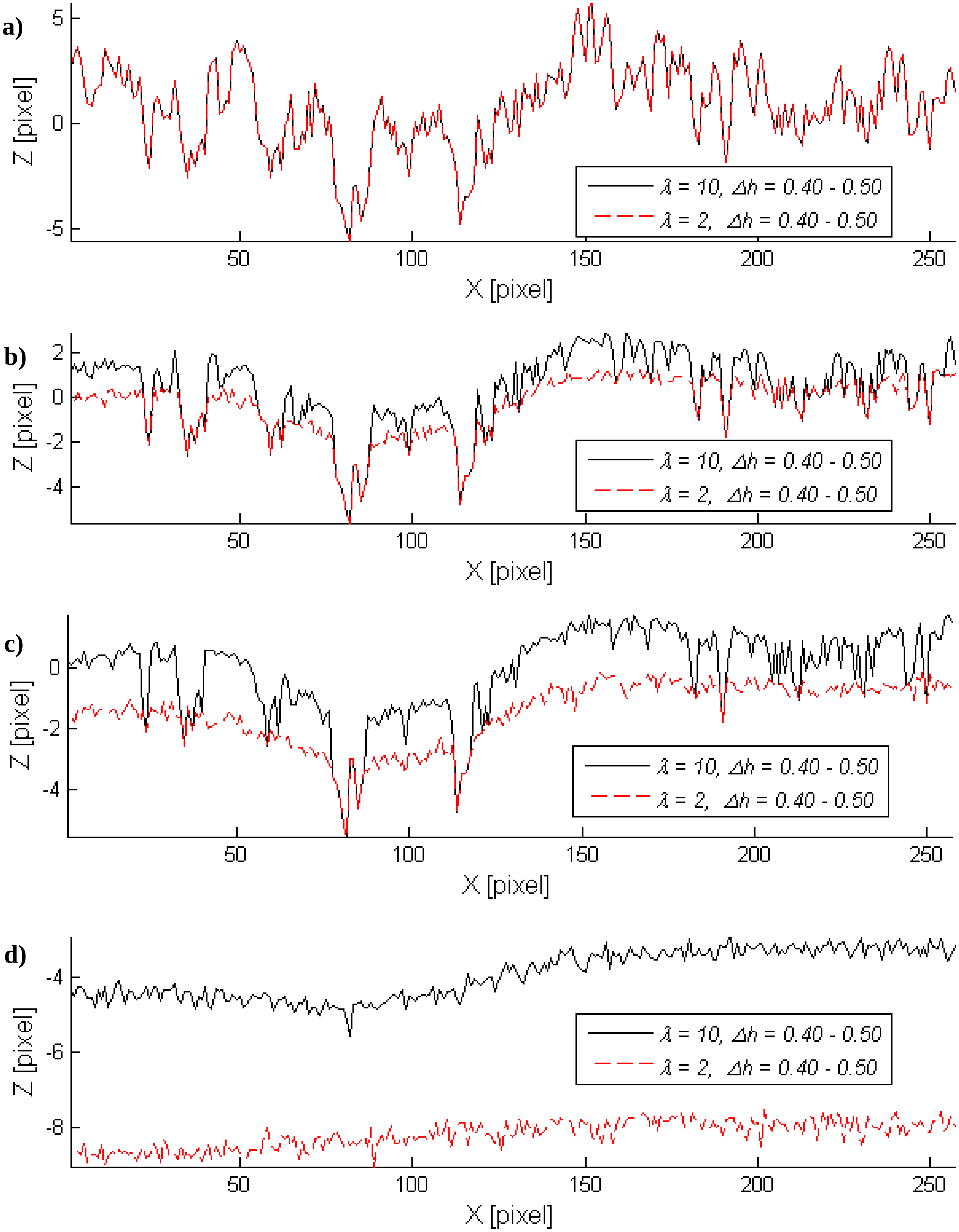

Figure 4-14 – Comparing surface A line profiles after: a) unworn, b) 200, c) 250, and d) 500 iterations.

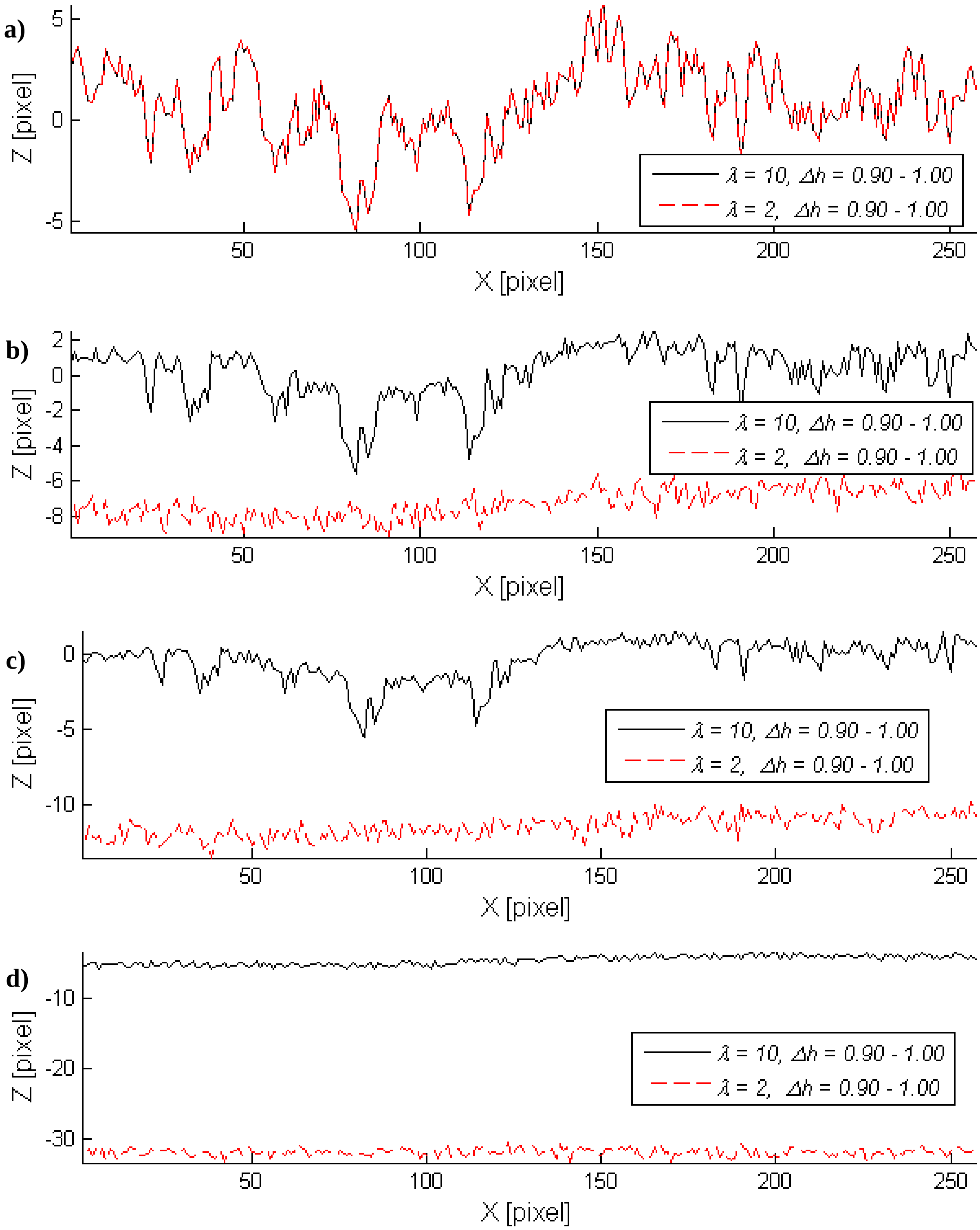

Figure 4-15 – Comparing surface A line profile at same location, after abraded for different λ at: a) unworn, b) 200, c) 250, and d) 500 iterations.

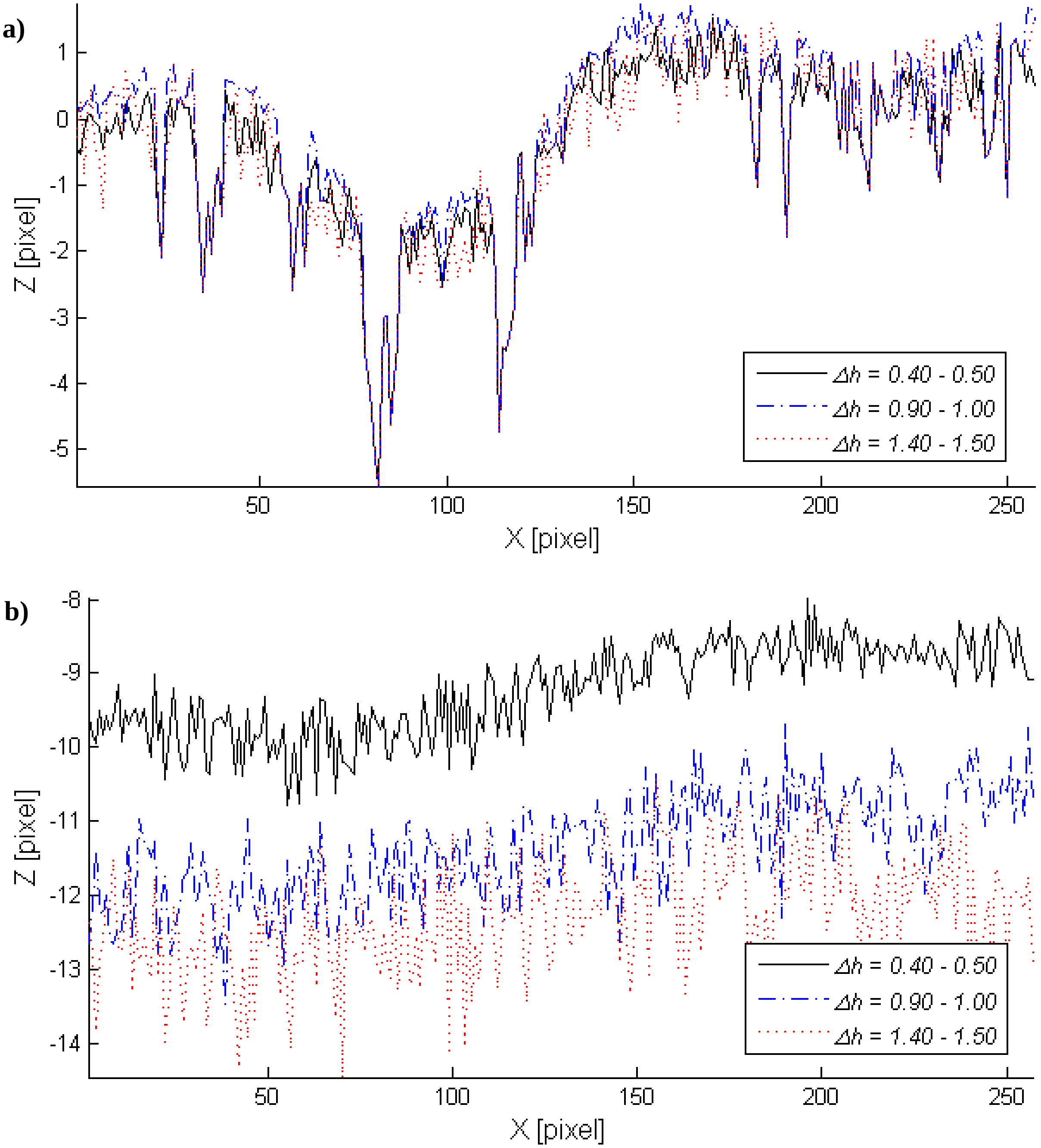

Figure 4-16 – Comparing surface A line profile at same location at 250th iteration, for a) λ = 10, and b) λ = 2.

Figure 4-14 shows the line profile at same location for a surface being abraded with different λ values. Figure 4-14 (b) shows that λ=2 abrades the surface faster, and also only peaks are prioritized. Also height magnitudes are reduced as abrasion iterations increase. Figure 4-14 (c) shows that in only 50 iterations, surface has abraded more rapidly by λ=2. Figure 4-14 (d) shows the surface has been abraded rapidly for λ=2, and peak heights have considerably less magnitude. It can be noted that the surface waviness is intact, and follow same trend for both values of λ. In Figure 4-15, *Δh* has been increased to [1.40, 1.45, 1.50]. Comparing Figure 4-14 (b) and Figure 4-15 (b) it can be seen that higher *Δh* has had more affect on surface being abraded with λ=2 than with λ=10. So higher *Δh* and higher λ abrade the surface aggressively. It can be noted that the surface has flattened almost completely in Figure 4-15 (d). As iterations increase, the surface height magnitudes increase progressively. Also, comparing Figure 4-15 (b) and Figure 4-14 (d) for λ=2, the line profiles are similar, showing that it takes longer iterations for smaller values of λ to arrive at similar topographies.

In Figure 4-16, surface line profiles are compared after 250th iteration for different values of *Δh* and λ. In Figure 4-16 (a), for λ=10 the surface does not show much different topography and is independent of *Δh*. In Figure 4-16 (b), higher values of *Δh* abrade the surface topography considerably faster, with [0.90 – 1.00] being more closer to [1.40 – 1.50] rather than being equidistant to [0.40 – 0.50]. Also, in Figure 4-16 (b), it can be seen that topography profiles for *Δh* =[0.90 – 1.00] is similar to *Δh*=[1.40 – 1.50], but the latter has more noise with former following the similar topography to *Δh*=[0.40 – 0.50]. Hence, small values of *Δh* should be used to avoid adding “noise” (unnecessary roughness) to the topography.

Hence, λ works akin to abrasion speed with smaller values being more aggressive on topography. Also, higher *Δh* has more effect on the surface topography if λ is small. There were six different random topology surfaces abraded with above procedures, and results are consistent among all of them. Smaller value of λ is efficient in abrading the topography fully in lesser number of iterations.

Ideal number of iterations for λ=2 are 250, with abrasion of selective percentage of peaks deemed unnecessary. For λ=10, ideal number of iterations for the surface to flatten are 500. Higher values of λ abrade surface slowly compared to lower values, and lower value of λ introduces comparable roughness in the topography with each abrasion algorithm iteration. The height to be deducted at each iteration, Δh, also affects the surface topography with lower values [0.40, 0.45, 0.50] abrading consistenly slowly than higher values of [1.40, 1.45, 1.50], although with low value of λ the effect is not prominent. Hence, to avoid introducing unnecessary roughness into the surface topography and a abrasion cycle that lasts within 400-500 iterations, λ should be between 2 and 10 with Δh being [0.90, 0.95, 1.00].

4.4.3 Effect of λ and Δh on Surface roughness parameters

Surface roughness parameters besides depending upon the topography, can depend upon how the surface is being abraded. To understand effect of λ and Δh on evolution of surface roughness parameters, surfaces were abraded by keeping either one of the two parameters fixed (Δh and λ) and changing the other. λ and Δh were chosen from the previously described group in Section 4.4.2. Following section shows the same surface being abraded by different parameters.

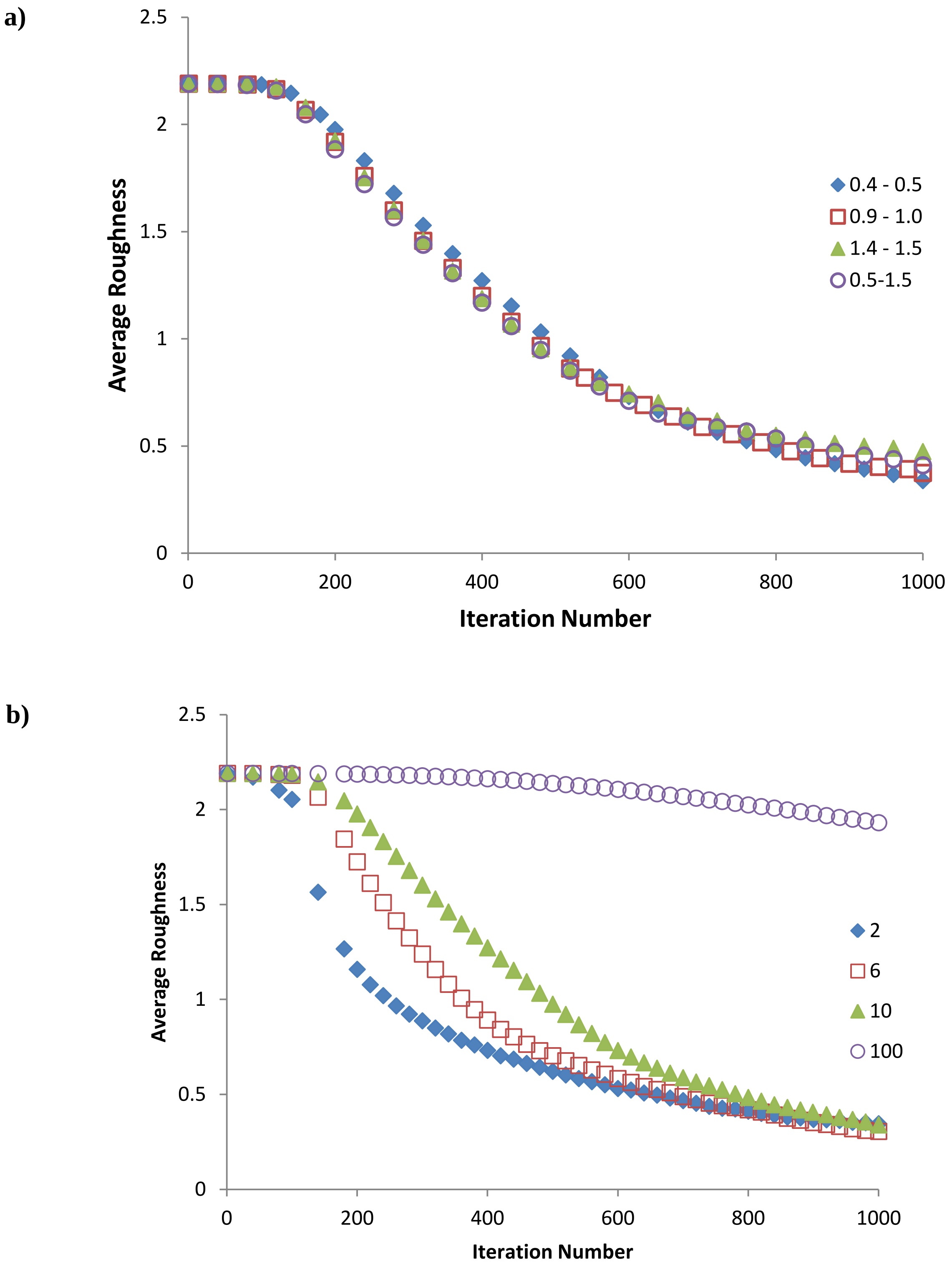

Figure 4-17 – Average roughness for the surface abraded with, a) λ=10, and Δh for a= 0.4-0.5, b=0.9-1.0, c= 1.4-1.5 and d=0.5-1.5., b) Δh=0.4 – 0.5, and λ for a= 2, b=6, and c= 10.

a)

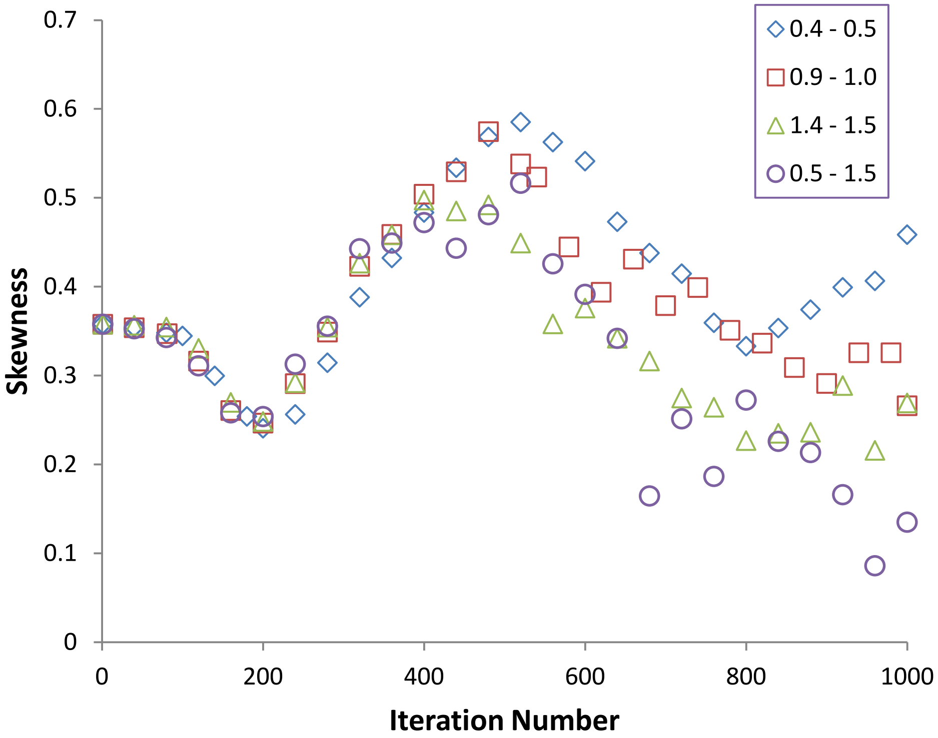

b)

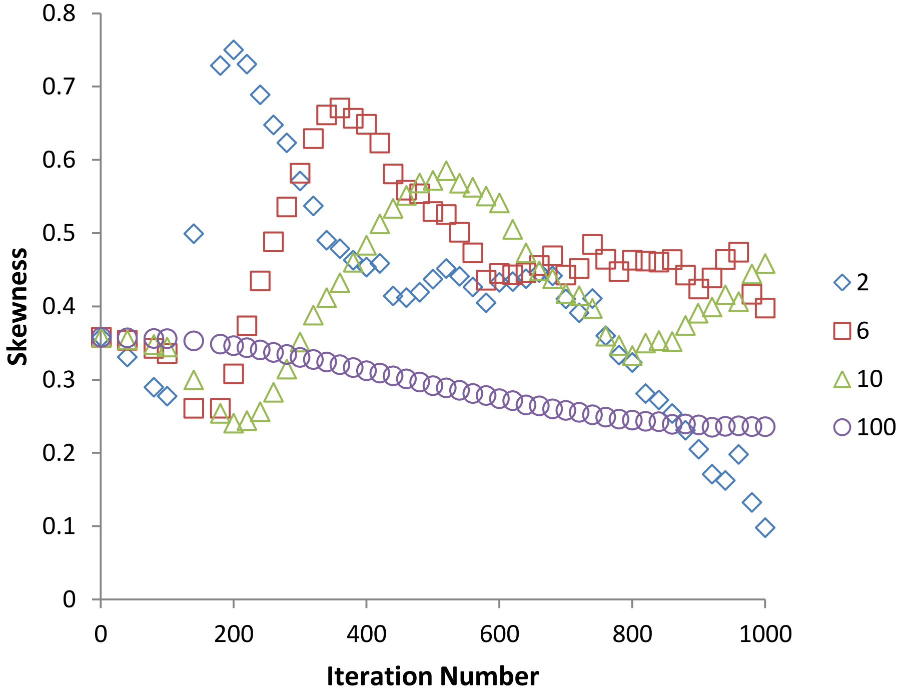

Figure 4-18 – Skewness for the surface abraded with, a) λ=10, and Δh for a= 0.4-0.5, b=0.9-1.0, c= 1.4-1.5 and d=0.5-1.5., b) Δh=0.4 - 0.5, and λ for a= 2, b=6, and c= 10.

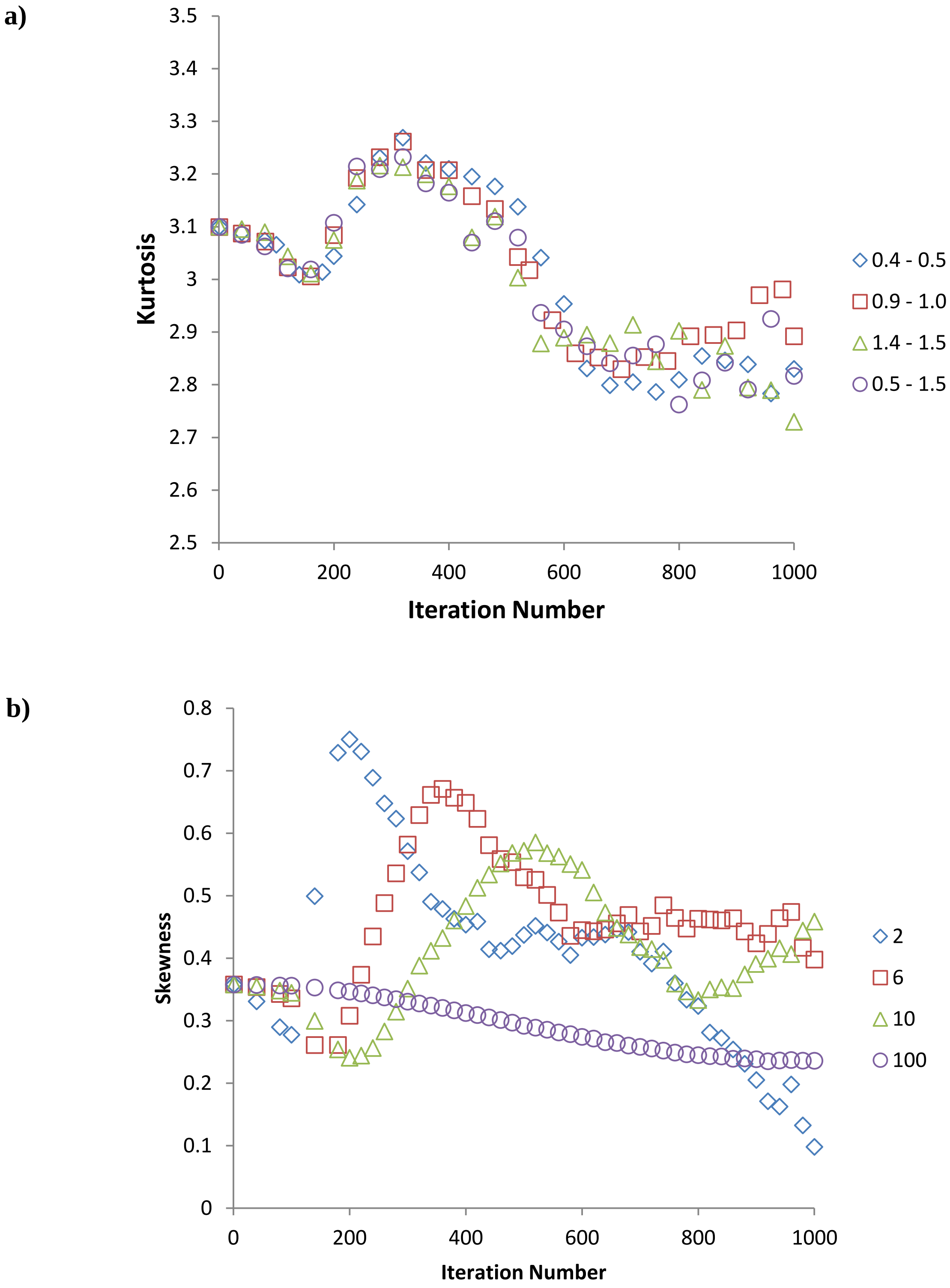

Figure 4-19 – Kurtosis for the surface abraded with, a) λ=10, and Δh for a= 0.4-0.5, b=0.9-1.0, c= 1.4-1.5 and d=0.5-1.5., b) Δh=0.4 – 0.5, and λ for a= 2, b=6, and c= 10.

From the above surface roughness parameter trends shown in Figure 4-17 (a), Figure 4-18 (a), and Figure 4-19 (a) it can be seen that Δh does not majorly affect the magnitude of the surface roughness parameters. This can be because the topography has the same shape but different height magnitudes, resulting in same trends for the surface parameters. The significant difference comes in after the 300 iterations when the surface flattens and the abrasion algorithm is iterating continuously introducing roughness contributing to wavering in roughness parameters. Here too, larger value of Δh generates significant roughness compared to smaller value of Δh. The same trends in average roughness, Skewness and Kurtosis were observed for different values of λ namely, 2, 6 and 100. Hence, Δh does not significantly affect the trends in surface roughness parameters.

Figure 4-17 (b), Figure 4-18 (b), and Figure 4-19 (b), used different value of λ for abrasions. The trends remain the same for all the roughness parameters although magnitudes differ due to λ working akin to abrasion speed. For different values of λ, the magnitudes achieved for all the roughness parameters are still similar albeit with minor variations, and are achieved with increasing number of iterations (depending upon value of λ). No significant deviation is found between parameters until the 500 iterations when the surface flattens and abrasion algorithm continues to iterate on surface topography. Also, it be seen through the effect of increasing values of λ, that the surface roughness parameters also shift right showing same trend after more iterations. This is directly correlated to surface topography, and the effect is more pronounced for $\lambda = 100$. Hence, it can be surmised that the parameter, λ, is artificial analogue of abrasion speed. Particularly, Figure 4-17 (b) shows how average roughness, hence surface heights, decreases slowly showing the mild behavior of low values of λ.

The same trend in all the above graphs *vis-à-vis* Figure 4-17, Figure 4-18, and Figure 4-19, is followed by different values of Δh. It can be seen that unlike changing Δh, λ produces a significant difference in trends. As λ increases, the trends of Skewness and Kurtosis spread out. Above graphs also show that with increasing λ, abrasion becomes milder.

The choice of value of *Δh* has an insignificant difference on roughness parameters than the value of λ. Value of λ should be chosen dependent upon the need to aggressively abrade the surface with less number of iterations. The other trade-off is the addition of noise into surface topography with lower values of λ. Hence, the value of λ should be decided upon choice of topography to be input into the algorithm. Table 4-1 summarizes how the parameters inputted to the abrasion algorithm influence the abrasion outcome.

Table 4-1: Effect of algorithm parameters on abrasion outcome

Abrasion Parameter	**Parameter behavior**	**Abrasion outcome**
Number of iterations	Defines the number of iterations to be performed upon the topography.	Number of iterations should be dependent on the magnitude of λ and Δh. Low magnitude of λ requires less number of iterations.
λ	Defines the "aggressiveness" of the abrasion, works akin to abrasion speed.	Smaller value of λ abrades topography faster, introduces noise with each iteration, and requires less number of iterations. Large values of λ abrade topography slowly, requires more number of iterations. λ is the most important parameter, which should be chosen first, depending upon the topography inputted to the algorithm. It influences the addition of noise more prominently, and the aggressiveness of the abrasion algorithm. Different values of λ, produce similar trends in roughness parameters.
Δh	The pixel height to be abraded at each iteration.	Large values of Δh abrade a surface in less number of iterations but introduce significant amount of noise in the topography, compared to small values. To avoid adding noise to the topography, it is advised to use $\Delta h \leq$ 1.00 pixels, with smaller values of λ ($\leq$2). While with larger values of λ, topography behavior is similar. Δh has insignificant effect on the surface roughness parameters trends.

4.5 Abrading PTFE SHS surfaces with abrasion algorithm

The abrasion algorithm was developed to make the time consuming process of gathering surface roughness parameters from physical PTFE SHS easier. The spatial information of the PTFE SHS was gathered from CSM imaging data. The spatial elevation matrix had dimensions of 1280 × 1024. In previous section, the suitable parameters for the surfaces were determined, and the response of the algorithm to various input parameters was analyzed. In this section, PTFE SHS surfaces are abraded using the abrasion algorithm and the simulated surface roughness parameters are analyzed and compared to actual roughness parameters. Other input parameters used were $\lambda=2$, and $\Delta h = [0.90, 0.95, 1.00]$. This combination will rapidly abrade the surface with less number of iterations required, and the "unnecessary roughness" introduced will be moderate. The abrasion algorithm was run for 250 iterations initially, as depending upon the roughness parameter behavior the iteration number could be changed afterwards too.

It is pertinent to mention again, that the abrasion is a stochastic phenomenon and surface roughness parameters trends are important. The abrasion algorithm is not an exact replication of physical abrasion done on PTFE SHS, but an approximate replication. Some of the factors not accounted in abrasion algorithm are: a) Physical abrasion was not point abrasion, as is being done by the abrasion algorithm, b) Physical abrasion generally generated flat domains and flat peaks, c) Valleys on PTFE SHS have tendency to be filled by flexible material bending due to abrasion, d) The abrasion on PTFE SHS was not uniform and was location dependent. Hence, there can be variability in results between surfaces abraded physically and by abrasion algorithm, and the focus of this study will be finding similar trends between the surface roughness parameters.

Simulated roughness parameters on PTFE SHS are shown in Figure 4-20, Figure 4-21, and Figure 4-22. The surfaces are named 2 and 4, signifying sample 2 and 4, respectively. Only 2 samples are shown for clarity purposes, as all the samples followed the same trend. Per surface, there was CSM imaging data available for three different locations. Hence, three spatial data matrices were inputted into abrasion algorithm for a single surface, and the data plotted is average of the three locations per surface. The error bars show the standard deviation among the data.

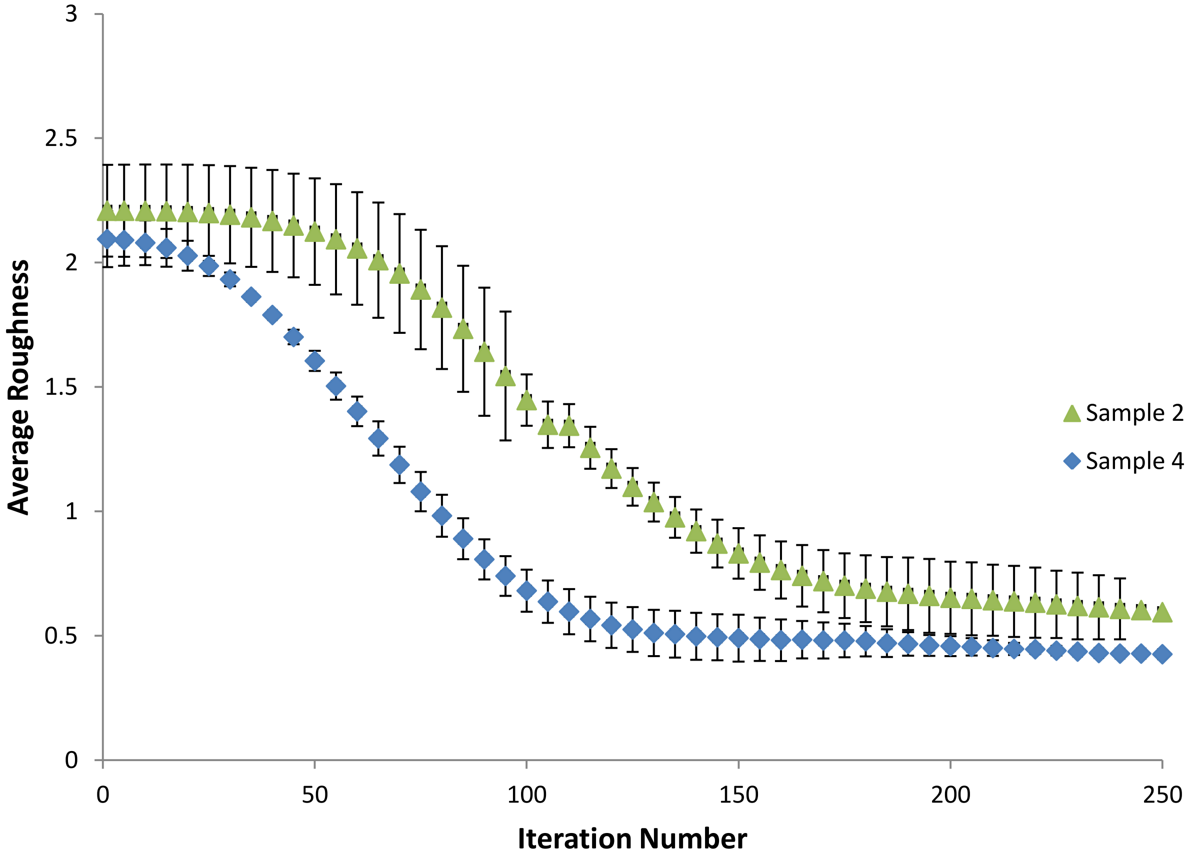

Figure 4-20 – Average roughness of the PTFE SHS abraded by abrasion algorithm; λ=2, and Δh = [0.90, 0.95, 1.00].

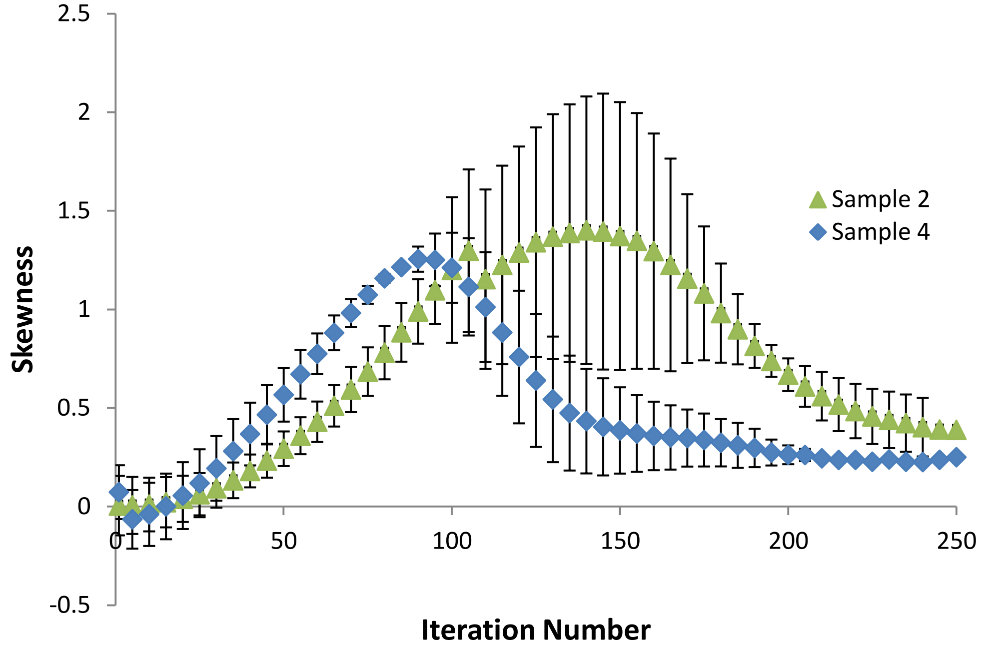

Figure 4-21 – Skewness of the PTFE SHS abraded by abrasion algorithm; λ=2, and Δh = [0.90, 0.95, 1.00].

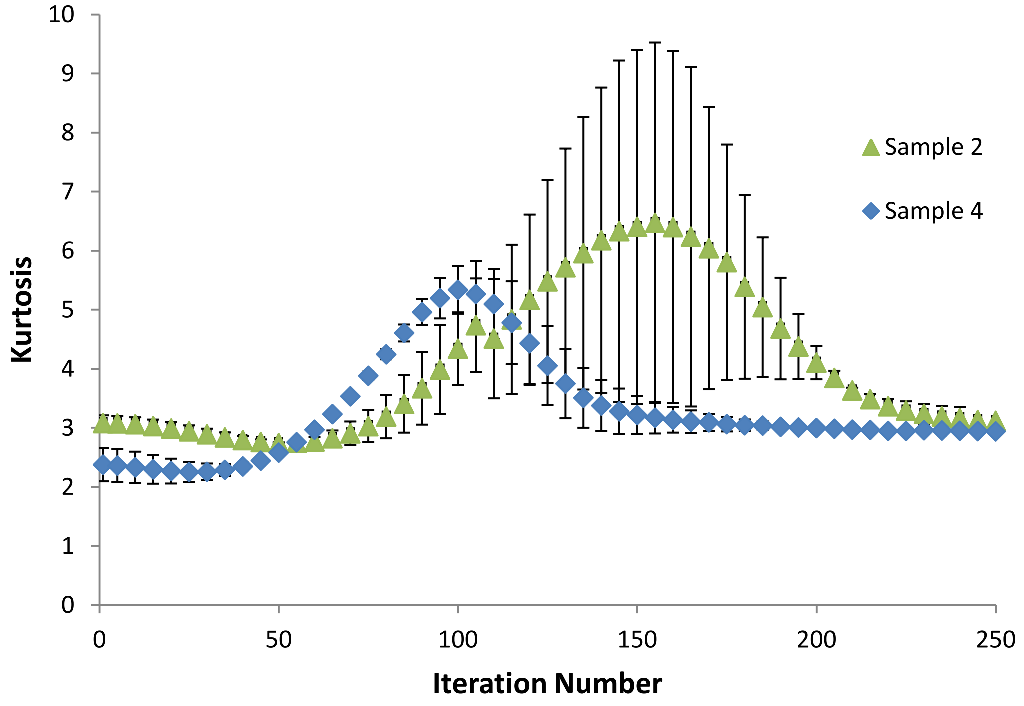

Figure 4-22 – Kurtosis of the PTFE SHS abraded by abrasion algorithm; λ=2, and Δh = [0.90, 0.95, 1.00].

Figure 4-20 shows the average roughness of the two samples, and it shows the same trend for both of the samples. The heights are being abraded, and the roughness decreases progressively as expected. Figure 4-21 shows the Skewness and the trends are the same, except sample 2 shows the greater magnitude and variation in values than sample 4. It takes more iterations for sample 2 to show the same trend in the curve. The crest for sample 4 is reached at approximately 90 iterations, but it takes 50 more iterations for sample 2. The difference arises due to topography difference, and attests to the uniqueness of the abrasion algorithm. Also to be noted is that the standard deviation for the Skewness values is significant, maximum of 0.69 for sample 2, and 0.33 for sample 4. The same trend is followed by the Kurtosis graph in Figure 4-22, with sample 2 Kurtosis peaking after 150 iterations, instead of around 100 iterations for sample 4.

Skewness increases as the peaks are getting removed, and as the valleys start decreasing, it shows a decreasing trend culminating with a nearly constant Skewness due to flattening of surface.

In Figure 4-23 to – Comparing physically and synthetically abraded Kurtosis of sample 4.Figure 4-28, the simulated roughness parameters are compared with physically calculated parameters. Since the abrasion algorithm lacked temporal resolution, so average roughness was the factor used to resolve the iterations into corresponding time scale. Average roughness was chosen as it was a simple parameter that only accounts for height magnitudes and is shape agnostic. Since, abrasion (physical and algorithmic) shaves heights, average roughness was a suitable choice. Simulated and physically calculated average roughness data magnitudes were compared, and corresponding iteration number and time of abrasion was used as a scale.

For sample 2, using average roughness as a factor, every 25 simulated algorithmic iterations are similar to 3 minute abrasion on PTFE SHS. Figure 4-23 shows both synthetic abrasion and physical abrasion on a single graph. It can be seen that the values are a very close match. Figure 4-26 shows the average roughness for sample 4 comparing values on both physically and synthetically abraded surfaces. For sample 4, 30 iterations equal 3 minute of iterations. Hence, all the other roughness parameters used this scale for the respective samples.

Average roughness graphs (Figure 4-23, and Figure 4-26) show the same trend for both the samples. The magnitude for both synthetic and physical abrasion align up for the samples, with minor deviation seen for sample 2 initially. This validates the abrasion aspect of the abrasion algorithm, and the scale used for calibrating temporal resolution for the samples. Also, 250 abrasions are sufficient for obtaining surface roughness parameters, as the surface is devoid of any superhydrophobicity after approximately 30 minutes of abrasion. The abrasion algorithm thus abrades surface heights in a similar magnitude as done by gyrotory shaker. Average roughness is only dependant on height though, and Skewness and Kurtosis are dependent on shape.

Figure 4-24 and Figure 4-27 compare the Skewness for actual and algorithmic abrasions on sample 2, and 4, respectively. Skewness is a measure of symmetry of the profile, specifically positive Skewness indicates abundance of peaks and negative Skewness points towards presence of valleys. Also, Skewness is sensitive to high peaks and deep valleys [31]. For both the samples, the actual Skewness trend aligns with the simulated Skewness trend. The simulated magnitude rises in same trend as actual Skewness, and the simulated crests match roughly with actual crests, and the Skewness then stays roughly constant for both the abrasions. This behavior is seen both the samples. Sample 2 trends and magnitudes for average roughness, Skewness, and Kurtosis are an exact match for both physically and synthetically abraded surface (taking note of standard deviation in both the abrasions). The difference in magnitude for sample 4 is addressed later in this Section.

Kurtosis comparison for physical and synthetic abrasion on all three samples is shown in Figure 4-25, and Figure 4-28. Kurtosis is a measure of “peakedness” and “flatness” of surfaces relative to normal distribution. A surface having few peaks and high valleys shows Kurtosis value lower than 3 and vice-versa. Comparing the sample 2 (Figure 4-25) the trend is similar for both physical and synthetic abrasion. Kurtosis stays constant until ~60 abrasions (6 minutes) and then starts increasing. After reaching at peak, the physical abrasion Kurtosis values show a large amount of deviation (~3), hence any conclusion will not be accurate but the general trend for algorithmic abrasion agrees with the physical abrasion. Figure 4-28 shows the Kurtosis comparison of physical and simulated abrasion, for sample 4. Kurtosis for physical abrasion follows a bell curve trend, with slope starting to increase around 40th iteration and reaching the crest around iteration number 110. Afterwards, the slope starts decreasing similarly and becomes approximately constant.

The difference in trends and magnitudes was expected due to some deficiencies in abrasion algorithm as discussed earlier. Reiterating, physical abrasion on surfaces was a stochastic phenomenon and the methodology was simulated using peppering the surfaces randomly with abrasion heights. The exact replication of abrasion, hence, is not possible and trends in roughness descriptors are the main focus. This was also dealt with in Chapter 2 and 3, that the trends in roughness parameters are a helpful pointer towards a wetting state of surface.

Importantly, the trends in all the roughness parameters are similar, and mimic the actual physical abrasion parameters. Average roughness values were an exact match, exhibiting confidence in the way the abrasion algorithm works regarding abrading the topography. Kurtosis trends were the same, except the magnitudes were considerably less and the trends were expedited by 30 iterations (or 3 minutes) approximately.

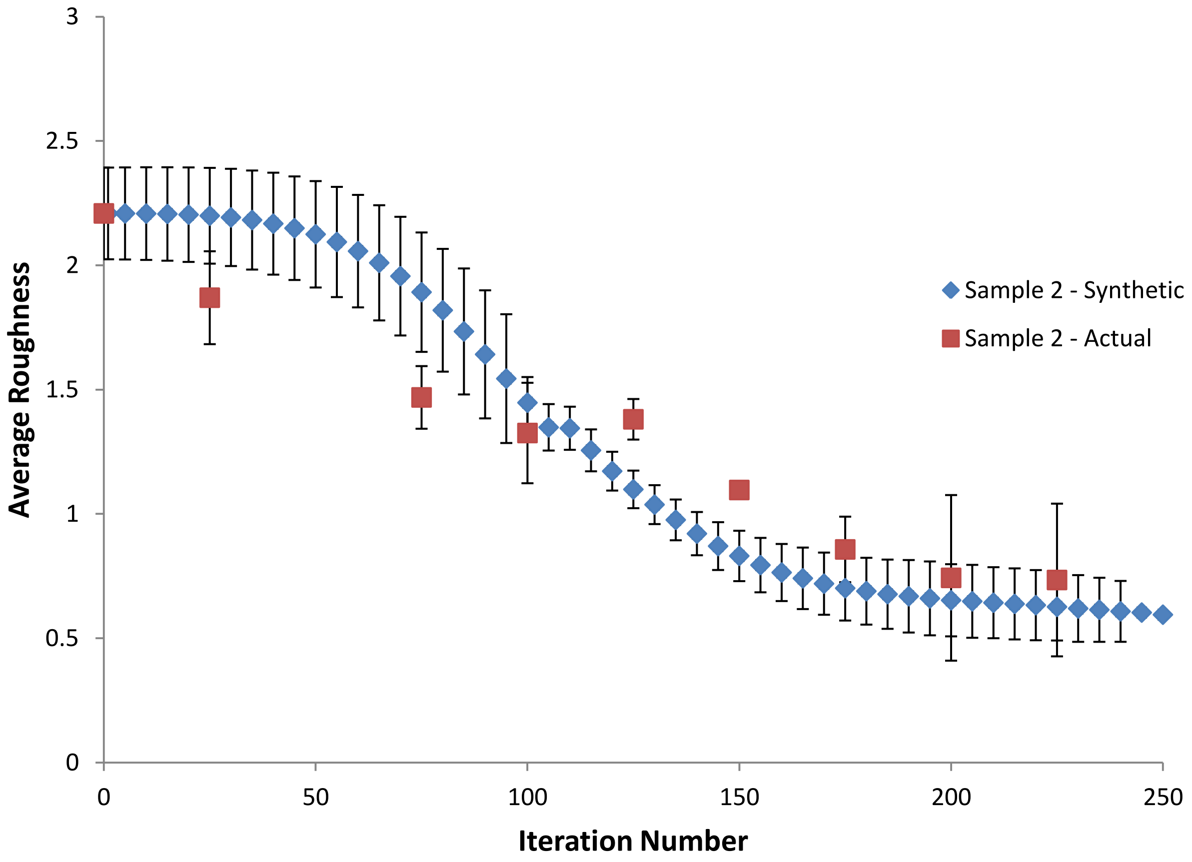

Figure 4-23 – Comparing physically and synthetically abraded average roughness of sample 2.

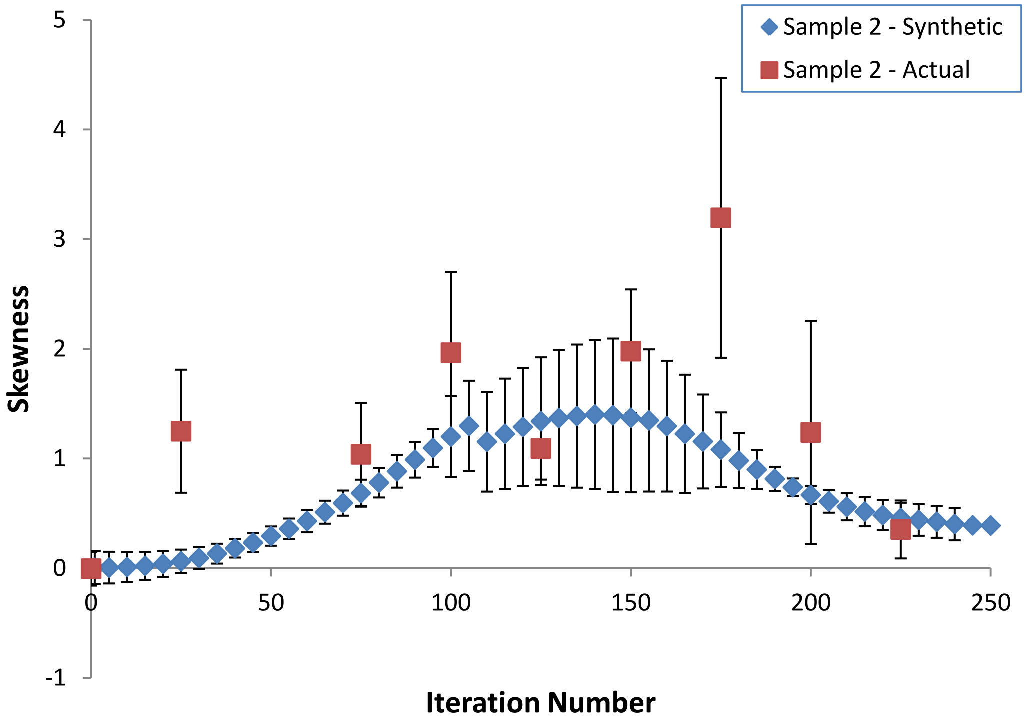

Figure 4-24 – Comparing physically and synthetically abraded Skewness of sample 2.

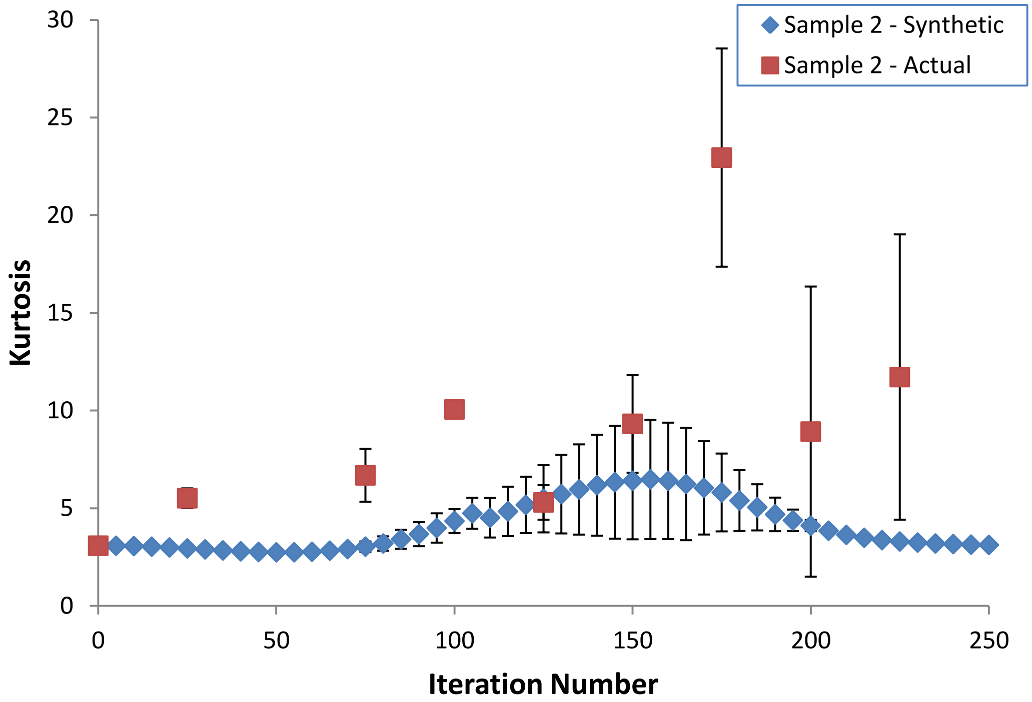

Figure 4-25 – Comparing physically and synthetically abraded Kurtosis of sample 2.

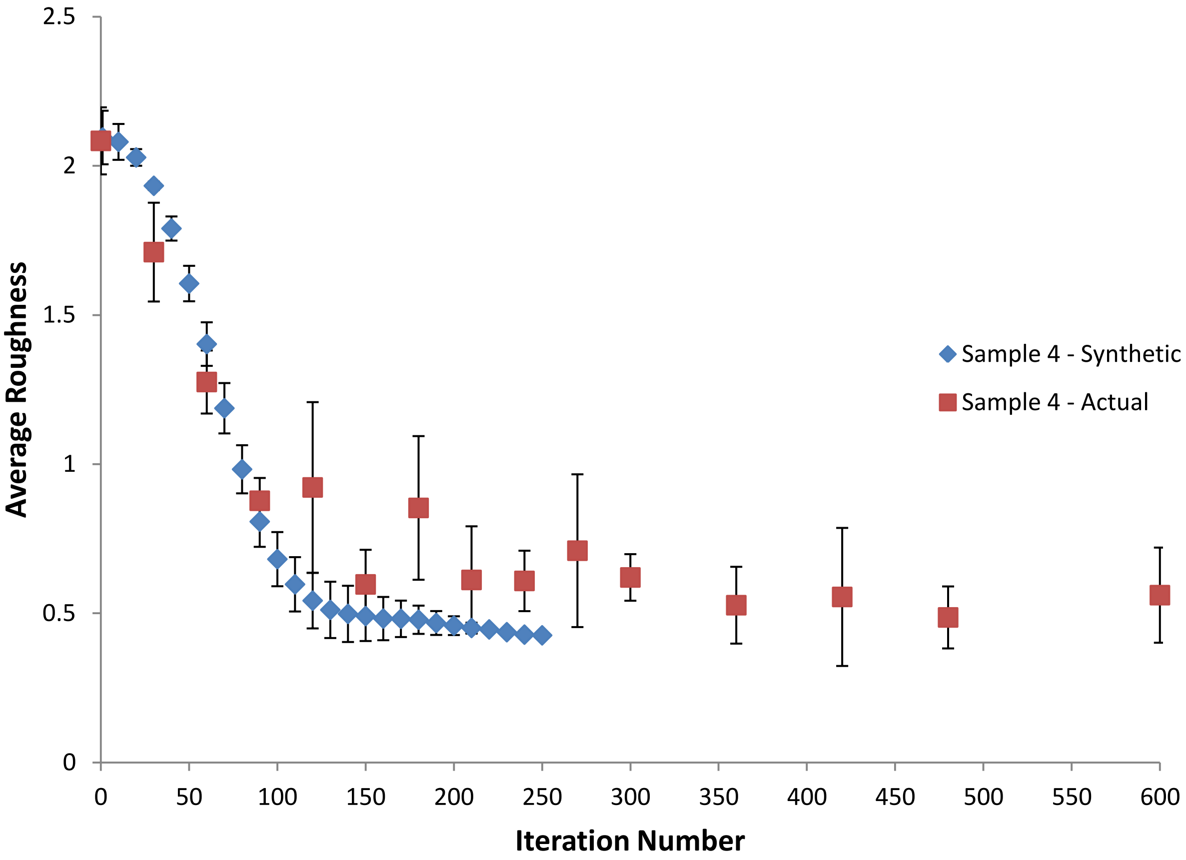

Figure 4-26 – Comparing physically and synthetically abraded average roughness of sample 4.

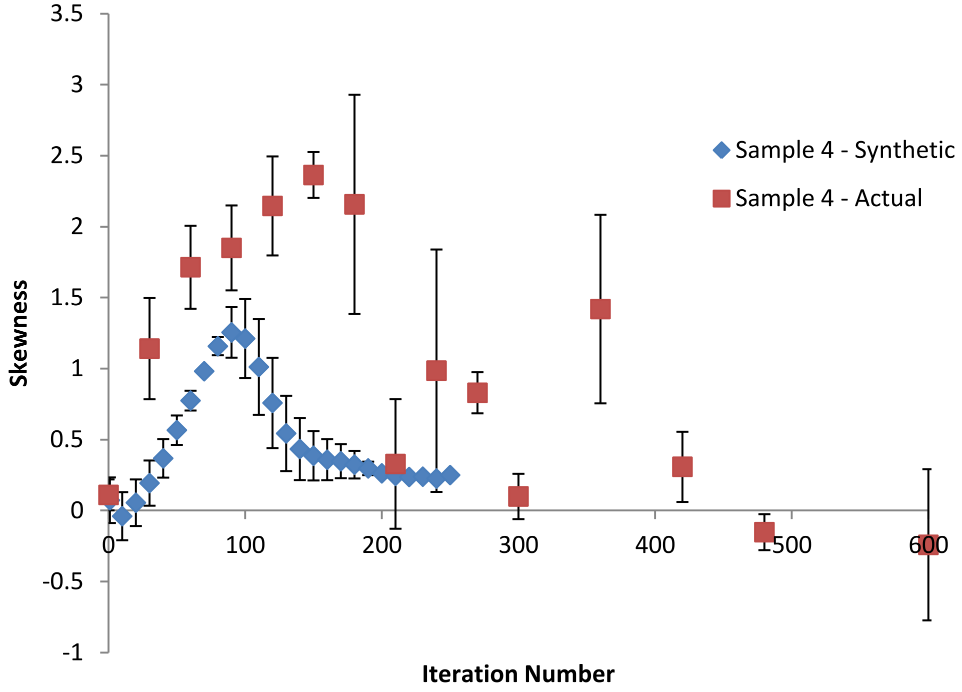

Figure 4-27 – Comparing physically and synthetically abraded Skewness of sample 4.

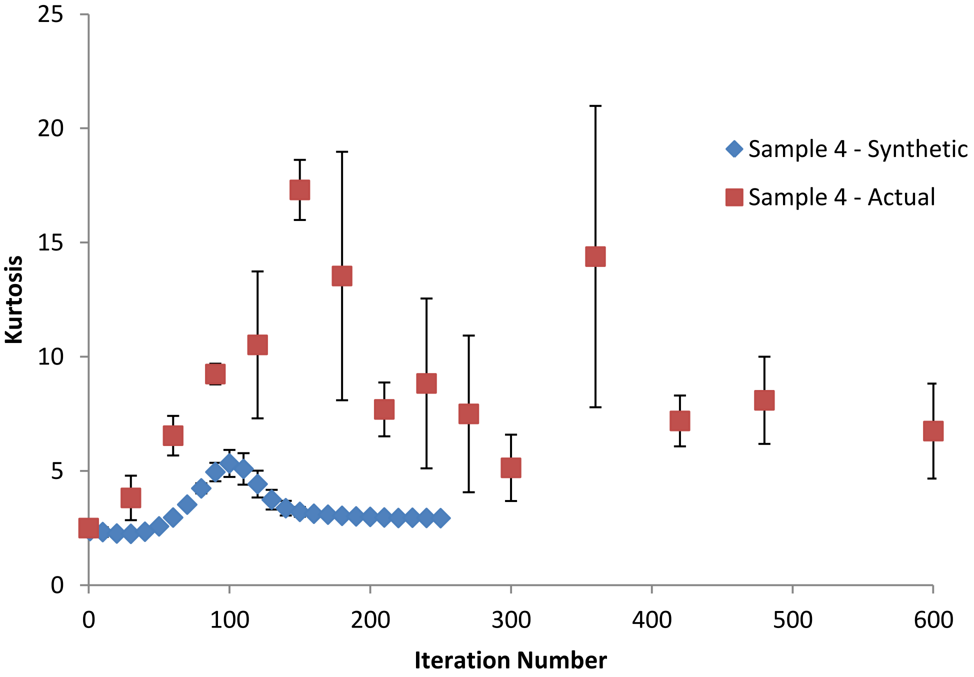

Figure 4-28 – Comparing physically and synthetically abraded Kurtosis of sample 4.

For sample 4, Skewness and Kurtosis magnitudes for synthetically abraded samples are approximately half that of physically abraded terrains, and are expedited by ~50 iterations (or 6 minutes). Since the difference is in the magnitudes and not the trends, it was decided to increase the magnitude of values (decided after numerical comparison) and compare with actual abrasion values. Figure 4-29 shows the comparison of twice magnified Skewness values with actual values. Figure 4-30 shows the comparison of the twice magnified magnitude values with actual Kurtosis values. Only the values after 30 iterations were magnified. The trend and magnitude display high degree of similarity for both Skewness and Kurtosis. Importantly, in the initial regime (see previous chapters) when the surface still is superhydrophobic, the values and trends are similar.

Skewness is a measure of tails of a height distribution, while Kurtosis is a measure of its peakedness. To attain the magnitudes attained by physical abrasion for Sample 2 and 4, a select number of peaks needed to be abraded rapidly such that the height distribution achieves a right tail, and a pointy peak. This is due to the fact that as shown in Section 2.4.1, a percentage of entire peaks were abraded after 3 minutes of wear and flat plateaus started appearing. The simulated magnitudes then would have achieved closer values to the actual Skewness and Kurtosis values. The abrasion algorithm was not trained to do so, as the aim of this thesis was a broader one, such as a stochastic abrasion can be simulated on a random topography and mapping the behavior of the algorithm. Training the algorithm would have meant, constraining it to only the present study, and only on a set of topographies. This being said, the abrasion algorithm is a robust one, as the probability heights are calculated at each iteration, allowing for a great degree of control over abrading behavior of peaks. Depending on the abrasion being done on surfaces, the surface heights can be abraded a certain way. For example, on surfaces used in this study, the abrasion algorithm can act aggressively on peaks lying in top 50% in the first 100 iterations to achieve a right handed tail, and a "spiked" distribution. This would give similar Skewness and Kurtosis magnitudes, to the physically abraded surfaces.

The focal point of this thesis was to observe the trends in surface roughness parameters and to simulate them without unnecessary external manipulation. The simulated trends mimic the observed trends. Hence, following the methodology detailed in Chapter 3, the trends can be used to identify regimes (as defined in Section 3.2.2). This can be a helpful guide towards predicting liquid mobility on the surface, based upon the parameter evolution. If strict adherence to magnitudes is required, a set of physical abrasion can be observed, and the abrasion algorithm adapted in this study can be calibrated as such.

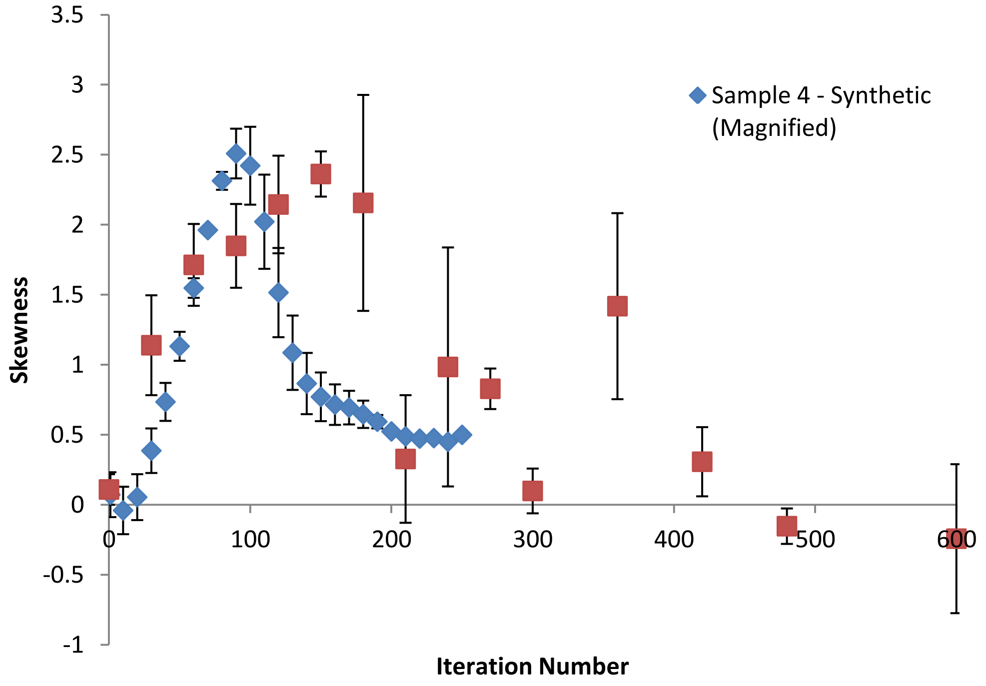

Figure 4-29 – Comparing physically and synthetically abraded Skewness of sample 4. The magnitude of the synthetically calculated Skewness values has been increased twice.

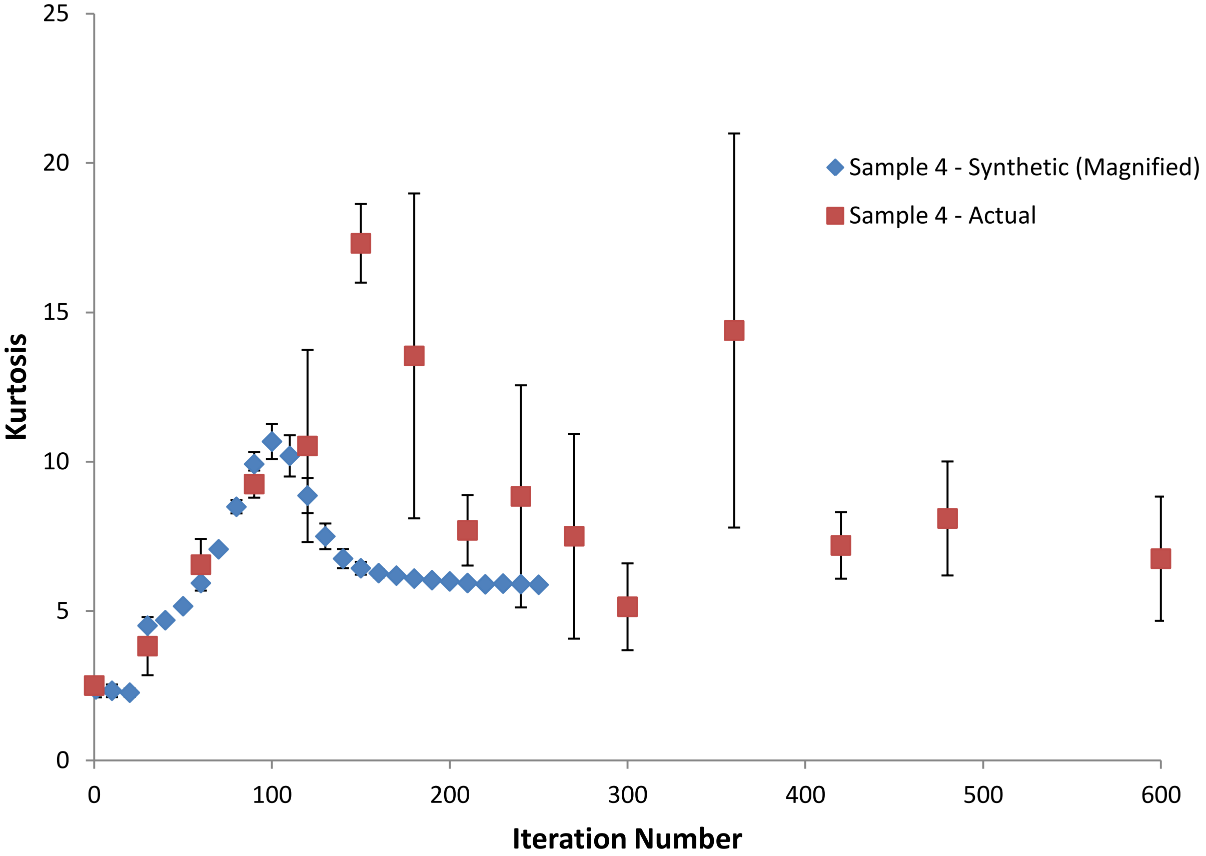

Figure 4-30 – Comparing physically and synthetically abraded Kurtosis of sample 4. The magnitude of the synthetically calculated Kurtosis values has been increased two fold.

4.6 Summary

This chapter has outlined the methodology for simulating abrasion on surfaces. Random topography surfaces were abraded by an algorithm, and the simulated trends of surface roughness parameters were found to align with the actual trends. Due to the stochastic nature of the abrasion phenomenon, timescale limitation of this project, and our desire to not externally influence the simulated abrasion, the magnitudes were three to four times smaller than the actual ones.

However, empirical methodology followed in this part of thesis, may help understand the role of topography on wetting in a detailed manner. First, relevant surface roughness indicators were identified on physically abraded surfaces, and the trends for identified indicators were simulated on artificial terrains. Stochastic nature of wear dictated that the trends should serve as better indicators then the magnitudes of parameters. Importantly, the methodology followed to abrade surfaces should serve as an introduction to this field. A combination of tribology and wettability, with a focus on durability of SHS should be able to produce empirical evidence needed to study role of topography on wetting in detail.

This chapter laid a foundation that a set of few physical abrasions can be helpful to generate large datasets of surface roughness parameters, which can then be statistically analyzed to find correlations between different topography aspects and wetting. A definite need to understand this connection is there, as a fundamental investigation can help solve the durability problem of SHS. Unfortunately, a full statistical investigation could not be done in this thesis's timeframe, but it is an essential part and it is hoped that the user can gain an understanding of wetting performance of worn SHS and behavior and simulation of surface topographical parameters.

References

1. Y. Ao, Q. J. Wang, and P. Chen, “Simulating the worn surface in a wear process,” *Wear*, vol. 252, no. 1, pp. 37–47, 2002.
2. Y. R. Jeng and C. C. Gao, “Changes of surface topography during wear for surfaces with different height distributions,” *Tribology transactions*, vol. 43, no. 4, pp. 749–757, 2000.
3. F. K. Musgrave, C. E. Kolb, and R. S. Mace, “The synthesis and rendering of eroded fractal terrains,” in *ACM SIGGRAPH Computer Graphics*, 1989, vol. 23, pp. 41–50.
4. P. Kristof, B. Benes, J. Křivánek, and O. St’ava, “Hydraulic erosion using smoothed particle hydrodynamics,” in *Computer Graphics Forum*, 2009, vol. 28, pp. 219–228.
5. A.D. Kelley, M.C. Malin, and G.M. Nielson, “Terrain Simulation Using a Model of Stream Erosion,” *Proc. 15th Ann. Conf. Computer Graphics and Interactive Techniques (SIGGRAPH ’88)*, pp. 263-268, 1988.
6. G. E. Tucker and K. X. Whipple, “Topographic outcomes predicted by stream erosion models: Sensitivity analysis and intermodel comparison,” *Journal of Geophysical Research,* vol. 107, no. B9, p. 2179, 2002.
7. P. Ramon-Torregrosa, M. A. Rodriguez-Valverde, A. Amirfazli, and M. Cabrerizo-Vilchez, “Factors affecting the measurement of roughness factor of surfaces and its implications for wetting studies,” *Colloids and Surfaces A: Physicochemical and Engineering Aspects*, vol. 323, no. 1–3, pp. 83–93, Jun. 2008.
8. B. B. Mandelbrot and J. W. Van Ness, “Fractional Brownian Motions, Fractional Noises and Applications,” *SIAM Review*, vol. 10, no. 4, pp. 422–437, Oct. 1968.
9. M. Frade, F. F. de Vega, and C. Cotta, “Modelling Video Games’ Landscapes by Means of Genetic Terrain Programming - A New Approach for Improving Users’ Experience,”

in *Proceedings of the EvoWorkshops on Applications of Evolutionary Computing*, M. Giacobini, A. Brabazon, S. Cagnoni, et al., Eds., vol. 4974 of Lecture Notes in Computer Science, pp. 485–490, Springer, Naples, Italy, 2008.

10. "Why Virtual Terrain?", Internet: http://vterrain.org/Misc/Why.html, [accessed Sept. 5, 2012]
11. M. Frade, F. F. de Vega, and C. Cotta, "Breeding Terrains with Genetic Terrain Programming: The Evolution of Terrain Generators," *International Journal of Computer Games Technology*, vol. 2009, pp. 1–13, 2009.
12. F. Losasso and H. Hoppe, "Geometry clipmaps: terrain rendering using nested regular grids," *ACM Transactions on Graphics*, vol. 23, no. 3, pp. 769–776, 2004.
13. B. Pelton and D. Atkinson, "Flexible generation and lightweight view-dependent rendering of terrain," Tech. Rep. COEN-2003-01-22, Department of Computer Engineering, Santa Clara University, Santa Clara, Calif, USA, 2003.
14. A. A. Rahman, "Digital terrain model data structures," *Buletin Ukur*, vol. 5, pp. 61-66, 1994.
15. E. Puppo, L. Davis, D. De Menthon, and Y. A. Teng, "Parallel terrain triangulation," *International journal of geographical information systems*, vol. 8, no. 2, pp. 105–128, Mar. 1994.
16. H. Samet, "The quadtree and related hierarchical data structures," *ACM Computing Surveys (CSUR)*, vol. 16, no. 2, pp. 187–260, 1984.
17. I. D. Moore, R. B. Grayson, and A. R. Ladson, "Digital terrain modelling: a review of hydrological, geomorphological, and biological applications," *Hydrological processes*, vol. 5, no. 1, pp. 3–30, 1991.

18. J. Olsen, “Realtime procedural terrain generation - Realtime synthesis of eroded fractal terrain for use in computer games,” *Department of Mathematics and Computer Science (IMADA) University of Southern Denmark*, 2004.
19. R. Voss, “Fractals in nature: characterization, measurement, and simulation,” in *Proceedings of the 14th Annual Conference on Computer Graphics and Interactive Techniques (SIGGRAPH ’87)*, Anaheim, Calif, USA, July 1987.
20. H. O. Peitgen, H. Jürgens, and D. Saupe, *Chaos and Fractals: New Frontiers of Science*, Springer, New York, NY, USA, 2nd edition, 2004.
21. G. Miller, “The Definition and Rendering of Terrain Maps,” *Computer Graphics* (Proc. SIGGRAPH), Vol. 20, No. 4, Aug. 1986, pp. 39-48.
22. A. Fournier, D. Fussell, and L. Carpenter, “Computer rendering of stochastic models,” *Communications of the ACM*, vol. 25, no. 6, pp. 371–384, 1982.
23. Paul Martz. “Generating random fractal terrain.” Internet: http://gameprogrammer.com/fractal.html, [accessed 6 Sept., 2012]
24. Alexander Carette. Internet: https://code.google.com/p/shader-artist/source/browse/Matlab/diamondsquare.m, [accessed 6 Sept., 2012]
25. “GNU Lesser General Public License.” Internet: https://www.gnu.org/copyleft/lesser.html, [accessed 25 Dec., 2012].
26. A. Zmitrowicz, “Wear patterns and laws of wear-a review,” *Journal of Theoretical and Applied Mechanics*, vol. 44, no. 2, pp. 219-253, 2006.
27. M. Godet, “The third-body approach: a mechanical view of wear,” *Wear*, vol. 100, pp. 437-452, 1984.

28. J.A. Williams, “Wear and wear particles – some fundamentals,” *Tribology International*, vol. 38, no. 10, pp. 863-870, 2005.
29. J. F. Archard, “Contact and rubbing of flat surfaces,” *Journal of Applied Physics*, vol. 24, no. 8, pp. 981-988, 1953.
30. M. Bigerelle, B. Hagege, and M. El Mansori, “Mechanical modelling of micro-scale abrasion in superfinish belt grinding,” *Tribology International*, vol. 41, no. 11, pp. 992–1001, Nov. 2008.
31. E. Gadelmawla, “Roughness parameters,” *Journal of Materials Processing Technology*, vol. 123, no. 1, pp. 133–145, Apr. 2002.

Chapter 5 - Summary and Conclusions

The aim of this research was outlined in Chapter 1, relating back the outlined objectives for this research, the following aims have been achieved in this thesis:

- A literature review was undertaken, where the durability studies done on SHS until now were detailed. The main deficiencies exposed were the probable directional nature of wear and influence of surface chemistry on wetting data reported. Furthermore, no empirical experimental datasets exist in literature that followed a systematic wear methodology and reported quantitative topographical changes.
- Abrasion methodology based upon a standard ASTM testing procedure was used to abrade a random topography consisting of a hydrophobic bulk. This ensured that a standardized abrasion approach was followed, and not an approach specially suited to the nature of topography under investigation. It was also ensured that surface chemistry did not factor into wettability changes by using Teflon bulk polymer, and having a contamination free abrasion process. Wetting characteristics at each wear duration were documented. The topography undergoing wear was evaluated quantitatively using confocal microscopy. The trends in surface topographical descriptors were monitored. This introduced a considerable advantage of relating wetting to topography analytically.
- An abrasion algorithm was adapted from an earlier tribological study, which was concerned with simulating the abrasive conditions occurring in belt finishing process. The abrasion algorithm used in the study was refined and extended to 3D topographies, and a Gaussian filter was incorporated in the algorithm. This ensured abrasion of only the surface roughness features and not waviness. The abrasion algorithm worked by calculating abrasion probabilities of surface relief features and abraded them randomly.

> The refinements were done in the algorithm including incorporating a waviness filter to abrade only the roughness of the topography, and using a height matrix from which different height values to be abraded at each iteration can be chosen instead of a single value. Another refinement included divided the abrasion into parts, such that initial abrasions can be milder using a larger value of λ. The only input to the algorithm were two physical numbers i.e. height to be abraded at each iteration, and a parameter simulating abrasion speed, besides the topography to be abraded. The trends of the surfaces roughness parameters were found to simulate the actual physical abrasion trends.

The developed abrasion method was wearing the PTFE surfaces in a random unbiased fashion, which was essential as to not bias wetting characteristics. It was verified by SEM that there was no contamination left on surfaces after abrasion, as it would have introduced chemical heterogeneities. It was shown that during initial wear, tip of the peaks wear immediately but advancing and receding CA are not adversely affected. As the wear time period increases, the surface peaks abraded rapidly with plateaus appearing and receding CA showing a large jump. The time for this jump varied for different sample surfaces used in this study, and sometimes the CAH decreased for subsequent wear intervals before showing a final large jump/increase. This affected the liquid mobility on the surface, with surfaces losing superhydrophobicity. Quantitative CSM observation was validated through physical SEM evidence. Quantitative observations showed that the surfaces wore in similar fashion, showing similar topography for similar wear times for different samples. The small differences were due to inherent stochastic nature of the wear. *Popular* form of Cassie equation was found to be a good prediction mechanism for advancing CAs, while *original* Cassie equation remained indeterminate for all the unworn and worn surfaces. Surface topographical descriptors from the amplitude, spatial, and functional family were calculated. All the surfaces showed similar trend for a descriptor under consideration. Surface descriptors trends were explained using topographical condition, and showed a good correlation to the observed and expected trends. Wetting data was also correlated with surface descriptors. Only RMS roughness, Skewness and Kurtosis used in conjunction were able to act as a good guide towards prediction the liquid mobility on the surface, based upon the slopes of the parameter trends. Otherwise, magnitude of these parameters alone was not able to predict the liquid mobility on the surface. For the purpose of a statistical investigation, it is critical to have large datasets, but physical abrasion of surfaces is time consuming. Hence, abrasion was simulated on synthetic terrains and the surface roughness parameters were found to be an exact match in terms of trends and magnitudes barring minor differences. Hence, artificial terrains can be used to simulate physical abrasion, and the roughness parameters simulated can be compared to wettability. The trends of physical abrasion surface roughness descriptors were used to temporally calibrate the simulated roughness descriptor trends. This achievement of the thesis increases the chance of relating wetting and topography, using statistical means, and can lead to fabrication of surfaces with tuned roughness features suited towards durability.

Whilst using surface roughness parameters as a topographical representation are not new, this study is novel in the field by comparing them with wettability. This thesis has been able to generate a body of empirical and analytical evidence which can be reproduced and studied for further work done in this area.

5.1 Future work

Connection between surface roughness parameters and wettability was explored, but a possibility still exists for a statistical investigation to find correlation among them. Possibilities include using rank correlation methods given by Spearman, Kendall, and Goodman and Kruskal [1-2].

Also, correlation between roughness parameters and wettability was explored in solitude. Multiple surface roughness parameters can be combined to form an equation, such as to explain wettability trends. This will lead to detailed study of how different topographical aspects exactly affect the surface wettability, probably leading to an explanation of CAH. This in turn, will help control surface roughness so as to fabricate robust SHS.

The challenge lies in generating a substantial body of data to do a meaningful and statistically sound analysis of correlating each roughness parameter with wetting characteristics. Furthermore, it can be challenging to fabricate surfaces with a given roughness details, as some parameters are dependent on each other.

Ordered geometry structures can also be abraded, to extend the results derived in this thesis. One interesting project can be on another hydrophobic polymer bulk like PDMS. One aspect that can be further improved is choice of a SHS whose wetting characteristics change gradually with a slope and show a lot of variation after each duration of wear. It can be beneficial such as it can offer benefit of correlating with a dynamically changing wetting data which can have a slope. The challenge here will be addition of another degree of variability in the task of correlating topography with wettability.

One another interesting project can be to use CSM to examine the liquid penetration on surface asperities, and using it to predict the Cassie contact angle. CSM has been used to examine liquid penetration on surfaces by Butt *et al.* [3], and using methodology developed in this thesis to find Cassie equation parameters, Cassie CAs can be predicted with relatively high accuracy. This combination of two methodologies will help extending knowledge on state of Cassie equation and its limitations in a more detailed manner. This will further lead to an impetus on extending the investigation to surface topography, and finding a more robust and encompassing way to predict liquid mobility on a surface.

Abrasion algorithm can be extended to regular geometries, by adding another degree of control by choosing to abrade topography lying between certain heights, in a certain pre dictated way. This calibration of abrasion algorithm can further help in refining the roughness parameter magnitudes.

Furthermore, understanding the influence of surface chemistry on wetting can be studied. A conjunction of a fundamental investigation into both aspects is the way towards a future with durable self cleaning surfaces. One way to keep surface topography constant, and vary the surface chemistry can be to use polystyrene or PMMA structures [4], and modify the chemistry by sprinkling a solvent like Toluene/THF/cyclohexane either in an ordered pattern or randomly. This can ensure a minimum change in surface topography, but a significant change in surface chemistry [5].

References

1. C. Spearman, “The proof and measurement of association between two things,” *The American journal of psychology*, vol. 15, no. 1, pp. 72–101, 1904.
2. J. T. Litchfield and F. Wilcoxon, “Rank Correlation Method,” *Analytical Chemistry*, vol. 27, no. 2, pp. 299–300, Feb. 1955.
3. P. Papadopoulos, X. Deng, L. Mammen, D. M. Drotlef, G. Battagliarin, C. Li, K. Mǘllen, K. Landfester, A. del Campo, and H. J. Butt, “Wetting on the Microscale: Shape of a Liquid Drop on a Microstructured Surface at Different Length Scales,” *Langmuir*, vol. 28, no. 22, pp. 8392–8398, 2012.

4. C. W. J. Berendsen, M. Skeren, D. Najdek, and F. Cernỳ, “Superhydrophobic surface structures in thermoplastic polymers by interference lithography and thermal imprinting,” *Applied Surface Science*, vol. 255, no. 23, pp. 9305–9310, 2009.
5. I. Bernagozzi, S. Torrengo, L. Minati, M. Ferrari, A. Chiappini, C. Armellini, L. Toniutti, L. Lunelli, and G. Speranza, “Synthesis and characterization of PMMA-based superhydrophobic surfaces,” *Colloid & Polymer Science*, pp. 1–8, 2012.

Appendices

Appendix A

A.1 Noise filtering of the Topography data

Confocal scanning is a top down imaging technique which requires no contact with the topography, hence topography details can be mapped without damaging any surface features. CSM used in this thesis, Zeiss Axio CSM 700, used white light as an illumination source and observed a single point at a time. The reflected light was collected by a tube lens after passing through the objective [1]. This data is then collected and interpreted for various information, for e.g. depth, focus, noise etc. Light reflectivity can be problematic on certain areas of the topography, such that the light cannot be entirely reflected back to the detector. The data from these areas can see a dropout in spatial information, or can be interpreted as an outlier by the CSM software. These outliers can skew the topographical descriptors values. In this thesis, outliers were observed while scanning sharp edges where the gradient change was steep, around particularly steep valleys and peaks. This tended to create artificial spikes around edges on the scanned topography, introducing noise and biasing the data. Height profile across an engraving edge on the coin shows these artifacts in Figure A-1 (a, b). These artifacts distort the reality and this extra noise is removed by inbuilt noise cut filter in the CSM software, as shown in Figure A-1 (c) and detailed below.

The noise cut filter employs a variation of the Laplacian pyramid filter, commonly used in image processing to detec edges or regions with intensity change [2-4]. Input given to the inbuilt noise cut filter (simply ‘filter’ hereafter) is an image intensity matrix and a threshold value. Threshold value lies between 0 and 255, the intensity range in an 8-bit image. Threshold value is dependent on the topography, as noise is topography dependent. Pixels above the threshold intensity are identified by the filter, and are given a weight of zero in further calculations as illustrated graphically in Figure A-2. A set of four neighboring pixels in the original image are taken, and a new image is created replacing those four pixels by one pixel. Intensity of this pixel is calculated according to the modified pyramid algorithm formula (propriety to Carl Zeiss and confidential, hence not detailed here) and is dependent on set of those four pixels. This process is continued iteratively on subsequent image matrices, until only one pixel is left. This process is called image downsampling, and resembles an inverted pyramid. From this one pixel, original steps are traced back, from the top of the pyramid to the base, until the original image is created. The pixels above threshold value (given zero intensity) are replaced by a new pixel, whose intensity pixel is calculated from a given preset equation (confidential to Carl Zeiss). A visual representation is given in Figure A-2. This filter is robust and can be calibrated such that only the noise is filtered, and the fine features on topography remain as such. This was critical for PTFE SHS surfaces used in this study, such that only the outliers are filtered and all the fine roughness features remain unfiltered. This ensured removal of un-realistic features restoring “normalcy” to data. For unworn surfaces, no filtering was done as even a small threshold value interferes heavily with data. Sample threshold values for different wear intervals are given in Table A-1.

Table A-1: Threshold values for used for noise filtering. Threshold values vary depending upon the wear time and surface topography.

Time (minutes)	**Threshold Value for Sample 1**	**Threshold Value for Sample 2**	**Threshold Value for Sample 3**
0	0	0	0
6	60	60	65
12	65	70	65
18	70	75	75
24	80	85	85
30	85	90	85

The CSM imaged PTFE samples contain artifacts which do not correspond to reality on physical samples. Figure A-3 shows the Teflon sample abraded for 27 minutes, and its CSM 3D representation. It was shown in Chapter 2, that sample has become completely flat, and there are no protruding peaks, but CSM line profile shows the peaks of 10 μm on the surface. This is not representative of the sample surface, since SEM data shows flat surface with peaks flattened out. This “contamination” of data is considered as noise in the data and is removed by using noise cut filter option in the software. Figure A-4 shows line profile after noise filtering, it is noticeable that fine features are intact and the high peaks have been removed. Some pits have been affected too, and as noticeable in Figure A-4 (c), a peak of 9 μm height is still present. Noise filtering by the software filter was constrained to a mild degree as the aim was to reduce artifacts while shielding fine features from the filter. Increasing the threshold interferes with the fine features, which affects roughness features. These remaining artifacts were screened by histogram analysis method detailed below.

The height data in the *z*-image of the samples is stored in a sheet of 1280 × 1024 cells, with each cell containing height at each pixel. The spatial data, after noise filtering, was used to find cumulative probability distribution (CDF) plot. CDF plot helped to find the probability of the height values occurring on the surface. From this whole distribution, height data falling within 0.975 and above 0.025 of the probability was taken, and the rest of height values were considered to be outliers. Hence, values from cumulative probability of 0.025 to 0.975 were considered as heights present within our data for further analysis.

Figure A-5 shows the histogram filtering for various wear intervals; and the shaded portion shows the heights outside 0.025 and 0.975 of probability. Height distribution of unworn Teflon sample starts with a normal distribution with wide distribution of heights and, with wearing it down becomes a distribution with right handed tails, and then gradually becoming normal distribution again with narrower base. As the unworn topography has more sharp edges, the quantity of filtered peaks are more, and as the surface becomes worn and flat the quantity of peaks under the filtering decrease progressively.

So filtering was done in two stages on PTFE SHS data; through noise cut and histogram analysis for our samples to represent as closely as possible the sample surface topography.

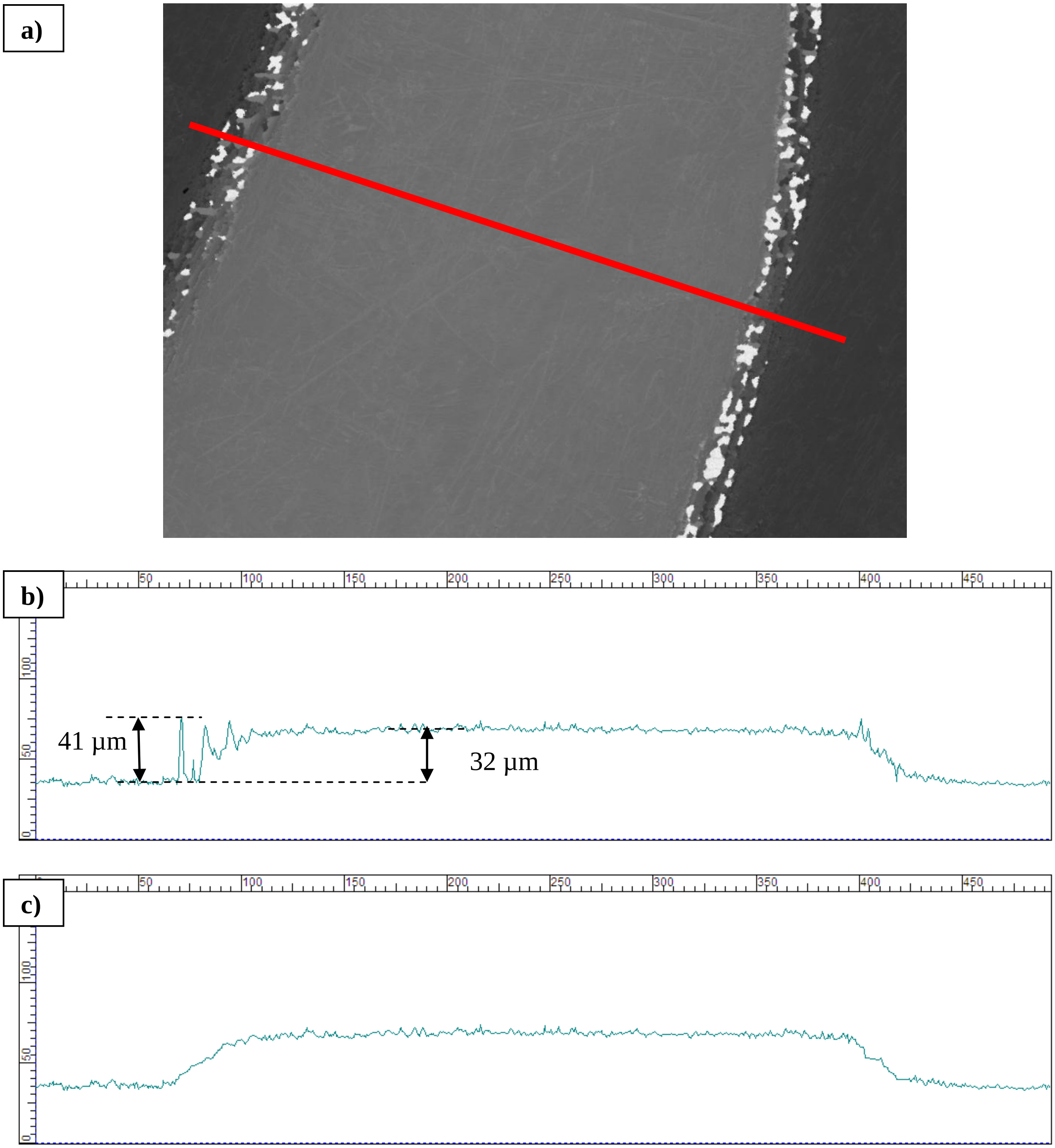

Figure A-1: a) CSM scan across an engraving on a coin, line depicts the position of the line profile, b) before filtering, and c) after filtering the noise around the edge. In (a), all the white spots on the edge are the noisy spikes, which are filtered after the data is processed with a noise removal filter.

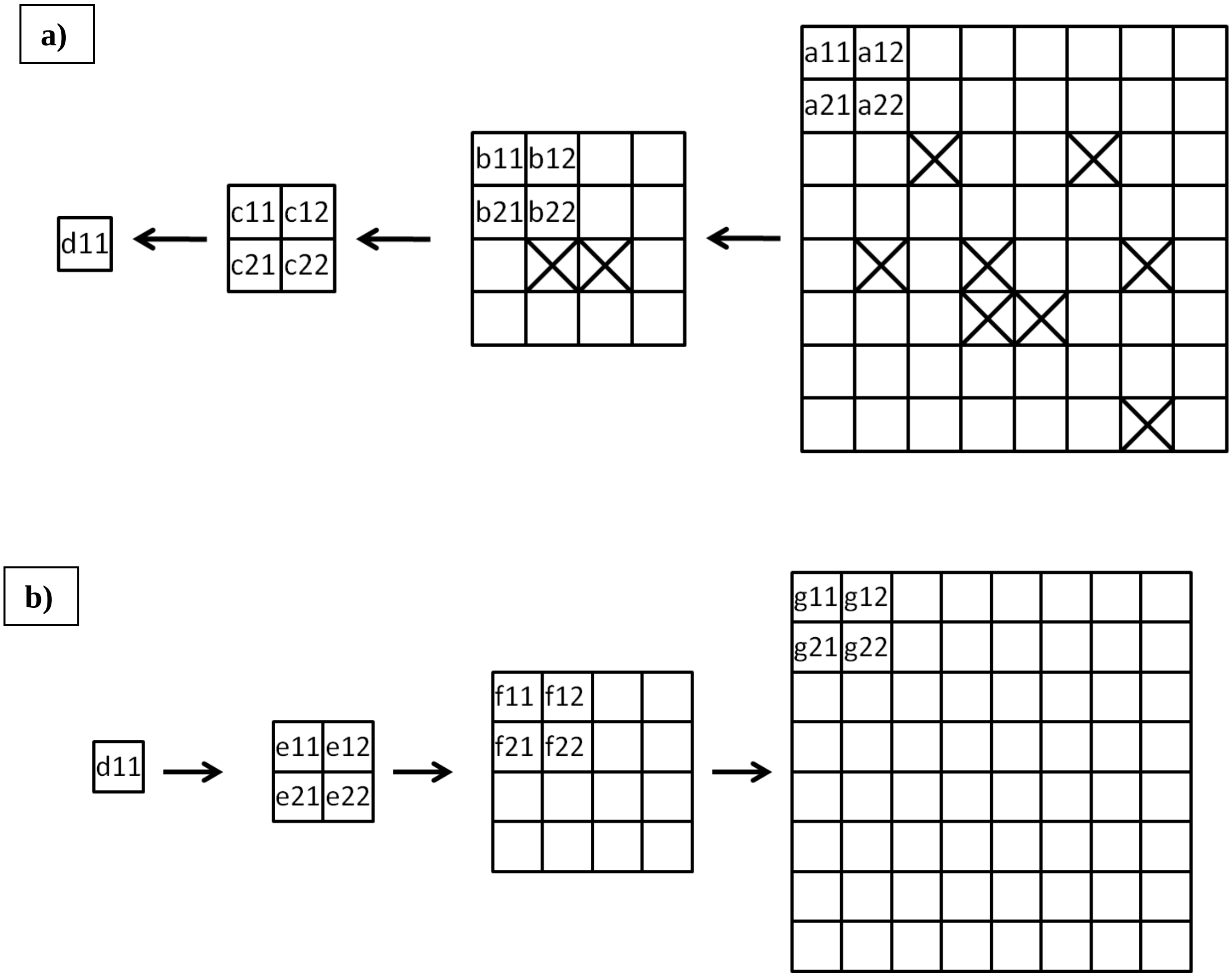

Figure A-2: Schematic of pyramid algorithm used for filtering the noise, a) In downsampling, each pixel in image is analyzed for values above threshold and given a weightage intensity of zero shown by crossed out pixels here, and further the image matrices reduced step by step using modified Gaussian pyramid, b) In resampling, original image is recreated by replacing zero-weight pixels (crossed out boxes) with new pixel values given by pyramid function. Adapted from [5].

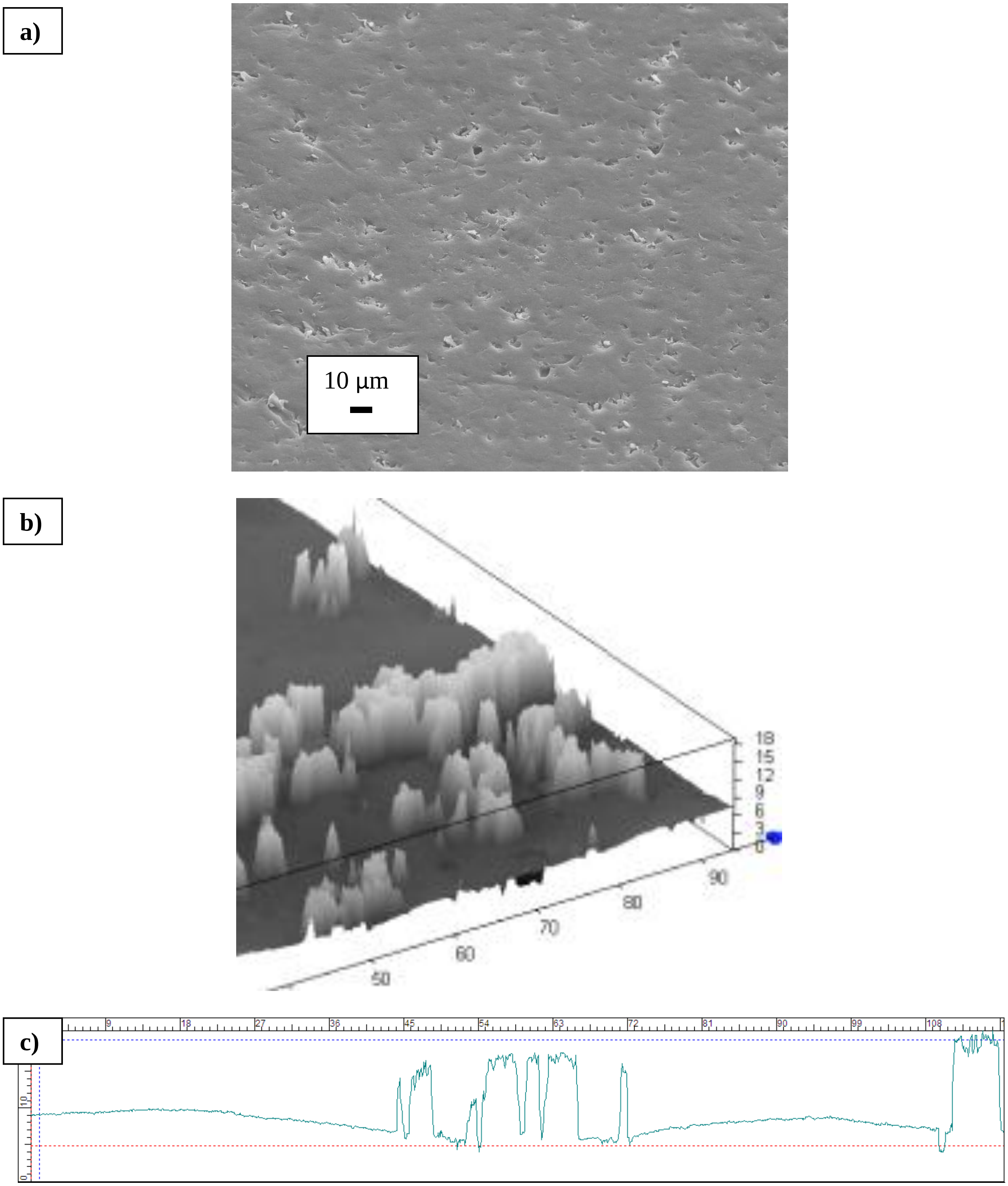

Figure A-3: a) SEM of a Teflon sample abraded for 27 minutes, and its b) CSM representation, c) and a line profile on the sample.

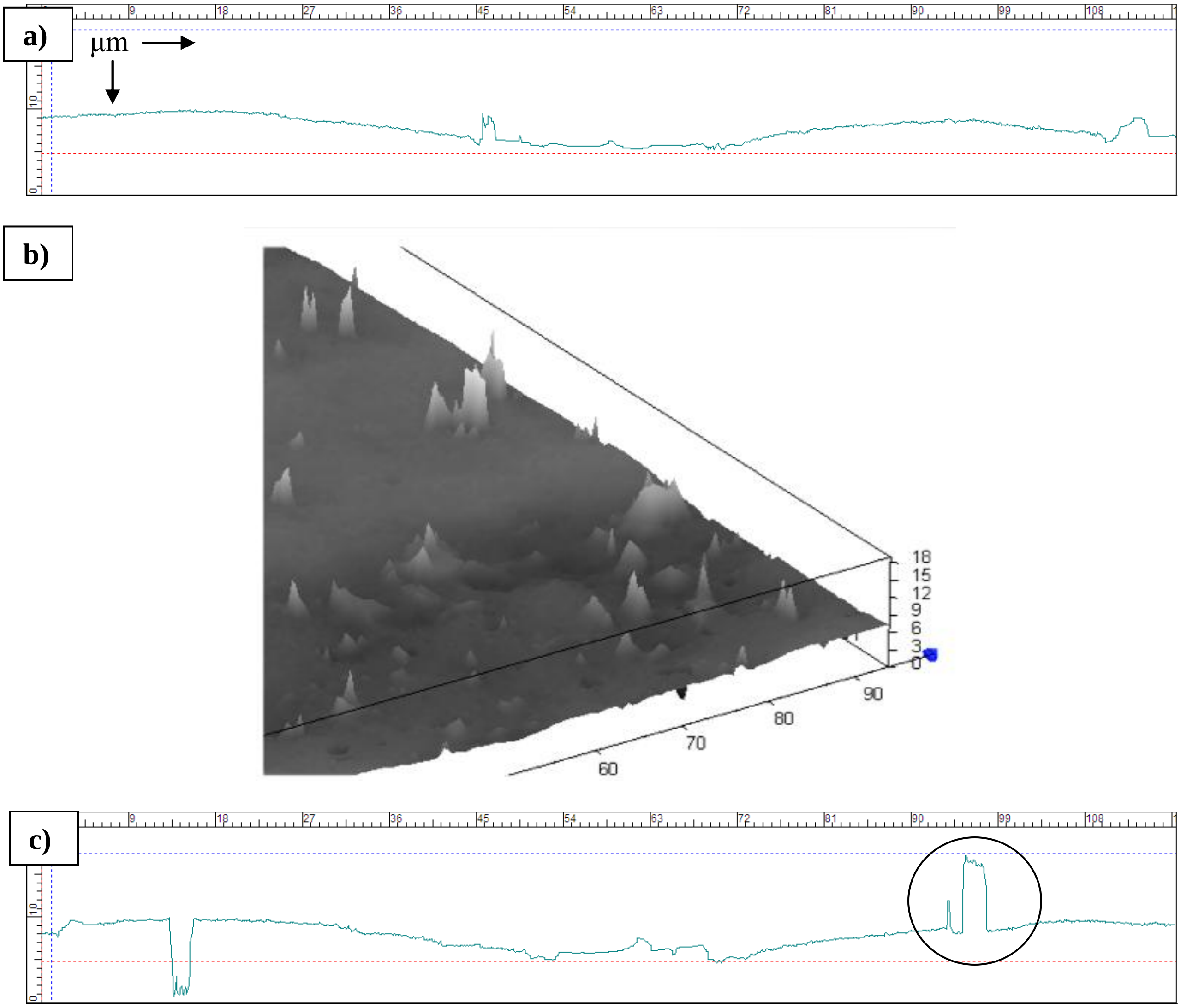

Figure A-4: a) Line profile, shown in Figure A-3, after noise filtering, b) CSM 3D representation of the surface, and c) Line profile at another area after Noise filtering. Notice the peaks (circled) that have remained unfiltered in both (b) and (c)

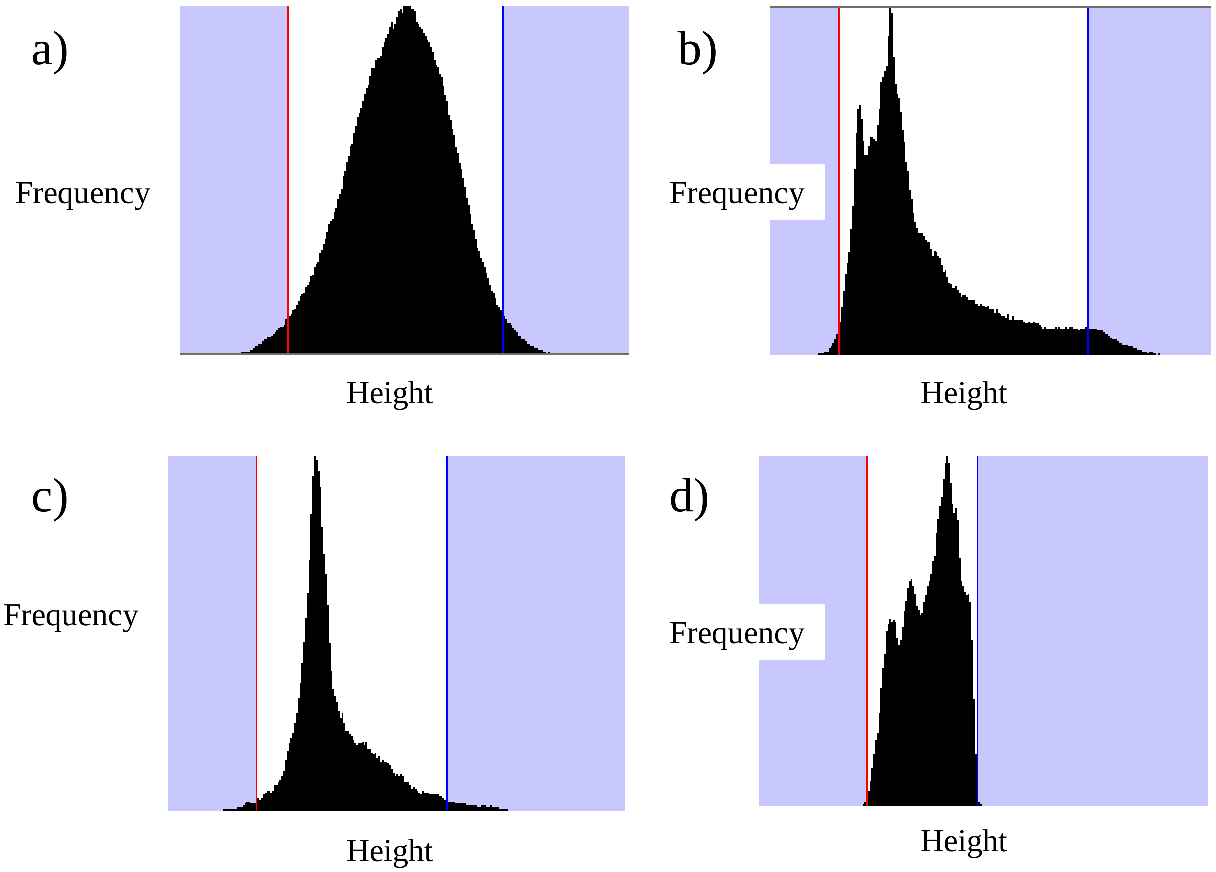

Figure A-5: Histogram filtering to remove artificial spikes remaining after noise filtering. Histogram shows the distribution for unworn (5.949 µm – 18.579 µm) (a), 3 minutes worn (3.148 µm – 13.323 µm) (b), 15 minutes worn (5.245 µm – 16.483 µm) (c), and 27 min worn sample (4.901 µm – 9.883 µm) (d). Shaded portions in blue (light black in print) are for visualizing the 0.025 and 0.975 probability range.

References

1. "Axio CSM 700." Internet: http://applications.zeiss.com/C125792900358A3F/0/4BDAFB1DCE1C4D33C12579060047BC6A/$FILE/70-1-0010_e_Axio_CSM_700.pdf, [accessed Dec. 19 2012].
2. A. Huertas and G. Medioni, "Detection of Intensity Changes with Subpixel Accuracy Using Laplacian-Gaussian Masks," *IEEE Transactions on Pattern Analysis and Machine Intelligence*, vol. PAMI-8, no. 5, pp. 651–664, Sep. 1986.
3. F. Neycenssac, "Contrast Enhancement Using the Laplacian-of-a-Gaussian Filter," *CVGIP: Graphical Models and Image Processing*, vol. 55, no. 6, pp. 447–463, Nov. 1993.
4. P. Burt and E. Adelson, "The Laplacian pyramid as a compact image code." *Communications, IEEE Transactions*, vol. 31, no. 4, pp. 532-540, 1983.
5. Robert Collins, "Lecture 10: Pyramids and Scale Space", Internet: www.cse.psu.edu/~rcollins/CSE486/lecture10_6pp.pdf [accessed Jan. 10 2013].

Appendix B

B.1 Supplementary Experimental Data for Chapter 2

B.1.1 CSM Line profiles and Histograms

Figure B-1 and Figure B-2 repeat the observations from CSM data for sample 4, as done in Section 2.4.1 for sample 2. It can be seen that the trend in Figure B-1 and Figure 2-16 very closely mimics each other, with same wear intervals showing similar topography. The height distribution histograms in Figure B-2 and Figure 2-18 also show the same evolution. The difference in initial height distributions (Figure 2-18a and Figure B-2a) arise due to being different samples, but the height distribution trend is nearly Gaussian for both the samples. As the surface wears, the peaks become scarce and then completely flatten out in same manner as shown in previous sample (Figure B-1 and Figure 2-16, Figure B-2 and Figure 2-18). The difference in Figure B-1 (f) and Figure 2-16 (f) arises due to absence of major curvature on the surface, and hence the respective histograms differ too as shown in Figure 2-18 (d) and Figure B-2 (d).

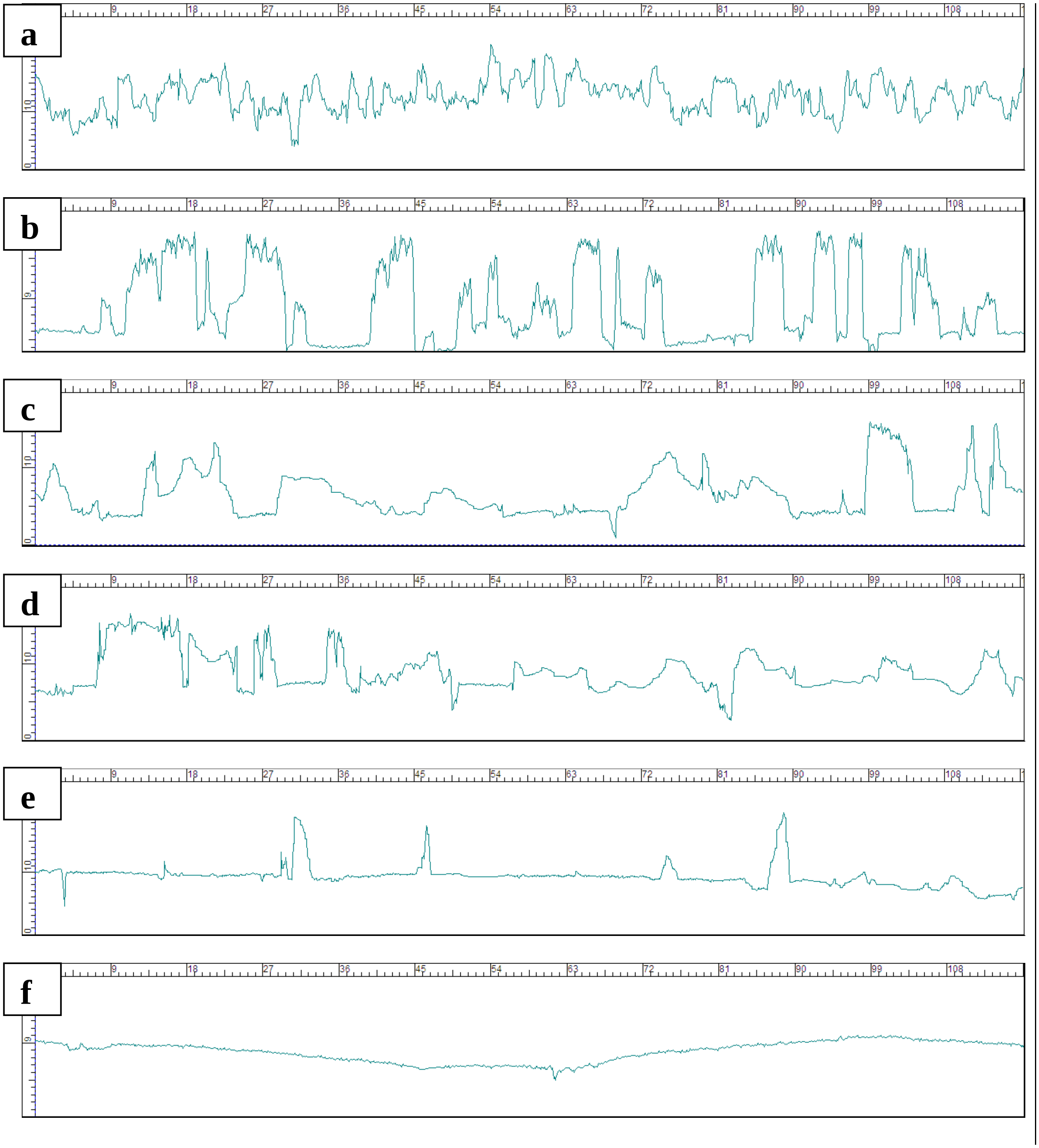

Figure B-1: Surface profiles for (a) unworn, (b) 3 minutes, (c) 12 minutes, (d) 18 minutes, (e) 21 minutes and (f) 27 minutes worn samples evaluated from CSM data. The profiles are for sample 4.

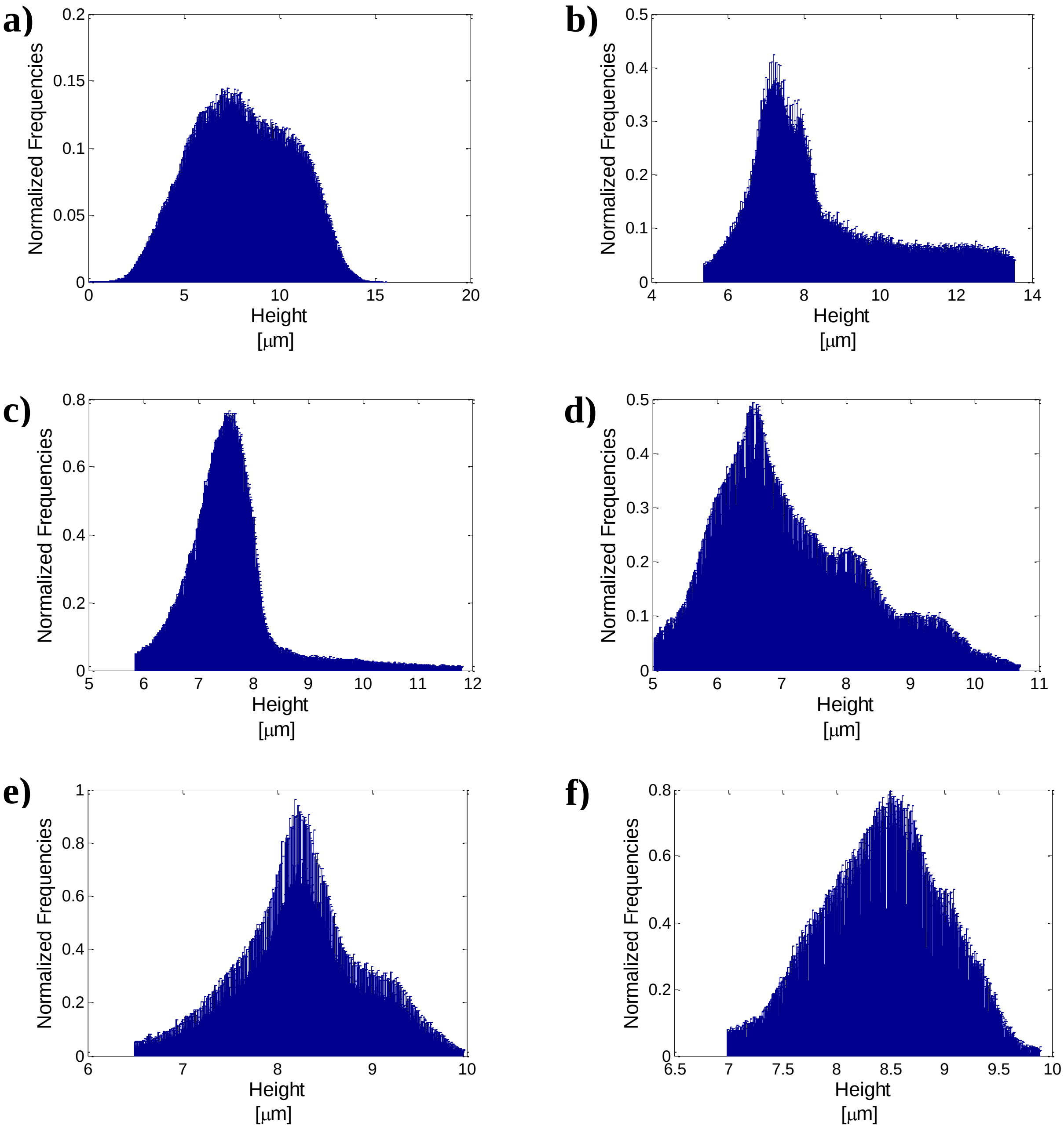

Figure B-2: Normalized histograms for (a) unworn, (b) 3 min, (c) 12 min, (d) 18 min, (e) 21 min, and (f) 27 minutes worn samples evaluated from CSM data. The corresponding height profiles are displayed in Figure B-1. It can be seen that height distribution starts as Gaussian, becomes positively skewed, and then returns to Gaussian but with high peaks and low valleys removed. The profiles are for sample 4. The data has undergone noise filtering to remove artificial peaks and valleys.

The above discussion, and the discussion in Section 2.4.1 shows that despite slightly different nature of unworn topography and stochastic wear on surfaces, the abrasion behavior is consistent among all the samples.

B.2 Supplementary Experimental Data for Chapter 3

B.2.1 RMS roughness

Continuing the discussion from Section 3.2.1 where RMS roughness and CAH were correlated for sample 2. In Figure B-3 (a), the hysteresis jump is after 6 minutes of abrasion, and the RMS roughness values show a dip of ~28% at that time. But, comparing RMS roughness values at 6 and 9 minutes, there is a drop of nearly 25%, but the CAH increase (rather CAH decreases) is not as steep as witnessed between 3 and 6 minutes. The CAH is nearly stable at ~50° after 9 minutes of abrasion, while RMS roughness values show a slight decrease as wear progresses on the surface. The same trend is observed for sample 5 (Figure B-3 b) where the RMS roughness show a continuous decrease, and showing no difference where the CAH jumps steeply (24 min). Also, when CAH increases, RMS roughness values for sample 2 and 4 lie in close vicinity, but for sample 5 it is roughly half that of sample 4 magnitude.

Hence, the trend for RMS roughness is not a good fit to correlate with CAH.

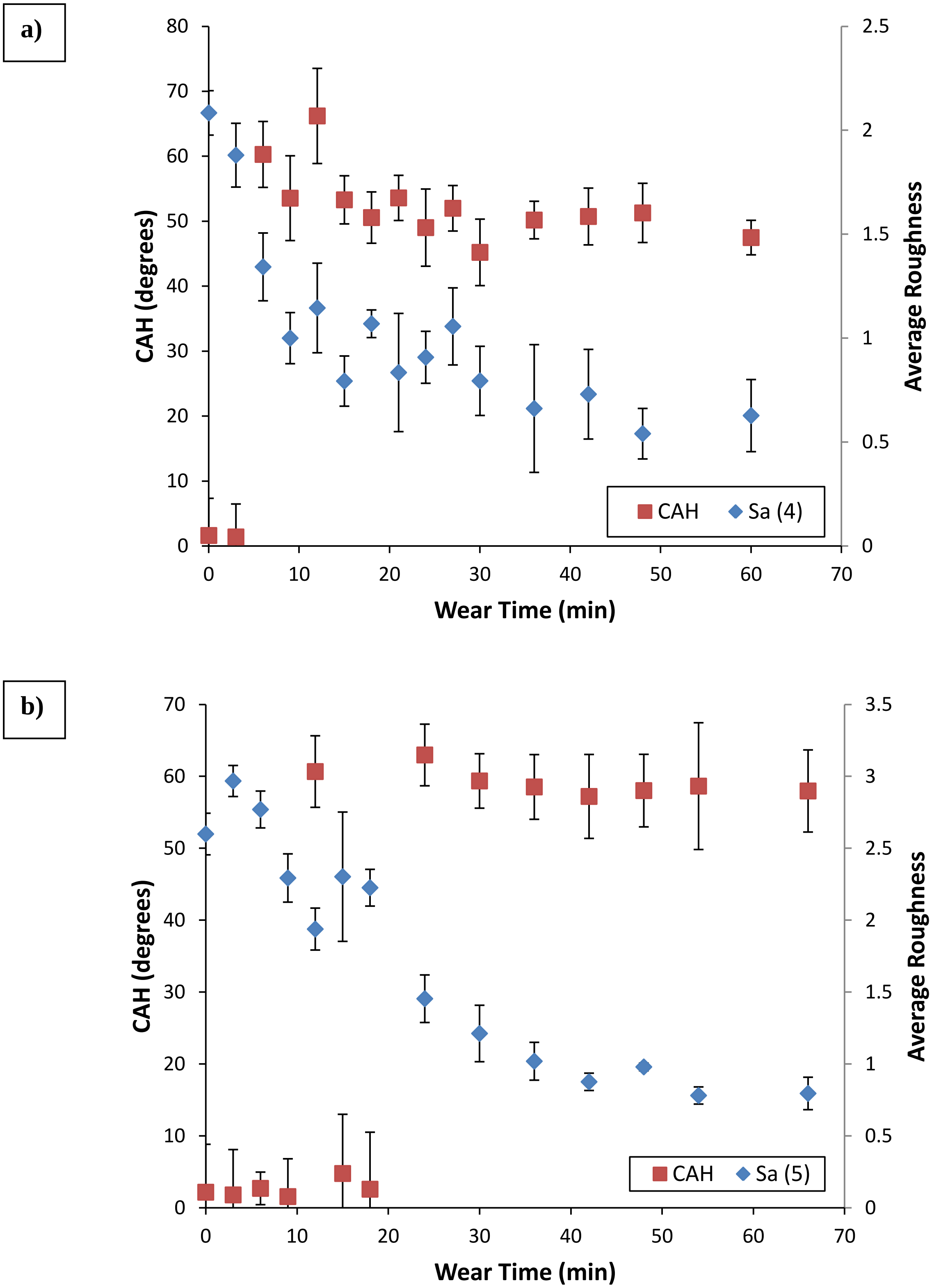

Figure B-3: Comparing CAH and RMS roughness for, (a) Sample 4, and (b) Sample 5.

B.2.2 Skewness

In Section 3.2.2 Skewness was shown for sample 2, 4 and 5. In this Section, Skewness trends for surfaces worn for a long time (Figure B-4) and for initial wear period are shown (Figure B-5), and shown to align nicely for all the samples.

Sample 4 Skewness increased until 18 minutes, while CAH rose at 6 minutes. Sample 5 shows CAH and Skewness increase at and until 21 minutes. This observance can help predict the region where the surface liquid mobility will be lost, but by looking at slope of Skewness curve. CAH displayed at 6 and 66 minutes for sample 5 is different, but the Skewness magnitude is roughly the same.

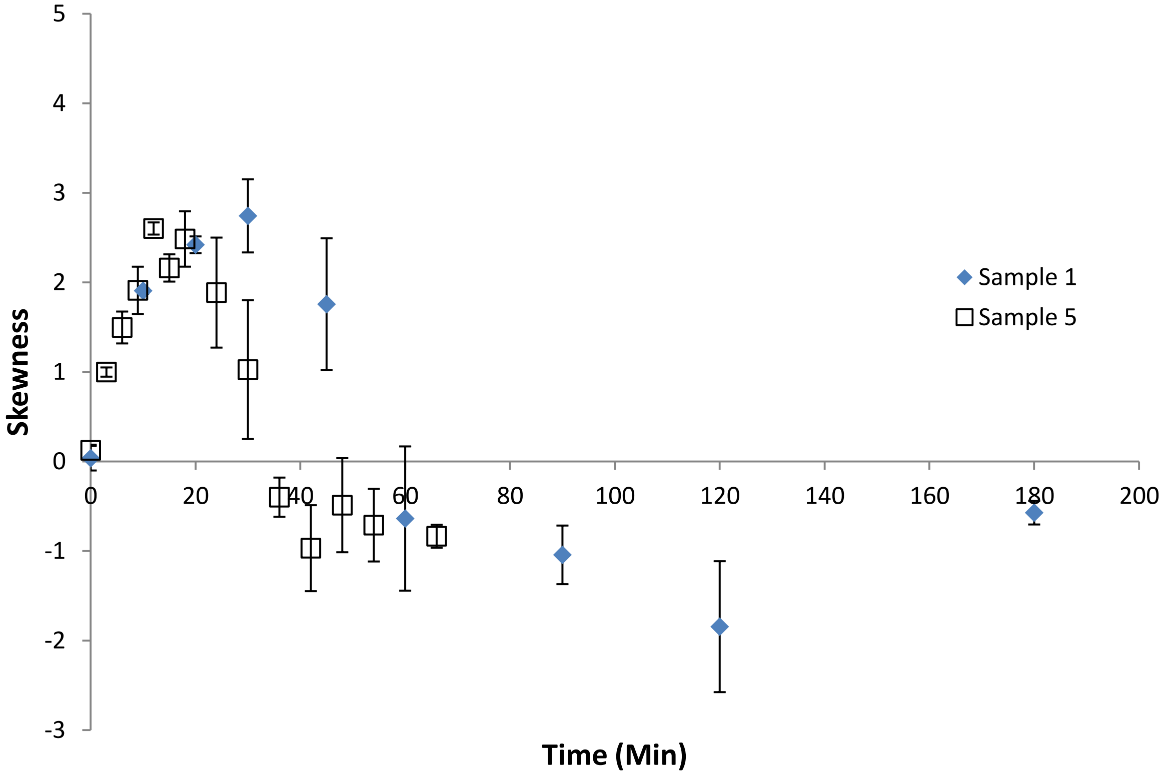

Figure B-4: Skewness for PTFE worn surfaces showing the long term behavior, for a period of 180 minutes.

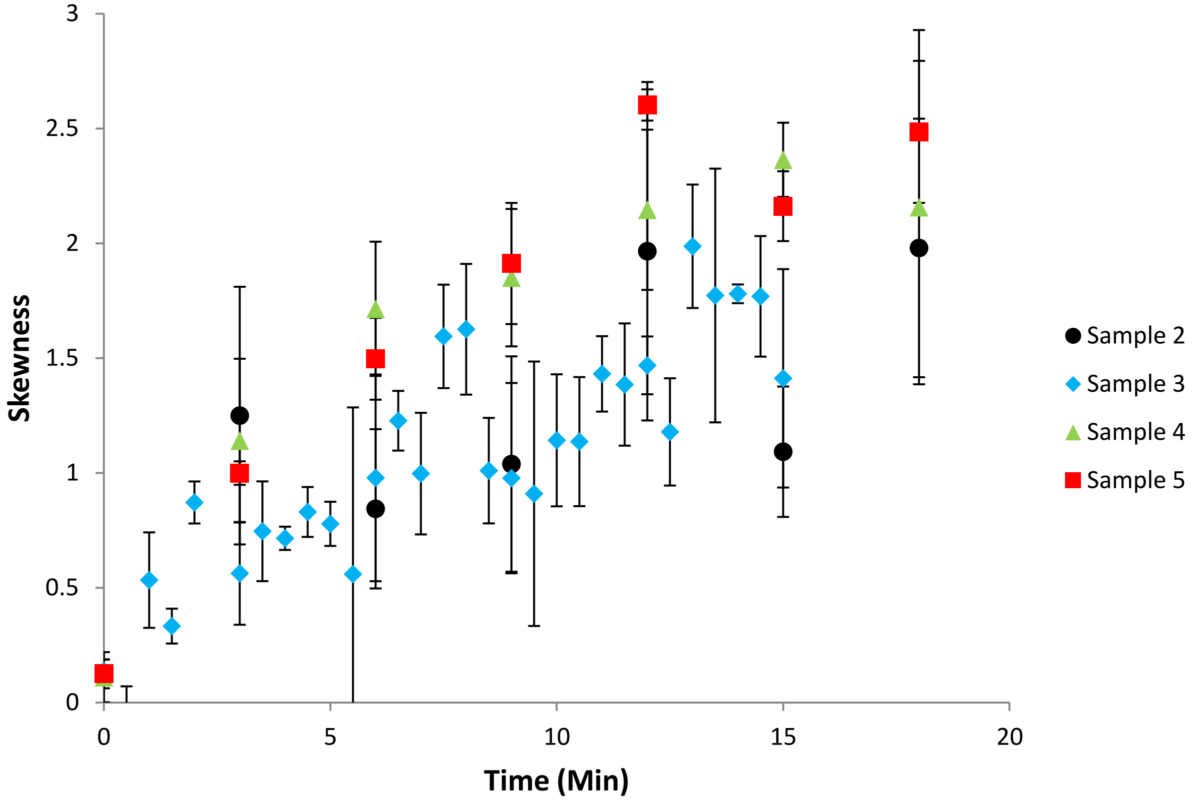

Figure B-5: Skewness for PTFE worn surfaces showing the short term behavior in initial 18 minutes of abrasion.

B.2.3 Kurtosis

In Section 3.2.3 Kurtosis was shown for sample 2, 4 and 5. In this Section, Kurtosis trends for surfaces worn for a long time and for initial wear period are shown in Figure B-6 (a) and (b), respectively. The trends align nicely for all the samples.

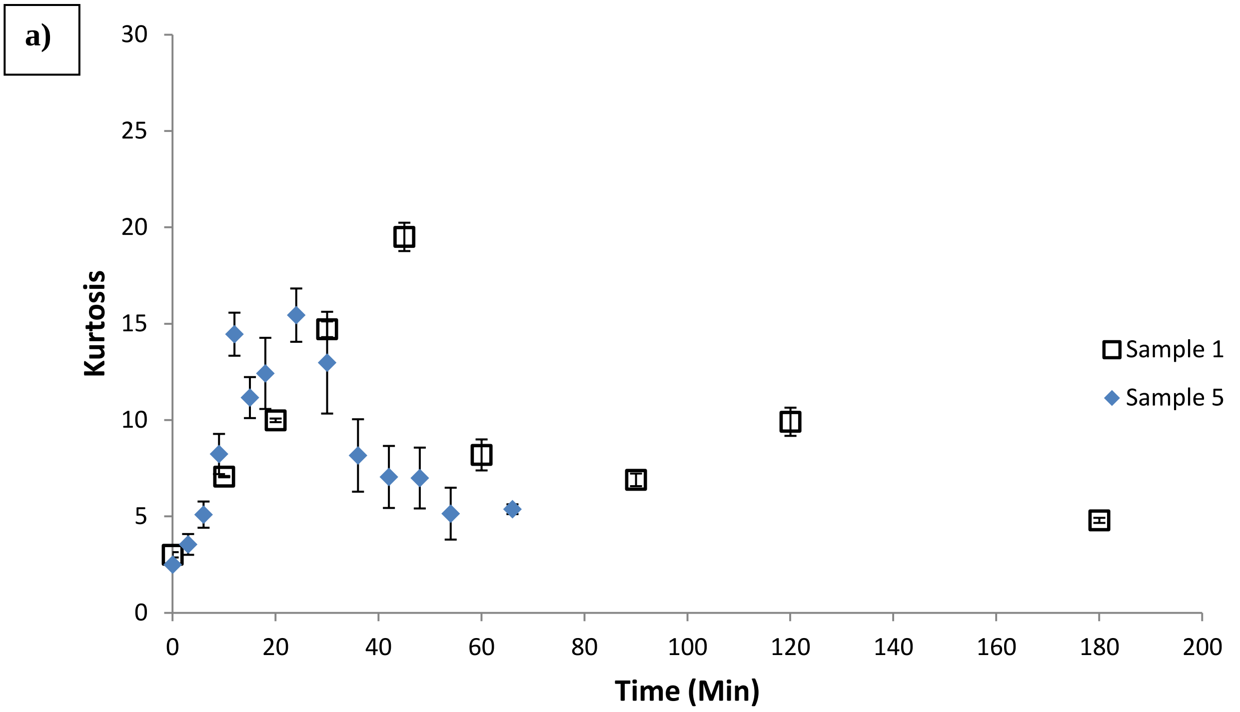

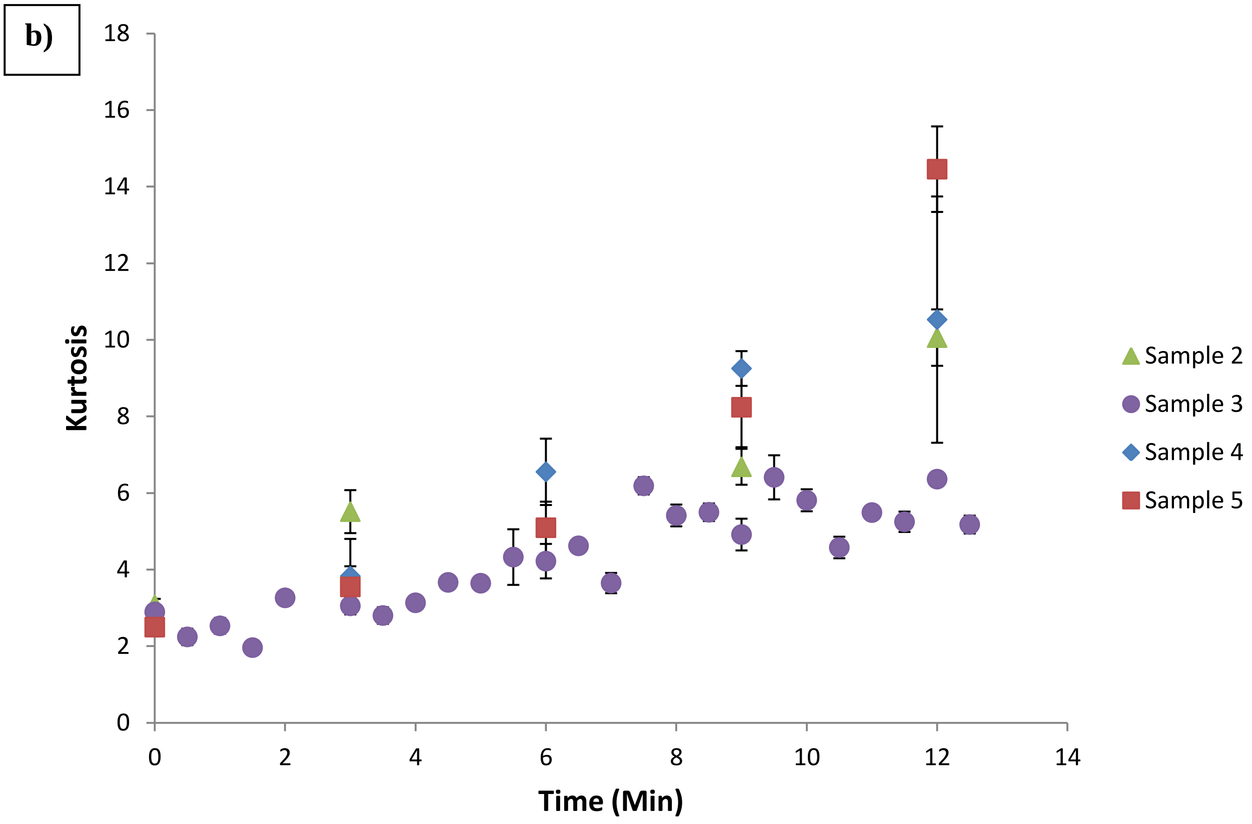

Figure B-6: Evolution of Kurtosis as a surface wears for, (a) long wear time, and (b) initial 15 minutes.

B.2.4 Other height parameters

These parameters are calculated on the whole area topography, and hence S_p is global height maxima, while S_v is global height minima, while S_z is simply the difference between S_p and S_v. Figure B-7 illustrates this on a surface topography profile. Figure B-8 shows the S_p and S_v parameter evolution for three samples (2, 4 and 5). As can be seen, there is large standard deviation between all of the values for both parameters. As progressive wear is expected to decrease peak height and increase depth height, the general trend for all the samples agrees with this observation.

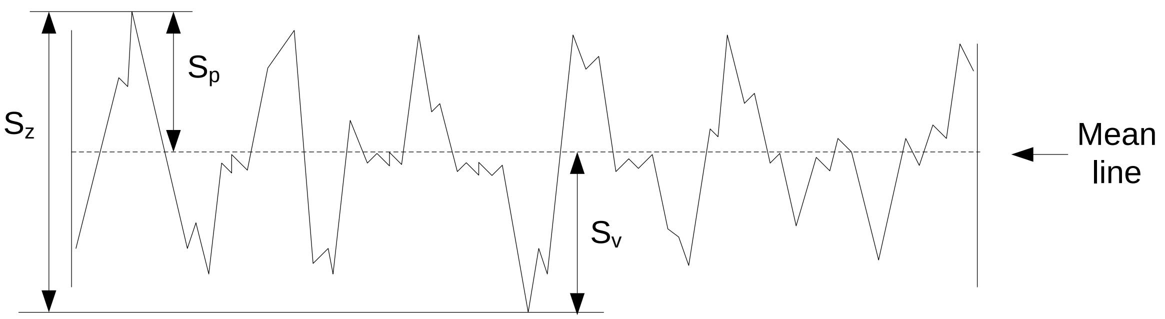

Figure B-7: Schematic showing how amplitude parameters (Sp, Sv, and Sz) are calculated on a surface topography line profile. The line profile incorporates both the global height maxima and minima on the whole area topography.

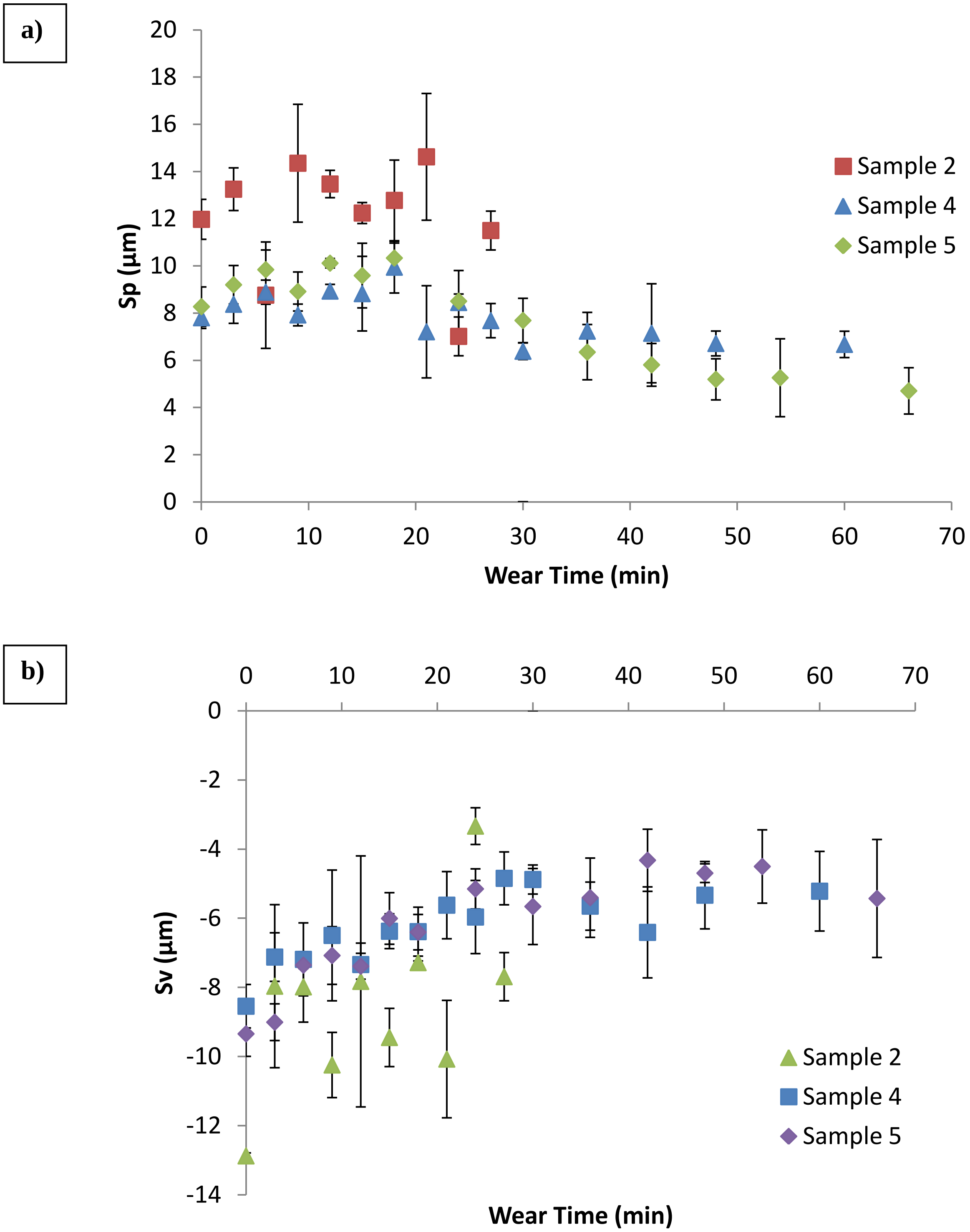

Figure B-8: Evolution of, (a) maximum peak height (S_p), and (b) maximum depth height (S_v) as a surface wears. Error bars show the standard deviation in the parameter.

B.2.5 Functional Parameters

Figure B-9 (a) and (b) show the evolution for S_{mr1}, for surfaces worn for long and short time period, respectively. The rest of the discussion is in Section 3.2.6.

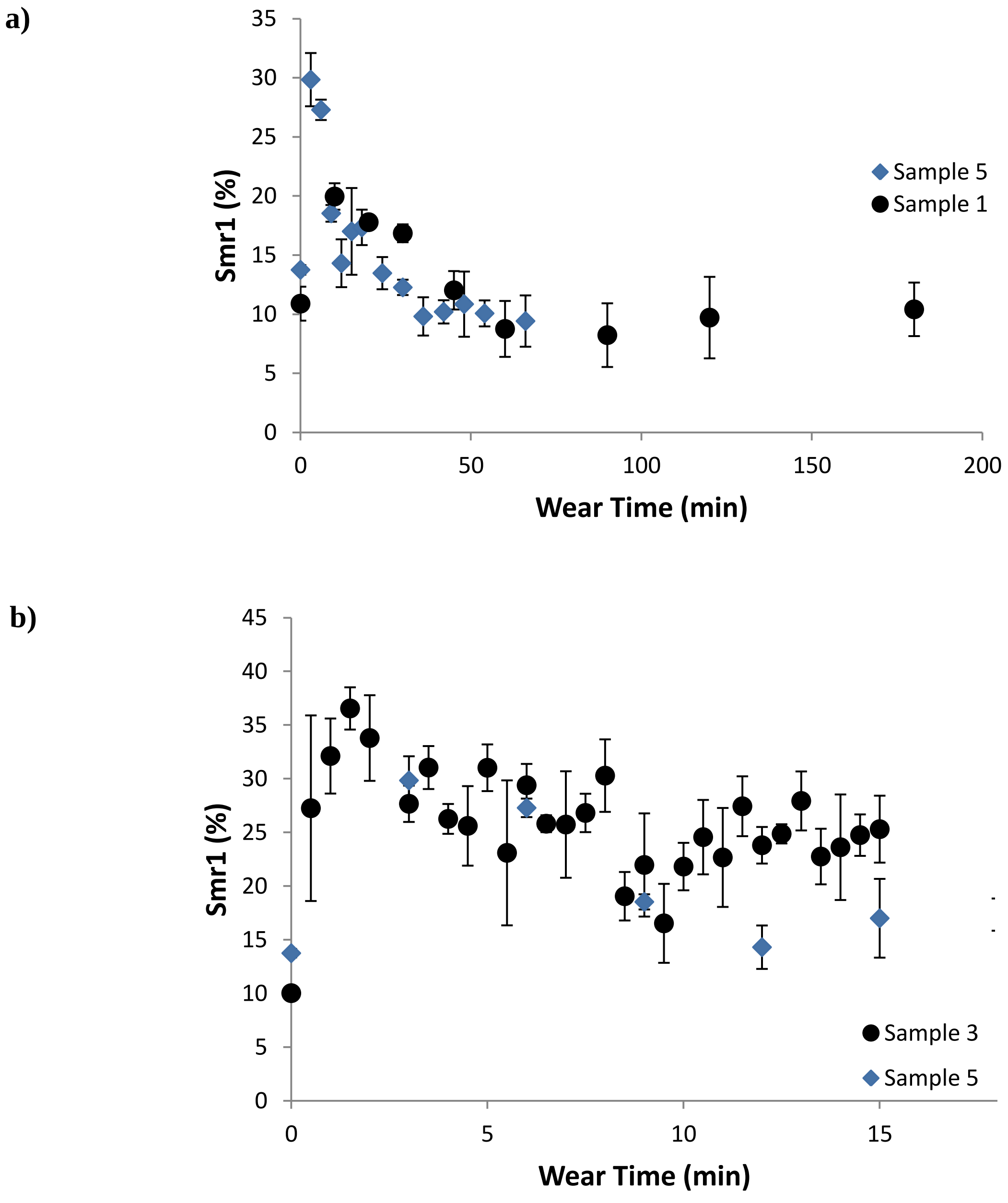

Figure B-9: (a) Evolution of S_{mr1} as a surface wears, parameter evolution for (b) long time wear, and (c) short time wear. Error bars show the standard deviation in the parameter.

Figure B-10, Figure B-11, Figure B-12, and Figure B-13 show the evolution for S_{pk}, S_k, S_{mr2}, and S_{vk}, respectively. The graphs show surfaces worn for long and short time period, for all the parameters except S_{mr2}. The rest of the discussion is in Section 3.2.6.

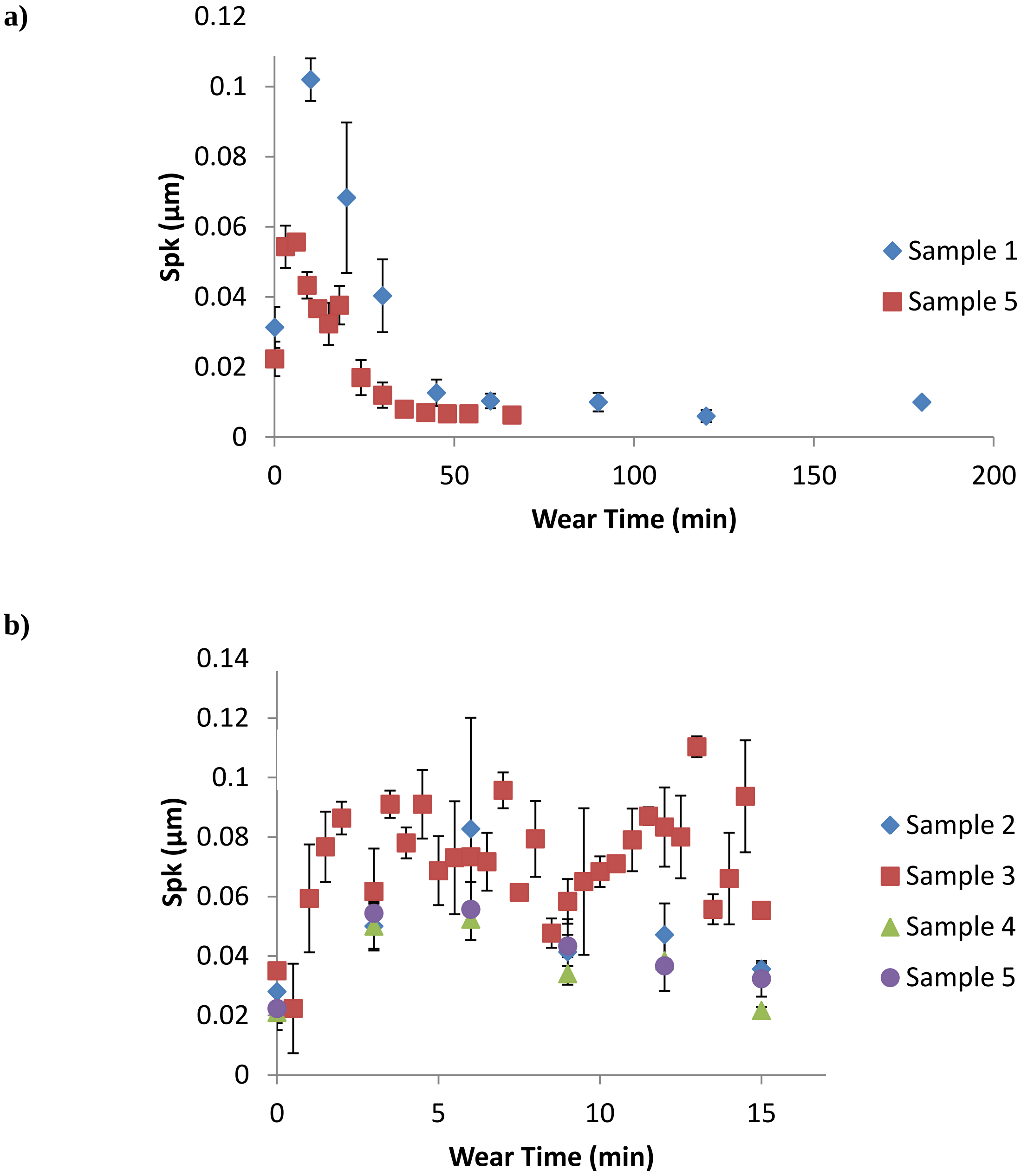

Figure B-10: Evolution of S_{pk} as a surface wears for, (a) long time period, and (b) short time period.

a)

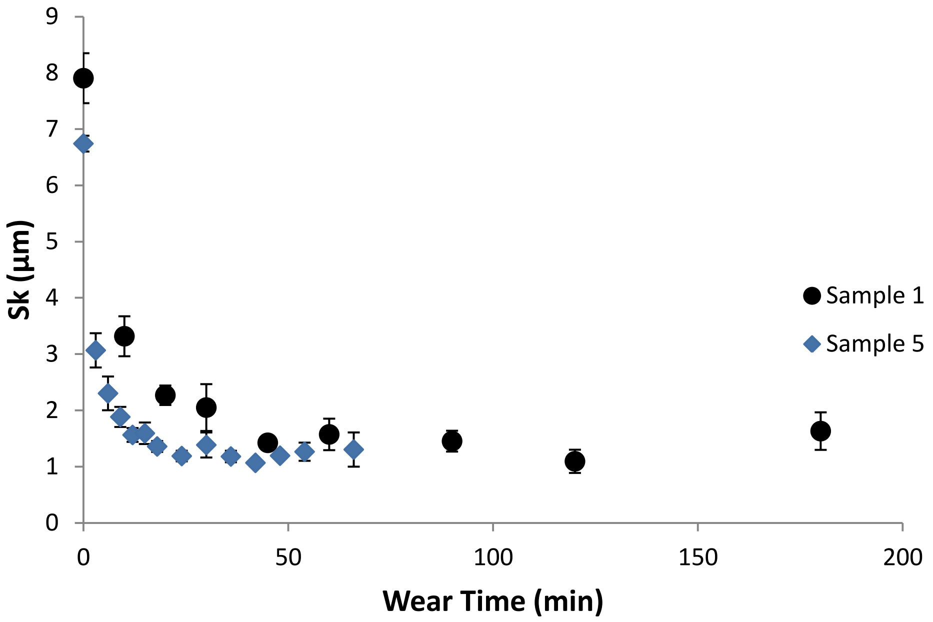

b)

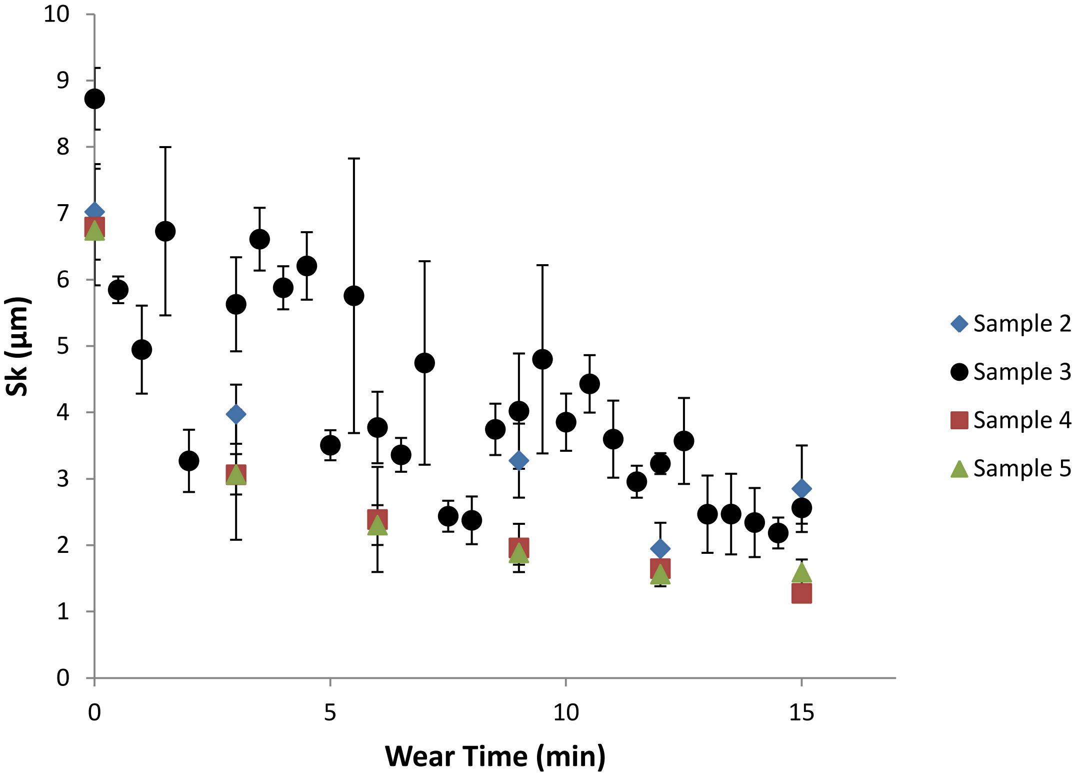

Figure B-11: Evolution of S_k as a surface wears for, (a) long period of time, and (b) short period of time. Error bars show the standard deviation in the parameter.

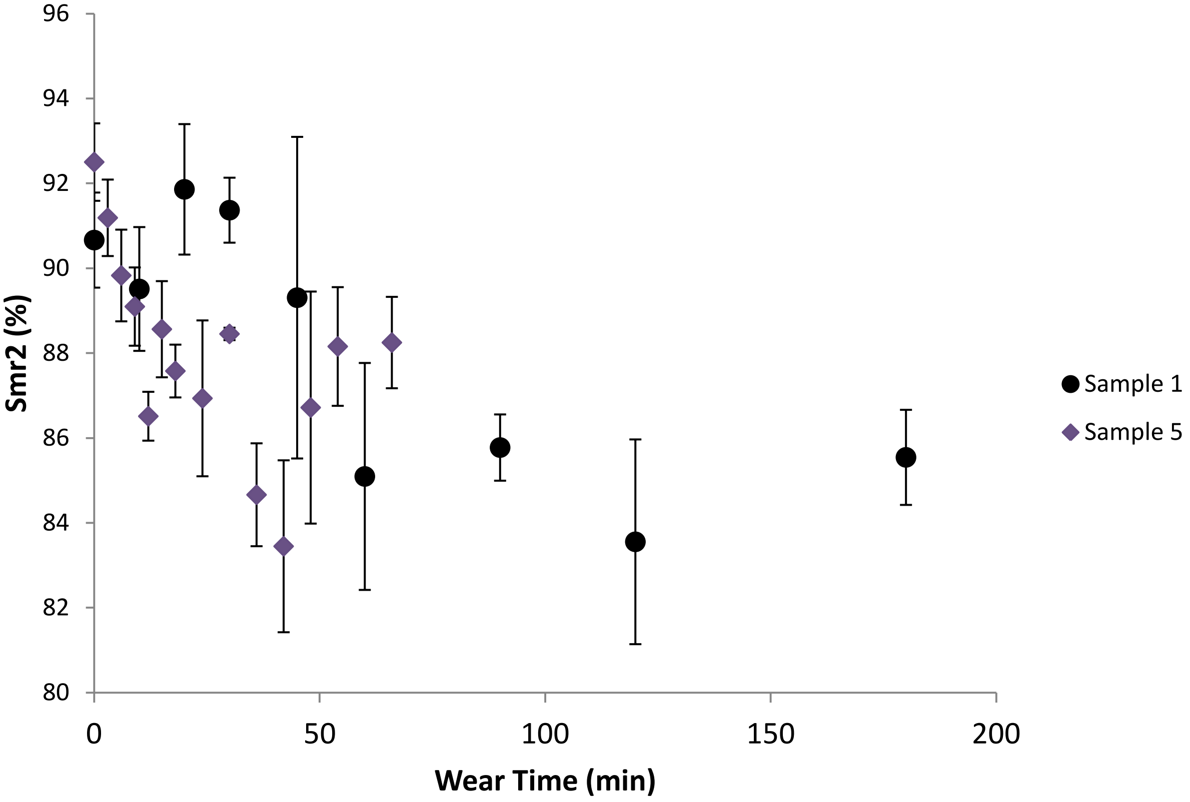

Figure B-12: Evolution of S_{mr2} as a surface wears for a long duration of time. Error bars show the standard deviation in the parameter.

a)

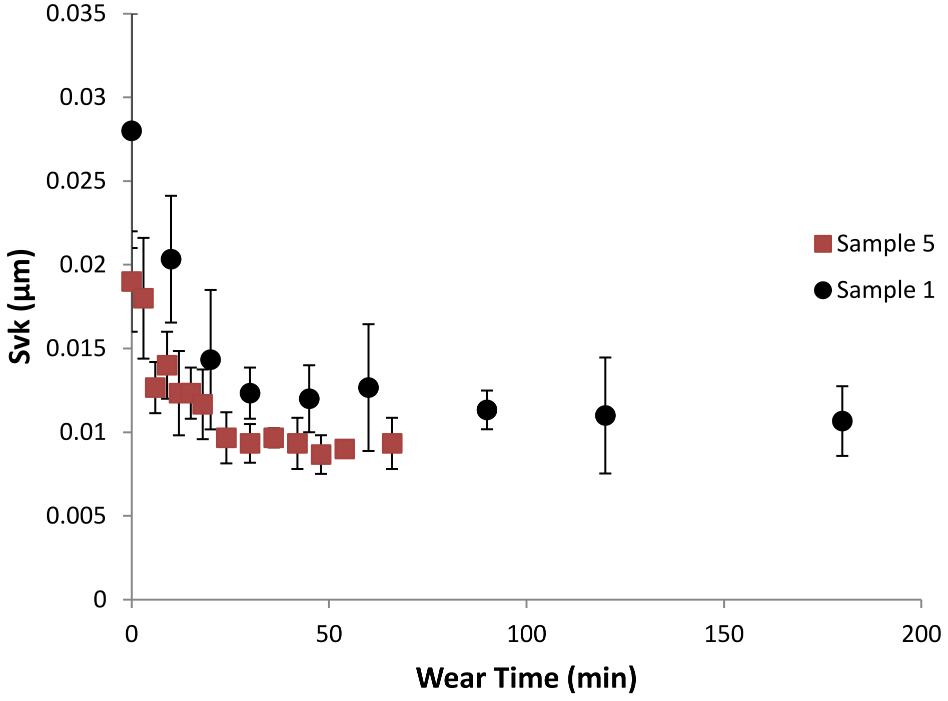

b)

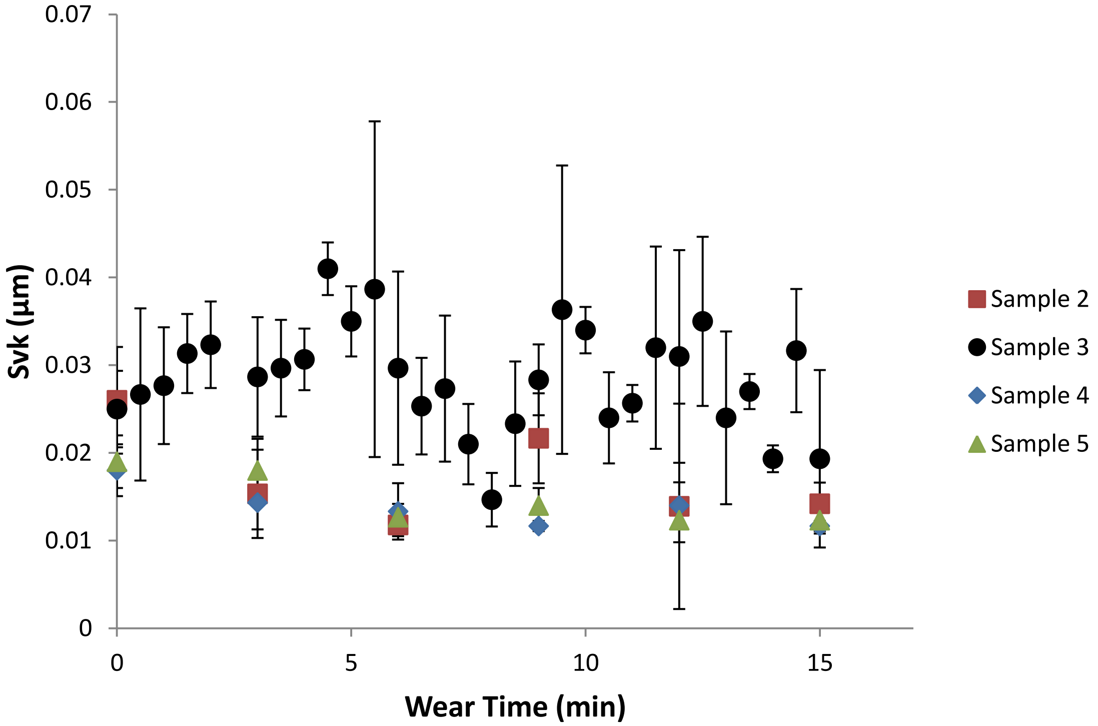

Figure B-13: Evolution of S_{vk} as a surface wears for, (a) long time period, and (b) short time period. Error bars show the standard deviation in the parameter.

Appendix C

C.1 Diamond Square algorithm MATLAB® code.

The code is originally written by Alexandre Carette and can be found at

https://code.google.com/p/shader-artist/source/browse/Matlab/diamondsquare.m?r=36203a084f65e443ef6bc0f4e751b1915c1ceac6

The code is licensed under GNU Lesser general public license [1], which permits copying and distribution of the code and any modification done to the code should be stated. The only modification done to the code was addition of annotations, to help explain the code in a functional way. The modification was done on 6 August, 2012.

Function takes typically five parameters and generates a virtual terrain. Input parameters are *nbIt_*,, which is the size of the terrain adhering to (2^n + 1), and *tl_*, *tr_*, *bl_*, *br_* which are the seeder values for the corner of the matrix and help define the overall elevation of the terrain. Output is in the shape of a spatial matrix with size as defined in parameter, *nbIt_*.

```
% Diamond square algorithm
function I = diamondsquare( nbIt_, tl_, tr_, bl_, br_ )

% function I=diamondsquare( nbIt_, tl_, tr_, bl_, br_ )
% creates fractal terrain by midpoint displacement (diamond square algorithm)
% size must be (power of 2) +1, e.g. 257
% The points on the terrain can be seeded. The algorithm first performs
% the diamond step, and then the square step.
% input: size of terrain, (must be (2^x)+1 )
%        and the height values of all the corners of the surface
% output: terrain I


if nargin < 1
    nbIt_ = 3;             % Resolution of the surface
    tl_   = 150;           % upper left corner height value
    tr_   = 10;            % upper right corner height value
    bl_   = 10;            % lower left corner height value
```

```
    br_   = 10;           % lower right corner height value
end

% Setup the 4 corners
I_size = 2^( nbIt_ ) + 1;           % Size of the terrain
I = zeros( I_size, I_size );  % Seeding the matrix with all zeros
I( 1     , 1      ) = tl_;          % Seeding the upper left corner height
value
I( 1     , I_size ) = tr_;          % Seeding the upper right corner height
value
I( I_size, 1      ) = bl_;          % Seeding the lower left corner height
value
I( I_size, I_size ) = br_;          % Seeding the lower right corner height
value

DiamondRandomConstant = 50.0;
SquareRandomConstant = 50.0;

for i = nbIt_ : -1 : 1              % Perform the steps for all the terrain

    squareSize = 2^i + 1;

      ----------------
    % Diamond step
      -----------------

    for j = 1 : squareSize - 1 : size( I, 1 ) - 1
        for k = 1 : squareSize - 1 : size( I, 2 ) - 1
            slope = floor( squareSize/2 );
            centerX = j + slope;
            centerY = k + slope;

            corners = [ I( centerX - slope, centerY - slope ) ;
                        I( centerX - slope, centerY + slope ) ;
                        I( centerX + slope, centerY - slope ) ;
                        I( centerX + slope, centerY + slope ) ];

            I( centerX, centerY ) = mean( corners ) +
DiamondRandomConstant*i*rand( 1 );
        end
    end

      -------------------
    % Square step
      -------------------

    for j = 1 : squareSize - 1 : size( I, 1 ) - 1
        for k = 1 : squareSize - 1 : size( I, 2 ) - 1
            slope = floor( squareSize/2 );
```

```
            centerX = j + slope;
            centerY = k + slope;

            I( centerX - slope, centerY ) = mean( [ I( centerX - slope,
centerY - slope) I( centerX - slope, centerY + slope) ]) +
SquareRandomConstant*i*rand( 1 );
            I( centerX, centerY - slope ) = mean( [ I( centerX - slope,
centerY - slope) I( centerX + slope, centerY - slope) ]) +
SquareRandomConstant*i*rand( 1 );
            I( centerX, centerY + slope ) = mean( [ I( centerX - slope,
centerY + slope) I( centerX + slope, centerY + slope) ]) +
SquareRandomConstant*i*rand( 1 );
            I( centerX + slope, centerY ) = mean( [ I( centerX + slope,
centerY - slope) I( centerX + slope, centerY + slope) ]) +
SquareRandomConstant*i*rand( 1 );
        end
    end
end
```

References

1. "GNU Lesser General public License, version 2.1." Internet: https://www.gnu.org/licenses/lgpl-2.1.html, February 1999 [Dec. 25, 2012].

Appendix D

D.1 MATLAB® code for implementation of the abrasion algorithm

Abrasion methodology followed here to abrade artificial terrains is described by Bigerelle *et al.* [1] in detail. In brief, surface heights are given an erosion probability calculated by an exponential function, and then the surface heights are chosen randomly and abraded. The following section describes the abrasion algorithm code. The code is well annotated. The function is invoked after a call is received from the GUI (described in Appendix D.2). The input values are all received through the GUI itself, and no additional input is needed.

```
function start_clb_mult

% Abrasion algorithm written at Surface Engineering and Instrumentation
%Laboratory, University of Alberta, Canada. Abrasion methodology followed
% here is described by Bigerelle et al.
%[http://dx.doi.org/10.1016/j.triboint.2008.03.015]. In brief, surface
%heights are given a probability to erode according to an exponential
%function, and then the surface heights can be abraded according to the
%desired characteristic. The abrasion process is random. Input to the program
%is through the GUI, including terrain and the other factors used in
%algorithm.

global hds

%global TT % to memorize all the surfaces

global start
global dx0 dy0 dxx dyx  h H sz fromfile sfln
global dh1 dh2 ddh lb1 lb2 c1 p1 cmax
global npb                          % number of processes in a batch
global proc_no


% To check if start button has been pressed on the GUI

if start
    return;
else
    start=true;
    set(hds.stoping,'string',' ');
end



matchExpr='\"[^\"]+\"';
```

```
[startIndex, endIndex, tokIndex, matchStr, tokenStr, exprNames, splitStr] =
regexp(sfln, matchExpr);

% Taking input parameters from the GUI

if fromfile
    npr=length(matchStr);                 % number of processes
else
    npr=npb;                              % number of processes
end

% Adding the name to be appended to the file for storage after the abrasion
%happens. The matrices are stored after each abrasion iteration.

            for pc=1:npr                        % for each process
                proc_no=pc;
                set(hds.edit12,'string',['process No. ' num2str(proc_no)]);
                           if ~start
                               set(hds.stoping,'string','stopped');
                               break;
                           end

% The name of the directories to be created in the root folder
% Topography folder stores the iterated matrixes as .xlsx file,
% Parameters folder stores the roughness parameters after each iteration.

pth1='Topography';
pth2='Parameters';

[s,mess,messid]=mkdir(pth1);
[s,mess,messid]=mkdir(pth2);


if fromfile
    [pathstr, name, ext] = fileparts( matchStr{pc}(2:end-1));
    fln=[name '_' get(hds.pref,'string')   '_roughness.xlsx'];
else
    fln=['proc' num2str(pc) '_' get(hds.pref,'string')   '_roughness.xlsx'];
end
fln20=get(hds.tpref,'string');

yy=get(hds.y,'value');

dha=dh1:ddh:dh2; % range of height to be abraded at
                 % each iteration from pixels


% Defining the parameter names

pn={'Sa';
'Sq';
'Ssk';
'Sku';
'Ssc';
'Sdq';
'Sdq6';
'Sdr';
```

```
'Sds';
'Std';
'Stdi';
'Srw';
'Srwi';
'Shw';
'Sfd';
'Scl20';
'Scl37';
'Str20';
'Str37';
'Sal';
'Str'};


XL=horzcat('Surf. Parameters',pn'); % for excel
XL=vertcat(XL,cell(1,1+length(pn)));
X1=horzcat('Iteration No.',cell(1,length(pn)));
XL=vertcat(XL,X1);

cml=[-25 25]; % colormap limits (on the GUI)

% Checking if the file in input, or if the terrain has to be created

if fromfile

    T = xlsread(matchStr{pc}(2:end-1));
    dx=dxx;
    dy=dyx;

else

    startRandRange=sz/2;
    T=createFractalTerrain(sz, startRandRange, H);
    T=T-mean(T(:));           % make around 0
    T=h*T/max(abs(T(:)));     % set maximal height as h

    dx=dx0;
    dy=dy0;

end

sT=size(T);             % Size of the created terrain
sTt=sT(1)*sT(2);

res=dx;                 % Row resolution of the terrain

% filter size: to be used in various filters further down
% the size needs to be varied according the terrain.
% Hence, the parameters should be calibrated accordingly.

hsizepm=10;                       % pm
hsize=round(hsizepm/res);         % pixels
sigma=hsize/4;


y=(0:sT(1)-1)*dy;             % y-coordinates of pixel's grid
```

```
x=(0:sT(2)-1)*dx;             % x-coordinates of pixel's grid

[X Y]=meshgrid(x,y);          % creating the mesh grid for plotting purposes
ct=round((sT+1)/2);           % center
P = atan2(Y-y(ct(2)),X-x(ct(1)));   % angles for calculating parameter, Sdr

dx2=dx^2;
dy2=dy^2;
dx2y2=dx2+dy2;


hi=imagesc(x,y,T,'parent',hds.axes3);
mx=max(T(:));                             %maximum height of terrain
mn=min(T(:));                             %minimum height of terrain

%colorbar;
colorbar('peer',hds.axes3)    % creating colorbar on the GUI
                              % to see the 3D profile

set(hds.axes3,'Clim',cml);
hs=surf(x,y,T,'parent',hds.axes1);
set(hs,'EdgeColor','none');
axis(hds.axes1,'equal');
light('Parent',hds.axes1);

yyy=round(yy*sT(1));
if yyy<1
    yyy=1;
end

% Labelling the axis on the various GUI
% plots 3D, 2D and line profiles.

hp=plot(x,T(yyy,:),'b-','parent',hds.axes4);

ht=title(hds.axes3,' ');

xlabel(hds.axes1,'x, pm');
ylabel(hds.axes1,'y, pm');
zlabel(hds.axes1,'z, pm');

xlabel(hds.axes3,'x, pm');
ylabel(hds.axes3,'y, pm');

xlabel(hds.axes4,'x, pm');
ylabel(hds.axes4,'z, pm');

xlabel(hds.axes5,'iteration number');



hh = fspecial('gaussian', hsize,sigma);   % prepare Gaussian filter

lap = fspecial('laplacian');              % Laplacian filter, used in Ssc

sob = fspecial('sobel');            % Sobel operator, gradient, used in Sdq
```

```
R=zeros(cmax,21); % to memorize roughnes parameters,   R( iteration_number ,
roughnes_parameter_number)


% for parameter, Std:
stth=pi/64;
theta=0:stth:pi-stth;
rho=10:1:(min(sT)-1)/2;
[th rh]=meshgrid(theta,rho);
[Xm,Ym] = pol2cart(th,rh);
sT=size(T);
ct=(sT+1)/2; % center
Xm=[-Xm+ct(2); Xm+ct(2)];
Ym=[-Ym+ct(1); Ym+ct(1)];
rhoe=[rho, rho];


[Xp Yp]=meshgrid(1:sT(2),1:sT(1));

% for autocorrelation:
sTa=2*sT-1;
stth=pi/64;
thetaa=0:stth:2*pi-stth;
rhoa=1:1:sqrt(2)*max(sTa);
[th rh]=meshgrid(thetaa,rhoa);
[Xma,Yma] = pol2cart(th,rh);
ct=(sTa+1)/2; % center
Xma=Xma+ct(2);
Yma=Yma+ct(1);
[Xpa Ypa]=meshgrid(1:sTa(2),1:sTa(1));

% before abrading:
% The matrix and parameters are saved in a .xlsx file.

if fromfile
    fln2=[pth1 '/' name '_' fln20 '_topography_unworn.xlsx' ];
else
    fln2=[pth1 '/' 'proc' num2str(pc) '_' fln20 '_topography_unworn.xlsx' ];
end
xlswrite(fln2,T);

Rb=zeros(21,1);         % to memorize roughness parameters,
T1=T-mean(T(:));        % delete mean

% The parameter values are calculated before abrading

Sa=calc_Sa(T1);
Sq=calc_Sq(T1);
Ssk=calc_Ssk(T1,Sq);
Sku=calc_Sku(T1,Sq);
Ssc=calc_Ssc(T1,lap);
Sdq=calc_Sdq_v2(T1,dx,dy);
Sdq6=calc_Sdq6(T1,dx,dy);
Sdr=calc_Sdr(T1,dx,dy);
Sds=calc_Sds(T1,dx,dy);
[Std Stdi Srw Srwi Shw Sfd]=calc_Std(T1,Xp,Yp,Xm,Ym,theta,rhoe);
```

```
[Scl20              Scl37              Str20              Str37              Sal
Str]=autocorrelation_parameters(T1,Xpa,Ypa,Xma,Yma,thetaa,rhoa);


Rb(1)=Sa;
Rb(2)=Sq;
Rb(3)=Ssk;
Rb(4)=Sku;
Rb(5)=Ssc;
Rb(6)=Sdq;
Rb(7)=Sdq6;
Rb(8)=Sdr;
Rb(9)=Sds;
Rb(10)=Std;
Rb(11)=Stdi;
Rb(12)=Srw;
Rb(13)=Srwi;
Rb(14)=Shw;
Rb(15)=Sfd;
Rb(16)=Scl20;
Rb(17)=Scl37;
Rb(18)=Str20;
Rb(19)=Str37;
Rb(20)=Sal;
Rb(21)=Str;
X11= num2cell(Rb');
X1=horzcat('unworn',X11);
XL=vertcat(XL,X1);

% select graph:
sgv=get(hds.listbox1,'value');
set(hds.sg,'string',pn{sgv});
hpg=plot([0 0],[Rb(sgv) Rb(sgv)],'b.-');

xlabel(hds.axes5,'iteration number');

% The abrasion loop starts and continues
% iteratively until 'cmax' abrasion are completed

for c=1:cmax
    if ~start
        set(hds.stoping,'string','stopped');  % To check if program has not
                                              % been stopped from the GUI
        break;
    end

    if c<=c1
        lb=lb1;               % Lambda for first half of the program
    else
        lb=lb2;               % lambda for second part
    end


    Tf=imfilter(T, hh, 'replicate');    % apply Gaussian filter,
                                        %'replicate' - to prevent edge effect

    % apply abrasion algorithm relative to Tf smooth level:
```

```
    dT=T-Tf;
    dTs=dT-min(dT(:));

    Rt=max(dT(:))-min(dT(:));

    % Calculating abrasion probability of the peaks
W=1-((1-exp(-lb*(Rt-dTs)))/(1-exp(-lb*Rt)));

% Compare abrasion probability with a generated random number

    if c<=c1
        bi=(rand(sT)<W)&(rand(sT)<p1);    % not for all pixels but
                                          % to a fraction p1
    else
        bi=(rand(sT)<W);                  % to all pixels
    end

    dhai=randi(length(dha));              % find random index of dha
    dh=dha(dhai);
    T(bi)=T(bi)-dh;                       % Abrade the pixel
    set(hi,'CData',T);
    set(ht,'string',['c=' num2str(c)]);

    T1=T-mean(T(:));                      % delete mean

% Calculate all the roughness parameters

    Sa=calc_Sa(T1);
    Sq=calc_Sq(T1);
    Ssk=calc_Ssk(T1,Sq);
    Sku=calc_Sku(T1,Sq);
    Ssc=calc_Ssc(T1,lap);
    Sdq=calc_Sdq_v2(T1,dx,dy);
    Sdq6=calc_Sdq6(T1,dx,dy);
    Sdr=calc_Sdr(T1,dx,dy);
    Sds=calc_Sds(T1,dx,dy);
    [Std Stdi Srw Srwi Shw Sfd]=calc_Std(T1,Xp,Yp,Xm,Ym,theta,rhoe);
    [Scl20            Scl37            Str20            Str37            Sal
Str]=autocorrelation_parameters(T1,Xpa,Ypa,Xma,Yma,thetaa,rhoa);

% Write in the excel file with first row being
% the values detailed underneath.

    R(c,1)=Sa;
    R(c,2)=Sq;
    R(c,3)=Ssk;
    R(c,4)=Sku;
    R(c,5)=Ssc;
    R(c,6)=Sdq;
    R(c,7)=Sdq6;
    R(c,8)=Sdr;
    R(c,9)=Sds;
    R(c,10)=Std;
    R(c,11)=Stdi;
    R(c,12)=Srw;
    R(c,13)=Srwi;
```

```
    R(c,14)=Shw;
    R(c,15)=Sfd;
    R(c,16)=Scl20;
    R(c,17)=Scl37;
    R(c,18)=Str20;
    R(c,19)=Str37;
    R(c,20)=Sal;
    R(c,21)=Str;

    X11= num2cell(R(c,:));
    X1=horzcat(num2str(c),X11);
    XL=vertcat(XL,X1);
    xlswrite([pth2 '/' fln],XL);

 % Appending filenames to the excel
 % file including the iteration number

    if fromfile
        fln2=[pth1  '/'  name  '_'  fln20  '_topography_iteration_'  num2str(c)
'.xlsx' ];
    else
        fln2=[pth1  '/'  'proc'  num2str(pc)  '_'  fln20  '_topography_iteration_'
num2str(c) '.xlsx' ];
    end
    xlswrite(fln2,T);

    set(hs,'ZData',T);

    % y=const line graph:
    yy=get(hds.y,'value');
    yyy=round(yy*sT(1));
    if yyy<1
        yyy=1;
    end
    set(hds.ytx,'string',num2str((yyy-1)*dy));
    set(hp,'YData',T(yyy,:));

    set(hds.text20,'string',num2str(min(y)));
    set(hds.text21,'string',num2str(max(y)));


    % select graph:
    sgv=get(hds.listbox1,'value');
    set(hds.sg,'string',pn{sgv});
    %hpg=plot([0 0],[Rb(sgv) Rb(sgv)],'b.-');
    set(hpg,'XData',1:c,'YData',R(1:c,sgv));

% Draw the various 3D, 2D and line profiles after the iteration

    drawnow;
end

xlswrite([pth2 '/' fln],XL);  % write the values to the files


end % end of process loop
```

```
start=false;
```

D.2 GUI code

The code for implementing the GUI. This code is compiled to initiate the GUI, no other parameter needs to be entered manually. The GUI records all the variables and sends the required calls to the needed MATLAB files by itself. The GUI was created using GUI Development environment provided by Mathworks [2]. Following figures (Figure D-1 and Figure D-2) detail the GUI.

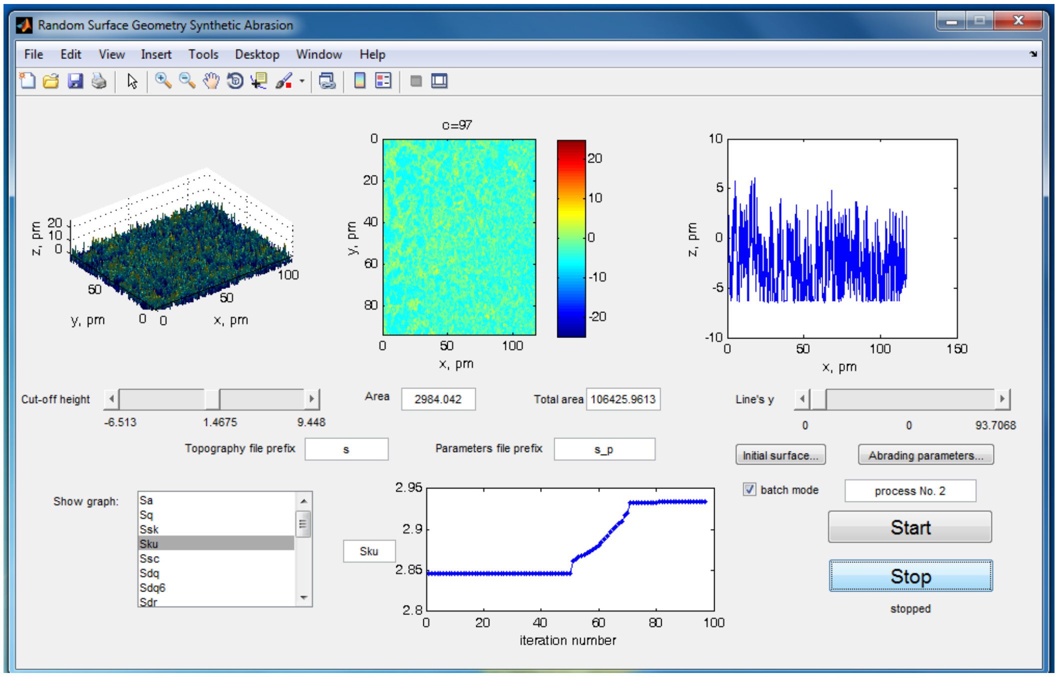

Random Surface Geometry Synthetic Abrasion

Cut-off height -6.513 1.4675 9.448

Area 2984.042

Total area 106425.9613

Line's y 0 0 93.7068

Topography file prefix s

Parameters file prefix s_p

Show graph: Sku

☑ batch mode

process No. 2

stopped

Figure D-1 – GUI implementaion of the abrasion algorithm. Upper part shows the 3D, 2D and line profiles. The slider bar menus underneath 3D profile allows to calculate the surface area above a cut-off height, the values are displayed alongside. Slider bar menu underneath the line profile shows the profile at selected row. The parameter behavior is displayed in the graphs, which can be selected from the options given alongside. Pressing ‘Initial surface’ and ‘abrading parameters’ button displays a popup, shown in Figure C-2.

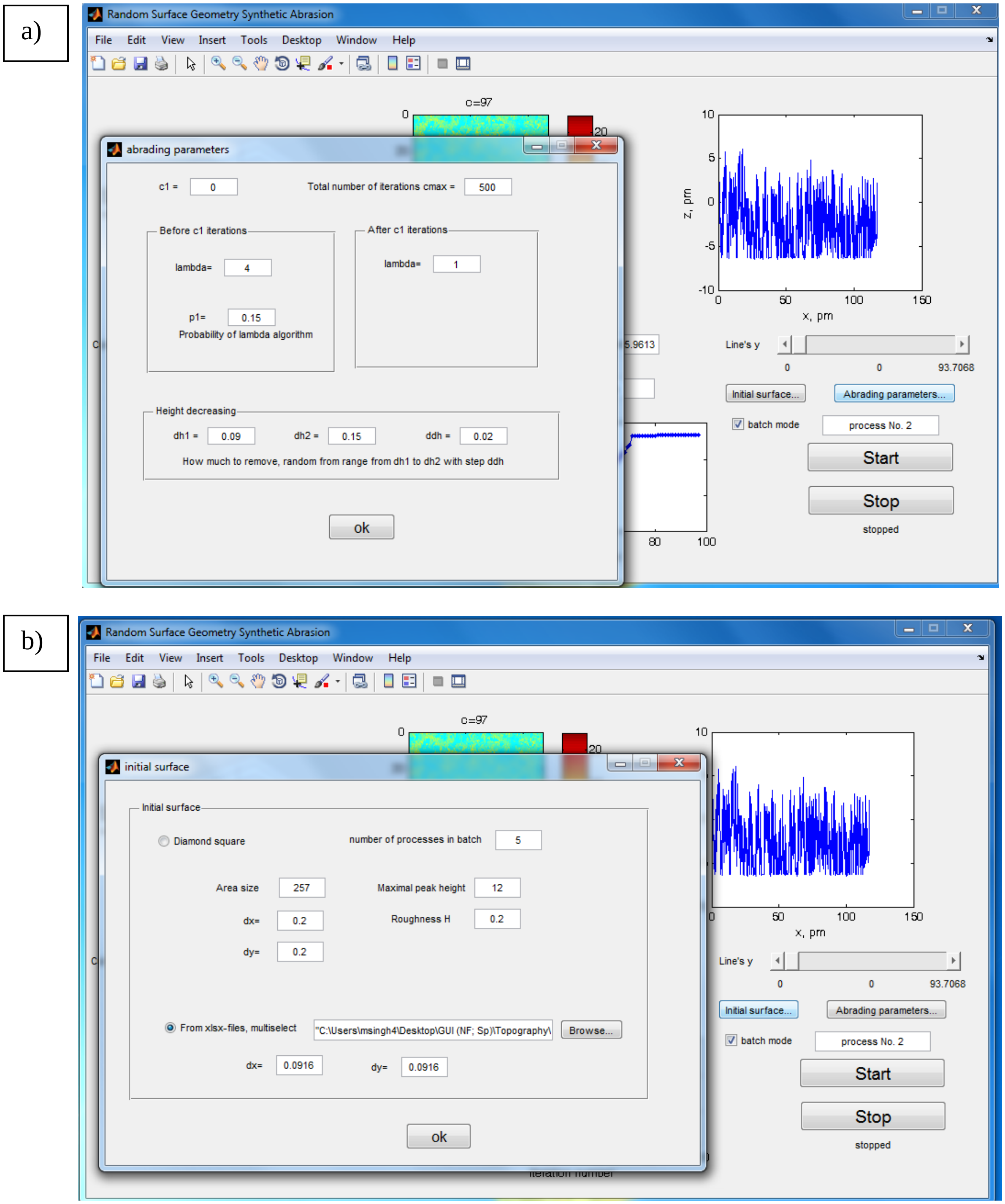

abrading parameters

c1 = 0

Total number of iterations cmax = 500

Before c1 iterations

lambda= 4

p1= 0.15

Probability of lambda algorithm

After c1 iterations

lambda= 1

Height decreasing

dh1 = 0.09 dh2 = 0.15 ddh = 0.02

How much to remove, random from range from dh1 to dh2 with step ddh

5.9613

Line's y 0 0 93.7068

☑ batch mode process No. 2

stopped

initial surface

Initial surface

○ Diamond square

number of processes in batch 5

Area size 257

Maximal peak height 12

dx= 0.2

Roughness H 0.2

dy= 0.2

● From xlsx-files, multiselect "C:\Users\msingh4\Desktop\GUI (NF; Sp)\Topography\

dx= 0.0916 dy= 0.0916

Line's y 0 0 93.7068

☑ batch mode process No. 2

stopped

Figure D-2 – a) Abrading parameters popup. *c1* is the iterations to be performed in first part on p1 percent surface topography. The Δh height matrix iteration limits are also to be inputted here, and b) The initial surface popup giving granular control over input of terrain. Either the terrain can be created using Diamond square algorithm, or files can be inputted directly.

```
function varargout = gui1(varargin)
% GUI1 MATLAB code for gui1.fig
%      GUI1, by itself, creates a new GUI1 or raises the existing
%      singleton*.
%
%      H = GUI1 returns the handle to a new GUI1 or the handle to
%      the existing singleton*.
%
%      GUI1('CALLBACK',hObject,eventData,handles,...) calls the local
%      function named CALLBACK in GUI1.M with the given input arguments.
%
%      GUI1('Property','Value',...) creates a new GUI1 or raises the
%      existing singleton*.  Starting from the left, property value pairs are
%      applied to the GUI before gui1_OpeningFcn gets called.  An
%      unrecognized property name or invalid value makes property application
%      stop.  All inputs are passed to gui1_OpeningFcn via varargin.
%
%      *See GUI Options on GUIDE's Tools menu.  Choose "GUI allows only one
%      instance to run (singleton)".
%
% See also: GUIDE, GUIDATA, GUIHANDLES

% Edit the above text to modify the response to help gui1

% Last Modified by GUIDE v2.5 11-Aug-2012 09:42:53

% Begin initialization code - DO NOT EDIT
gui_Singleton = 1;
gui_State = struct('gui_Name',       mfilename, ...
                   'gui_Singleton',  gui_Singleton, ...
                   'gui_OpeningFcn', @gui1_OpeningFcn, ...
                   'gui_OutputFcn',  @gui1_OutputFcn, ...
                   'gui_LayoutFcn',  [] , ...
                   'gui_Callback',   []);
if nargin && ischar(varargin{1})
    gui_State.gui_Callback = str2func(varargin{1});
end

if nargout
    [varargout{1:nargout}] = gui_mainfcn(gui_State, varargin{:});
else
    gui_mainfcn(gui_State, varargin{:});
end
% End initialization code - DO NOT EDIT


% --- Executes just before gui1 is made visible.
function gui1_OpeningFcn(hObject, eventdata, handles, varargin)
global hds
global start
global dx0 dy0 dxx dyx h H sz fromfile sfln
global dh1 dh2 ddh lb1 lb2 c1 p1 cmax
global npb % number of processes in a batch
global proc_no

% This function has no output args, see OutputFcn.
% hObject    handle to figure
```

```
% eventdata  reserved - to be defined in a future version of MATLAB
% handles    structure with handles and user data (see GUIDATA)
% varargin   command line arguments to gui1 (see VARARGIN)

% Choose default command line output for gui1
handles.output = hObject;

% Update handles structure
guidata(hObject, handles);

hds=handles;
start=false;

fromfile=false;
sfln='';

% All of the following values need to be inputted in the GUI itself, no
% modification is required here.


% defining resolution of the terrain

dx0=0.2;
dy0=0.2;
dxx=0.2;
dyx=0.2;

% height decreasing: Creating height matrix, from which Δh will be chosen
% which will abrade the height pixels

dh1=1.4;          % Lower limit of the height matrix
dh2=1.5;          % Upper limit of the height matrix
ddh=0.05;         % Step range


% lambda values

lb1=4;      % before c1 iterations
lb2=2;      % after c1 iterations

c1=100;     % Iterations to be performed in first part

p1=0.15;    % probability of lambda algorithm within first c1 iterations

cmax=500;   % total number of iterations

npb=5;      % number of processes in a batch

proc_no=0;

% UIWAIT makes gui1 wait for user response (see UIRESUME)
% uiwait(handles.figure1);


% eventdata  reserved - to be defined in a future version of MATLAB
% handles    structure with handles and user data (see GUIDATA)
```

```
% Get default command line output from handles structure
varargout{1} = handles.output;


% --- Executes during object creation, after setting all properties.
function y_CreateFcn(hObject, eventdata, handles)
% hObject    handle to y (see GCBO)
% eventdata  reserved - to be defined in a future version of MATLAB
% handles    empty - handles not created until after all CreateFcns called

% Hint: slider controls usually have a light gray background.
if isequal(get(hObject,'BackgroundColor'),
get(0,'defaultUicontrolBackgroundColor'))
    set(hObject,'BackgroundColor',[.9 .9 .9]);
end


% --- Executes during object creation, after setting all properties.
function coh_CreateFcn(hObject, eventdata, handles)
% hObject    handle to coh (see GCBO)
% eventdata  reserved - to be defined in a future version of MATLAB
% handles    empty - handles not created until after all CreateFcns called

% Hint: slider controls usually have a light gray background.
if isequal(get(hObject,'BackgroundColor'),
get(0,'defaultUicontrolBackgroundColor'))
    set(hObject,'BackgroundColor',[.9 .9 .9]);
end

% --- Executes during object creation, after setting all properties.
function area_CreateFcn(hObject, eventdata, handles)
if ispc && isequal(get(hObject,'BackgroundColor'),
get(0,'defaultUicontrolBackgroundColor'))
    set(hObject,'BackgroundColor','white');
end

if ispc && isequal(get(hObject,'BackgroundColor'),
get(0,'defaultUicontrolBackgroundColor'))
    set(hObject,'BackgroundColor','white');
end

% --- Executes during object creation, after setting all properties.
function tpref_CreateFcn(hObject, eventdata, handles)
% hObject    handle to tpref (see GCBO)
% eventdata  reserved - to be defined in a future version of MATLAB
% handles    empty - handles not created until after all CreateFcns called

% Hint: edit controls usually have a white background on Windows.
%       See ISPC and COMPUTER.
if ispc && isequal(get(hObject,'BackgroundColor'),
get(0,'defaultUicontrolBackgroundColor'))
    set(hObject,'BackgroundColor','white');
end
```

```
% --- Executes during object creation, after setting all properties.
function pref_CreateFcn(hObject, eventdata, handles)
% hObject    handle to pref (see GCBO)
% eventdata  reserved - to be defined in a future version of MATLAB
% handles    empty - handles not created until after all CreateFcns called

% Hint: edit controls usually have a white background on Windows.
%       See ISPC and COMPUTER.
if ispc && isequal(get(hObject,'BackgroundColor'),
get(0,'defaultUicontrolBackgroundColor'))
    set(hObject,'BackgroundColor','white');
end

% Hint: edit controls usually have a white background on Windows.
%       See ISPC and COMPUTER.
if ispc && isequal(get(hObject,'BackgroundColor'),
get(0,'defaultUicontrolBackgroundColor'))
    set(hObject,'BackgroundColor','white');
end

% --- Executes during object creation, after setting all properties.
function res_CreateFcn(hObject, eventdata, handles)
if ispc && isequal(get(hObject,'BackgroundColor'),
get(0,'defaultUicontrolBackgroundColor'))
    set(hObject,'BackgroundColor','white');
end

function h_Callback(hObject, eventdata, handles)
if ispc && isequal(get(hObject,'BackgroundColor'),
get(0,'defaultUicontrolBackgroundColor'))
    set(hObject,'BackgroundColor','white');
end

function HH_Callback(hObject, eventdata, handles)
if ispc && isequal(get(hObject,'BackgroundColor'),
get(0,'defaultUicontrolBackgroundColor'))
    set(hObject,'BackgroundColor','white');
end

% --- Executes on button press in start.
function start_Callback(hObject, eventdata, handles)
global hds
if get(hds.checkbox1,'value')
    start_clb_mult;
else
    start_clb;
end

if ispc && isequal(get(hObject,'BackgroundColor'),
get(0,'defaultUicontrolBackgroundColor'))
    set(hObject,'BackgroundColor','white');
end

% --- Executes on button press in stop.
function stop_Callback(hObject, eventdata, handles)
global start
if start
```

```
    start=false;
    set(handles.stoping,'string','stopping...');
    drawnow;
end

% --- Executes on button press in isf.
function isf_Callback(hObject, eventdata, handles)
global start
if ~start
    init_surf_window;
end

% --- Executes on button press in ap.
function ap_Callback(hObject, eventdata, handles)
global start
if ~start
    adb_pars_window;
end

% --- Executes on button press in checkbox1.
function checkbox1_Callback(hObject, eventdata, handles)
global proc_no
global start
if ~start
    set(handles.edit12,'string',['process No. ' num2str(proc_no)]);
    if get(hObject,'Value')
        set(handles.edit12,'visible','on');
    else
        set(handles.edit12,'visible','off');
    end
end

if ispc && isequal(get(hObject,'BackgroundColor'),
get(0,'defaultUicontrolBackgroundColor'))
    set(hObject,'BackgroundColor','white');
end
```

References

1. M. Bigerelle, B. Hagege, and M. El Mansori, "Mechanical modelling of micro-scale abrasion in superfinish belt grinding," *Tribology International*, vol. 41, no. 11, pp. 992–1001, Nov. 2008.
2. "MATLAB GUI", Internet: http://www.mathworks.com/discovery/matlab-gui.html [accessed 16 Aug., 2012].